CHARACTERISATION OF IN718 FASTENERS FOR AERO-ENGINE APPLICATIONS

By

YUEAN MA

UNIVERSITY OF BIRMINGHAM

A thesis submitted to The University of Birmingham for the degree of

DOCTOR OF PHILOSOPHY

School of Metallurgy and Materials

College of Engineering and Physical Sciences

University of Birmingham

May 2023

Abstract

Standard IN718 fasteners are widely employed in aeroengine applications owing to their exceptional mechanical properties, including tensile, fatigue and creep strength at temperatures up to 650°C. Notably, IN718 is a cost-effective choice compared with other alloys [1]. However, the flexibility allowed by the industrial manufacturing specification in the choice of raw material and determining the solution treatment temperature range introduces variations in microstructure of bolt and consequently mechanical performance of the bolts [2].

This project focused on examining the microstructure and mechanical properties in the threaded section of IN718 bolts. Bending tests were carried out on the split bolts at 650°C to evaluate the influence of possible microstructural variation and associated failure mechanism. Further investigations into fatigue and creep behaviours were accomplished using the ½" IN718 large bolts through the axial-tension dwell fatigue and stress relaxation tests. These tests also verified the microstructural evolution at the threads under the long-term thermal exposure. As a result, cold rolling in the threaded section demonstrated a clear enhancement in fatigue mechanism at the investigated tempeature. In addition to the shank properties, the IN718 test pieces with simulated microstructures were tested, revealing a profound influence of annealing temperature on dwell fatigue life and a noticeable change in failure mechanism. Microstructural characterisation and fractographic examination were conducted throughout to aid understanding. A manufacturing route of IN718 aero-engine bolts was proposed in the end to better control the microstructure, subsequently the performance of the final products.

Acknowledgements

Firstly, I would like to sincerely thank my academic supervisors Dr Hangyue Li and Prof. Paul Bowen (University of Birmingham) for their invaluable guidance during my postgraduate and doctoral studies. This thesis would not be possible without their continuous support, I will always be grateful for the PhD opportunity and this incredible experience.

I would also like to give the special thanks to my industrial supervisor Dr Wei Li (Rolls-Royce Plc.) for his kind help, insightful suggestions, and intellectual inspirations in my project. His effective feedback kept me improving during the research.

I have the deepest appreciation to Dr Timothy Doel for proofreading my thesis and assisting my mechanical testing. I also thank Mr David Price for teaching me how to operate the testing machines. It has been a great pleasure working in the laboratory with them throughout this research. Additionally, I thank Mr Paul Stanley and Ms Theresa Morris in the Centre for Electron Microscopy (CEM) for helping me with microstructural characterisation.

The financial support provided by the Engineering and Physical Sciences Research Council (EPSRC) in collaboration with Rolls-Royce Plc. has been gratefully received.

Finally, my thanks go to my friends Tom Hobson and Chang Che for the mental support whenever I needed, and my parents for their unwavering love and encouragement throughout my studies.

Table of contents

Chapter 1

1. Background

1.1 The Gas Turbine Aero-Engine

The gas turbine engine has a history of over 100 years. After much research by scientists and engineers, it has become one of the fastest growing technologies and is still being developed today. Turbofan, turbojet, turboshaft and turboprop are the four types of gas turbine used in various applications [1, 2]. The turbofan is the most common in civil aviation. Figure 1-1 shows a schematic of a high-bypass turbofan engine [3, 4]. The fan, compressor, combustion chamber, turbine and exhaust nozzle are the fundamental parts in a turbofan engine. The high-pressure zone is coloured in purple and low-pressure zone is coloured in green in figure 1-1. For instance, the Rolls-Royce Trent 800 is a classic example of a high-bypass turbofan. The temperature and pressure at the different sectors of this engine is shown in figure 1-2 [5]. The high-pressure compressor, combustion chamber and higher-pressure turbine experience the harshest conditions with the temperature reaching 1400-1500°C.

The temperature of the gas determines the efficiency of the engine. Therefore, the turbine entry temperature (TET) is one of the most important factors when designing the engine. The performance of a gas engine can be improved if the TET is increased, in the other words, the TET determines the capability and efficiency of a jet engine. With the great development of materials over 60 years on, until 2000, the TET has been increased by 700K with the significant civil aero-engine evolution [6-8]. The nickel-base superalloys are the best choice to sustain the elevated TET and maintain

the aero-engine properties. Figure 1-3 indicates the materials usages in a typical gas engine. Nickel-base superalloys are utilised for the hottest parts (in red) in the high-pressure compressor and high-pressure turbine embracing the hot air [9].

To achieve a sustainable aviation strategy, aeroengines are expected to be more efficient and consume less fuel. It has been proposed that the compressor exit temperature (T_{30}) should be even higher in some modern aeroengines. This increases the in-service temperature for the aero-engine materials, especially for the high-pressure turbine and high-pressure compressor [10, 11]. One the other hand, re-using materials in aeroengines reduces a great amount of material waste, which benefits not only the environment but also the costs. The fasteners are one of the most important parts facing the challenges of the increasing temperature and the requirement of a longer service life [12].

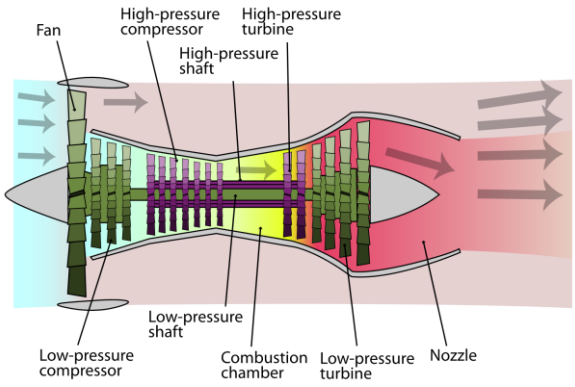

Figure 1-1 Schematic diagram illustrating the operation of a turbofan engine [4].

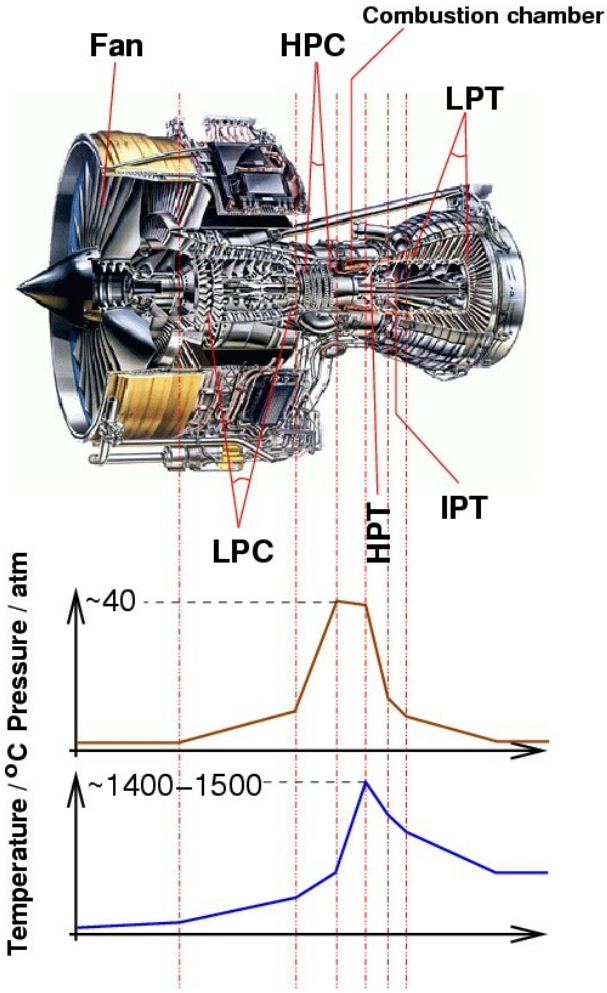

Figure 1-2 A jet engine (Rolls-Royce Trent 800) showing the different stages with the pressure and temperature profiles along the engine. [5]

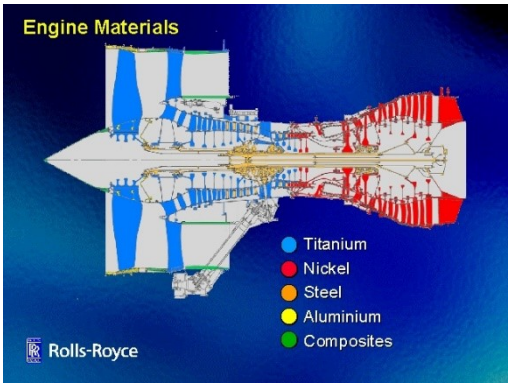

Figure 1-3 An aero-engine profile indicating the material usage [9]

1.1.1 Fastening joints in aeroengine

The fastening joints play a critical role in aeroengines by sealing and connecting the components tightly to guarantee safety. The elastic modulus and stiffness are the primary factors to be considered when designing the fastening joints to keep them from losing the clamping force [13].

The past decades have seen a great development on aero-engine bolts under a wide range of scientific as well as industrial innovation [13-17]. The existing nickel-base superalloys for aero-engine bolts include Inconel 718, ATI Allvac 718Plus, Waspaloy, MP159, AEREX350. These fastener materials are employed in different sectors depending on their properties. Fatigue life, creep resistance, toughness, tolerance to damage, stiffness, weight, manufacturing process and cost are the factors to be considered when choosing the materials for the bolts in an aero-engine [13]. The most vulnerable parts of an aero-engine bolt are the threads and the fillets under the bolt head. Figure 1- 4 presents the crack developing at the thread root, and Figure 1-5 illustrates how an aero-engine bolt fails at the threads and the fillet during the in service conditions [18, 19].

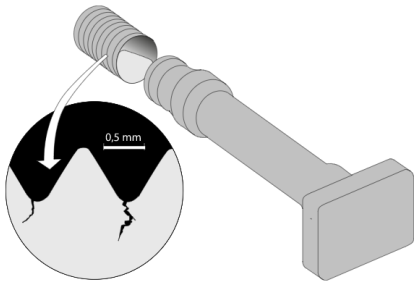

Figure 1- 4 The penetration of cracks at the threads root [19]

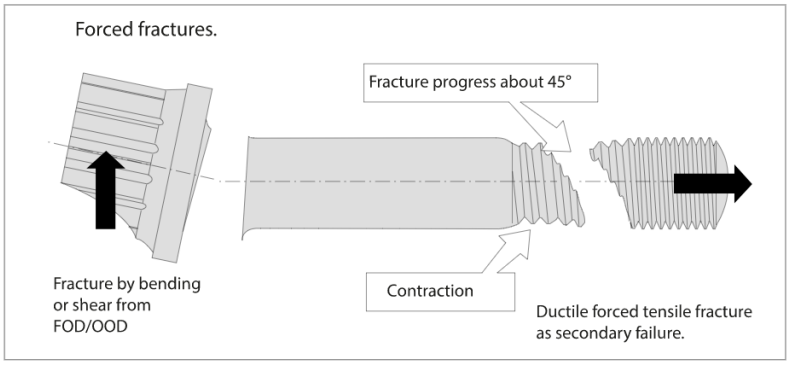

Figure 1-5 The fracture at the threads and fillet during engine operation [20]

In addition, the design of an aero-engine should be based on the worst possible situations in an aero-engine, and the bolts must pass those very strict criteria to provide safe sealing for aero-engine components.

The requirements for aero-engine bolts are:

I. Adequate clamping force during service. To firmly separate different sections and seal the liquid or gas, a sufficient clamping force is vital. A reduced clamping force may lead to undesired high-cycle fatigue (HCF) at the joints. The clamping force loosens mainly due to two causes related to bolts directly in an operating aeroengine. The first one is creep behaviour and sudden overload during running in service. The second possible cause is the different thermal expansion coefficients between the blots and the flange [7].

II. Excellent fatigue resistance. The low-cycle fatigue life should be long enough to cover the service life of the part and the fatigue endurance limit should be higher than the high-cycle fatigue stress which shall be avoided during a flight cycle. The fastened joints may also experience a shear load from the imbalanced cyclic force in some rare cases.

III. High yield strength. The bolts must be able to sustain the impact due to severe failure from other parts, such as fractured fan blades. One of the roles of the bolts is to support the structure/sector to prevent further damage in the engine.

IV. Low notch sensitivity. The bolts with complex geometry need to satisfy a low notch sensitivity to prevent premature crack initiation, especially at the relatively sharp features, such as threads or fillet. The manufacturing process has been improved regarding this. Cold rolling instead of machining introducing the compressive residual stress to the fillet and threads enables the notch sensitivity to be significantly reduced [21].

V. Excellent corrosion resistance. Lubricant or silver coating is needed for installing the bolts, which causes a wet and greasy in-service environment. Corrosion resistance is another challenge for fastener materials while working in hot and high-stressed conditions.

1.2 Project Aims

IN718 is used for up to 70% of fasteners take in most aero-engines due to its excellent properties and low cost [22]. However, with limited IN718 fasteners research in the past, technical specifications for aerospace fasteners allow a wide range of raw material and heat treatment processes, which means further material characterisation work is needed within the required window of the specification to understand the microstructure variations

The following chapters present and analyse the results of microstructural characterisation and a series of mechanical testing, including: three-point bending fatigue on the IN718 bolts, axial fatigue, and dwell fatigue testing on the IN718 bolts,

dwell fatigue and stress rupture testing on the plain and notched IN718 test pieces. Usually, 630°C is suggested to be the IN718 maximum in-service temperature, and the tests conducted in this project were at 650°C to be more conservative. The properties investigated are associated with the typical requirements of an aero-engine bolts. Overall objective is to understand the microstructure variation and mechanical behaviours of the bulk and local cold work regions.

Combining the testing results, Chapter 5 Discussion is to address the questions relevant with the current fastener applications and to put forward an optimised solution of optimising the IN718 manufacturing specification.

- What are the differences in microstructure of IN718 matrix under the different solution-heat-treatments within the specification for IN718 aero-engine bolts?
- Does the microstructure of IN718 bolts change after thermal exposure?
- How does the solution temperature affect the dwell-fatigue behaviour of solution treated IN718?
- How does the cold work affect the fatigue and creep behaviour of IN718 bolts?

Apart from the discussion of the IN718 materials in the academic way, the analysis and discoveries in this project will also help the industry optimise the manufacturing parameters for a safer operation within the specification requirement.

Chapter 2

2. Literature Review

2.1 Nickel-base superalloys

Both chemical composition and manufacturing process of superalloys have been developed significantly over the past decades. With excellent fatigue, creep and corrosion resistance, superalloys are a suitable choice for the harshest working environment. Nickel-base superalloys as one of the most important materials are largely used in aerospace applications, especially the hottest part in aero-engine, i.e., turbine blades [23-24]. The superalloys are mainly strengthened by solid solution and secondary phases precipitates. This study focuses on the strongest strengthening mechanism, precipitation hardening.

The principle of precipitation hardening in nickel-base superalloys is secondary phases precipitating in the disordered Face Centred Cubic (FCC) Gamma matrix (γ). The secondary phases include the ordered FCC gamma prime (γ') i.e. $Ni_3(Ti,Al)$, gamma double prime (γ") i.e. Ni_3Nb. The γ' phase is coherent to the γ matrix, offering the anti-phase boundary (APB) to effectively restrict the dislocation movement at elevated temperature. Gamma double prime (γ") has an ordered Body Centred Tetragonal (BCT) crystal structure and strengthens some nickel alloys below 650°C. It is the main strengthening phase in IN718. Carbides are also common in superalloys. Intragranular carbides provide resistance to dislocation movement. Nano-intergranular carbides help control the grain size [25]. Other phases such as η and δ phases strengthen the materials under certain circumstances but are not always ideal for mechanical

properties. The topologically close pack (TCP) phases, such as σ, μ and laves, significantly decrease the materials ductility [26]. Further study of intermetallics is discussed in the following sections.

2.1.1 Composition

Each type of superalloy has a unique composition. Ni is the fundamental element. Fe and Co are also important participants in solid solution strengthening. Al/Ti combine with Ni to form the strongest γ' precipitates. In the Fe-rich nickel alloys, the main strengthening precipitate is Ni_3Nb (γ"), allowing the materials to operate at a temperature up to 650°C [27-29]. Also, Al and Cr react with oxygen to create a protective layer of Al_2O_3 and Cr_2O_3 which largely helps oxidation and corrosion resistance at high temperature. C actively reacts with metal elements to form carbides, such as MC or $M_{23}C_6$ (M is metal). Borides at grain boundaries have a pinning effect. Additionally, B and Zr are critical for polycrystalline superalloys, especially for creep resistance [30]. Other elements such as Hf, Ta, W, Mo and Re are optional, not all nickel-base superalloys contain them depending on the applications. Such heavy atoms offer solid solution strengthening and very high melting points [8, 31]. Overall, the selection of the composition in superalloys needs to be well-balanced. This is because each composition might benefit one property but compromise another. The key elements and their function and effects is shown in table 2-1.

Table 2-1 The key alloying elements and their functions in superalloys [32].

Elément	Matrix strengthening	Increase in γ′ volume fraction	Grain boundaries	Other effects
Cr	moderate	moderate	$M_{23}C_6$ and M_7C_3	improves corrosion resistance; promotes TCP phases
Mo	high	moderate	M_6C et MC	increases density
W	high	moderate		promotes TCP phases σ et μ (Mo, W)
Ta	high	large		
Nb	high	large	NbC	promotes γ′ and δ phases
Ti	moderate	**very large**	TiC	Al improves oxidation resistance
Al	moderate	**very large**		
Fe		γ->β, η, γ′ or δ		decreases oxidation resistance; promotes TCP phases σ, Laves
Co	slight	moderate in some alloys		raises solidus; may raise or lower solvus
Re	moderate			retards coarsening; increases misfit
C	moderate		carbides	
B, Zr	moderate			inhibit carbide coarsening; improve grain boundary strength; improve creep strength and ductility

2.1.2 Grain Structure

The grain size largely affects a wide range of mechanical properties. Figure 2-1 summaries how the grain size influences the creep resistance, dwell crack growth, low-cycle-fatigue life (LCF) and tensile strength. It clearly shows that the grain size impacts each property differently. Hence, controlling the grain size of a component in aeroengine requires adequate consideration in terms of the in-service conditions, i.e., temperature and stress [33-35].

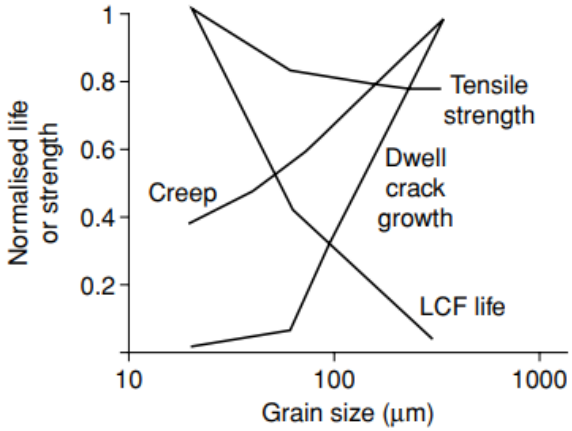

Figure 2-1 Illustrating the important mechanical properties associating with grain size in turbine disc alloys [36]

The grain boundaries are well known to stop dislocation movement within grains and impeding plastic deformation [37]. Grain-boundary or Hall–Petch strengthening is a common method to improve the yield strength by introducing more grain boundaries as the pinning locations for the movement of dislocations within grains. Finer grains offer more grain boundary strength as a result of a higher density of grain boundary [38]. Widely used approaches to adjust the grain size in alloys include recrystallisation and controlling the cooling rate. Small grains can usually be achieved by a fast-cooling rate quenching at the early stage of dynamic recrystallisation [39,40].

The Low-cycle fatigue (LCF) life of the aero-engine components is primarily determined by the take-off period of a flight cycle. Previous studies have proved that grain refinement is an ideal choice for nickel alloys to improve the low-cycle fatigue performance especially crack initiation life, due to the abundant grain boundaries, the refined phases and the other factors [41]. A well acknowledged view by researchers is that smaller grains significantly restrict the number of persistent slip bands (PSBs).

PSBs form during cyclic loading in metal, they actively contribute to crack initiation and the early-stage crack propagation in fatigue [42, 43]. The fine grains with more grain boundaries can effectively impede the development of PSBs and slow down the progress [42].

On the other hand, coarse grain size improves the creep resistance and dwell fatigue performance. Creep failure is one of failure modes in aeroengine, especially for those sections experiencing constant stress under long-term thermal exposure, such as turbine discs. An effective method to prevent creep behaviour is the key to maintain the safety in aeroengine. At a high temperature, a higher rate of diffusion at grain boundaries helps creep to facilitate in alloys. Reducing the grain boundary area effectively slows down the creep process. Specifically, when diffusional creep occurs, the grain boundaries start sliding to stop the grain-boundary separation and avoid formation of voids or cracks. However, if the sliding rate cannot cope with the diffusion rate, the voids or cracks occur, leading eventually to creep failure. A typical example is microvoid coalescence [42, 44].

As previous discussed, dwell fatigue behaviour exists in the engine-run progression. The time-dependant fatigue crack growth involves creep behaviour and induced environmental degradation such as interaction with oxygen [45]. Both mechanisms are highly associated with the grain boundaries and often compete during cycling. Creep resistance can be considerably increased by coarsening the grain size. Dynamic embrittlement (DE) or stress accelerated grain boundary oxidation (SAGBO) under the dwell fatigue condition are the other failure mechanisms and are caused by oxygen induction at the crack tip. The oxides form at the crack tip after exposure for a long period at high temperature with a certain volume expansion, which results in an

increasing stress concentrating at the adjacent grains and the grain boundaries, leading to further crack propagation [46-49].

Other studies also have shown that a faster crack growth rate was observed in nickel alloys under a longer dwell time and a higher stress. This is because intergranular failure was switched on instead of transgranular behaviour. As a result, a faster crack propagation rate was detected [50]. Additionally, smaller grain size promotes the accumulation of the dislocations which encourages environmental embrittlement. Thus, a larger grain size with reduced grain boundaries improves dwell fatigue performance in nickel alloys. Further discussion demonstrated that a well-controlled degree of deformation by local creep could relax the concentrated stress at the crack tip once the crack has formed, resulting in the bluntness of crack tip and lowering the propagating speed [51].

Apart from strength, grain size also influences material toughness, weldability, and ductility. From figure 2-2, all these properties can be increased at different degrees by refining the grain size [52].

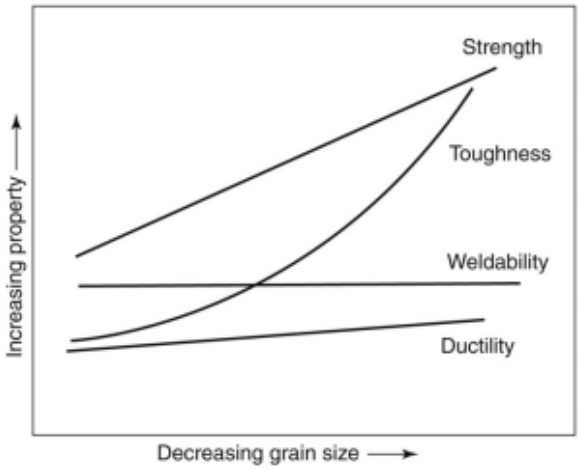

Figure 2-2 The correlation between grain size and material property [52].

2.1.3 Intermetallic Phases

The ageing process is to obtain the target strengthening precipitates, γ' and γ", the most common strengthening phases in nickel-base superalloys. Such precipitates form in the disordered FCC γ matrix during heat treatment to improve the mechanical properties [53, 54].

Gamma Prime γ'

The strengthening phase, γ' precipitates, grows coherently with a small misfit in the γ matrix to ensure a certain ductility of nickel alloys [55]. The crystal structures of γ and γ' are shown in figure 2-2. Both are FCC crystal structure; the latter is ordered with Ni in the face centres and Al or Ti at the corners. Many studies have focused on controlling the γ' size, morphology, and volume fraction to optimise the properties. γ' phase is shown as the fine cubic or spherical shape. At a certain thermal condition (600-850°C), γ' phase tends to transform to eta (η) precipitates after long-term thermal exposure [56].

The thermal stability of nickel alloys is strongly related to the volume fraction of γ'. A higher amount of γ' and a lower amount of η lead to better thermal stability. Some studies show that the volume fraction of γ' can be control by adjusting Al/Ti ratio. The loss of γ' volume fraction is a result of a lower Al/Ti ratio, causing lower thermal stability [57, 58]. The excellent high-temperature strength of superalloys is largely contributed by Anti-Phase Boundary (APB) strengthening due to increasing flow stress of γ' particles from ambient temperature to 700°C, making it more difficult for dislocation motions to cut through. Even though the dislocations would climb pass the γ' phase at

high temperature with a lower steady stress, the γ' particles still largely constrain the movement [60].

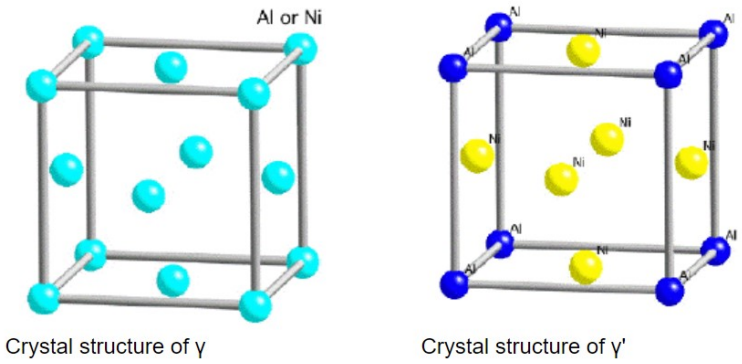

Figure 2- 2 The disordered FCC structure of γ matrix and the ordered FCC structure of γ' phase [59]

Gamma Double Prime γ"

Gamma double prime (γ"), Ni_3Nb / (Ni_3V), is another common strengthening phase in nickel-base superalloys, which is preferred in Fe-rich superalloys, such as IN718. At 620 to 900°C, γ" phase precipitates and grows coherently in the γ matrix. It dissolves above 900°C. However, it is widely acknowledged that the metastable γ" phase struggles to maintain the strength when the temperature is over 650°C, referring the APB strengthening mentioned in the previous section. Long-term thermal exposure over 650°C leads to a transformation of γ" phase to the thermodynamically stable δ phase. Both types of precipitates share the same composition but have different crystal structures. The γ" phase is shown as very small discs with the geometrically close-pack D022 (ordered BCT) structure, dispersed in the FCC matrix.

The precipitation time and temperature are critical to optimise the γ" phase in superalloys. A fast-cooling rate after solution treatment and a double ageing process

largely promotes γ” precipitates. This is because the rapid cooling rate, such as water quenching, creates many nucleation sites for γ” phase and high residual stress, and the following double ageing process offers the conditions for the γ’ and γ” phases to grow intragranularly, as well as partially relieving the induced residual stress [61]. Studies also show that the typical ageing process at 575°C – 720°C within 100 hours benefits the growth of γ” phase. At the lower ageing temperature, the number of γ” precipitates increases with prolonged ageing time; at the higher ageing temperature, the γ” precipitates start coarsening yet the volume fraction remains the same [60, 61]. For the latter case, the coarsening γ” phase may cause a decrease in interfacial area between γ’ and γ” phases, deteriorating the mechanical properties [61].

Some studies found that very fine γ” precipitates are not helpful for the material strength. More nucleation sites for γ” phase are formed by applying the external compressive or tensile stress to the alloy prior to the ageing process. After ageing for 8 hours, the γ” precipitates (25-30nm) are smaller than the ones (36nm) without external stress, and the material strength decrease with the finer γ” precipitates [62].

Apart from the inherent strength provided by γ’ and γ” phase, the anti-phase boundaries formed by the movement of dislocations in such ordered structures introduce a substantially increased creep resistance in IN718 [60, 63]. A great number of studies focus on optimising the interface of γ’ precipitates/matrix and γ” precipitates/matrix to create a compact structure of γ’ and γ” phases. This is created by modifying the content of Al, Ti, and Nb. The smaller cube-shape γ’ precipitates coated on the surface of γ” precipitates can be found in the modified IN718, resulting in a higher thermal stability. This is because γ” precipitates are perpendicular to each other, the driving force of coarsening γ” precipitates is constrained by the coating

structure to prevent the formation the of the large disc-shape γ” phase, and all the interfaces of γ’/γ, γ”/γ and γ”/γ’ become coherent without any weaker transition region [64-66].

Carbides

Carbides, as one of the grain-boundary strengtheners, are also critical in the nickel-base superalloys [67]. Carbon (up to 2% in weight) actively interact with the metal elements such as Nb, Mo, W, Cr, Ta, Ti, and Hf to form FCC structured carbides, the common types of carbides found in the nickel alloys include MC, $M_{23}C_6$ and M_6C, where the carbide former M is metal element. It should be noted that carbides strengthening is not applicable to most superalloys. However, the fine carbides evenly distribute at the grain boundaries to improve the creep resistance, holding the grains tightly from sliding under stress [8, 68-70]. Moreover, they were found to effectively help the phase stability in the superalloys [71].

However, many studies have shown that carbides could deteriorate the material properties depending on the composition and manufacturing process of the superalloys [71]. Often, the carbides might be oxidised when near to the surface, leading to the degrading fatigue life and notch sensitivity for the materials when being thermally exposed [72, 73].

The intragranular MC carbides with the desired size and distribution have been proved to strongly block dislocation movement [8]. The external stress tends to focus on the carbides as they are usually harder than the other phases in superalloys, leading to microcracks around the grain boundaries to alleviate the local stress, slowing down the crack propagation [73]. Additionally, MC carbides at grain boundaries are likely to

encourage the transformation of transgranular fracture to intergranular under a stress concentration at room temperature [73]. The primary MC carbides is one of the common carbides which normally form at the Nb-rich areas in IN718, such as NbC or a mixed compound (Nb,Ti)/C with a certain ratio of Ti/Nb, whereas eutectic carbides normally show a variety of Ti/Nb ratio [74-76].

Overall, the factors to be considered in terms of the advantages and disadvantages of carbides in nickel alloys include carbides distribution, oxidation, carbides size and in-service requirements of the superalloys.

Delta δ

The non-close-packed orthorhombic δ phase widely exits in IN718, sharing the same chemical composition with γ” phase, Ni_3Nb. δ phase contributes very little hardening effect in the alloy. However, it significantly prevents grain growth during heat treatment by pinning the grain boundaries and it also helps the grain boundary against creep fracture in service [61]. The solvus temperature of δ phase is normally within 990~1020˚C, depending on the fluctuations in chemical composition of the alloy, especially the Nb content [77]. When the solution treatment temperature is above the δ solvus, the intragranular γ” phase is maximised while δ phase is significantly diminished, causing the material to be prone to creep fracture and leading to high notch sensitivity. When the temperature is below the δ solvus temperature, more δ phase is precipitated with a lower content of γ” phase, decreasing the strength of IN718 [61].

Many studies have proved that the morphology of δ precipitates significantly affects the properties of nickel alloys. The common shapes of δ phase observed in IN718 are spherical, acicular, or plate-like. The acicular and plate-like δ phase weakens the

mechanical strength in IN718, whereas the intergranular spherical δ phase can effectively pin the grain boundaries [78-80]. Hot working processing is a typical method to deform the plate or needle-like δ precipitates into blocky ones, due to deformation breakage and dissolution breakage during isothermal forging. The precipitates boundaries become the nucleate sites and the transformation can be achieved [81]. In addition, other studies have shown that needle-like δ phase was precipitated below 930°C and the spherical phase formed at a higher temperature [82, 83]**.** The large bolts received in this project were heat treated at 1000°C and contain a small amount of spherical δ phase.

Since the composition of both δ phase and γ” phase is Ni_3Nb, a competitive relationship exists in the alloy with one arising at expense of the other. Long-term thermal exposure above 650°C encourages the transformation of γ” phase to the plate-shape or granular δ phase at the grain boundaries or in the grains. Studies prove that γ” is a metastable phase whereas δ phase is thermally stable in the alloy. The transformation occurs under high temperature or after a prolonged ageing period [84]. To better demonstrate the phase stability in IN718, the equilibrium and nonequilibrium step diagram of IN718 is shown in Figure 2-3 (a) and (b) [96]. It should be noted that the phase fraction of γ” phase in the nonequilibrium diagram was predicted by postponing the formation of δ phase. The temperature and time required to precipitate γ” phase is lower and shorter than δ phase. This allows γ” phase to precipitate first, then δ phase appears when the thermal exposure is long enough or the temperature reaches 900°C. This is above the γ” solvus temperature and γ” phase can no longer precipitate and the existing γ” phase starts transforming to δ phase. [85, 86].

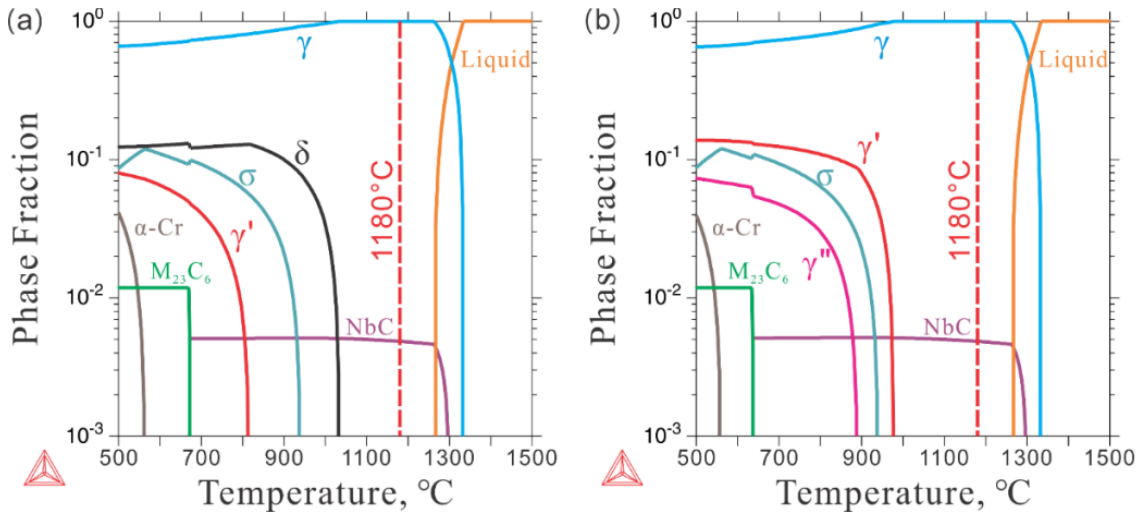

Figure 2-3 Equilibrium (a) and nonequilibrium (b) step diagram of IN718 [96]

The formation of δ phase is closely dependent on the Al/Ti ratio and Al+Ti content. Specifically, γ" precipitates are smaller when the Al/Ti ratio or Al+Ti content is higher, decreasing the mismatch between γ" and γ matrix. It is well known that δ phase is an incoherent Ni_3Nb-based phase in γ matrix precipitating at the grain boundaries and twin grain boundaries or within the grain at a higher temperature [74, 87, 88].

2.2 IN718

Inconel 718 (IN718) is a well-known and time-tested nickel-based alloy with excellent mechanical properties and high resistance to corrosion. Compared with other high-strength superalloys, IN718 is very competitive in aerospace industry and relatively cheap. Combining these two factors, the applications of IN718 are versatile from cryogenic temperature to relatively high temperature. It has been successfully used in-service for decades in a variety of industries [89].

2.2.1 Microstructure of IN718

IN718 is strengthened by precipitates in the face centred cubic matrix (γ). The strengthening secondary phases are mainly γ" phase i.e. Ni_3Nb, and a small amount of γ' phase i.e. $Ni_3(Ti,Al)$. The γ" phase normally precipitates below 900℃ in IN718. Theoretically the volume fraction of γ" phase takes up to 21% [61, 90], and the 4% γ' phase provides very little strength in IN718 [74]. Apart from the primary precipitates, another precipitate forming along the grain boundaries in IN718 is δ phase, making a positive contribution on controlling the grain size and benefiting some mechanical properties under certain circumstances [86]. It should be noted that δ phase and γ" share the same composition (Ni_3Nb), however, the crystal structure of γ" is body-centred tetragonal (BCT) whereas that of δ is orthorhombic [91]. IN718 TTT diagram is shown in Figure 2-4 (a) [92].

As previously discussed, the grain size in IN718 highly depends on the amount of δ phase precipitated at the grain boundaries. When the solution temperature is lower than δ solvus temperature but high enough to precipitate δ phase, a great amount of δ phase appears and the pinning effect is maximised, thus, the grain size is smaller. When the solution temperature is higher than the δ solvus temperature, no δ phase can be precipitated, and the grain size is larger. For example, solution treatment at 955°C for an hour followed by a double ageing process resulted in a grain size of 20-40um, whereas increasing the solution temperature to 1035°C, the grain size was increased to 80μm shown in Figure 2-4 (b) [93].

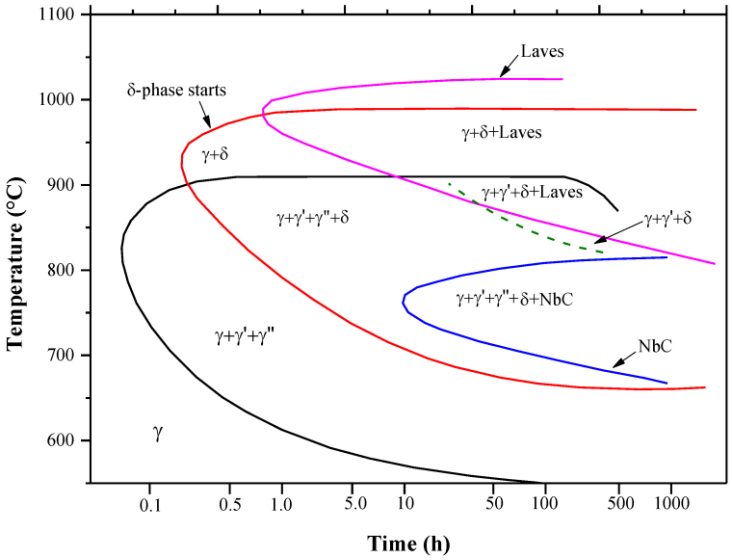

Figure 2-4 (a) IN718 TTT diagram [92]

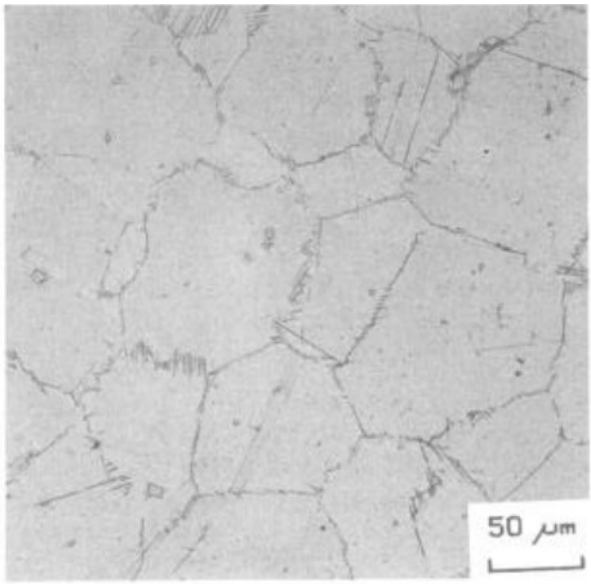

Figure 2-4 (b) Coarse grains in IN718 after solution treatment at 1032°C followed by double ageing process [93].

2.2.2 IN718 Fasteners

IN718, as a common and highly processable superalloy, is a suitable choice for aero-engine fastener applications at a low to moderate temperature. The past decades have

seen a great amount of research on IN718 development under a wide range of scientific as well as industrial attention [16, 27]. IN718 aero-engine fastener (referring as bolt in this project) is one of the common IN718 applications with excellent high-temperature mechanical property and its relatively low in cost [29, 94]. It is well known that the materials used in aeroengine need to meet very high requirements. IN718 fasteners have been verified as a reliable aero-engine component working under 650°C. With higher demands in the operating temperature to further improve the aero-engine efficiency of civil aviation, the question of whether IN718 fastening joints are still competent in this case has been put forward.

It has been observed that the microstructure changes at the heavily cold work parts of IN718 bolts under in-service conditions, such as the thread root or the fillet under the bolt head. Such situation has triggered the exploration of the behaviour at these locations of IN718 bolts and reviewing its manufacturing process for aero-engine applications. In-depth research of failure mechanism of IN718 bolt and its microstructural evolution during service are still not fully available, which raises concerns in terms of efficacy and safety of the bolts considering that it has been in-service for years. Additionally, the question that whether the IN718 fasteners could continue in service at a higher temperature (over 650°C) without losing strength needs to be investigated. Thus, it is necessary to carry out relevant mechanical testing.

2.2.2.1 Mechanical behaviour

To investigate the mechanical behaviour of the bolts, analysing the bolt structure separately is the key to study the local mechanical behaviour. The thread and fillet of a bolt indicate a higher stress concentration comparing to the shank (the smooth section between bolt head and threads) or bolt head. The possible failure and

mechanical fracture of the aero-engine bolts potentially occur at the indicated locations in Figure 2-5 [95], and the locations of bolted joints in the turbofan engine is shown in Figure 2-6.

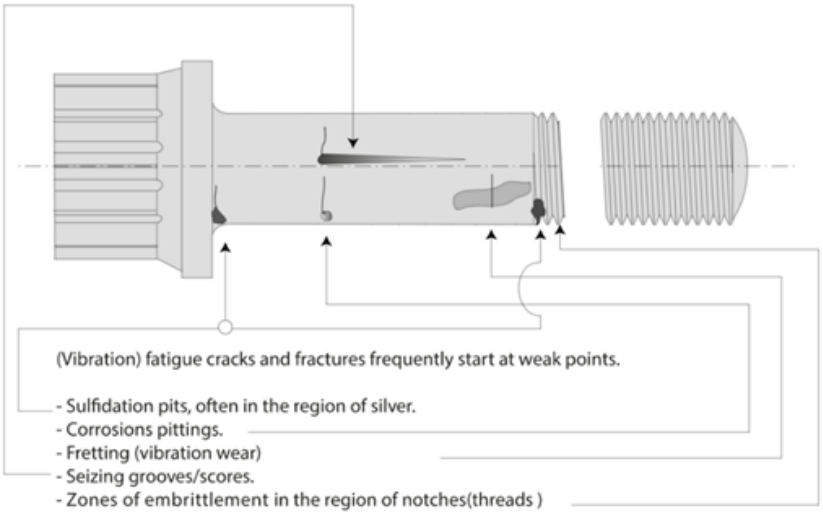

Figure 2-5 The failures or fractures initiation locations of an aero-engine bolt during the operation [95]

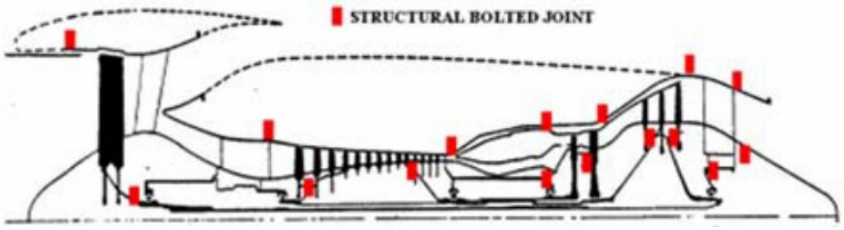

Figure 2-6 Location of bolted joints in a turbofan engine [7]

This project focuses on the investigation of the mechanical behaviour at the bolt shank, fillet, and threads.

The tensile test is a fundamental mechanical test, measuring the material ductility and the tensile-strength data. Another mechanical test heavily related to the high-temperature application is creep testing. From Akli. et al., the bolts under high temperature conditions can lose its clamping force and tightness because of creep relaxation of the material [97]. The other deteriorating factors for engine-run bolts include fatigue under the corrosive environment at the high temperatures [15]. As previously discussed, the aeroengine might experience both LCF and HCF (some chance) in service. The operations such as take-off, require the components to produce excellent LCF strength at a high temperature with a high R ratio.

The finishing procedure of an IN718 bolt is thread rolling and fillet rolling, which delivers an extra burnishing effect compared to thread cutting, while introducing beneficial compressive residual stress accompanied with hardening [98]. As a result, the performance of the bolt significantly improves, especially, the fatigue resistance at room and intermediate temperatures [21, 98-99]. Thereby, the high-temperature fatigue testing on real IN718 bolts would be helpful. The following section reviews the manufacturing process of IN718 aero-engine fasteners, revealing that the mechanical properties may be affected by the existing manufacturing process.

2.2.2.2 Manufacturing process

To optimise the properties of IN718 aero-engine bolts, the manufacturing process requires multiple heat treatments combined with metal forming e.g., forging, and rolling. Such complex procedures change the microstructure of the material constantly at each step. A thorough analysis of the manufacturing process considering how the microstructure is affected is essential.

For aerospace applications, the production of bolts is controlled by two sets of specifications, the raw material manufacturing, such as AMS 5662, and the specification of the bolt manufacturing, such as TS24.

Two AMS for IN718 aero-engine bolts commonly accpeted are AMS5962 [100] and AMS5662 [101], which cover the melting practice at the beginning, to the following heat treatments of the IN718 bars and the metal forming before the material is delivered to the bolt manufacturer. The main AMS specifications related to this project are:

- Both AMSs require the melting practice to be performed in a vacuum environment by using either induction melting (VIM) or electroslag remelting (ESR) on the VIM-produced electrodes.
- Then the alloy shall be hot rolled, followed by turning or grinding for a better surface condition.
- The solution treatment shall be applied within the range of 941°C – 1010°C for a period, ensuring the alloy is soaked homogeneously at the chosen temperature, followed by cooling at a very fast rate.
- AMS6962 requires a further operation of work strengthening. The resulting solution treated bars shall be cold-drawn [100], whereas AMS5662 requests no further processing of the solution-treated bars [101].

The bars then are delivered to the bolt manufacturers. The standard procedure for producing IN718 aero-engine bolts follows TS24 (rolled threads and fillets) [102]. A flowchart of the AMS5962 / AMS5662 process and TS24 is shown in figures 2-7 and 2-8. It should be noted that the cold worked bars are not mandatory (AMS5962), some manufacturers include the work hardening step, some choose not to.

The benefits of ageing at 620 to 720°C include partially relieving the residual stresses induced by water quenching after the solution treatment, and precipitating γ' and γ" phases intragranularly which are critical to the high temperature creep resistance [103].

The bolts supplied by Rolls-Royce plc for this project are made of EN2952/AMS5962 bolts, requiring the products to be laves phase free.

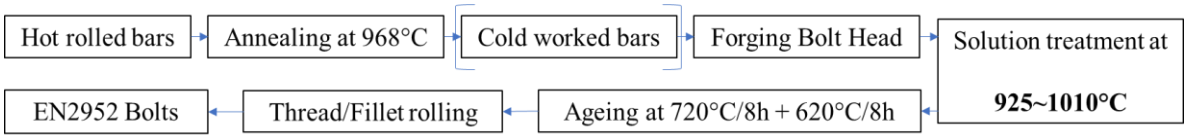

Figure 2-7 The manufacturing history of large bolts used in the project (AMS5962), cold work is optional here [100, 101]

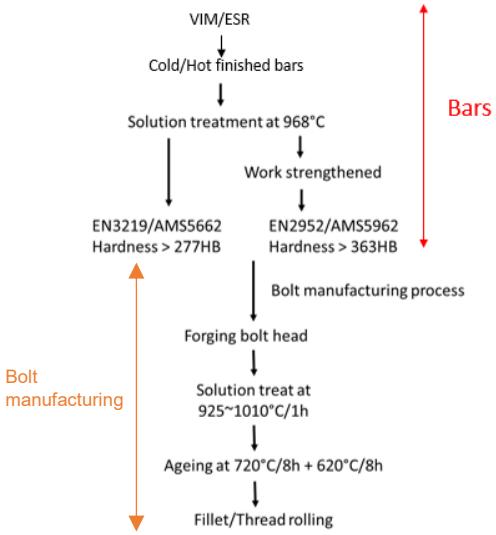

Figure 2-8 Manufacturing route of IN718 bolts according to AMS5962 or AMS 5662 followed and required by TS24 [100-102]

2.3 Cold-working and annealing

Cold-working and annealing are heavily involved in manufacturing the IN718 bars and IN718 fasteners, having a profound influence on microstructure and the subsequent products. Especially with a higher demand in temperature and pressure on the aerospace fastened joints, optimising the treatments on the materials to improve the fasteners properties for aero-engine applications is necessary. First, the understanding of cold-working and annealing on IN718 aero-engine bolts needs to be established, followed by utilising these processes to obtain desired the microstructure and the ideal performance of IN718 fasteners.

2.3.1 Cold-working

Cold work or work hardening, referring to the common manufacturing processes such as rolling, bending, or drawing etc. below the recrystallisation temp, or normally at ambient temperature, is one of the most important metal forming operations, which primarily aims at shaping the metal and strengthening the materials properties. The crystallographically ordered texture decreases as the grains are largely distorted, while considerable energy is being stored by cold work and accumulating dislocations [104].

The higher degree of cold work with extensive plastic strain causes a higher density of dislocations and stores more energy [105]. As a result, the strength and hardness of the metal increases and ductility decreases [106]. Cold work is performed below the metal recrystallisation temperature, depending on the situation, sometimes at room temperature. The cold work percentage is described as the degree of plastic deformation. The cold work degree of a cylindrical bar is shown in equation 1, where D_0 is the original cross-section diameter of the bar, and D is the plastically deformed

diameter after cold working. This can be derived into the area equation, applying to all shapes of the cross-sectional areas. A_0 is the original cross-section area, A_d is the plastic deformed area.

$$CW\% = (D_0^2 - D^2) / D_0^2 \quad \text{(equation 1)}$$

$$CW\% = \frac{A0 - Ad}{A0}$$

2.3.2 Cold work in IN718

The bolts possess complex geometry with multiple manufacturing processes at the local areas, leading to a non-uniform mechanical property. The manufacturing process has been improved to alleviate the impact of high-stress concentrations, as previously mentioned. Rolling the threads instead of cutting smooths the surface bringing a burnishing effect, as well as fillet rolling process [21, 98]. However, these processes to improve fatigue resistance also bring the severe cold work effect which is still a controversial topic for bolts. This is because the residual stress introduced by cold rolling or shot peening is relaxed as a result of the oriented dislocation motions triggered by heat treatment or plastic loading, leading to stress relaxation [107]. Studies found that the appropriate surface-enhancement methods introducing the compressive residual stress but minimising the cold work should be applied to IN718 for aero-engine applications [108]. Cold work deforms the material and introduces a great number of dislocations to boost the strength and hardness. However, such heavy cold work could alter the precipitation in IN718 including the main strengthening γ" phase and δ phase.

IN718 is a typical nickel alloy that responds well to cold work processing. From Li et al., pre-straining creates a great number of dislocations where δ phase can nucleate, and the vacancies with a high volume of Nb provide the conditions for δ phase to grow. In other words, cold work promotes the precipitation and growth of δ phase [109]. Cold work not only influences δ phase but also γ” phase as it has the same composition i.e., Ni_3Nb. The question has been raised on how δ and γ” precipitates compete against each other under the cold work condition during the following thermal exposure.

A completed view is summarised by Liu et al. who suggest cold work encourages the generation of δ phase and the transformation of γ” to δ phase. More specifically, at a temperature in the range between 810˚C to 960˚C, the γ” phase precipitates first, with the ageing time increasing until it reaches a saturation point where γ” starts transforming to δ. The higher percentage of cold work leads to a lower γ” phase saturation point, which means the heavy coldwork makes the transformation from γ” to δ easier during the ageing process. At 810˚C, δ phase reaches the highest ultimate percentage by consuming the maximum γ” phase shown in Figure 2-9 [77]. The bolts received for this project have been cold rolled at the threads and fillets and are ready for use in aeroengines. Previous studies can be used as a reference to further understand the in-service behaviour of IN718 bolts.

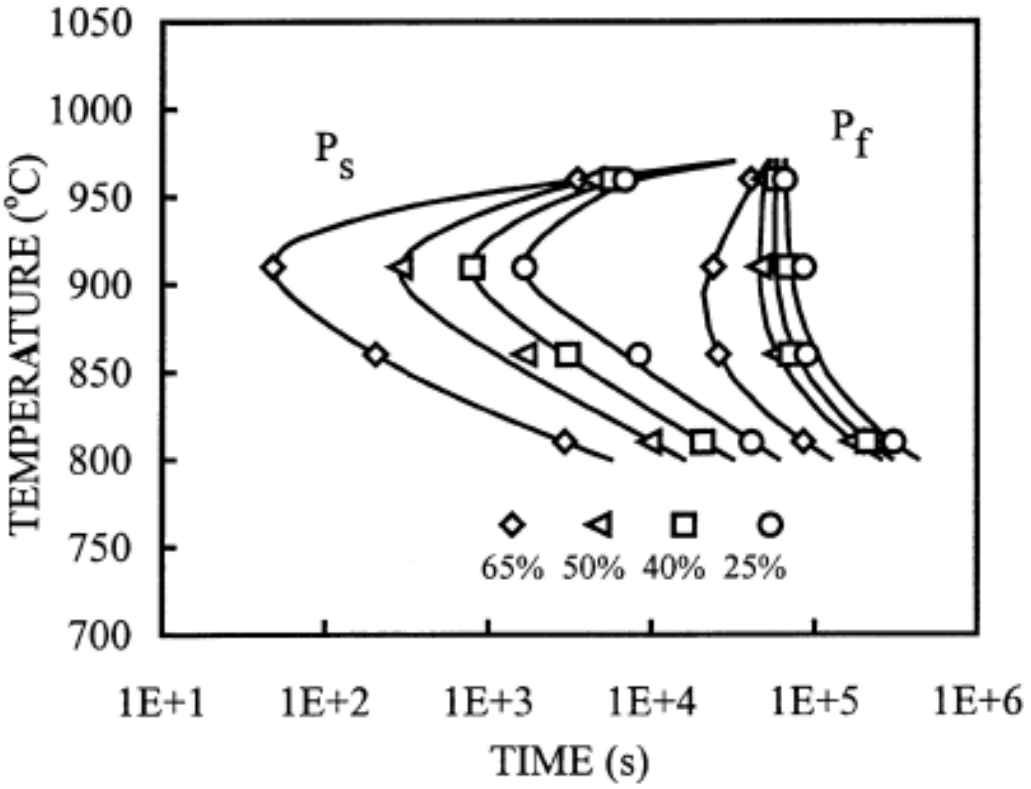

Figure 2-9 The time-temperature-transformation diagram of IN718 with different cold work reduction, Ps (δ phase) is the starting precipitation and Pf is the finishing precipitation.

The TTT (time-temperature-transformation) is a good way to show the effect of cold work on precipitates. Cold work shifts the TTT (δ phase) left, as pre-straining stores a great deal of energy in the alloy. As a result, the required temperature and time to reach the point of precipitating δ becomes lower. The heavier cold rolling reduction promotes the faster δ phase formation [110].

Apart from δ phase distribution, the morphology of δ phase varies according to the different degree of cold work. The grain boundaries or cell walls in IN718 with or without a small amount of cold work allow the δ phase to grow and connect, turning into the

long and thin shape. When the materials are cold worked, the grain boundaries are heavily distorted, which blocks δ phase alignment and offers an environment to form the blocky δ phase. Hence, δ phase tends to display the long and thin shape without cold work in IN718, whereas the globular δ phase is more favourable under the heavy cold work condition [109]. Another perspective on δ phase morphology from Zhang and Hassan et al. suggests that δ phase nucleates and grows into a thin-plate shape at grain boundaries and the breakage by cold work stores great energy at the grain boundaries [86]. The plate-like δ phase can transform to short globular δ by dynamic recrystallisation at a temperature between 950 to 980°C with the stored energy. The long thin or plate-like δ phase are normally dissolved above 980°C [81]. Páramo Kañetas et al. also proved that the globular δ phase can be transformed from needle-like δ during hot deformation at 960°C which made a positive contribution on controlling the grain size. They argue that thin needle-like δ phase deteriorates IN718 strength by embrittling the material [78]. The typical plate-like δ phase with intersection behaviour in IN718 and the globular δ phase by δ-processing at 1000°C for 2500s are shown in Figure 2-10 and 2-11 respectively [87, 111]. Therefore, by altering the δ morphology, the mechanical properties of IN718 can be modified.

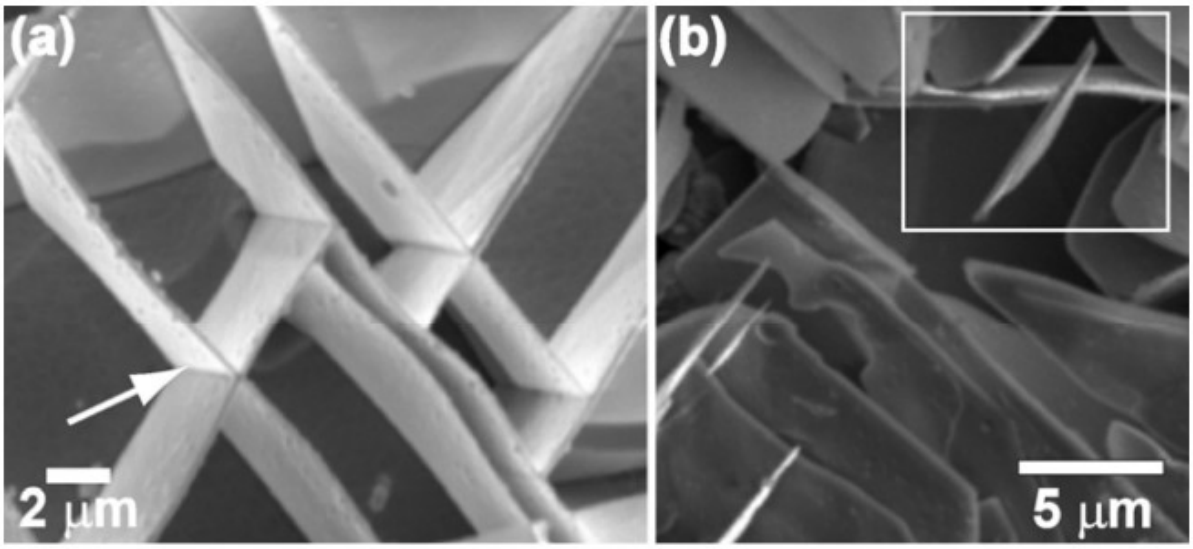

Figure 2-10 Plate-like δ phase with intersecting growth presented by SEM in etched IN718 [87].

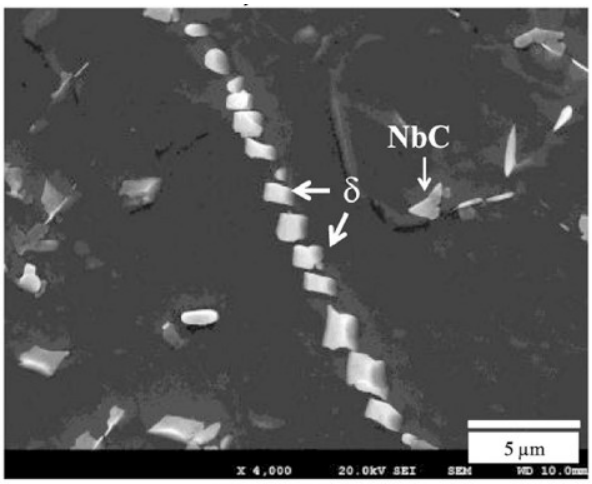

Figure 2-11 The globular δ phase created by hot deformation [111].

Previous study has investigated the overlapping influence of plastic cycling deformation and high temperature on IN718. Fatigue tests at 700°C were carried out on annealed and aged IN718. An obvious phase transformation was found where the quantity of δ phase massively increased leading to a drop in mechanical strength due to the consumption of γ” phase [112]. However, the behaviour of δ and γ” phase in the

real IN718 bolts for aero-engine applications has not yet been investigated. One of the aims of this study is to understand different mechanisms and limitation of IN718 bolts.

2.3.3 Annealing

Annealing or solution treatment is a heat treatment widely used in different kinds of alloys to increase the ductility and workability, decrease the hardness, dislocation density and internal stress such as undesired residual stress. More specifically, if the annealing temperature is above the recrystallisation temperature, the pre-cold worked alloy recrystalises and recovers to the cold work free state with nucleation and growth of new equiaxial grains [113, 114]. The other approach is annealing at a suitable temperature lower than the recrystallisation temperature for a period followed by cooling at an appropriate rate to precipitate or eliminate a phase and subsequently to control the grain size. Both cases contribute to changes in material microstructure and mechanical properties. For instance, annealing at 968°C during manufacturing of IN718 bars is to unify the microstructure, promote grain growth and relief residual stress during hot rolling and to homogenise the microstructure.

2.3.4 Recovery and recrystallisation in IN718

Recovery is a process that occurs at a lower temperature during annealing. The microstructure stays the same, but dislocations introduced by cold work are either annihilated or rearranged into low energy configurations. However, the overall effect of recovery on dislocations is small [114].

The driving force for static recrystallisation is stored strain energy. A minimal deformation of the alloy is required to ensure the occurrence of recovery [115]. During the cooling process, strain-free grains with a new crystal structure replace deformed

grains by nucleating and growing. Apart from the degree of deformation, the original grain size in the alloy also affects the recrystallisation process. This is because a finer grain size with a higher density of grain boundaries offers more nucleation sites than coarser grains. Therefore, a lower recrystallisation temperature is required in this case [114].

2.3.5 Annealing and precipitation hardening in IN718

Annealing (solution treatment) followed by precipitation hardening is a vital step before cold rolling the fillet and threads of the IN718 bolts. TS24 requires a solution treatment temperature within the range of 925 to 1010°C, which covers the δ phase solvus temperature [102]. This is one of the key issues in the manufacturing specifications of IN718 bolts. This flexibility results in final products with different content of δ phase.

The precipitation hardening of γ” phase is achieved by a double ageing process at 720°C for 8 hours and 620°C for 8 hours after solution treatment. It can be estimated that the amount of γ” phase should be adequate in the finished products when the solution temperature is close to the δ solvus temperature (997°C). The double ageing process largely benefits IN718 by removing the undesired residual stress introduced by the fast cooling and more importantly, precipitating the intragranular γ” phase and a small amount of γ’ phase to improve the strength and creep resistance. During the double ageing process, the number of γ” precipitates considerably increase during the first stage at 720°C, then during the second stage ageing at 620°C, γ” precipitates start growing and coarsening. However, it can worsen the mechanical properties if the ageing time is too long, such as up to 100 hours. The large size of γ” precipitates bring disadvantages to the alloy, such as the lower tensile strength and creep resistance [61,

66]. Thus, both ageing temperature and time need to be perfectly adjusted to maximise the strengthening in IN718. Further research shows that external stress provides extra nucleation sites for γ” precipitates [80]. However, when the ageing time is too short in this case, the very fine γ” precipitates cannot effectively strengthen the alloy. Only when the ageing time is over 2 hours, can γ” precipitates stabilise and grow to an appropriate size for strengthening. The average γ” size after ageing for 8 hours is between 29nm to 37nm [62, 80].

Chapter 3

3. Experimental Methodology

The detailed microstructural and mechanical characterisation involved in this project is summarised in Appendix 1-3.

3.1 Materials, heat treatments and test pieces

3.1.1 Materials

The IN718 alloy used in this project was supplied by Arconic Manufacturing (GB) Limited in two forms. These were nineteen hot rolled bars which were 12” long with finishing diameter of ½” and a batch of Φ ½” large bolts, as shown in Figure 3-1. Nine Φ 3⁄8-inch IN718 bolts were also provided by Rolls-Royce plc. for microstructure characterisation only, named IN718 small bolts in this project.

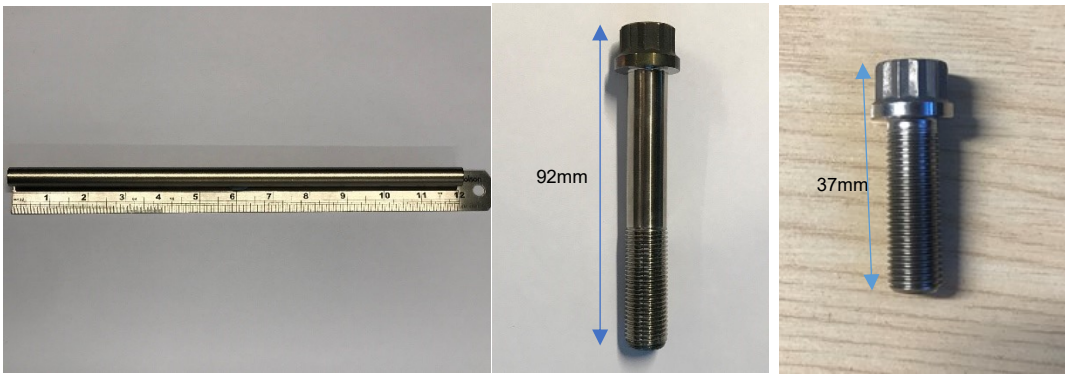

Figure 3-1 Twelve inches long as-received IN718 bar, IN718 large bolt and IN718 small bolts from left to right

The manufacturing process of the as-received IN718 bars follows the AMS (Aerospace Material Specification) 5662M of SAE (Society of Automotive Engineers) International group, summarised in chart (Figure 3-2). The composition and the weight percentage are shown in table 3-1 from AMS 5662M. The alloy multiple melting practice requires

a vacuum environment by using induction melting (VIM) or electroslag remelting (ESR) process on the VIM-produced electrodes. AMS 5662M allows both hot finished and cold finished bars to be solution treated at 968˚C as the finishing condition, the IN718 bars used in this project were in the hot-rolled condition and the delta phase solvus temperature was assumed to be at ~997°C in-line with previous literature.

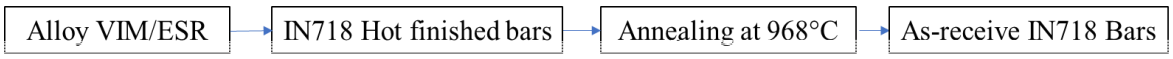

Figure 3-2 The manufacturing process of as-receive IN718 bars

Table 3-1 Composition and weight percentage in IN718 bars by AMS 5662M

Element	min	max
Carbon	--	0.08
Manganese	--	0.35
Silicon	--	0.35
Phosphorus	--	0.015
Sulfur	--	0.015
Chromium	17.00	21.00
Nickel	50.00	55.00
Molybdenum	2.80	3.30
Columbium (Niobium)	4.75	5.50
Titanium	0.65	1.15
Aluminum	0.20	0.80
Cobalt	--	1.00
Tantalum (3.1.1)	--	0.05
Boron	--	0.006
Copper	--	0.30
Lead	--	0.0005 (5 ppm)
Bismuth	--	0.00003 (0.3 ppm)
Selenium	--	0.0003 (3 ppm)
Iron	remainder	

3.1.1.1 As-received IN718 small bolt

A general flow chart of manufacturing IN718 aero-engine bolts is shown in Figure 3-3. The bar manufacturing process follows either AMS5962 (cold worked/cold finished bars) or AMS5662 (solution treated/hot finished bars), then bars in either condition are sent to the fastener manufacturer to procedure bolts of different sizes and forms. This is done by firstly forging the bolt head, followed by solution and ageing heat treatment, and finally filleting and thread rolling. For the as-received IN718 small bolts, the solution treatment after forging the bolt head was conducted per TS24 at 925 to 950°C, which is lower than delta-phase solvus temperature (~997°C).

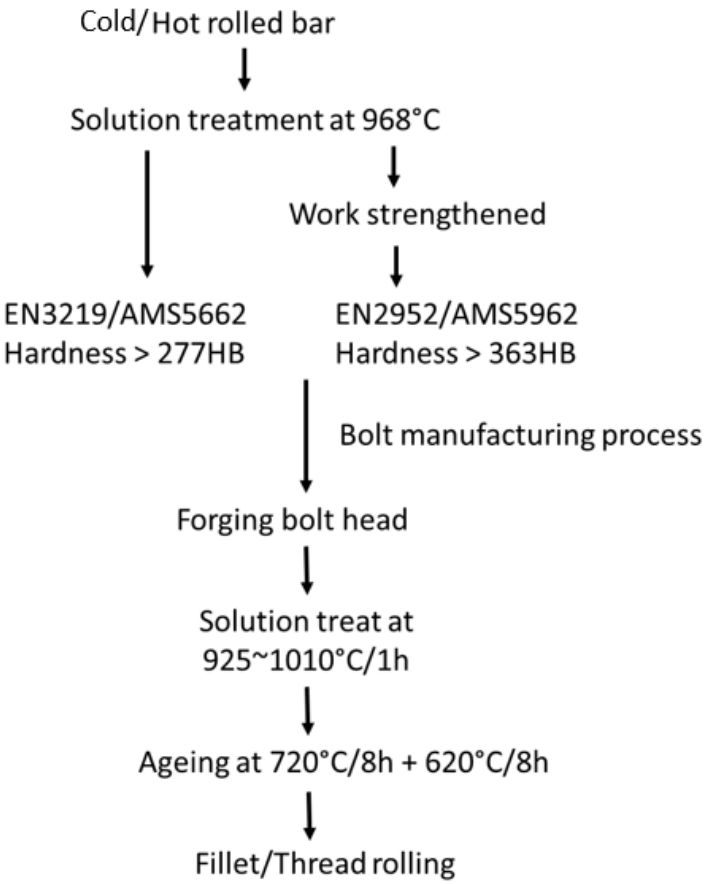

Figure 3-3 Flowchart of manufacturing IN718 aero-engine bolts

3.1.1.2 As-received IN718 large bolt

The manufacturing process of the as-received IN718 large bolts is very similar to the small bolts. The IN718 large bolts received in this project has a full record of the treatment history (Figure 3-4). Before delivering to bolt manufacturer, the IN718 bars were cold drawn following AMS5962. Then, the bolt manufacturer solution-treated the products at 1000˚C by TS24 (between 925 – 1010˚C), which is slightly above the delta phase solvus temperature (~997°C).

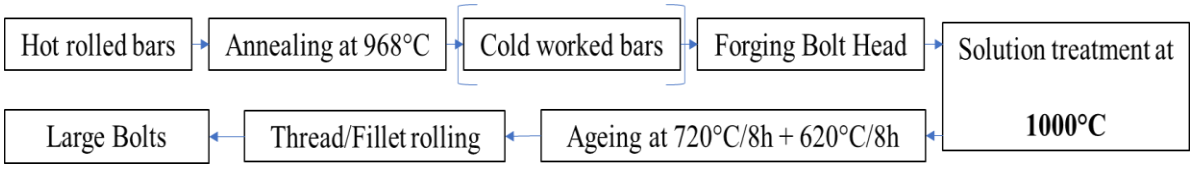

Figure 3-4 Manufacturing history of IN718 large bolts for aero-engine use (see Figure 3-3 for the generic process)

3.1.2 Heat treatment

3.1.2.1 HT samples

The as-received IN718 bars were utilised for microstructure characterisation and mechanical testing. According to TS24 (*Technical Specification 24*), the solution-treatment temperature for manufacturing fasteners is between 925°C to 1010°C. To understand the microstructural variation within this wide range of solution temperatures, samples were heat treated at three different temperatures of 925, 975 and 1010°C which designated HT1, HT2 and HT3 respectively. A fast-furnace cool (oil quench or fast gas quench) followed the solution heat treatment and a standard double ageing treatment at 720˚C and 620˚C was applied for all HT 1-3 samples. The heat treatment on the IN718 bars was carried out in a vacuum environment using a cold wall vacuum

furnace, Camco G1600, an initial cooling rate of 14°/s was achieved from the solution heat treatment temperatures. A typical heating diagram in the furnace is shown in Figure 3-5.

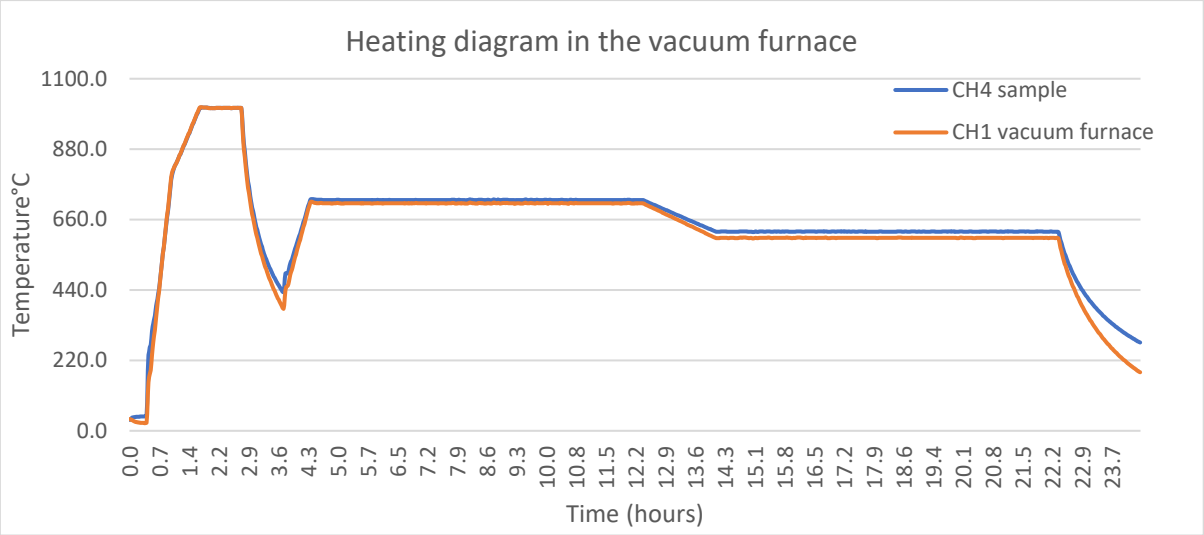

Figure 3-5 An example of a heating diagram (HT3 condition)

The HT conditions have been defined as follows.

HT0: As received.

HT1: Solution treatment at 925°C/1h – gas fan quench– ageing treatment at 720°C/8h - furnace cooling to 620°C within 1h – 620°C/8h – fast furnace cool.

HT2: Solution treatment at 975°C/1h – gas fan quench - ageing treatment at 720°C/8h - furnace cooling to 620°C within 1h – 620°C/8h –fast furnace cool.

HT3: Solution treatment at 1010°C/1h – gas fan quench - ageing treatment at 720°C/8h - furnace cooling to 620°C within 1h – 620°C/8h – air cool fast furnace cool.

3.1.2.2 Bending test pieces

Three bending test pieces (See Figure 3-8 for the geometry of bending specimen) machined from the as-received large bolts were directly placed on the bending fatigue tests (See Section 3.3.2), called “CW (cold-work)” bending test pieces.

Two bending samples were heat treated in a vacuum cold wall furnace, called “CWF (cold-work free)” bending test pieces. The heat treatment was a solution treatment at 1000°C for 1 hour to relieve cold working at the thread area, followed by the same double ageing process as TS24, shown in Figure 3-6.

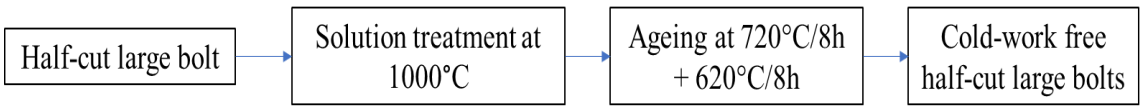

Figure 3-6 Heat treatment for cold work free test pieces

3.1.3 Test pieces

The majority of as received bars and large bolts were subjected to the machining and heat treatments for the following microstructure and mechanical characterisations. More specifically:

- The bars were machined into plain (HTP) or notched test pieces (HTN).
- Some large bolts were kept in the original features and subjected to fatigue testing in the axial-tension.
- Some bolts were machined into bending test pieces for bending fatigue testing, including the cold work free bending test pieces (Section 2.1.2.2).
- The rest of bolts were used for microstructure characterisation under long-term thermal exposure with or without stress applied.

3.1.3.1 Heat treated (HT) plain and notched samples

The HT bars were machined into two types of test pieces for axial tensile fatigue testing, notched samples and plain samples as shown in Figure 3-3. The HT bars were machined into Φ 3⁄8" threads (9.525mm) for 20 mm length at both ends. The plain samples displayed a narrow Φ5 mm cylinder plain centre area, the transition from the ends to the centre was smooth. For the notched samples, the middle section of the bars was Φ7.2 mm where a circumferential V shaped notch was introduced with a depth of 1.1mm, a root radius of 0.25mm and an angle of 60°. The resulted stress concentration factor, K_t, is 3 (The Kt was calculated by Stress Concentration Calculator). The diameter at the notch root is the same as that of the plain samples, 5mm. The total length of all the test pieces is 80mm, the design is shown below in Figure 3-7.

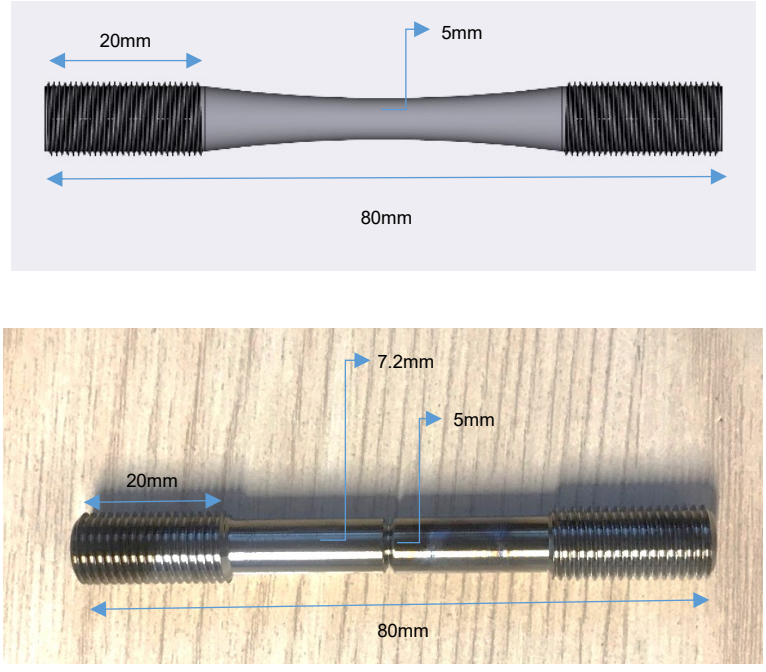

Figure 3-7 HT plain sample and HT notched sample

3.1.3.2 Bending test pieces

To conduct bending fatigue tests on a threaded section of IN718 bolts, test pieces which retained some threads were designed as shown in Figure 3-8. The half-cut test pieces were machined from the as-received IN718 large bolts. The total length of the test piece is 50mm, with a 20mm thread section in the centre and 15mm smooth sections at both ends. Bending test pieces were subjected to the heat treatment before the bending tests to achieve the cold work free microstructure at the thread area (Section 2.1.2.2).

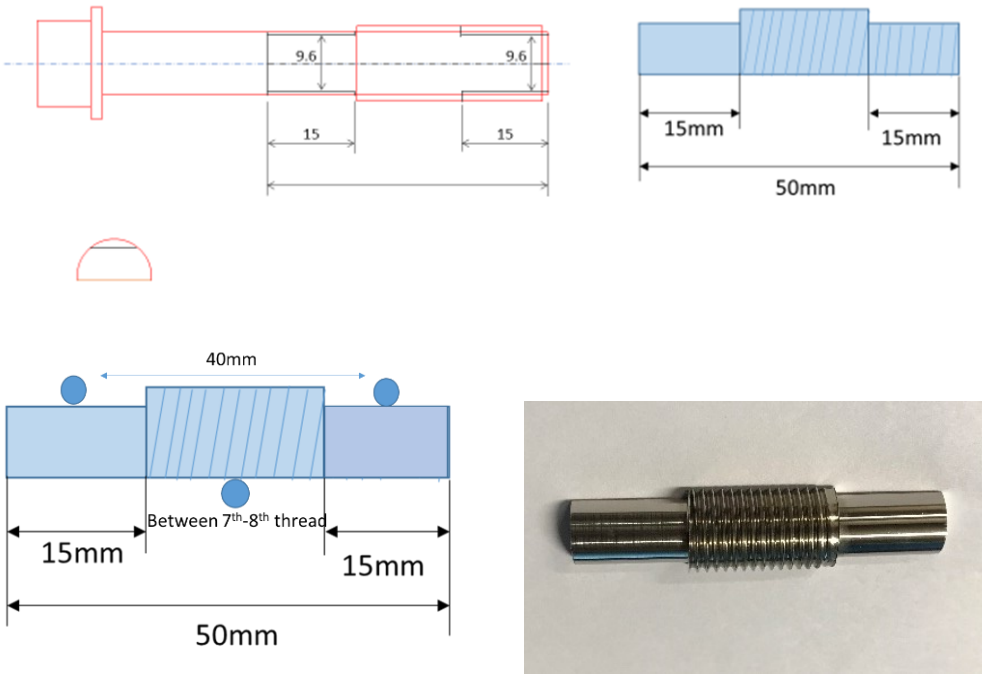

Figure 3-8 Schematic and photo of half-cut large bolts for three-point bending fatigue tests

3.1.3.3 Large bolts

As-received large bolts without further machining were directly subjected to the axial-tension fatigue testing.

3.2 Microstructure Characterisation

To achieve a comprehensive understanding of the changes in the microstructure of IN718 under the different conditions, both as received and heat-treated test pieces, as well as the tested samples were metallurgically prepared and investigated. The microstructure characterisation covers the analysis of grain size, phases, deformation by cold work, microhardness, and cross-sectional crack profiles.

3.2.1 Grain size and phase analysis in HT samples

Microstructural characterisation on the as received and the heat treated IN718 bars (HT samples) was carried out. The experimental techniques used to perform grain size analysis and phase analysis are described in this section.

3.2.1.1 Metallography - Cutting

Four 5 mm thick slices were cut from the Ø ½" bars in the as-received, HT1, HT2 and HT3 conditions as shown in Figure 3-9. A Struers Accutom-50 cutting machine was used with the medium force setting at a speed of 2500rpm. Then each piece was sectioned in the vertical direction, so examination of microstructure on both the transverse (circle face) and longitudinal planes can be made.

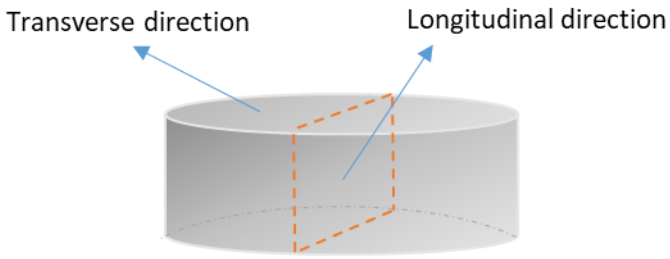

Figure 3-9 Schematic of cutting the HT samples (the transverse direction refers to the top face and the longitudinal direction refers to the square face)

3.2.1.2 Mounting

The cut samples were mounted in conducting Bakelite using an OPAL 460 mounting machine.

3.2.1.3 Grinding and polishing

Based on the conventional methods for IN718, the mounted samples were ground and polished using a Struers Pedemin-S polishing machine. The grades of SiC papers were chosen from P120 to P1200. Each grade was used for three minutes with running water. The applied load was varied from 0N to 40N depending on the surface condition. After grinding, polishing was carried out using four types of polishing cloth: MD (magnetic fixation)-Pan combined with 6μm-diamond solution, MD-Dac with 3μm-diamond solution, MD-Nap with 1μm-diamond solution and MD-Chem with OPA or OPS solutions. The running time and applied load used for each step were varied according to the surface conditions.

3.2.1.4 Etching

<u>For grain boundary observation</u>

Immediately after polishing the samples were fully immersed in Kalling's No.2 Reagent for 5 seconds.

<u>For phase observation</u>

The polished samples were electro-etched for phase observation using a solution of 10% phosphoric-acid electrolyte at a voltage of 2.0V. One electrode touched the sample surface while the other electrode was swiped above the sample for 5 times.

3.2.1.5 Micro-hardness

Without etching, the polished samples were used for microhardness testing with a load of 1kg. To make full use of the space on the sample and approach a higher veracity of

the testing result, the microhardness testing cross pattern (Figure 3-10) was designed with the horizonal interval of 0.2mm.

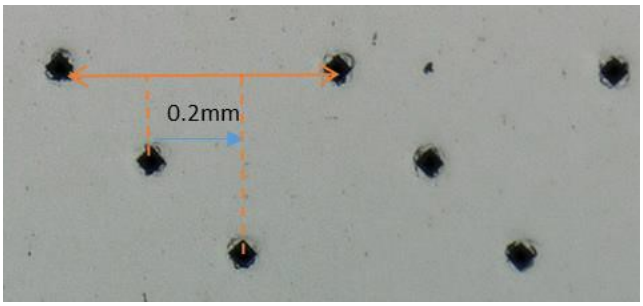

Figure 3-10 The cross pattern of hardness indentation marks

3.2.1.6 Optical microscopy

A Keyence VHX-6000 series digital optical microscope was used to conduct length and area measurements at lower magnifications (20X to 150X). It also helped the observation on grain boundaries and large carbides at the higher magnifications (200X to 1500X).

3.2.1.7 Scanning electron microscopy

Scanning electron microscopy

To observe the microstructure including precipitates and grains, the lower-magnification scanning-electron-microscopy (SEM) observation was performed using either a Philips XL-30 or a Jeol 6060 electron microscope, at an accelerating voltage of 20kV and a working distance of 10mm or higher. The higher-magnification SEM images were acquired using a Philips XL-30 FEG ESEM and a FEI Quanta 3D FEG FIB/SEM, also at an accelerating voltage of 20kV and a working distance of 10mm.

Backscattered electrons microscopy

Backscattered electrons microscopy was performed using a Philips XL-30 FEG ESEM electron microscope to further confirm the grain size and the volume fracture of particles.

Energy Dispersive X-Ray Analysis

Energy Dispersive X-Ray Analysis was applied to the polished samples for examining the elemental compositions using a Philips XL-30 FEG ESEM electron microscope. INCA software was used for compositional analysis.

3.2.2 Local-area characterisation of the bolts

Due to the complex geometry, several manufacturing processes are required to produce different parts of a bolt. This leads to a variation in microstructure in different parts of the bolt. The large and small bolts were longitudinally sectioned and divided into different pieces named “Bolt head”, “Shank”, “Upper threads” and “Lower threads” as shown in Figure 3-11. The samples were mounted and polished and tested for micro-hardness.

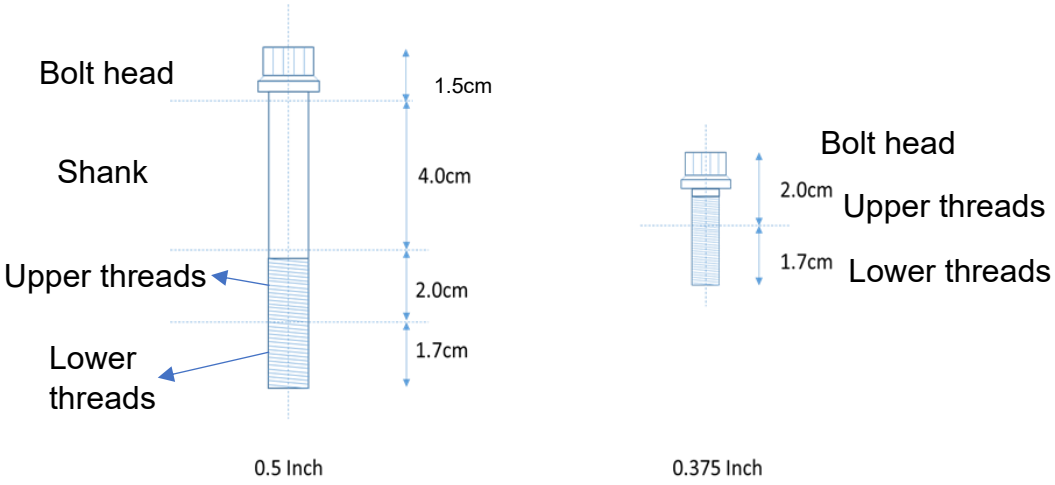

Figure 3-11 Illustration of local areas in IN718 bolts

3.3 Mechanical characterisation

A series of mechanical tests were designed to study the mechanical performance of IN718 aero-engine bolts under the in-service conditions. First, IN718 large bolts were thermally exposed with stress to study the microstructure changes under the harsh aero-engine environment (the thermal-exposure treatment without stress was carried out on IN718 small bolts, see 3.3.1.1), especially at the threads. It should be noted that small bolts were unable to install on the testing machines due to the nature of their dimensions (too small to fit in the machine fixtures). However, microstructure of the treated small bolts is used to compare with that of the treated large bolts. Three-point bending fatigue tests were carried out on CW bending test pieces and CWF bending test pieces (see 3.1.2.2), this is to study the fatigue behaviour of the bolt thread as the failure location is predetermined at the threads where the maximum tensile stress is. The axial-tensile fatigue testing was applied on the as-received large bolts to investigate the fatigue and stress relaxation resistance under longitudinal cyclic loading.

The HT samples without cold work are comparable to the shank section of the bolts, thus, the testing of the HT samples helps to isolate the performance of shank section alone and understand the influence of microstructural variations arising from manufacturing.

3.3.1 Thermally exposed bolts

To investigate the changes at the local areas of the bolts during in-service conditions, both as-received small and large bolts were subjected to thermal-exposure for 100 hours with or without static loading.

3.3.1.1 Thermal exposure of small bolts

The heat treatment was applied on the as-received small bolts for microstructural characterisation. A cold wall vacuum furnace was used to heat treat the as-received small bolts at 650°C for 100h, as Group B treatment (see 3.3.1.2).

3.3.1.2 Thermal exposure of large bolts

Two different heat treatments have been applied on the large bolts to investigate the effects of temperature, stress, and cold work. The resulting conditions include these following three types.

Group A: as received.

Group B: heat-treated at 650°C for 100 hours.

Group C: statically loaded in tension at 650MPa, at 650°C for 100 hours.

To achieve the Group B condition, the large bolts were placed in a cold wall vacuum furnace at 650°C for 100 hours. An ESH servo-hydraulic testing machine was used for preparing Group C in Figure 3-12. The large bolt was partially screwed in the lower

fixture with 7-8 threads exposed. An example of post-testing Group C large bolts is shown in Figure 3-13.

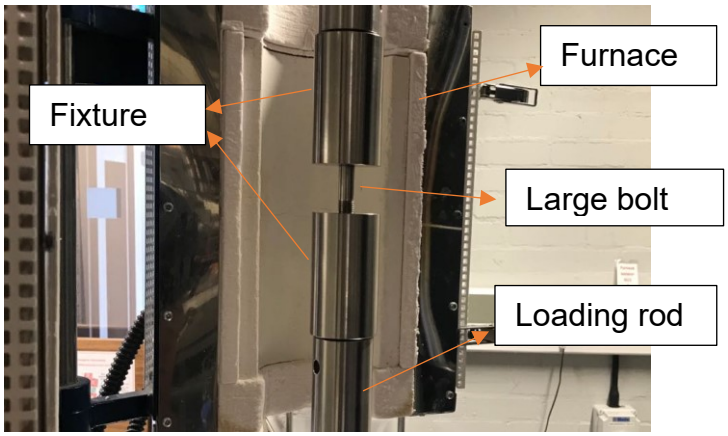

Figure 3-12 Group C IN718 large bolt installed in the testing machine by the customised fixture in the middle

Figure 3-13 Group C IN718 large bolts after treatment

3.3.2 Three-point bending fatigue testing

3.3.2.1 Cold-work sample on the bending test

The half-cut large bolts with retained cold-rolled threads were used for three-point bending fatigue testing, the stress concentration factor, K_t, resulting from the threads is about 3. Before setting up the test, the test piece was accurately measured and

marked for placing the Al_2O_3 ceramic rollers to achieve 3-point bending with a loading span of 40 mm. The configuration of the 3-point bending tests is shown in Figure 3-14.

The bending tests were conducted using a Phoenix servo-hydraulic testing machine at 650°C. After the test pieces were installed and well-aligned in the testing machine, the furnace was closed and heated up to 650°C with one extra hour heat-soaking time to ensure temperature homogeneity.

An R ratio of 0.5 and a trapezoidal waveform at the required frequency were applied in the bending tests. The frequency used varied from 5Hz (sine wave), quarter Hz (1-1-1-1) to two-minute dwell (1-120-1-1).

A direct current potential drop technique was used to monitor fatigue crack initiation. This method requires the passage of a constant current through the test specimen and the measurement of the resulting voltage across a growing crack. The voltage drop against time was monitored during the tests using a digital micro-voltmeter and a chart recorder. Two potential difference (p.d.) nickel wires were spot-welded onto the two-middle threads of the test piece surface, protected by the non-conductive sleeves. The current wires were also spot-welded on each end of the test piece and covered by non-conductive sleeves to make sure that the current only go through the test piece.

This method allows a certain incremental voltage to be selected for each test as the criterion for crack initiation, one microvolt growth was chosen in this project as the early sign of crack initiation, and the p.d. was set at 200uV before testing with a current of 4 to 5 Amps depending on the thickness of the samples. the p.d. output from this set-up is sensitive enough that one microvolt increase can indicate the early cracking of the

test pieces. The thermocouple covered by non-conductive sleeve were attached at the threads of the test piece.

As previously referred in the Fractography section, the failed test pieces then were observed on the fracture surface using a Keyence VHX-6000 optical microscope. The stitiching-3D-images technique was used to enable a complete fracture surface image and depth measurement.

The SEM images were also taken. Failed test pieces were sectioned and metallurgically prepared for micro-hardness testing and high-resolution SEM images.

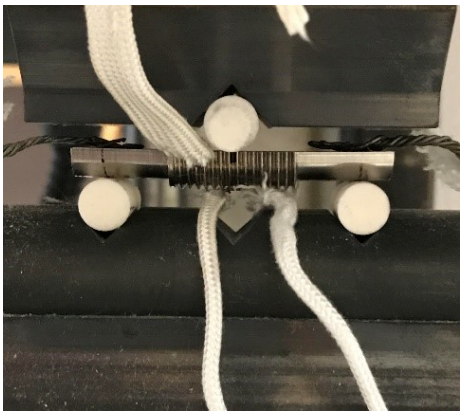

Figure 3-14 Three-point bending fatigue testing configuration

3.3.2.2 Cold work free sample on the bending test

To study the effect of cold work at threads on three-point bending fatigue performance, re-solution at 1000°C and ageing heat treatment cycle before testing (as specified in Section 3.1.2.2) was applied to some half bolt test-pieces. This aims to remove the cold work effect and residual stress contained in the test pieces, hence its influence on fatigue, dwell fatigue performance can be estimated. The testing setup of those stress relieved half bolt test-pieces remains the same as the as-receive half-bolts.

3.3.2.3 Stress calculation of three-point bending test

Due to the irregular shape of the three-point bending test pieces, the stress applied requires a series of calculations. The test pieces are considered as a beam with perfect-semicircle cross section. If R (R refers the minimum radius of the threads from the centre to the thread root) is the radius of the semicircle, the moment of inertia I of this situation is described as equation (1):

$$I = \frac{1}{8}\pi R^4 - \frac{8}{9}\frac{R^4}{\pi} \qquad (1)$$

The bend moment M as equation (2):

$$M = L*P/4 = 10P \qquad (2)$$

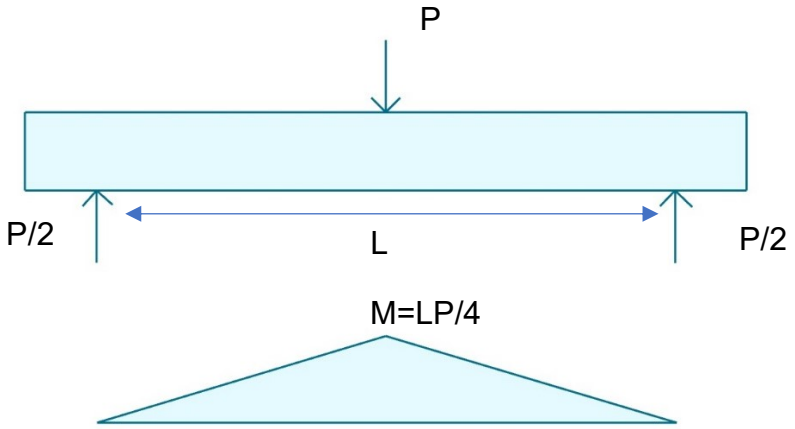

$$D = 4R/3\pi \qquad (3)$$

$$h = R - 4R/3\pi \qquad (4)$$

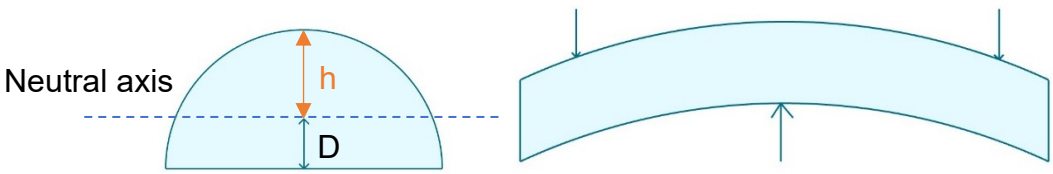

Figure 3-15 illustration of calculating load (P) used in three-point bending fatigue testing

As shown in Figure 3-15, h is the distance between the neutral axis of cross section and the outer surface. D is the distance from the neutral axis to the flat surface. The bending moment is given by as equation (5):

$$M/I = \sigma/h \qquad (5)$$

Thus, the load (P) for half-cut bolt bending test can be calculated. The testing matrix used in this project is shown as Table 3-2:

Table 3-2 The peak stress and peak load used in three-point bending fatigue tests

R (mm)	**I (mm^4)**	**h (mm)**	**σ (MPa)**	**L(mm)**	**P(kN)**
5.42	94.72	3.120	1300	20	3.947
5.42	94.72	3.120	1500	20	4.554
5.04	70.82	2.901	1500	20	3.662

3.3.3 Axial tensile fatigue testing

3.3.3.1 Large bolts

Some as-received IN718 large bolts were subjected to displacement controlled axial tensile fatigue testing. The fixtures for the tests were specially designed and shown in Figure 3-16. They were made from NIMONIC® alloy 90. The upper and lower holes were fixed in the Φ30mm loading rods in a ESH servo-hydraulic testing machine, and a large bolt were set in the centre of the fixtures. The bolt head was held in the upper fixture and the threads fitted in the lower fixture.

A Sander high-temperature extensometer was fitted at the centre of shank to monitor the strain changes for the baseline test. The ceramic arms with a gauge length of 15mm entered the side entry port of the furnace and were firmly attached to the sample. The extensometer was precisely adjusted and aligned before heating up the furnace. Stroke, strain, and load were recorded during the tests using LabVIEW software.

It should be noted that the strain-control test is the closest to the reality of the engine-run condition for the bolts, however, a minor fluctuation in strain in these large bolts causes very large change in load which could result in unexpected failure. Thus, displacement control is utilised in the tests. Although some strain could be contributed from the testing machine during the test, the results and testing method are still valid by producing the trend of load changes in the test pieces. All tests were carried out at 650°C with an R ratio of 0.5, using a trapezoidal waveform of 1-1-1-1 or 1-120-1-1. Two types of bolt installation on the tailored fixtures were applied. One is fitting the large bolts with partially screwed threads with 7-8 threads fully exposed and not being engaged with female threads of the lower fixture, which is called partially screwed bolts, and the other one is fully engaging the large bolts with no threads exposing in the air, called fully screwed bolts.

Stress relaxation testing

Stress relaxation testing was conducted on large bolts by removing the cycling mode used in fatigue testing, serving as a comparative reference, while maintaining all other testing conditions constant to the fatigue tests.

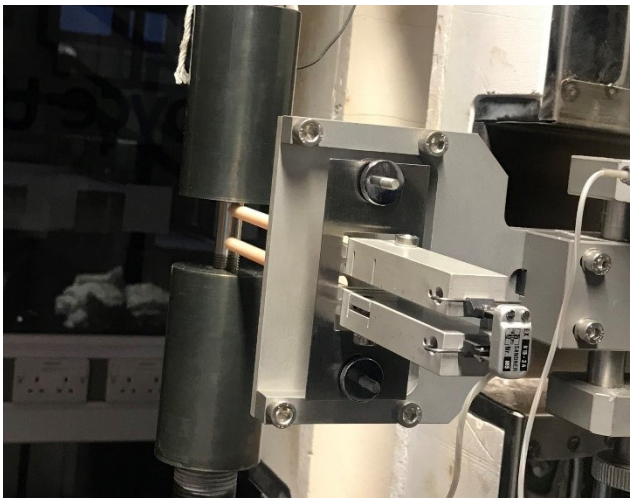

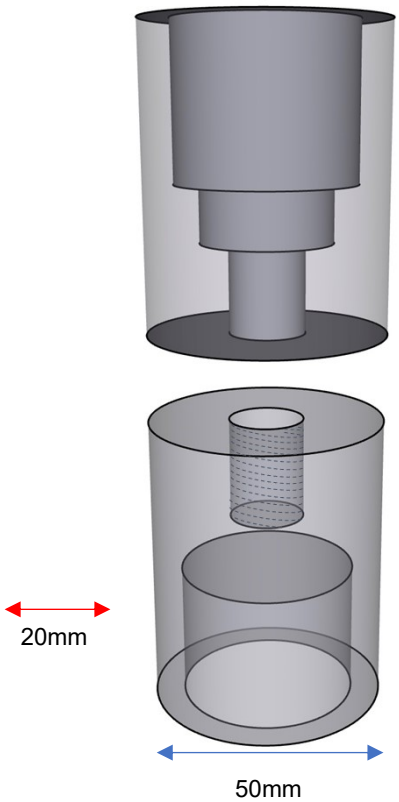

Figure 3-16 Axial tensile-fatigue testing setup and the special fixture used for fitting the IN718 large bolts

Stress calculation

In the axial tensile-fatigue testing of IN718 large bolts, the stress in the shank is lower than at the threads because of a larger cross-section area without Kt3 stress concentration. The applied loaded passing through the whole test piece largely concentrates at the narrower thread area. From TS24, the BS4084 ½" bolts containing a shank and UNJF threads possess a smaller effective tensile stress area, 99.10mm^2. Due to the tests covered both types of fully engaged threads and partially screwed threads, using the shank stress to determine the load applied in the tests would be sensible. All the stresses of the large bolts tested in this project refer the shank stresses.

The shank area of the large bolts is 110.47mm^2, hence the maximum load based on a shank stress of 678.9 MPa is 75kN. The large bolts were firstly loaded under load control to work out the stroke values corresponding to peak and minimum loads required, then the tests were conducted in stroke control using the recorded stroke values. The strain from the testing machine could contribute to the displacement, however, the trend of load changes in the test pieces was still closely monitored.

3.3.3.2 HT samples

The plain and notched fatigue test-pieces were machined from the as-receive IN718 bars, and the HT1 HT2 and HT3 conditions were applied to the machined samples, referring section 1.1.2 and 1.1.3. The testing of these plain and notched samples were carried out on an ESH servo-hydraulic testing machine under load control at 650°C with an R ratio of 0.5. A 1-120-1-1 waveform was chosen for the dwell fatigue tests, shown in Figure 3-17. And the stress relaxation tests were conducted by removing the cycling mode on the selected notched samples. After the test pieces failed in the centre, the subsequent fractography was conducted by Jeol 6060, and cross-sectional

microstructure below the fracture surface was measured using a Keyence VHX-6000 and observed by Electron Microscope Philips XL-30 FEG ESEM.

Figure 3-17 HT sample installed on ESH hydraulic testing machine

3.4 Fractography

The fracture surfaces of tested samples were observed to investigate the failure mechanism. This was carried out both by optical microscopy using a Keyence VHX-6000 and using a Jeol 6060 and Philips XL-30 FEG ESEM electron microscopes.

3.5 Metallography

The tested samples were sectioned in the longitudinal direction to observe the microstructure below the fracture surface and to measure the length of any secondary cracks. The longitudinally sectioned samples were mounted in conductive Bakelite with the revealed face for observing. The mounted samples then were ground, polished and electro-etched in 10% phosphoric acid. High-magnification SEM, FEI Quanta 3D FEG FIB/SEM was used for microstructure characterisation.

Chapter 4

4. Results

The results cover two major parts in this chapter. Microstructure characterisation is introduced in sections 4.1 – 4.2, analysing the gain size, precipitation, local deformation, and microhardness of the IN718 bars and bolts under the different conditions. Sections 4.3 – 4.5 focus on the mechanical characterisation, including bending fatigue testing, axial tensile fatigue, and stress relaxation testing on the IN718 test pieces and the actual IN718 bolts, followed by examining the fractography and cross-sectional microstructure.

4.1 Local area observation on the bolts

4.1.1 Terminology of the areas of the bolt

To manufacture the complex geometry of aero-engine bolts, different heat treatments and metal forming processes are involved. A systematic ‘name vs. location’ standard needs to be established for representing the local areas in a bolt. In this work the following convention is followed: (1) Bolt head, (2) Fillet, (3) Shank, (4) Threads and (5) Centre of the thread section as shown in Figure 4-1 on the left, a real large bolt received for this project is shown on the right. The small bolts do not have a (3) Shank section. Observations are mainly focused on local areas (3) Shank and (4) Threads and (5) Centre of the thread section.

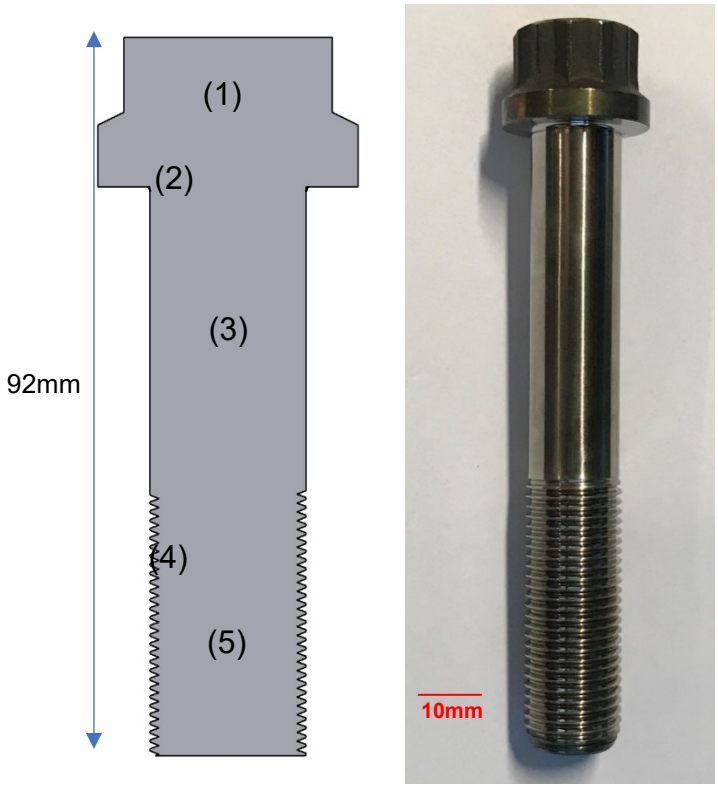

Figure 4-1 Local areas of IN718 bolts and a real IN718 large bolt

4.1.2 Large bolts

The large bolts are divided in three groups with different conditions; Group A is the as-received large bolts, Group B is the Thermally exposed large bolts at 650°C for 100 hours, and Group C is the static-loaded large bolts with 8 threads exposing in the air at 650°C for 100 hours. Group B and Group C conditions aim to understand microstructural evolution of cold work on IN718 bolts at a high temperature under stress.

4.1.2.1 As-received large bolt (Group A)

Figure 4-2 shows optical images at different locations of the as-received large bolt, numerous carbides were seen at each location at higher magnification (Figure 4-2 c & d, see literature review, section carbides). The carbides exhibit a vertical flow throughout the centre zone of the bolts at the thread section. This is caused by the cold-drawing process used before the material is sent to the bolt manufacturer. This is further shown in the etched condition, as shown in Figure 4-3. An obvious tortuous flow appeared at the bolt head due to the forging process to shape the geometry in Figure 4-3 (a & b). Cold rolling was applied at the fillet and threads, especially the latter, Figure 4-3 (c & d) show severe deformation at the thread root and the threads appearing to be darker than the centre zone, which is deemed to be the distorted grain boundaries piling up. From Figure 4-3 (c), the heavy cold work only deformed a small area close to the surface less than 300μm in depth for ½” large bolts, the centre of zone was not affected by cold rolling, resulting in the minor diameter (The smallest diameter of the thread) to 0.4392” as highlighted in Table 4-1. The stress at the thread section is uneven due to the difference between major diameter and minor diameter, using the shank area to discuss the stress is more sensible.

Table 4-1 standard dimensions of UNF bolt threads [116]

External Thread Dimensions for Unified UNF Screw Threads

Diameter	Threads Per Inch (TPI)	Thread Fit Class	Major Diameter (")		Pitch Diameter (")		Minor Diameter (")		Stress Area
			Max	Min	Max	Min	Max		in²
No 0	80	2A	0.0595	0.0563	0.0514	0.0496	0.0446		0.00180
No 1	72	2A	0.0724	0.0689	0.0634	0.0615	0.0559		0.00278
No 2	64	2A	0.0854	0.0816	0.0753	0.0733	0.0668		0.00394
No 3	56	2A	0.0983	0.0942	0.0867	0.0845	0.0771		0.00523
No 4	48	2A	0.1113	0.1068	0.0979	0.0954	0.0864		0.00661
No 5	44	2A	0.1243	0.1195	0.1095	0.1070	0.0972		0.00830
No 6	40	2A	0.1372	0.1321	0.1210	0.1184	0.1074		0.01015
No 8	36	2A	0.1632	0.1577	0.1452	0.1424	0.1301		0.01470
No 10	32	2A	0.1891	0.1831	0.1688	0.1658	0.1519		0.02000
No 12	28	2A	0.2150	0.2085	0.1918	0.1886	0.1724		0.02580
1/4"	28	2A	0.2490	0.2425	0.2258	0.2225	0.2064		0.03640
5/16"	24	2A	0.3114	0.3042	0.2843	0.2806	0.2618		0.05800
3/8"	24	2A	0.3739	0.3667	0.3468	0.3430	0.3243		0.08780
7/16"	20	2A	0.4362	0.4281	0.4037	0.3995	0.3767		0.10600
1/2"	20	2A	0.4987	0.4906	0.4662	0.4619	0.4392		0.16000
9/16"	18	2A	0.5611	0.5524	0.5250	0.5205	0.4950		0.20300
5/8"	18	2A	0.6236	0.6149	0.5875	05828	0.5575		0.25600
3/4"	16	2A	0.7485	0.7391	0.7079	0.7029	0.6740		0.37300
7/8"	14	2A	0.8734	0.8631	0.8270	0.8216	0.7884		0.50900
1"	12	2A	0.9982	0.9868	0.9441	0.9382	0.8990		0.66300
1.1/8"	12	2A	1.1232	1.1118	1.0691	1.0631	1.0240		0.85600
1.1/4"	12	2A	1.2482	1.2368	1.1941	1.1879	1.4190		1.07300
1.3/8"	12	2A	1.3731	1.3617	1.3190	1.3127	1.2739		1.31500
1.1/2"	12	2A	1.4981	1.4867	1.4440	1.4376	1.3989		1.58100

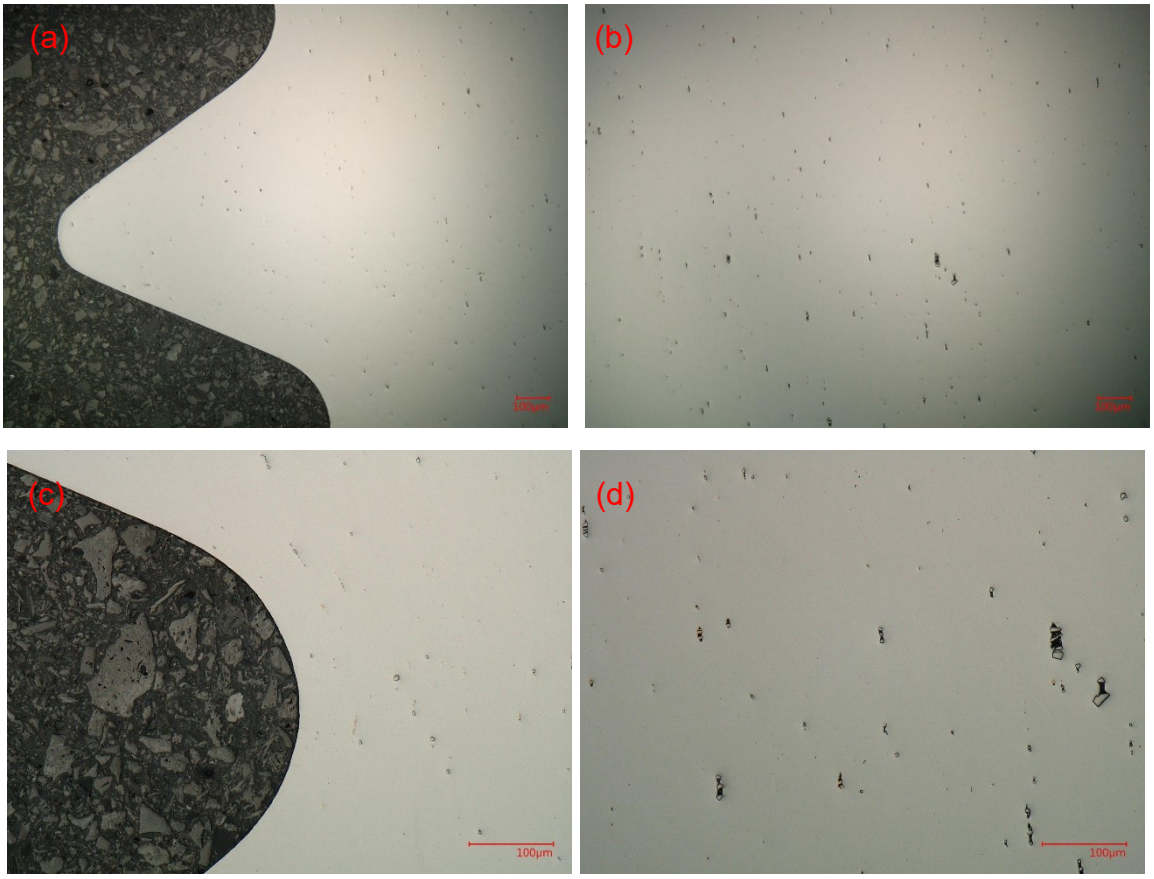

Figure 4-2 As-received large bolt in the polished condition. (a) and (b) were taken at the threads and the centre of thread section under 200 magnifications, (c) and (d) were taken at the thread root and the centre of thread section under 500 magnifications.

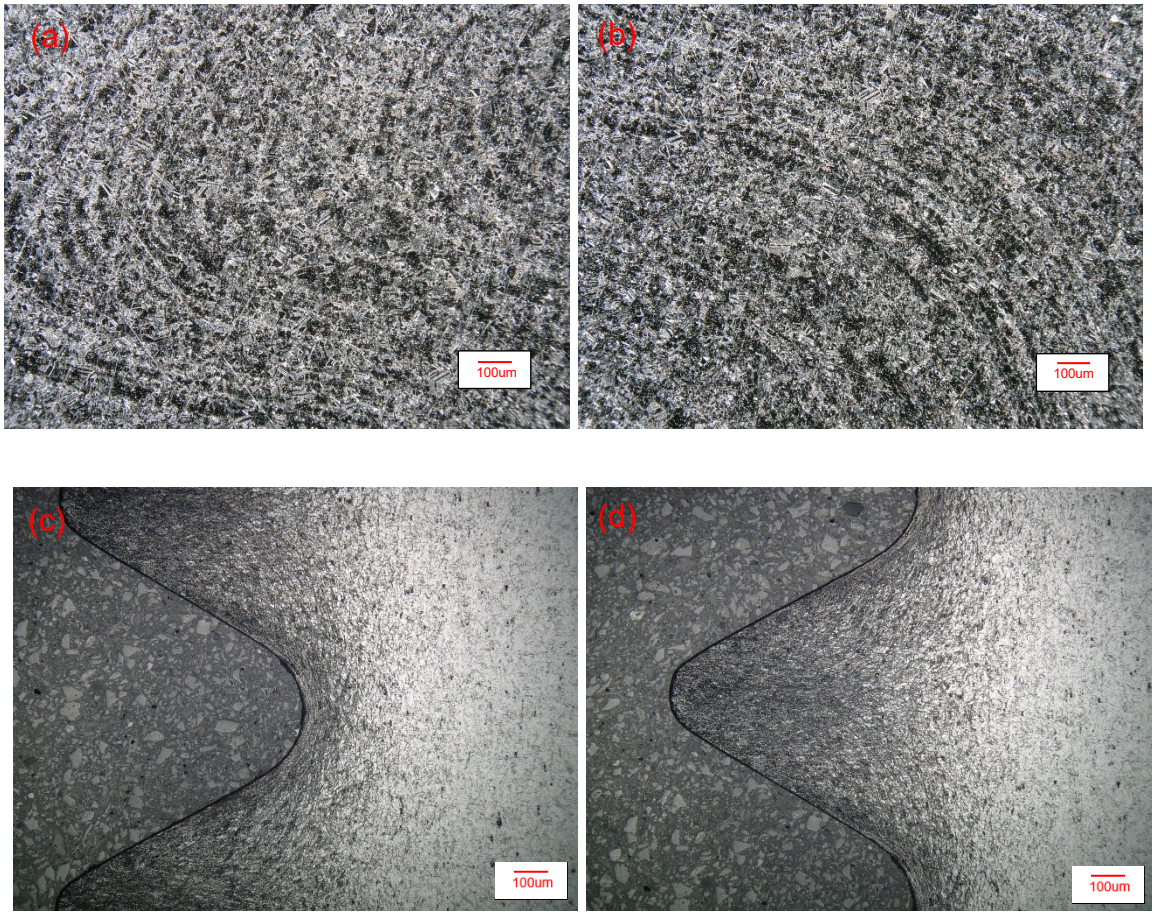

Figure 4-3 As-received large bolt in the etched condition under 200 magnifications. (a) and (b) show the clear deformation flows at the bolt head, (c) and (d) show the cold-rolling deformation at the threads.

Grain analysis

The grain analysis was carried out at positions (3) Shank and (4) Threads using optical microscopy. Large differences in grain morphology were exhibited at these two locations as shown in Figure 4-4. The grains at the shank are equiaxed. No deformation can be seen, and the grain size is relatively small. At the thread root, the grains are severely deformed and orientated along the thread root. Within about 300μm depth from the surface the grains can no longer be observed, as the grain boundaries are very distorted and piled up near the surface.

(a) (b)

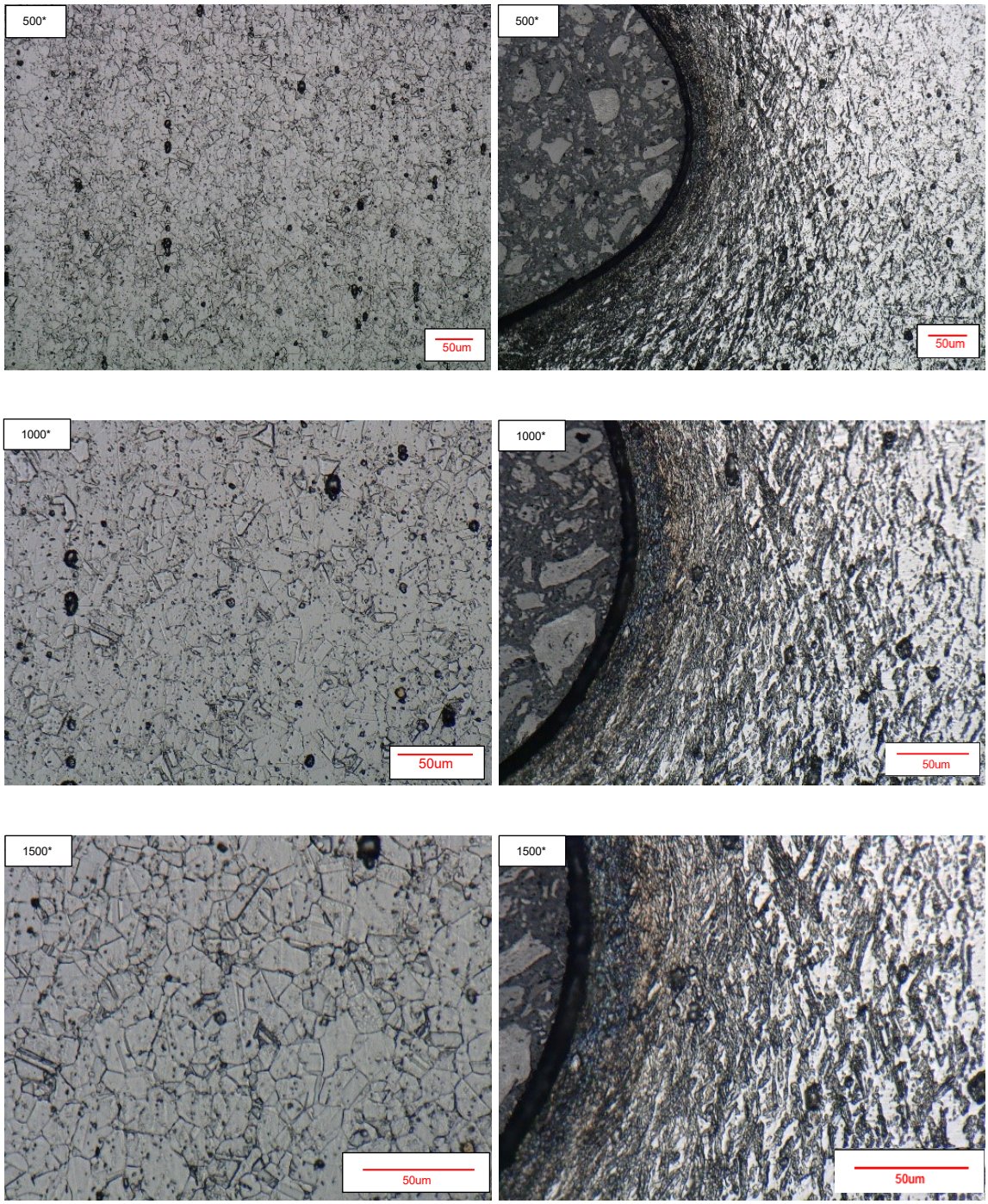

Figure 4-4 Optical micrographs of the shank (a) and thread root (b) in the as-received large bolt.

Phase analysis

An as-received large bolt was polished and etched by electro-phosphoric acid to reveal the precipitates. In Figure 4-5, only few δ precipitates are detected in the shank or the thread root. Unlike the HT conditions (Figure 4-16), δ precipitates (circled in red) are mainly short and blocky in the bolt instead of long and needle like.

(a) (b)

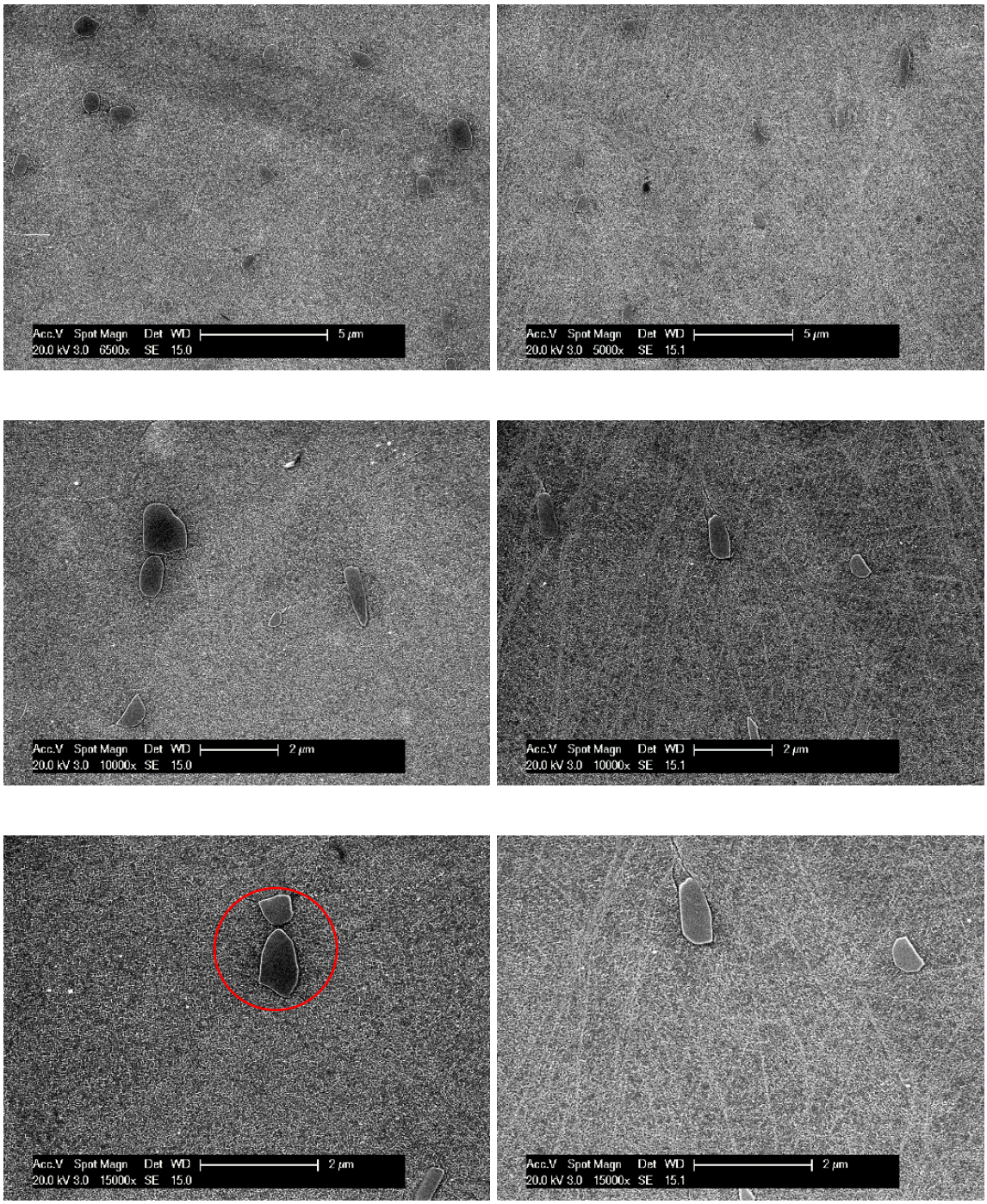

Figure 4-5 (a) Shank and (b) thread root in the as-received large bolt under the SEM

Microhardness analysis

The microhardness values measured differ at the thread area and the centre of thread section, which implied that the bolt material was not even over the bulk and was affected by different manufacturing processes locally. For instance, the hardness at the threads is noticeably higher than any other locations. Figure 4-6 shows that the hardness decreases with distance from the thread to the centre along the radius direction. The peak hardness at the threads is up to 560HV, which is nearly 100HV higher than the centre zone (approaching the distance at 3.0mm). The fundamental reason of the peak hardness at the threads and thread roots, as well as at the fillet, is the cold rolling process applied at these locations to form the bolt geometry. It is necessary to observe the localised deformation and microstructure changes it caused.

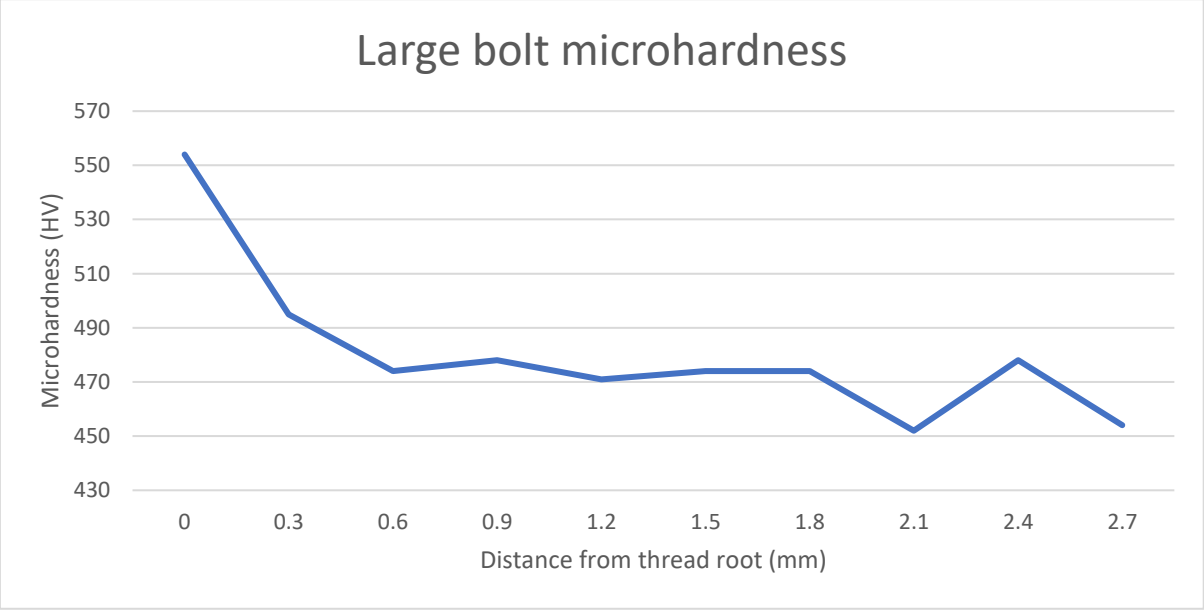

Figure 4-6 Microhardness of the large bolts at the thread root to the centre zone.

4.1.2.2 Treated large bolts (Group B)

The treatments used on the as-received large bolts are Group B; thermal exposure at 650°C for 100 hours and Group C; static axial-tensile loading at 650°C for 100 hours.

Group B condition: thermal exposure at 650°C for 100 hours

Phase analysis

The Group B samples were then polished and etched for phase analysis. Figure 4-7 shows high-magnification SEM images were taken at the thread root at a depth of 30μm from the surface, as well as at the shank. It is clear that a large number of lines which are considered as be distorted grain boundaires, stacking at the thread root . A considerable number of fine δ precipitates were found inside these lines at a high magification in Figure 4-7 (b). Moreover, the majority of fine δ precipitates were surrounded by microvoids. It is noticable that δ precipitates exsit in different sizes, the larger ones are detected, and the fine δ precipitates appeared

in the stacked grain boundaries at the thread root. Compared to Group A bolts in Figure 4-5, where only the blocky and larger δ precipitates can be seen, demonstrating that the fine δ precipitates were formed by the Group B heat treatment. In addtion, the blocky δ phase has a higher δ solvus temperature and can be retained after the solution treatment at 1000°C, whereas the fine and thin δ precipitates should have disolved by 1000°C. This also verifies such fine δ phase are newly preciptated. Some γ” precipitates were also revealed as very tiny dots in the background in Figure 4-7 (b) and (d).

At the shank area, no lines or fine δ precipitates can be seen, only larger blocky δ phase distributed evenly in the whole area. At high maginification in Figure 4-7 (d), a large amount of γ” phase in the background co-exists with δ phase.

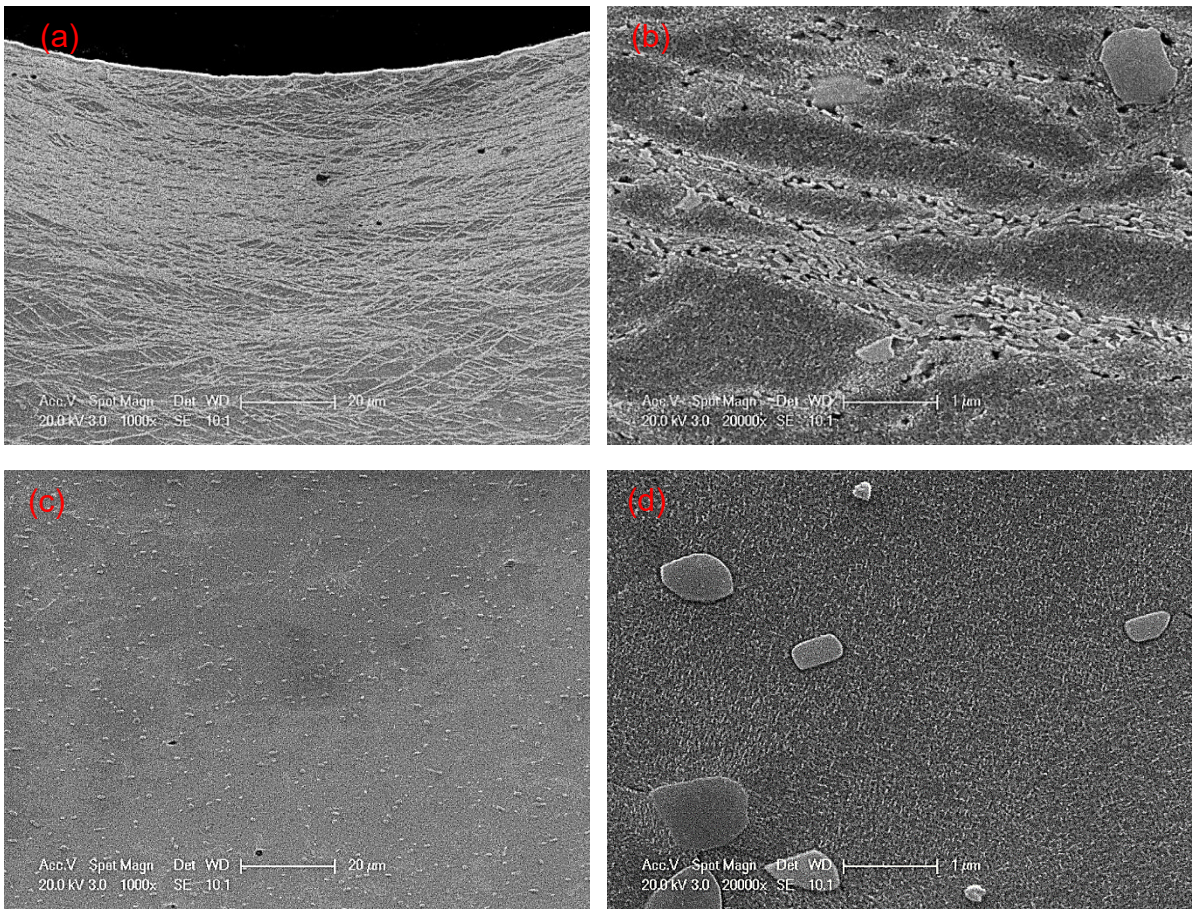

Figure 4-7 Thread root (a and b) and shank areas (c and d) of the Group B large bolts under the SEM.

Microhardness

The microhardness tests were carried out on the longitudinally cross-sectional surface of the bolts at the thread area. The microhardness indentations were taken from one end of the thread root and moved horizontally towards the centre area (shown as the arrow in Figure 4-8). Thus, the results covered the microhardness at the thread area as well as at the centre.

Figure 4-9 presents the microhardness results of the as-received large bolt as a grey dashed line and of the Group B large bolt as a solid red line. A significant drop in

hardness from the thread root to the centre area can be seen at 0.3mm in both conditions, and the results tend to be approximately constant away from the thread area. The microhardness of both Group A and Group B large bolts was highest at the threads compared to the central area, up to 550HV. The hardness of Group B large bolts away from the threads is overall slightly higher than Group A, whereas the hardness at the thread root for both conditions is similar.

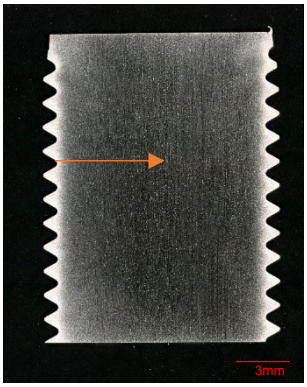

Figure 4-8 Demonstration of applying the microhardness tests on the thread root to the centre of the large bolt

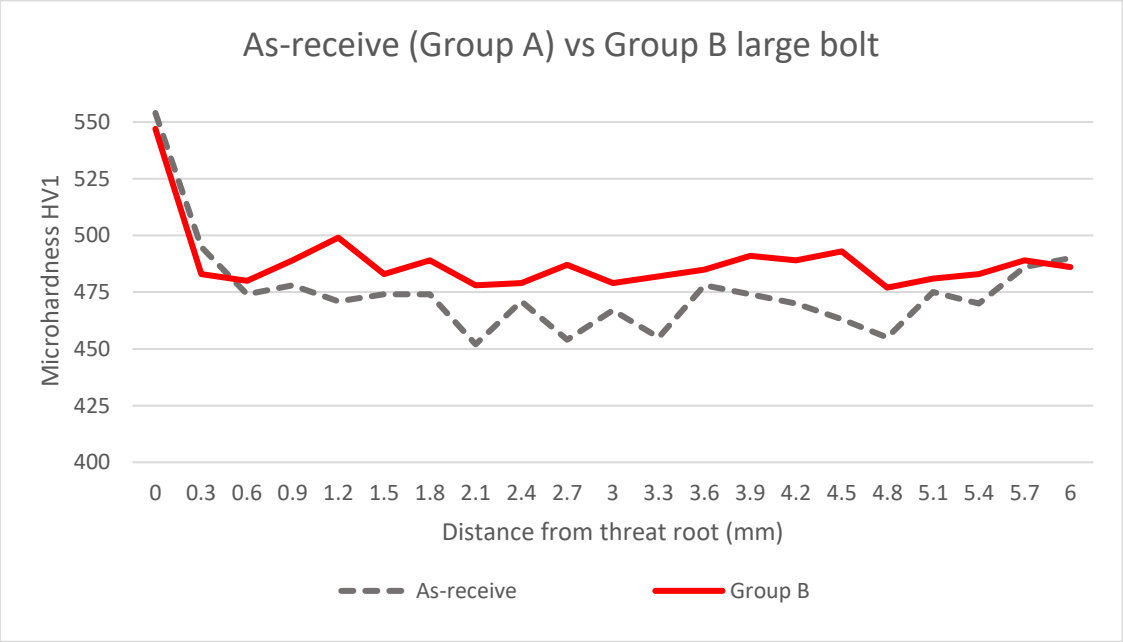

Figure 4-9 Comparison in microhardness of the as-received and Group B large bolts

4.1.2.3 Treated large bolts (Group C)

Group C: static axial-tensile loading (600MPa) at 650°C for 100 hours.

An as-received large bolt was treated by the Group C conditions, then vertically cut, and prepared for metallography in the cross-sectional microstructure at the shank and the thread area. Figure 4-10 shows the grains after being polished and etched in Kalling's No.2 reagent. No significant changes or cracks can be seen compared to the as-received bolt. The grain size in the shank is relatively fine with an average diameter of 15μm. Like the as received bolt, grains are severely deformed and grain boundaries are piled up at the thread area.

Phase analysis

The precipitates in a Group C large bolt were analysed using high-magnification SEM. Interestingly, a very similar microstructure to Group B was observed in Figure 4-11. A great number of fine and new δ precipitates are fulfilled in the deformed grain boundaries, and more microvoids appeared in Group C (Figure 4-11 d) than in Group B (Figure 4-7 b) around the δ phase. Also, the majority of new δ phase precipitates at a smooth and blank area without γ" phase, circled in red in Figure 4-11 (d). In contrast at the shank, very few microvoids appear at the grain boundaries in (f) and (g), and γ" precipitates are evenly spread all over the section in (h).

Shank Thread root

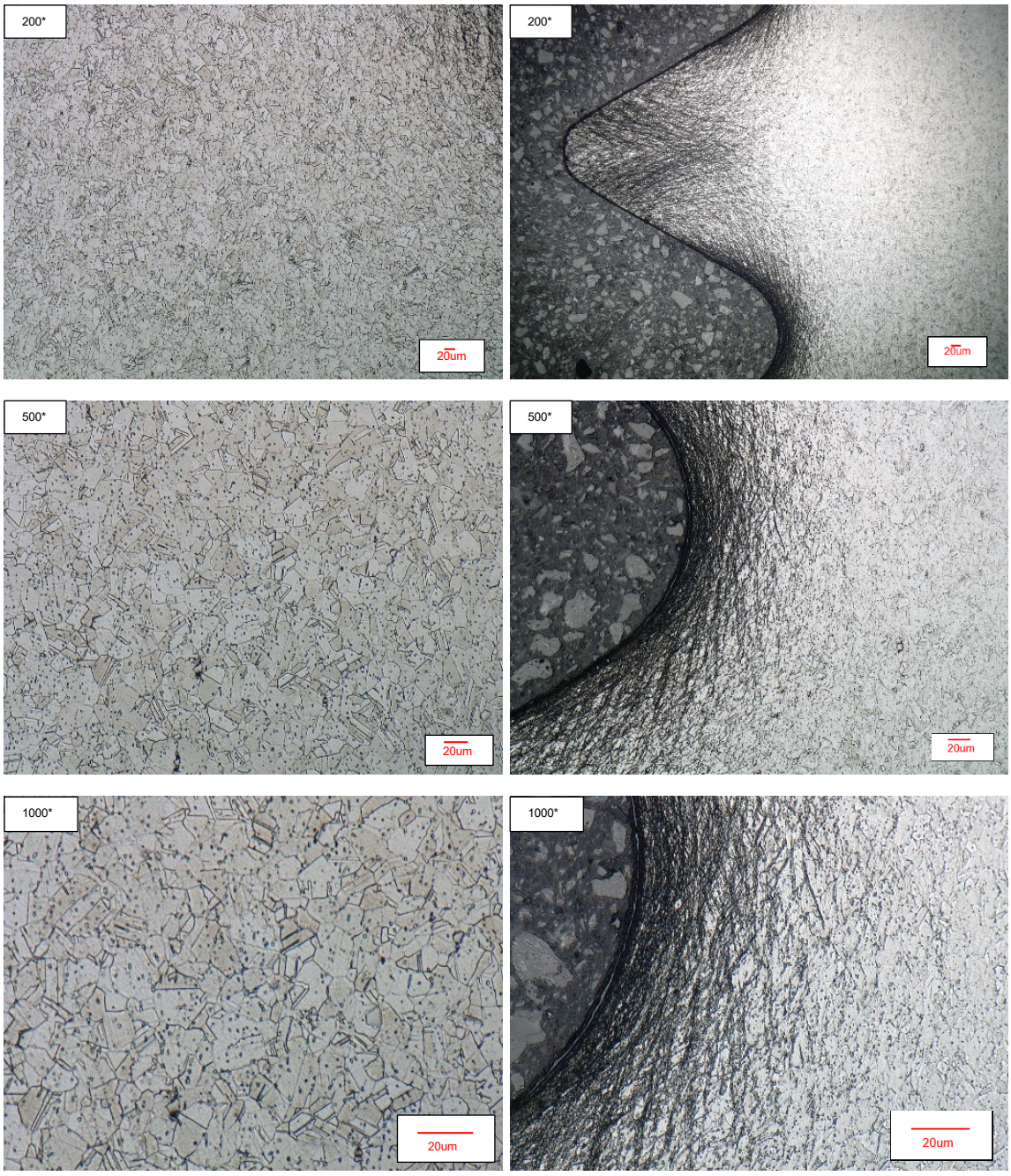

Figure 4-10 Optical micrographs of the shank and thread root areas of the Group C large bolts

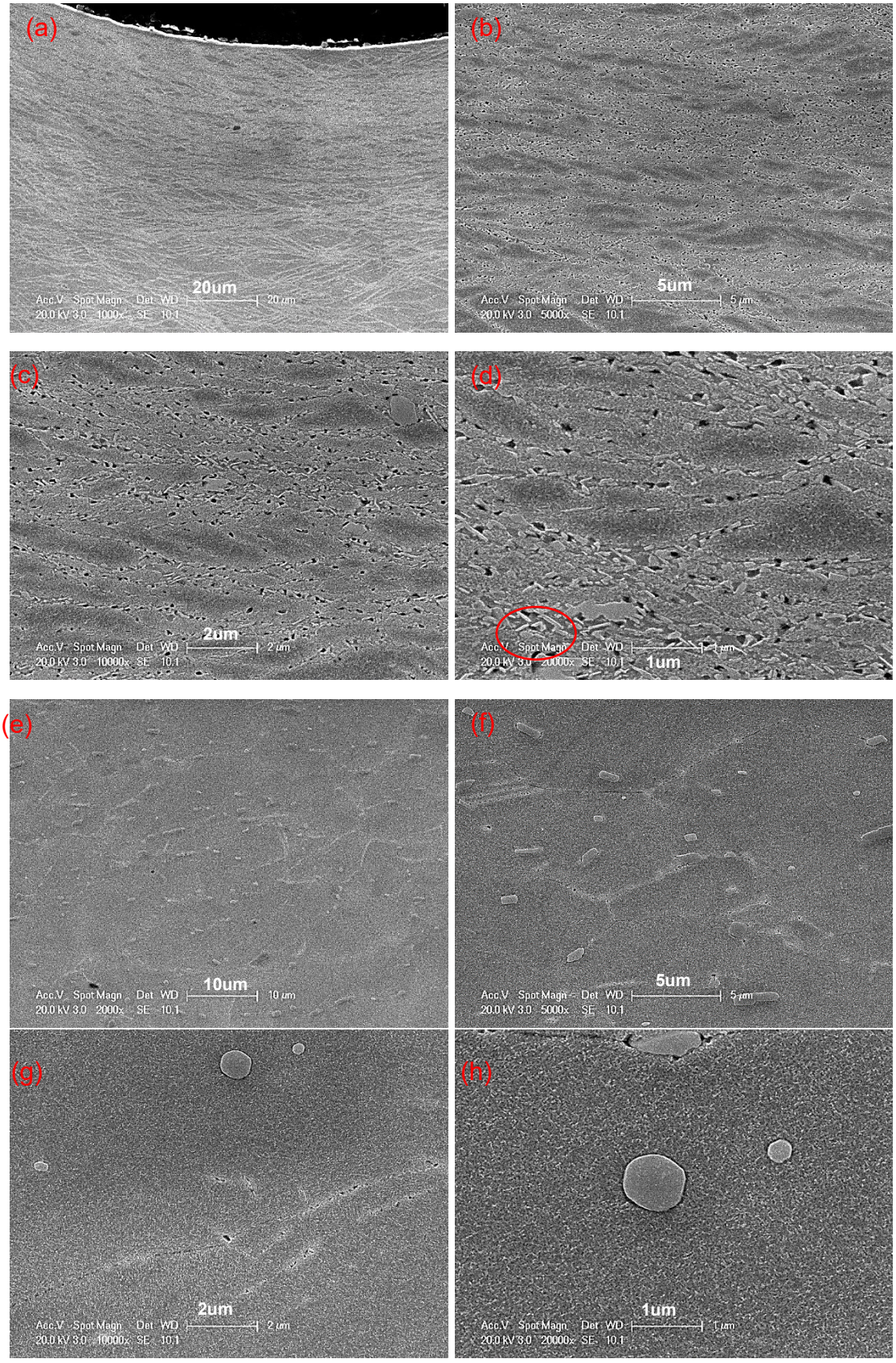

Figure 4-11 SEM Images of thread root and shank areas of the Group C large bolts.

4.1.3 Small bolts

Like the large bolts, the as-receive small bolts were treated with Group B conditions, thermal exposure at 650°C for 100 hours, then metallographic preparation was applied on both as-received and treated samples.

Phase analysis

Both Group A and Group B small bolts were prepared for phase analysis. As shown in Figure 4-12, the BSE images taken at the centre (c) indicated that most of grains are relatively fine (~20μm diameter) which is like the HT1 condition (Figure 4-16). Figure 4-12 compares the precipitates in Group A and Group B small bolts, it is apparent that both are delta-rich, and the morphology of the δ phase is short and granular. Interestingly, the microstructure at the thread root of Group A small bolt (Figure 4-12a) is very different from that of Group B (Figure 4-12d), likewise, in Group B small bolts many microvoids are observed at the grain boundaries where the δ phase precipitates, and there is no evidence to show if the δ phase is new or pre-existing. Whereas the microstructure at the centre of both conditions (b and e) is comparable. In the section 4.2.2.2, the comparison of the precipitates at the thread root among Group A, B and C large bolts shows that some microvoids appear around δ phase after heat treatment.

Lower magnification

Higher magnification

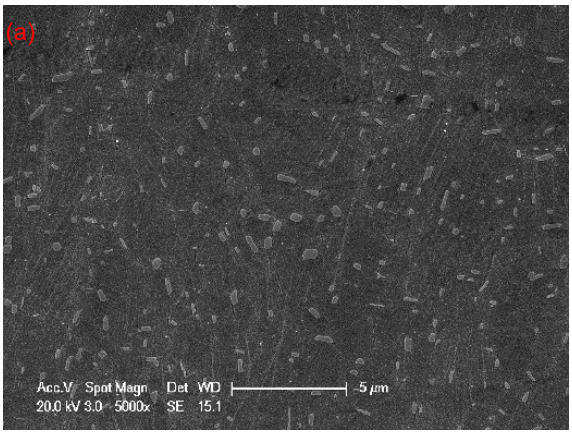

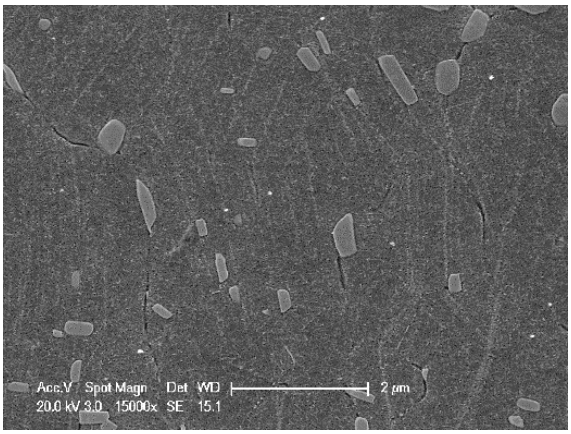

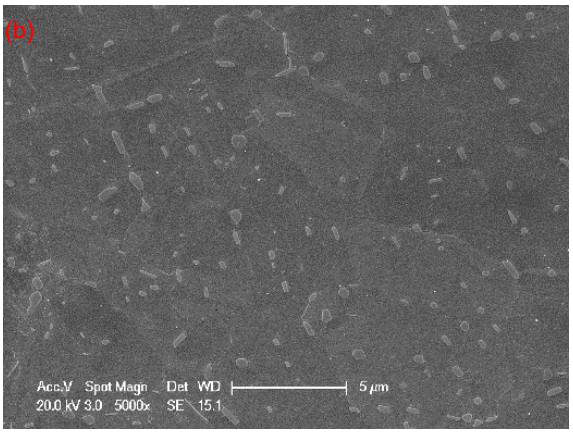

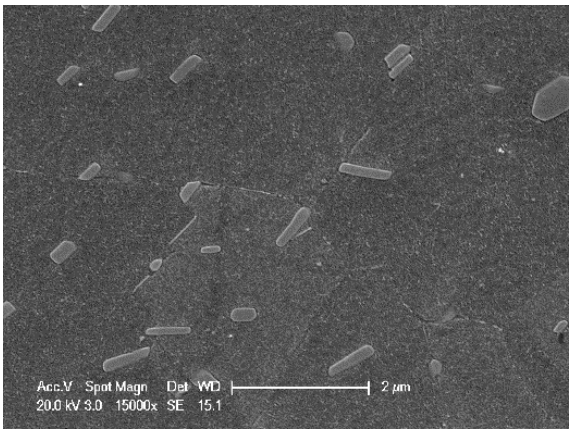

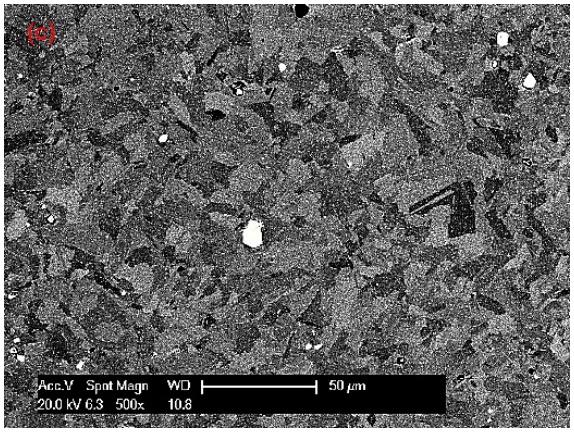

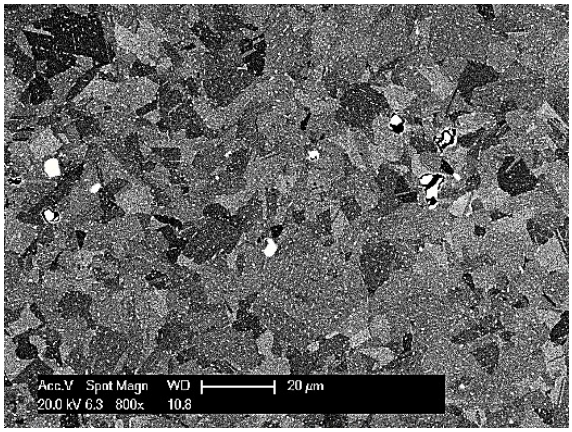

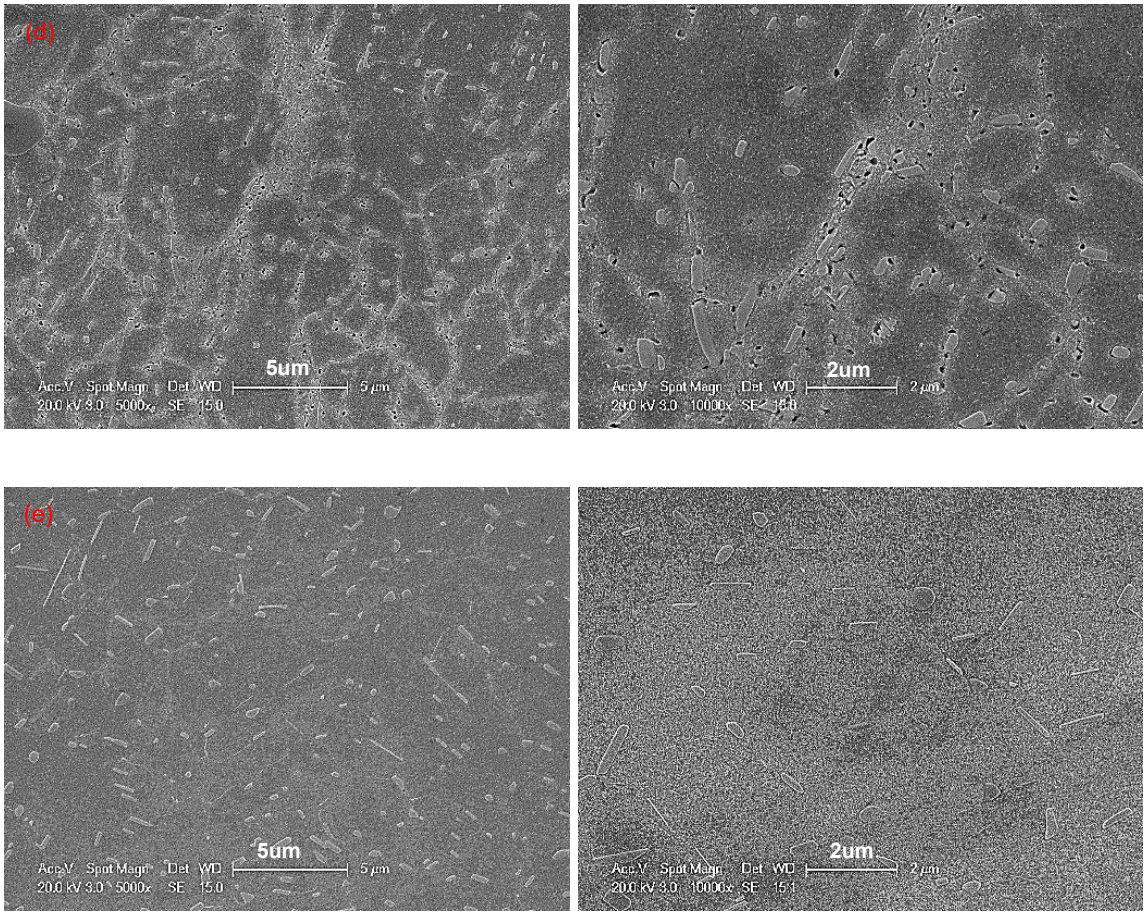

Figure 4-12 The thread root (a) and centre area (b) of As-received small bolts under SEM, the centre area of As-received small bolts under BSE (c), the thread root (d) and centre area (e) of Group B small bolts under SEM.

Microhardness

Microhardness testing from the thread root to the centre area was carried out on as received and Group B Small bolts. Figure 4-13 shows the comparison. It can be seen that the results of both conditions share the key features that the peak hardness appears at the thread root and rapidly drops towards the centre area of the bolts. Unlike the large bolts, the microhardness tends to decrease slightly overall after the heat treatment (Group B small bolt), and the difference is smaller moving closer to the centre.

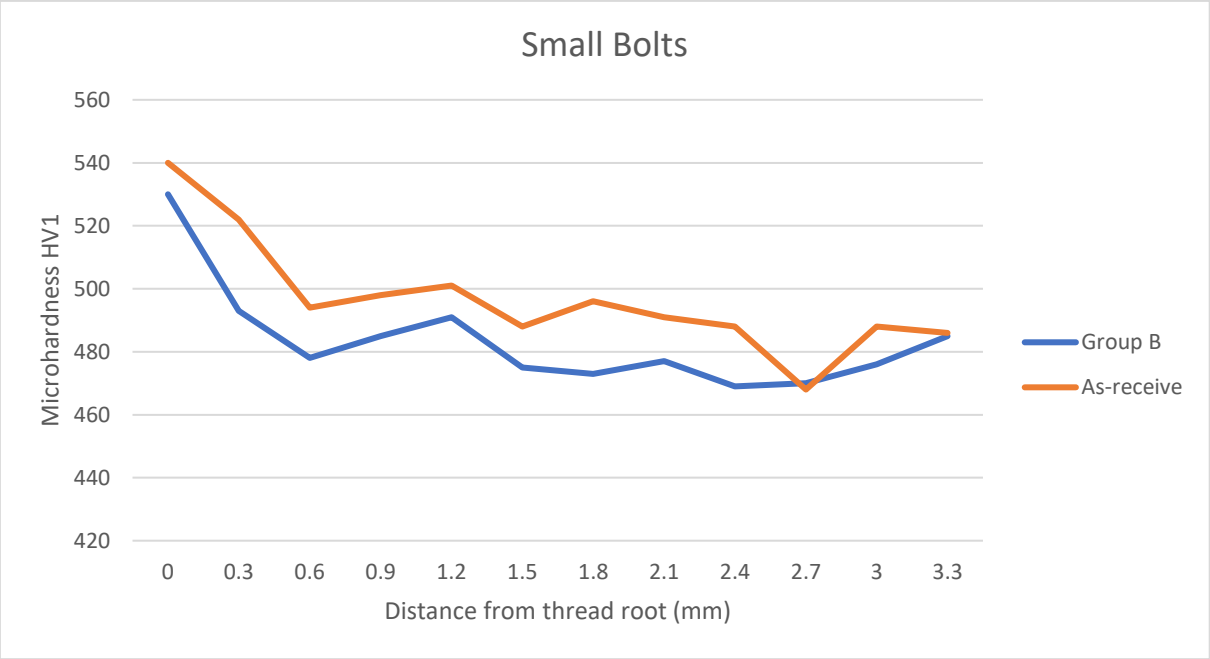

Figure 4-13 Microhardness of As-received small bolts and Group B small bolts

4.2 Grain size and phase analysis of HT samples

4.2.1 IN718 hot-rolled bars

The longitudinal and transverse sectioned as received and heat-treated bars were subjected to microhardness testing after polishing. Then the samples were repolished and etched by Kalling's No.2 or 10% phosphoric acid for grain boundaries or phase analysis, respectively.

Grain analysis

HT samples were cut from longitudinal and transverse directions to observe the grain structure. The latter was used to analyse the average grain size as the grain morphology is clearer without the hot rolling effect. Figure 4-14 shows an optical micrograph of HT0 after etching in Kallings No.2 reagent. The grain size (diameter) varies from 10μm to 55μm, and the twin grain boundaries can be observed. The same

etching procedure was applied on HT1 and HT3 samples. From Figure 4-14 (b) and (c) the grains revealed in HT1 are relatively fine and the average diameter is within 12μm, displaying the hot rolling deformation shown by the vertical dark flows. In HT3, the grains are very coarse up to 55μm in diameter (averagely 26μm) with no sign of hot rolling in Figure 4-14 (d) and (f).

A better contrast is shown in Figure 4-15 using BSE on HT1, HT2 and HT3, in the transverse direction. The grain size in HT1 is inhomogeneous and most grains are much finer than HT2 and HT3. The average grain area for conditions HT1, HT2 and HT3 were analysed by Image J software and the subsequent diameters are shown in Table 4-2.

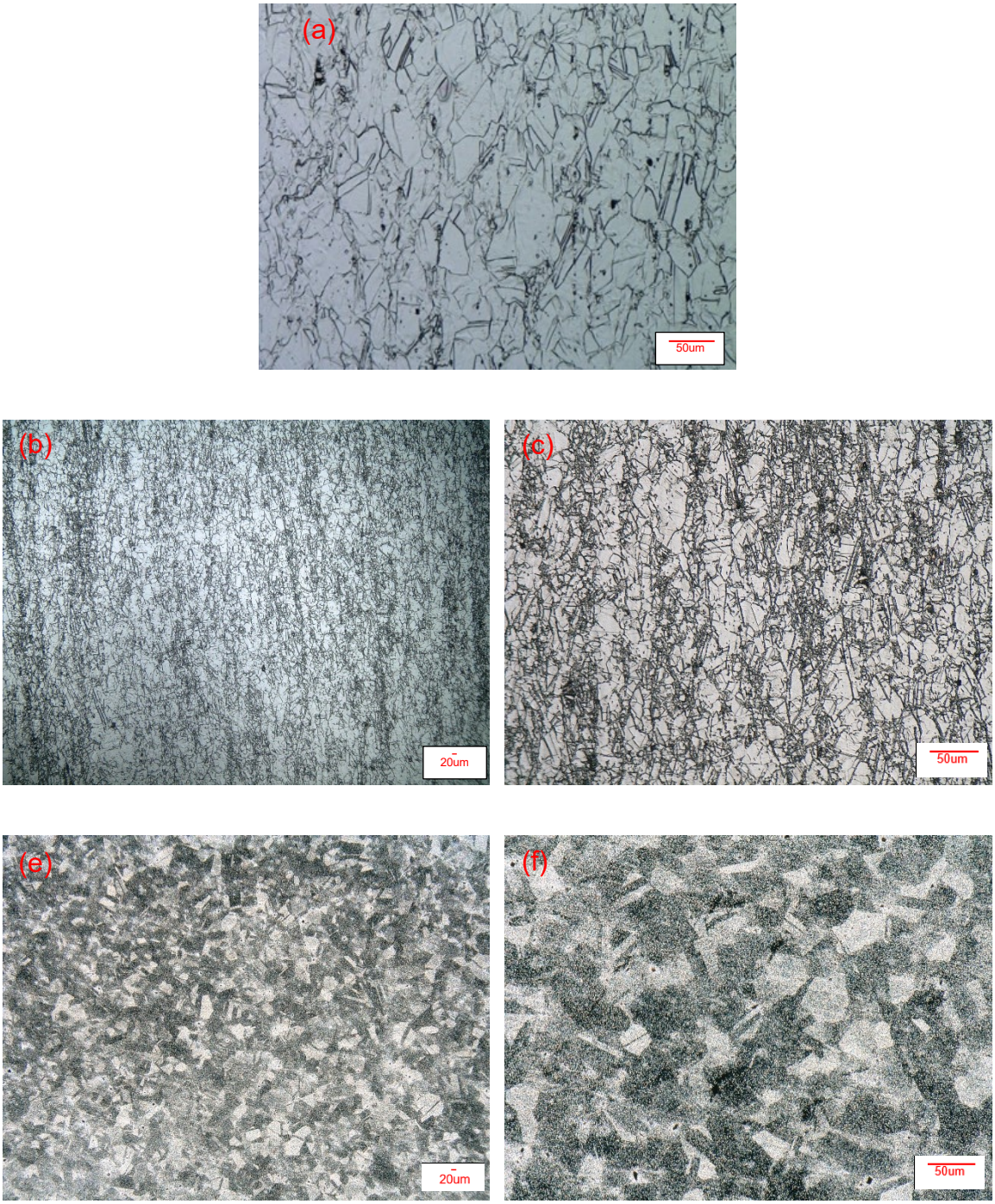

Figure 4-14 Optical micrographs of etched HT0 HT1 and HT3 samples in the longitudinal direction. (a) is HT0 at 500 magnifications, (b) and (c) are HT1 at 200 and 500 magnifications, (e) and (f) are HT3 at 200 and 500 magnifications.

HT1 SEM

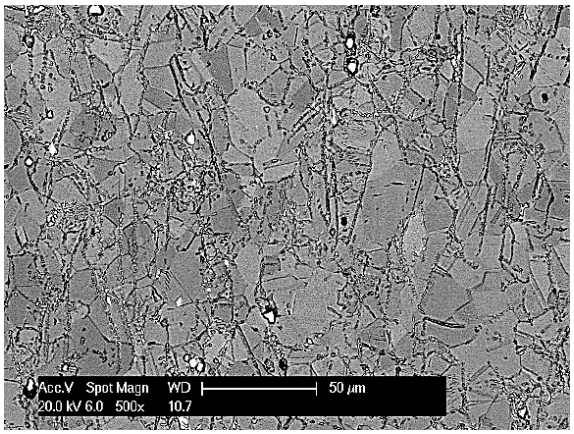

HT1 BSE

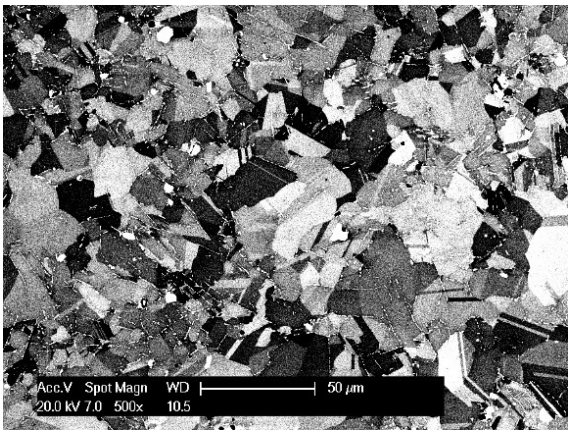

HT2 BSE

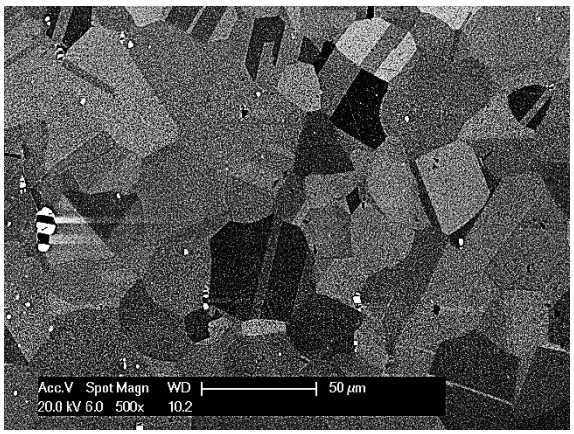

HT3 BSE

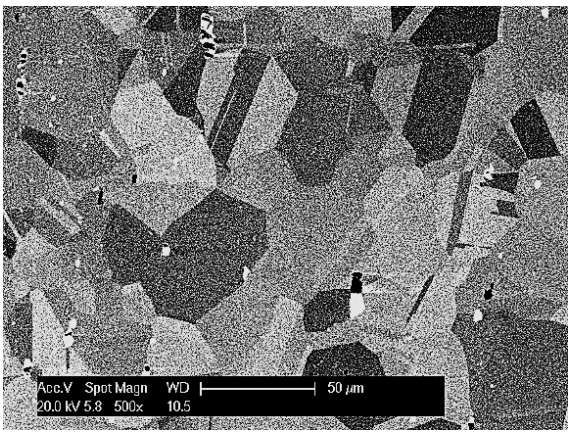

Figure 4-15 Grain observations of HT1, HT2 and HT3 in the transverse direction under the SEM and BSE

Table 4-2 Average grain size in HT1, HT2 and HT3

	HT1	HT2	HT3
Diameter (μm)	12	22	26

Phase analysis

Phase analysis was carried out on HT samples by taking images of δ phase under SEM and calculating the volume fraction. The precipitates stand out clearly in IN718 by electro-etching in 10% Phosphoric acid, and SEM images captured the δ precipitates shown in Figure 4-16. Image J software was used to calculate the volume fraction of δ phase in the images. HT0 as the baseline of the experiments only shows 1.8% δ precipitates and HT1 shows 3.2% δ precipitates, 2.5% of it in HT2 and zero in HT3

As shown in Figure 4-16, the needle-like particles are δ phase (the morphology of δ phase is introduced in Section 2.1.3) and the large blocky particles are likely to be carbides (circled in yellow). The majority of δ phase precipitates are along the grain boundaries, and some grow within the grains. HT1, HT2 and HT3 were characterised using higher magnification. The amount of δ phase in HT1 is considerably larger than that in HT2 and HT3. Less δ phase can be seen in HT2 and no δ phase can be observed in HT3. The morphology of δ phase in HT1 exhibits a long and thin needle-like shape and the fine γ” precipitates are displayed as very tiny dots in the background circle in red.

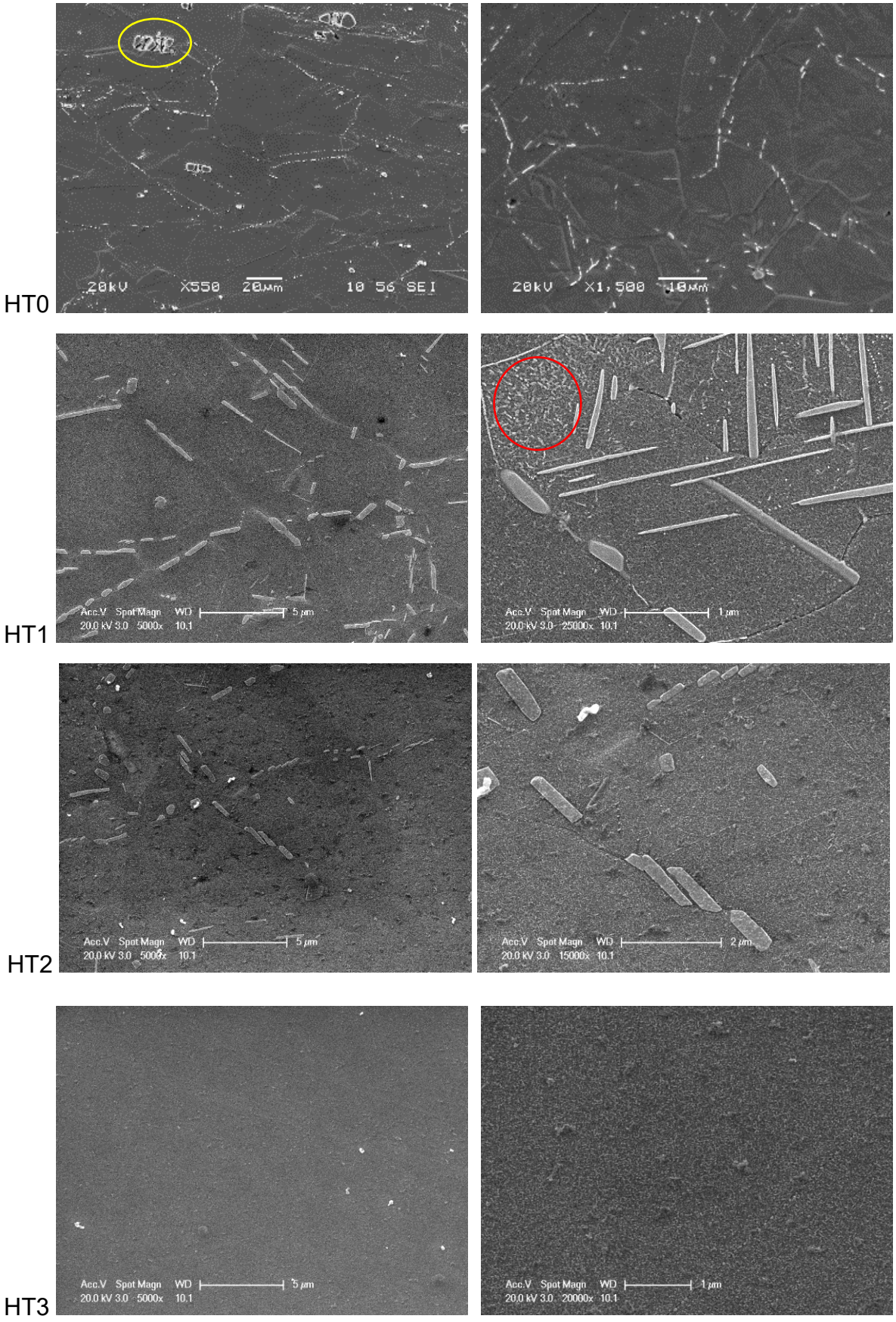

Figure 4-16 SEM images of HT*0, HT*1, HT2 and HT3 for δ phase observations

Microhardness analysis

The microhardness analysis of HT samples includes illustrating microhardness against radius and calculating the average microhardness within the sample in Table 4-3. Due to no cold work in the HT samples, the microstructure is homogenous throughout the bulk and the microhardness is not sensitive to the radius of the bar. The microhardness test was carried out on the whole transverse surface on each HT sample and the results were averaged, shown in Table 4-3.

The results indicate that the microhardness differs with the treatment procedures and the heat-treatment temperatures. The hardness of HT0 (369.2HV) is significantly lower than those of HT1, HT2 and HT3 (437.1, 445.5 and 449.8). This is because HT0 does not include an ageing treatment. Ageing treatment promotes the formation of the main strengthen γ” phase. HT1, HT2 and HT3 samples were solution treated at 925, 975 and 1010°C respectively and aged from HT0 condition. The microhardness is affected slightly by the solution temperature. The hardness of HT1 is lower than those of HT2 and HT3. HT3 is slightly higher than HT2. The δ phase solvus temperature is within 925-1010˚C. HT1 was solution treated at 925˚C which enabled more δ phase to precipitate prior to the ageing process, whereas HT3 was solution treated at 1010˚C to create a δ phase-free environment, as most δ phase dissolved at such high temperature. Hence, the amount of δ phase in HT1 condition is expected to be the highest followed by HT2, and no δ phase exits in HT3. Accordingly, the percentage of γ” phase formed during ageing treatment shows the opposite trend, since both δ and γ” precipitates are Ni_3Nb. Solution treatment at 925˚C (HT1) promotes a large amount of δ phase, the remaining Ni_3Nb in the γ matrix is less than HT3 condition, thus, more γ” phase precipitates in HT3 by the following ageing process, leading to a higher

hardness. The result is also balanced by the effect of grain size, which is considered in the following section.

Table 4-3 Microhardness of HT samples (error ±3.3)

	HT0	HT1	HT2	HT3
Hardness (HV1)	369.2	437.1	445.5	449.8

4.2.3 Thermal-exposure HT samples

A heat treatment at 650°C for 100 hours was applied on the HT1 and HT3 samples, which is the same as Group B treatment.

Like the results of the original HT samples, the microhardness of thermal-exposure HT3 (457.9) is greater than thermal-exposureTHERMALHT1 (443.6) and both have increased compared to the original the HT1 and HT3 condition respectively, shown in Table 4-4.

Figure 4-17 shows that after thermal exposure, no significant changes can be seen in terms of grain size and grain morphology in HT1, while the grains in the thermal-exposure HT3 condition is slightly larger than in the original HT3.

Figure 4-18 shows the volume fracture and morphology of the δ precipitates remain the same in the thermal-exposure HT1 as in the original condition. Similarly, no obvious changes in the HT3 condition after the exposure.

Table 4-4 Microhardness of thermal-exposure HT1 and HT3 (error ± 3.3)

	HT1	HT3
Original (HV1)	437.1	449.8
Thermal exposure at 650°C/100h (HV1)	443.6	457.9

Thermal-exposure HT1 Thermal-exposure HT3

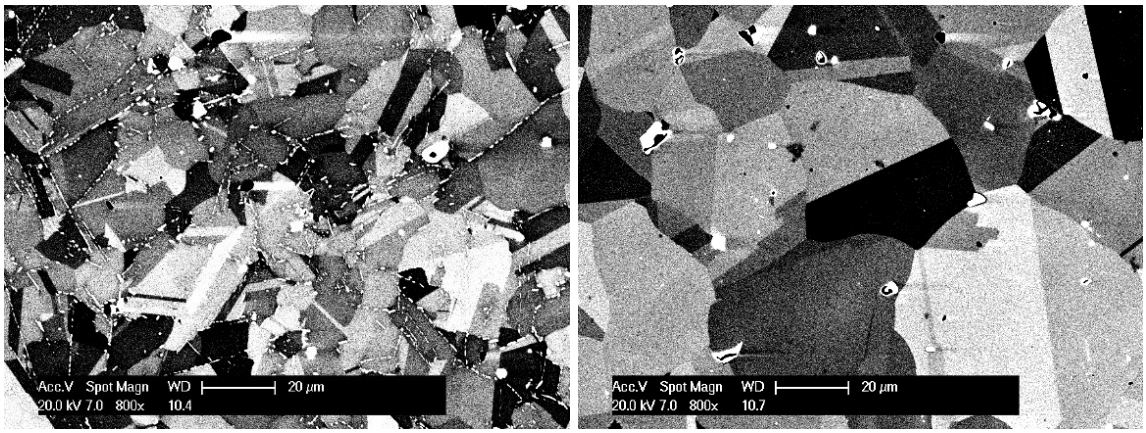

Original HT1 Original HT3

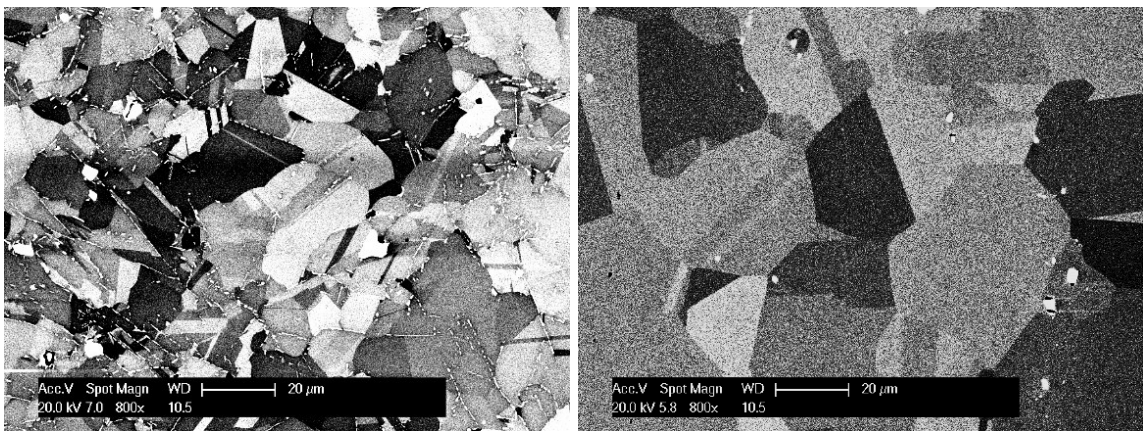

Figure 4-17 Thermal-exposure and original HT1 and HT3 under BSE

Thermal-exposure HT1

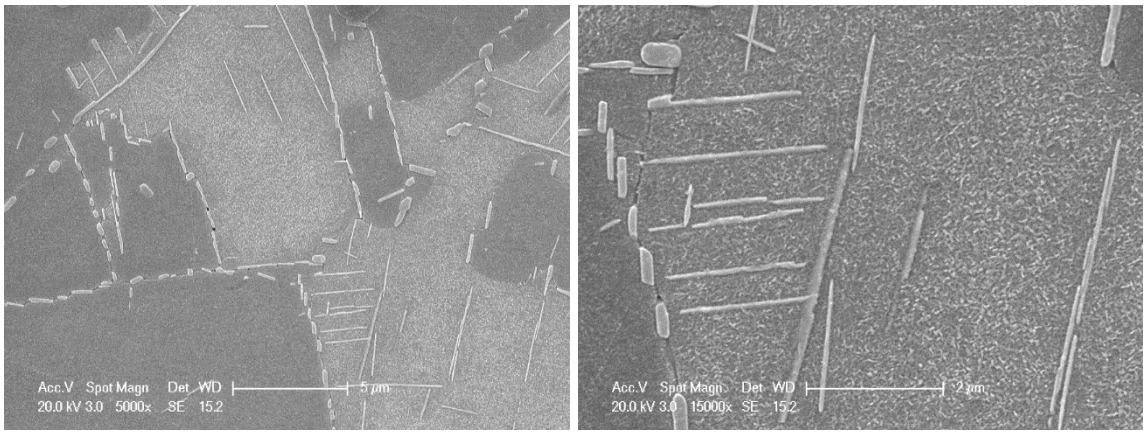

Thermal-exposure HT3

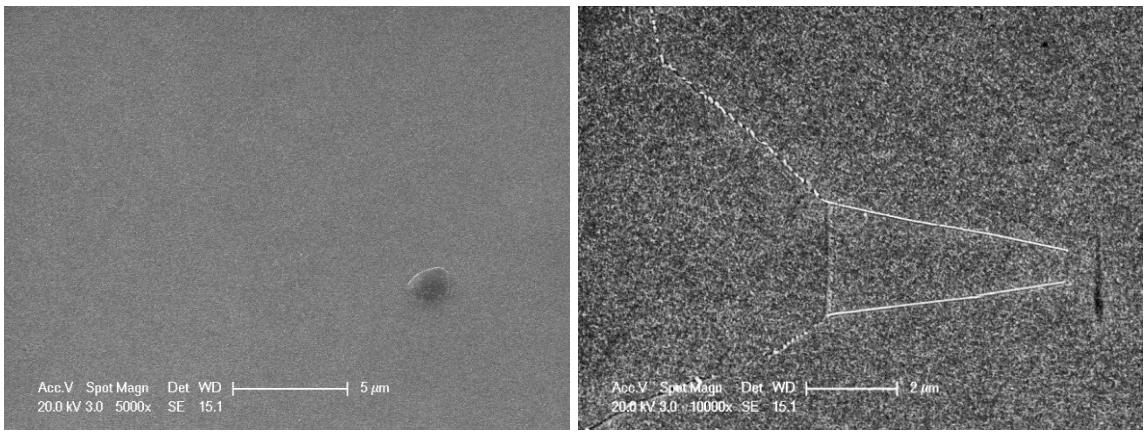

Figure 4-18 Phase observation in the thermal-exposure HT1 and HT3 samples

4.3 Bending fatigue behaviour

Research of the bending fatigue behaviour on IN718 bolts includes characterisation on the samples, testing results analysis, fractography and cross-sectional microstructure. The purpose of the bending-fatigue testing is to replicate closely the real situation of the IN718 bolts in-service performance as well as to study the effect of cold rolling at the thread area. The tests were carried out on the half-cut as-received large bolts (see

Figure 3-8, Section 3.1.3.2) with the retained threads area and the solution-treated samples which relieved the cold-rolling effect at the thread section, the former is referred to here as cold work (CW) samples and the latter cold work free (CWF) samples.

4.3.1 Characterisation

The pre-testing characterisation included the measurements of the test piece, microhardness and EBSD. The width measurements (W) were required for stress calculation, which was carried out by optical microscope measurement shown in Figure 4-19. The microhardness test and EBSD scanning at the thread section were applied to examine the presence of cold-rolling in CW samples and to show no cold-rolling remained in CWF samples.

The microhardness tests were taken from the thread tips, starting as close as possible to the surface, and then moving towards the centre of the samples to the core. The results of the CW samples and CWF samples are provided in Figure 4-20. For the CW samples, the microhardness within 1mm from the thread tip is very high, up to 600HV, then it shows a distinct drop after passing the thread root area which is indicated as the yellow dot in Figure 4-20 and tends to become steady towards the centre. By contrast, no such trend can be found in CWF samples, the microhardness overall is even from the thread tip to the centre of the sample and lower at the thread root than in the CW sample.

The EBSD mappings obtained from the thread tip of both conditions are presented in Figure 4-21. Figures 4-21(a) and (b) are the crystal orientation maps for CWF and CW respectively. The notable differences between CW and CWF samples are that most

grains in the CWF samples at the threads are equiaxed and the grain boundaries are coloured in black. In contrast, no grains can be observed in the CW samples and the grain boundaries are severely distorted.

A fine step-size EBSD mapping (band contrast) was taken at a further depth near the thread-root area in the CW sample in Figure 4-21 (c) and (d). This is to detect if the cold work still exists beyond 250μm from the thread-root surface. Figure 4-21(c) shows that the grain boundaries are very slightly distorted. However, by analysing the recrystallisation-deformation map in figure 4-21(d), some areas of heavy coldwork, shown in red zone can still be seen to exist, and the rest of the area is covered by sufficient cold work in yellow as the substructure. From the EBSD results, cold rolling heavily affects the threads and thread root surface to a depth of at least 250μm, and the remaining cold work still can be detected beyond the depth where the grains appear only slightly deformed. The following testing results investigate the influence of thread rolling on high-temperature fatigue performance, as well as the microstructural evolution under the dwell fatigue testing.

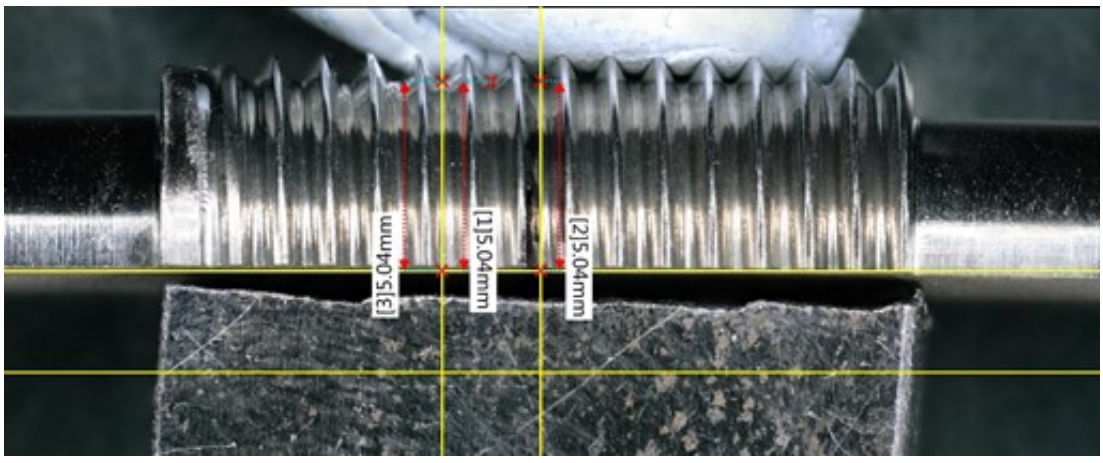

Figure 4-19 Width measurements of the bending samples

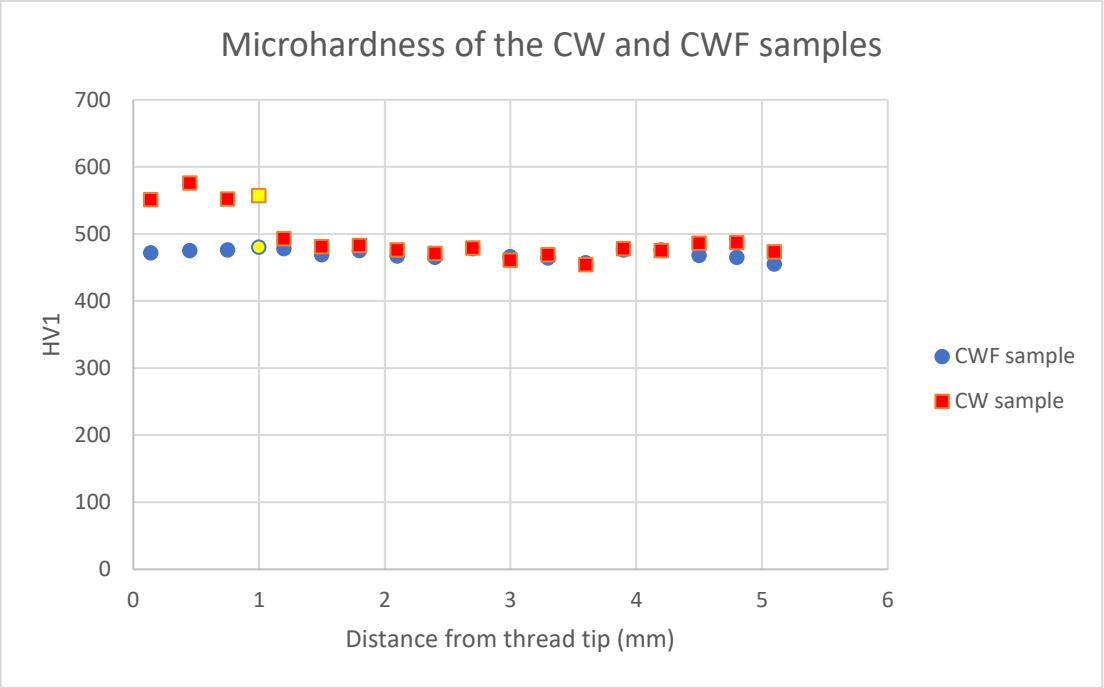

Figure 4-20 Microhardness of CW and CWF samples

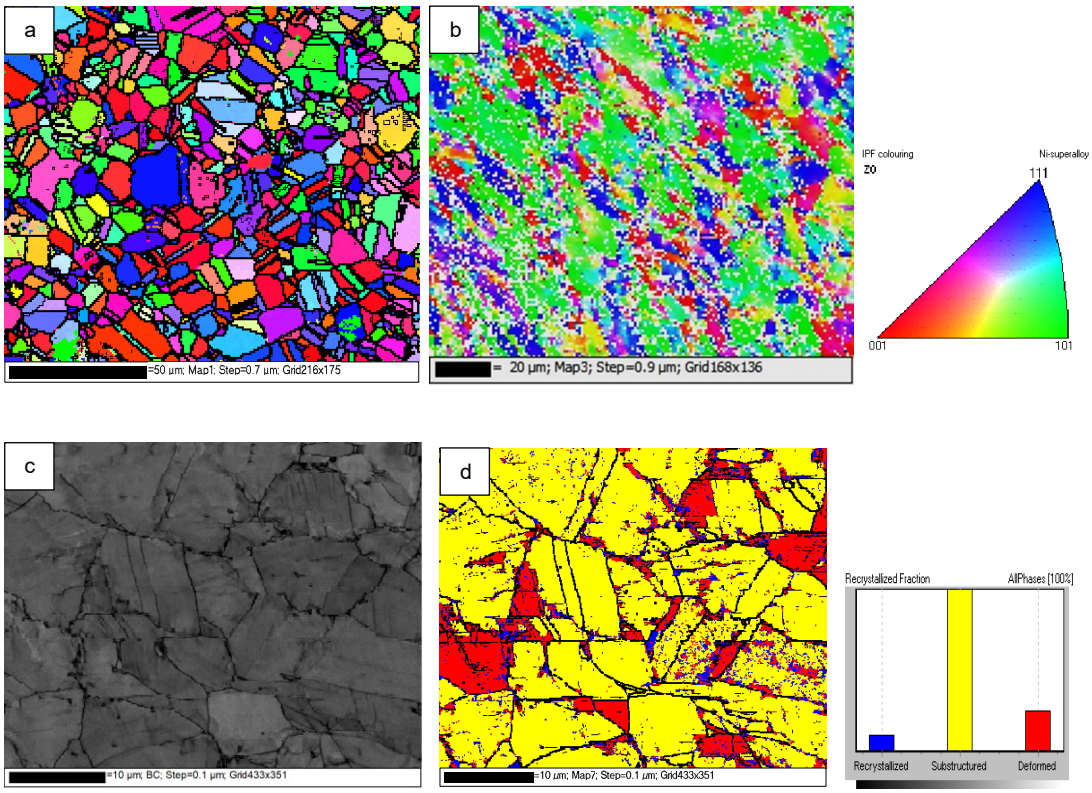

Figure 4-21 IPF mapping of (a) CWF and (b) CW samples at the threads; (c) band contrast and (d) deformation analysis of CW sample at a depth of 250μm below the threads root surface.

4.3.2 P.d. vs crack growth calibration

Since the shape of half-bolt bending samples is irregular, trial tests were performed to establish a relationship between the potential difference (p.d.) and the crack length (Δa) of the samples. Figure 4-22 represents the calibration outcome, depicted as Δa/W vs. $\Delta V/V_0$, with W denoting the sample width (measure in Figure 4-19), delta V indicating the voltage increase, and V_0 representing the initial voltage. Changing the conditions while testing a sample, such as stress and frequency, leaves beach marks on the fracture surface after the test, which are measured to give the crack length for each condition. The trial sample was tested to failure, and the errors of measuring the crack length cannot be neglected, such as cracks might initiate from multiple locations. Nevertheless, empirical evidence suggests that the calibration of potential difference (p.d.) against crack growth for half-cut-bolt samples shows promise. The trial test was conducted at 650˚C under 1300MPa or 1500MPa with 1-1-1-1 waveform or 5Hz frequency. The fracture surface of the trial sample is shown in Figure 4-23. Three distinct fatigue zones can be observed in Figure 4-23 (b):

1. The tiny light brown zone (1300MPa,1-1-1-1 waveform)
2. The darker brown zone (1500MPa,1-1-1-1 waveform)
3. The dark grey zone (1500MPa, 5Hz)

The large dark blue area in Figure 4-23 (a) is the overload zone that occurred during final failure, and the bottom silver line is caused by manually separating the sample after testing.

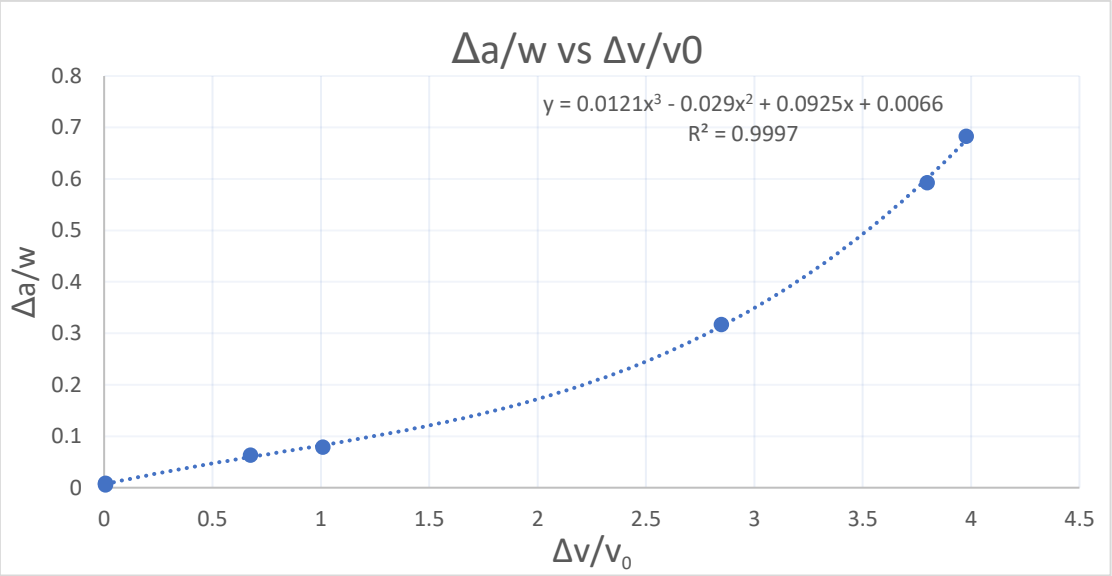

Figure 4-22 The calibration relationship between p.d. ($\Delta V/V_0$) and crack growth rate ($\Delta a/W$) of the bending test pieces

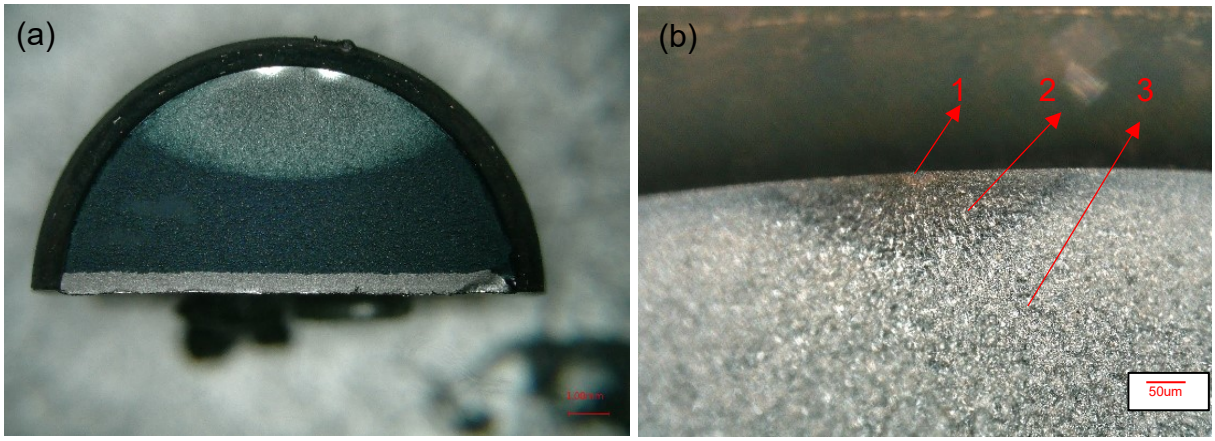

Figure 4-23 Optical images of (a) the fracture surface of the trail sample and (b) the three fatigue zones.

4.3.3 Baseline bending fatigue testing

To distinguish the CW and CWF conditions, both samples were tested for characterising the bending-fatigue properties under baseline (1-1-1-1) with an R ratio of 0.5, at 650˚C.

4.3.3.1 Results analysis

The testing results of the CW condition are summarised in table 4-5. Figure 4-24 (a) showing the overall p.d growth against time. From 0 to 6 hours (approximately 5400 cycles), no significant p.d. growth was observed. Then the p.d increased slightly until 10 hours was reached. This was followed by a rapid rise to 1000mV at 11 hours due to overload and the machine stopped cycling, the sample failed. The load redistributed since the machine failed to bring the load down to zero immediately when it stopped cycling at 11 hours and the sample completely broke at 14 hours. The valid life was from 0 to 10.95 hours. Closer inspection of the valid fatigue life in Figure 4-24(b) shows that p.d. started slowly increasing by 13 mV from 4.8 hours to 9 hours, followed by a surge until failure.

The CWF sample unexpectedly failed at the sharp edge between the shank and the threads, as shown in Figure 4-25. As the failure occurred outside the p.d. probes, the data recorded on crack growth at the thread root monitored by p.d. is invalid in terms of fatigue life at the thread section. Comparing with the CW sample under the same testing conditions, the CWF sample failed after less than half the life of the CW test, only lasting for 4.51 hours in table 4-5. However, the baseline result of the CWF sample cannot be analysed directly due to invalid failure location.

Table 4-5 Summary of the CW and CWF baseline testing results

	w	load	Stress	Frequency	cycles	time
CW	5.04mm	3.66kN	1500MPa	1-1-1-1	9857	10.95
CWF	5.04mm	3.66kN	1500MPa	1-1-1-1	4066	4.51h

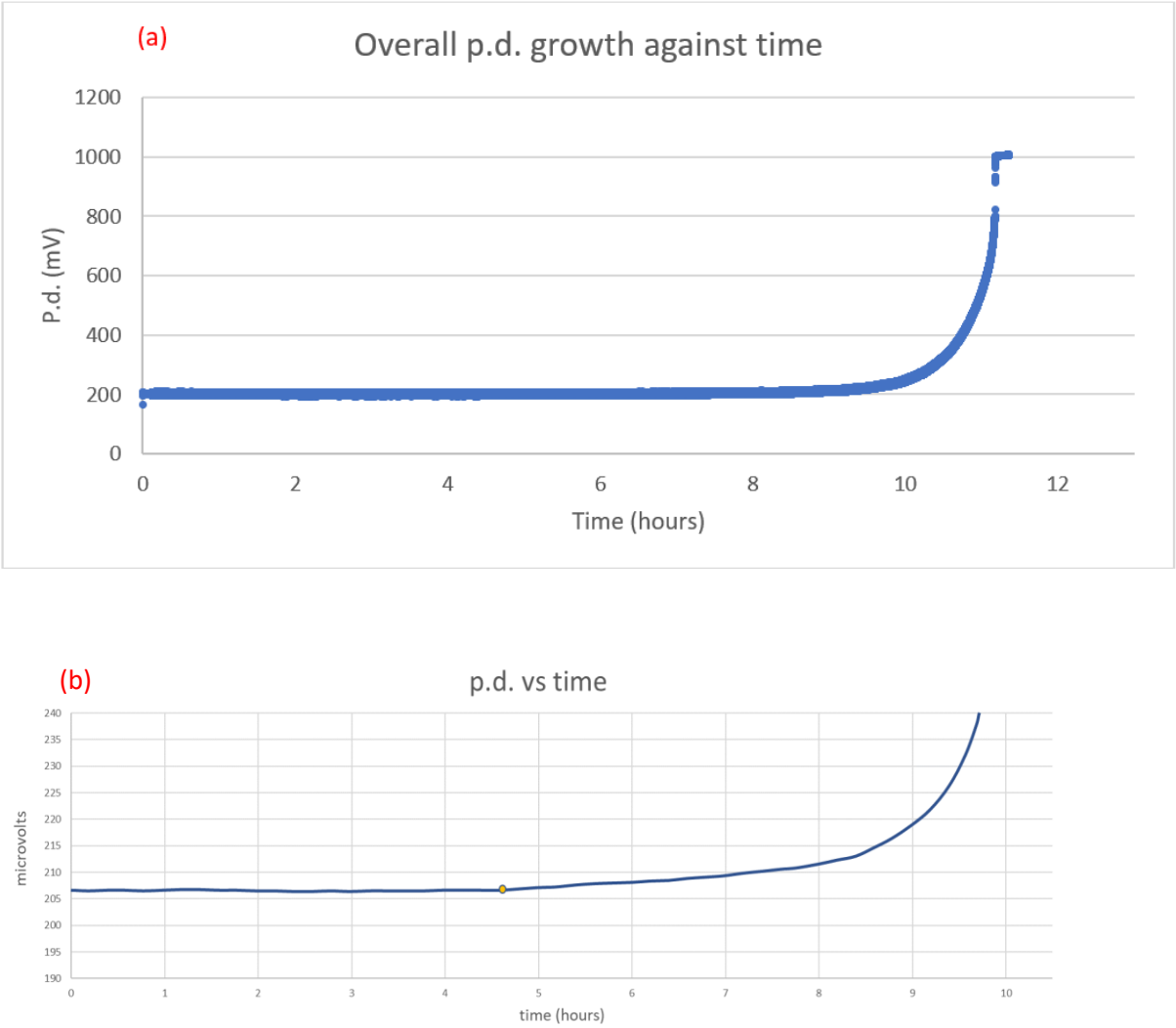

Figure 4-24 The baseline testing results of the CW sample presented by p.d against time (a) overall and (b) locally.

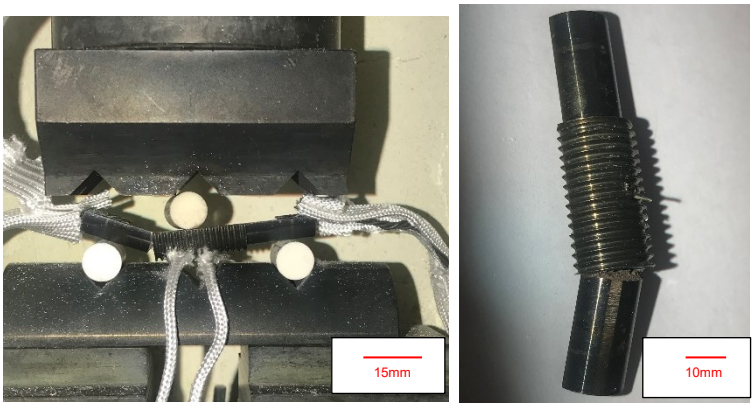

Figure 4-25 The tested CWF sample failing at the threads edge

4.3.3.2 Fractography

The fracture surfaces of CW and CWF samples were examined at the lower-magnification SEM. The optical images (Figure 4-26) show that both fracture surfaces consist of fatigue and overload areas, and a closer observation was carried out by SEM from the crack origin to the centre zone in Figure 4-27. Within 200μm from the origin in Figure 27 (a), the CW sample shows a flat fracture surface overall, especially within 30μm no grains can be observed. The crack growth mechanism then gradually becomes a mixture of intergranular and transgranular. The CWF sample shows bumpy intergranular failure with a small amount of transgranular behaviour from the crack origin to the end of the fatigue zone (see Figure 4-27 b). Due to the heat treatment on CWF sample, the recrystallisation layer at a depth of 60μm from the surface can be seen in Figure 4-27 (b).

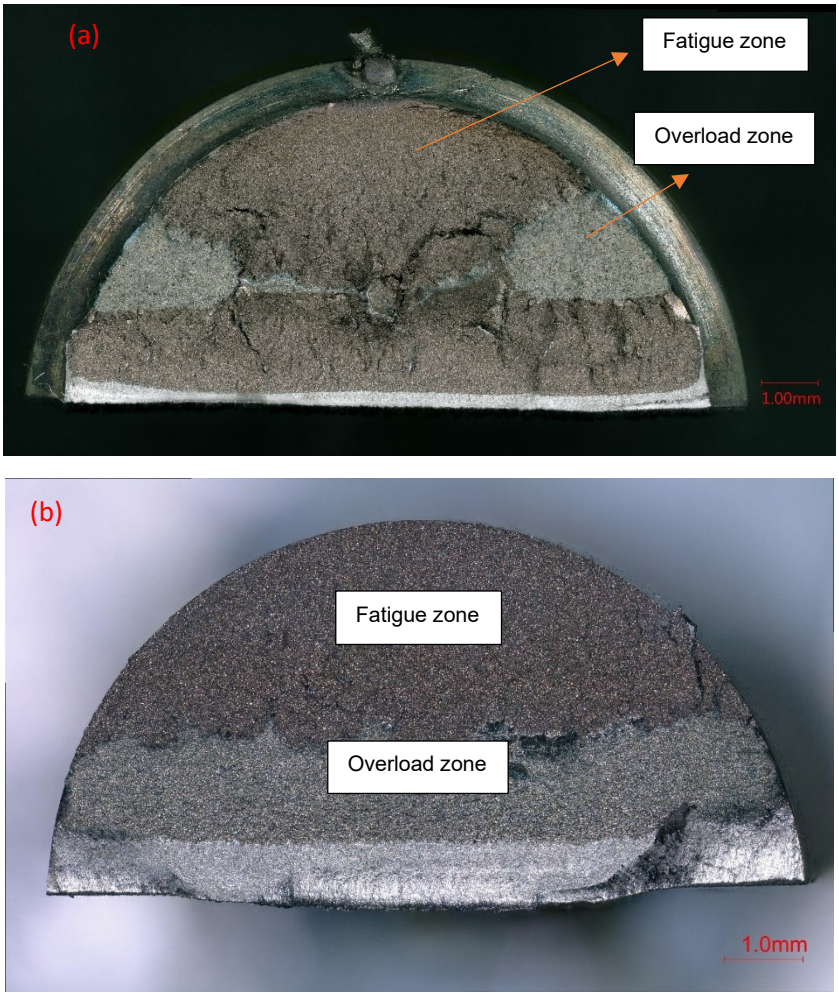

Figure 4-26 Optical images of the fracture surfaces of (a) CW and (b) CWF

(a)

Overview

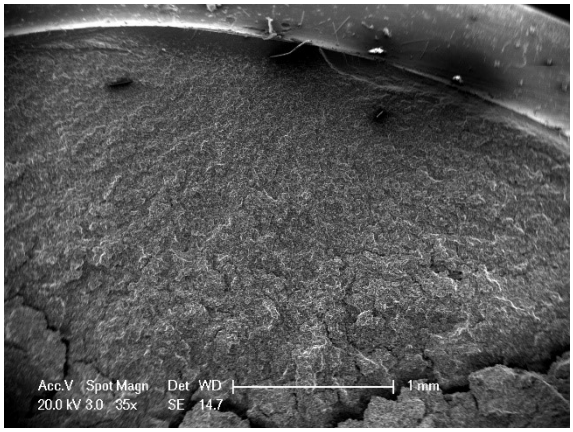

60μm

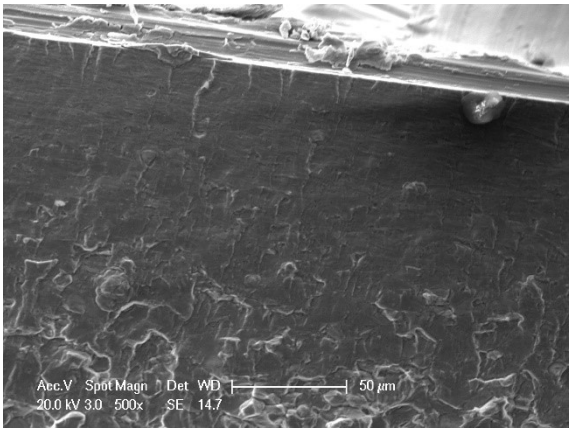

160μm

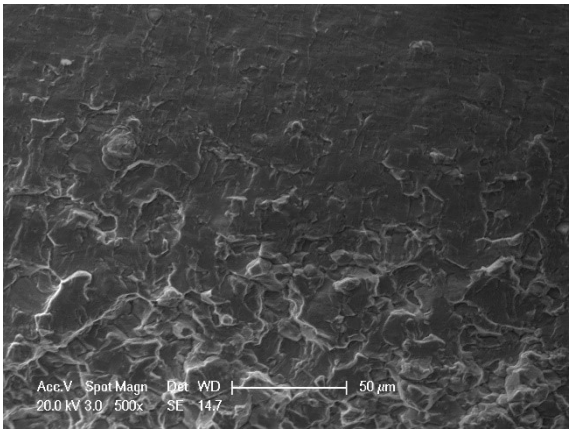

550μm

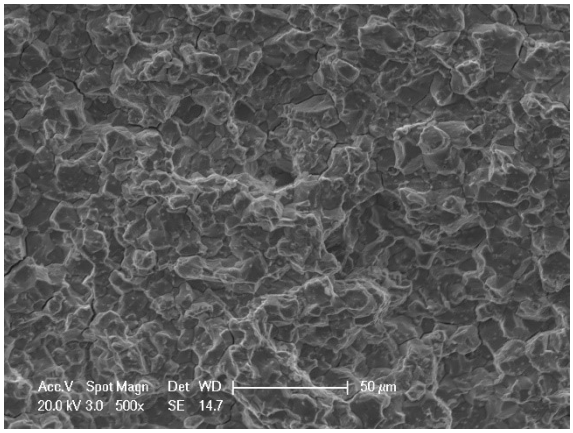

1200μm

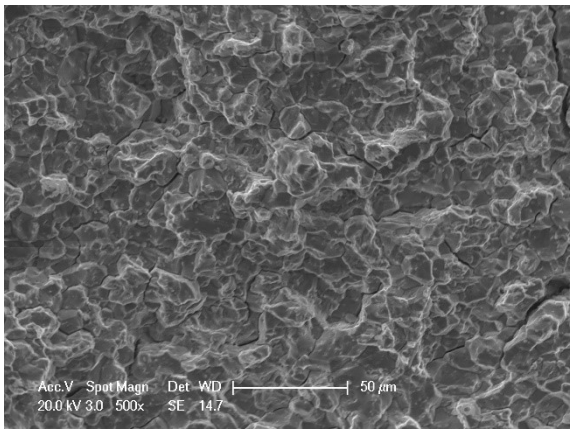

load-redistribution

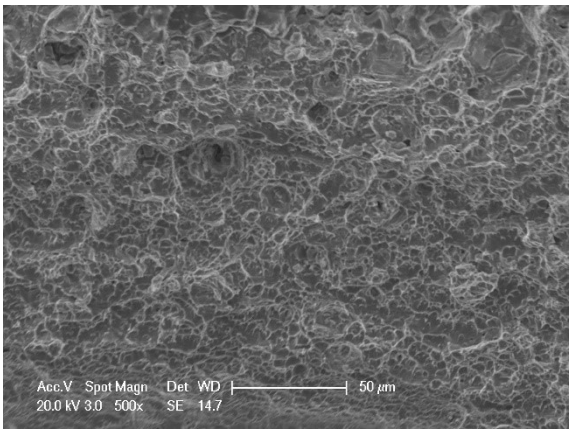

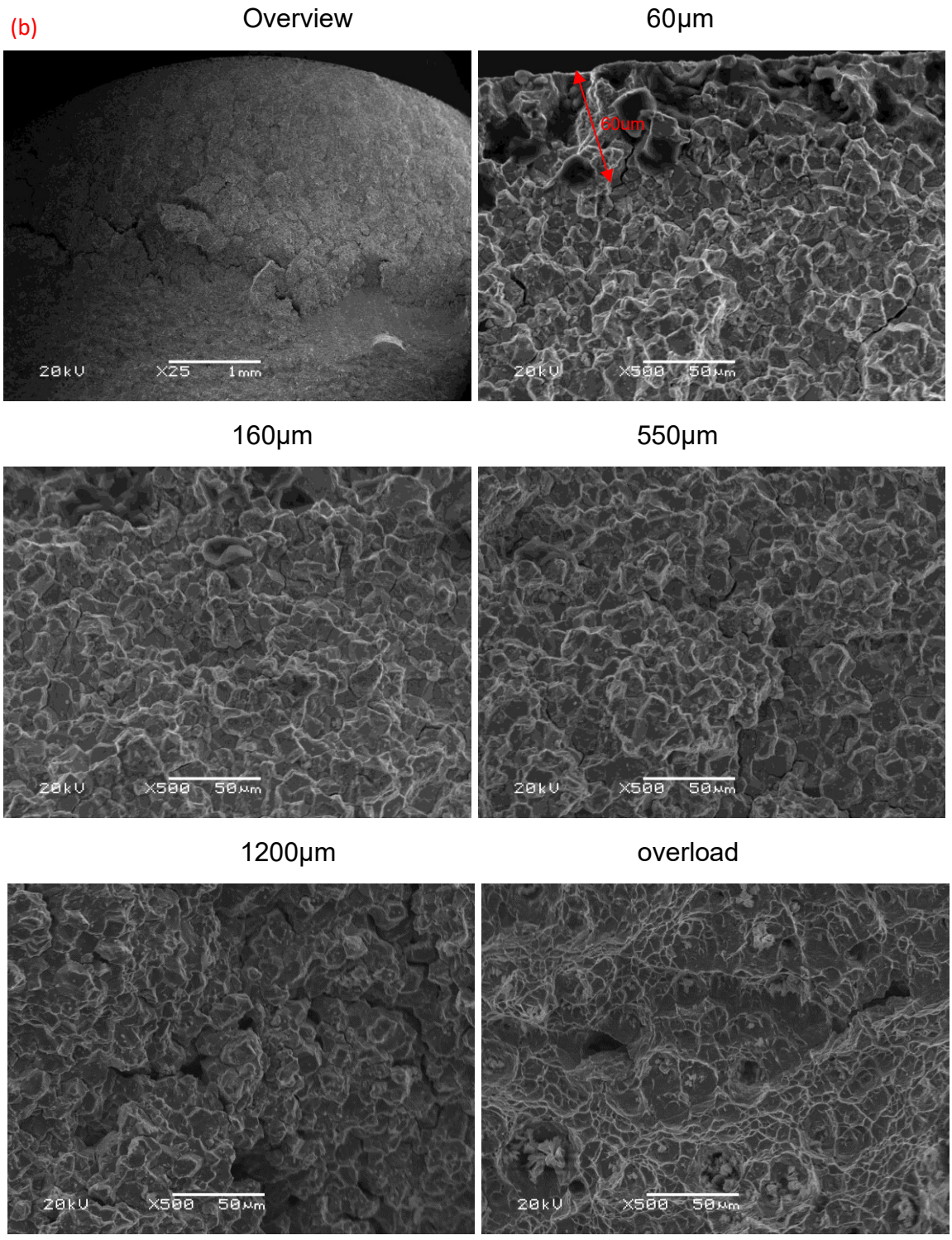

Figure 4-27 SEM images of the fracture surfaces of (a) CW sample and (b) CWF sample at different depth from the thread root surface

4.3.3.3 Cross-sectional microstructure

To investigate the phase changes of both conditions after the tests, the failed samples were sectioned along the centre (green dashed line, shown in Figure 4-28) and then metallographically prepared for characterising the cross-sectional microstructure. SEM images of the CW test piece are shown in Figure 4-29 (a). What is striking about the CW sample is the similarity in δ phase and γ” distribution to Group C large bolts (thermal exposure with load) in Figure 4-11. Although, no microvoids can be seen in CW sample, a large amount of newly precipitated δ phase can be seen within 80μm depth from the thread root surface towards the centre, which is thinner and smaller compared to the original blocky δ precipitates in Figure 4-11(h). The γ” precipitates dissolved around the newly precipitated δ phase, leading to a darker flat and clear area (circled in red). No newly precipitated δ phase can be seen at 100μm depth or deeper and the γ” phase is evenly distributed.

The characteristics of the CWF sample differs from those of the CW. Both δ phase and γ” phase are evenly distributed throughout the CWF sample. Additionally, the number of δ precipitates increases in the CWF sample at the thread area after the heat treatment in Figure 4-29 (b).

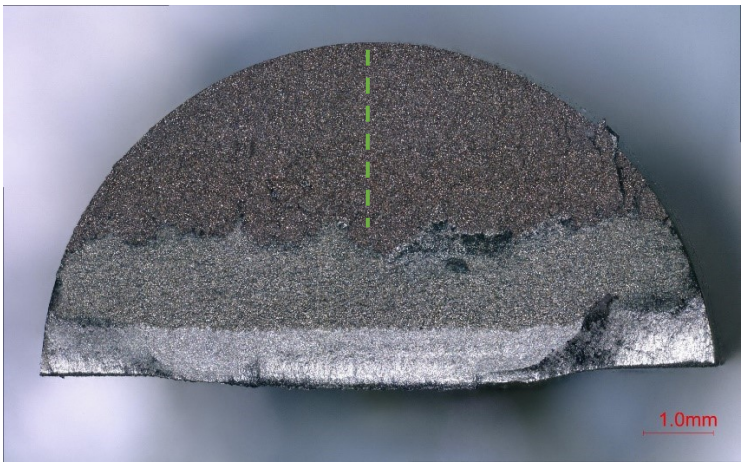

Figure 4-28 Preparation of cross-sectional microstructure on the CWF sample

(a)

Overview

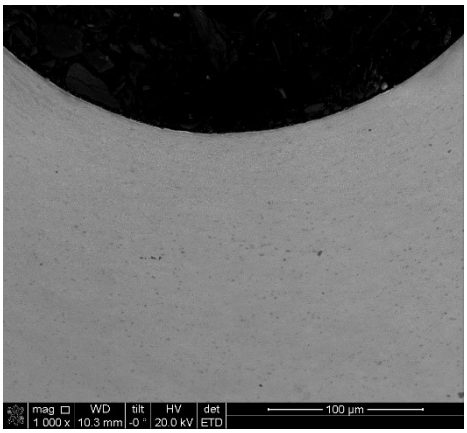

30µm

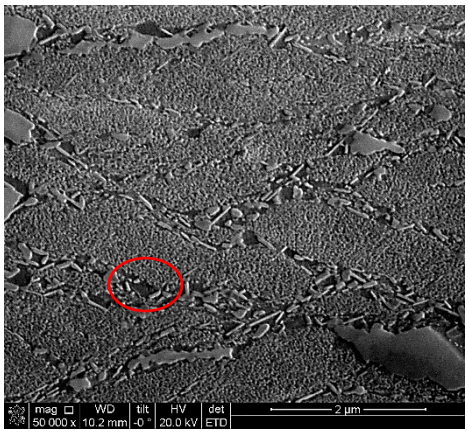

50µm

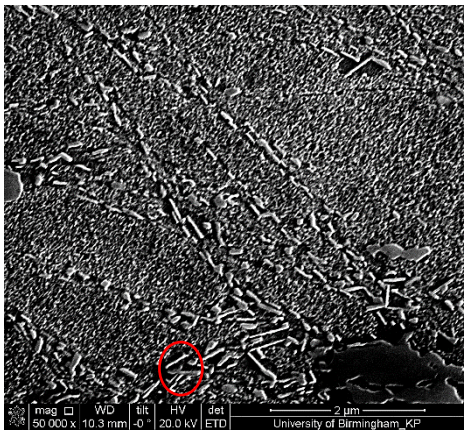

80µm

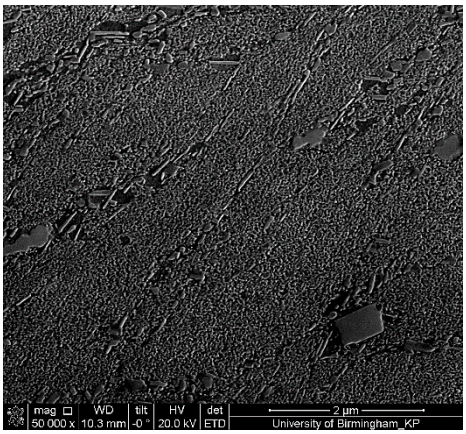

160µm

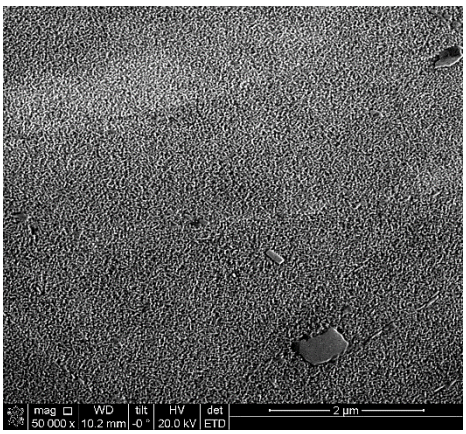

centre

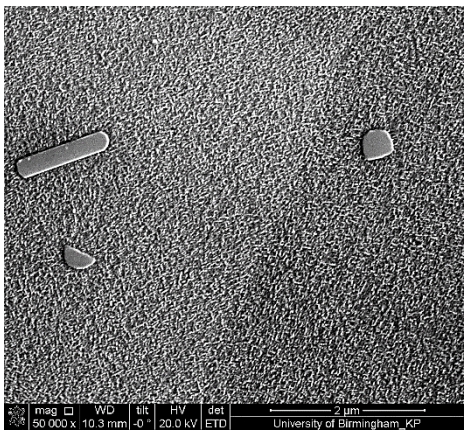

(b)

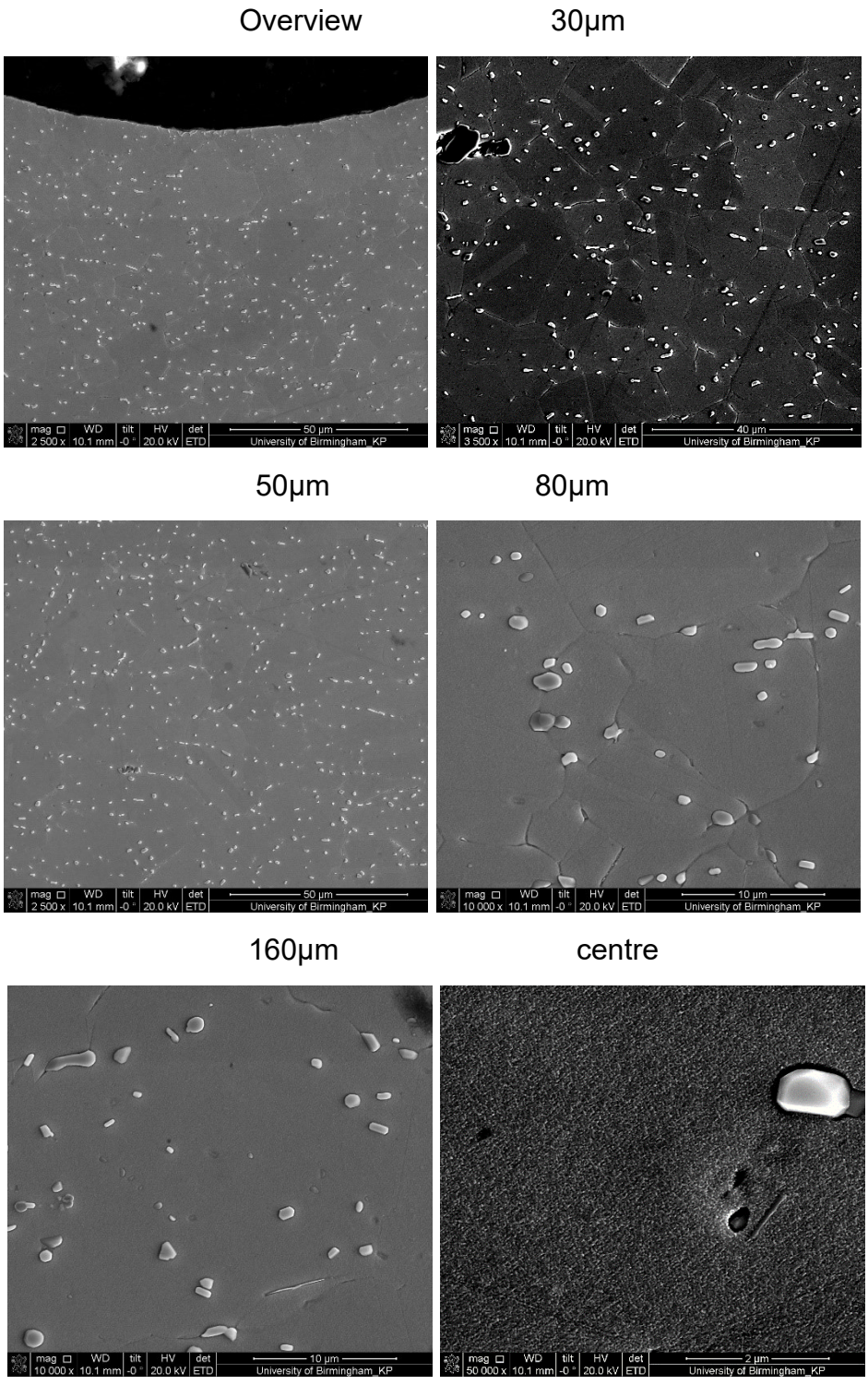

Figure 4-29 SEM images of cross-section profiles of the (a) CW and (b) CWF samples at the thread root.

4.3.4 Dwell bending fatigue testing

Dwell fatigue bending tests were conducted on the CW and CWF samples to study the effect of cold work on the bending fatigue performance. The cycling waveform was changed to 120-second holding time at the peak stress, followed by one second at the minimum stress and one second increasing or decreasing the stress (1-120-1-1). The rest of the conditions including R ratio (0.5) and the testing temperature (650˚C) remain the same.

4.3. 4.1 Results analysis

The testing results of both conditions are compared in Table 4-6, and the p.d. growth against time is plotted in Figure 4-30. The CW test was discontinued after 693 hours (over 20000 cycles) due to the bluntness of crack tip, since the p.d. trend tended to be steady, instead of aggressively growing after 20000 cycles in Figure 4-31 (b), the test was discontinued. The number of CW dwell fatigue cycles (20423) is over twice than that of the CW baseline fatigue cycles (9857). The p.d of the CWF sample showed a significant increase after 15000 cycles in Figure 4-32, The CWF sample underwent testing and exhibited deformation, resulting in a long crack formation after 21153 cycles.

A closer look was taken at a smaller range of p.d. against time or cycles for both conditions to enable the observation of crack initiation in Figure 4-31 and 4-32. The testing results show that the crack initiation life of the CW sample is approximately 216 hours over 6000 cycles (indicated by the black dot) and that of the CWF sample is approximately 192 hours (indicated by yellow dot). For the crack propagation life, the crack in the CW sample increases slowly and steadily, until 680 hours, when the p.d. tends to level off and the crack is likely to have stopped propagating due to crack tip

retardation. The crack in the CWF sample starts growing slowly until 520 hours, followed by a rapid propagation to failure.

Table 4-6 Summary of the CW and CWF dwell fatigue testing results

	w	load	Stress	Frequency	cycles	time
CW	5.42mm	4.55kN	1500MPa	1-120-1-1	20423 (discontinued)	693.39h (discontinued)
CWF*	5.42mm	4.55kN	1500MPa	1-120-1-1	21153	722.73h

*CWF: The machine came to a halt because the test piece exceeded the programmed displacement limit over bending.

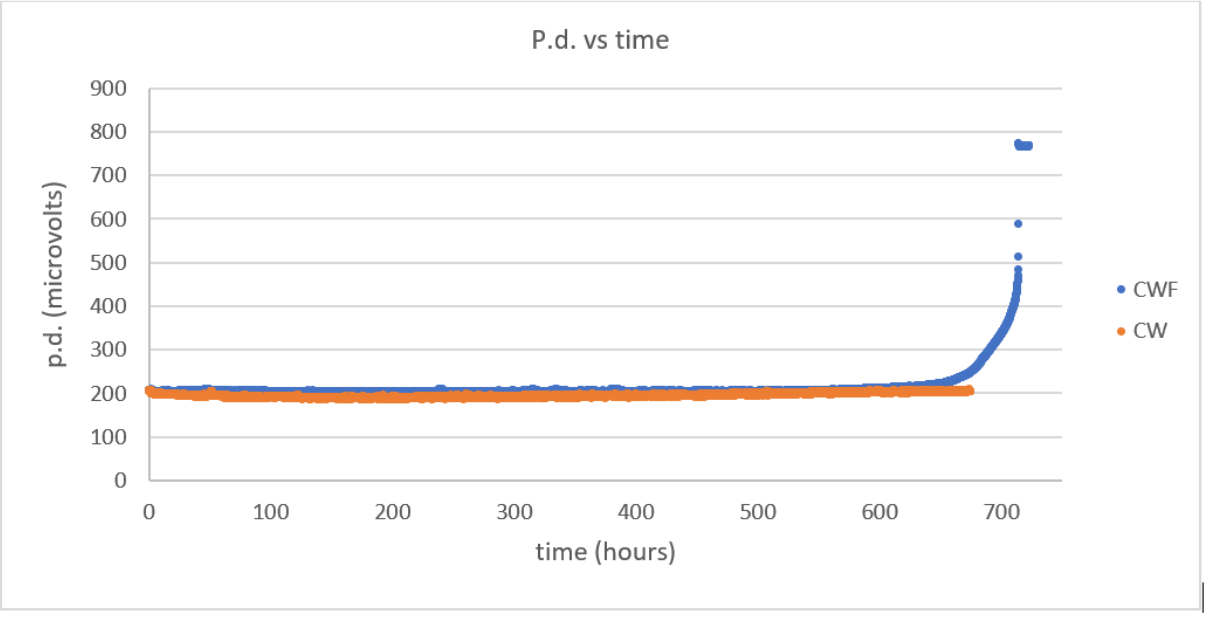

Figure 4-30 The p.d. against time of CW (in orange) and CWF (in blue)

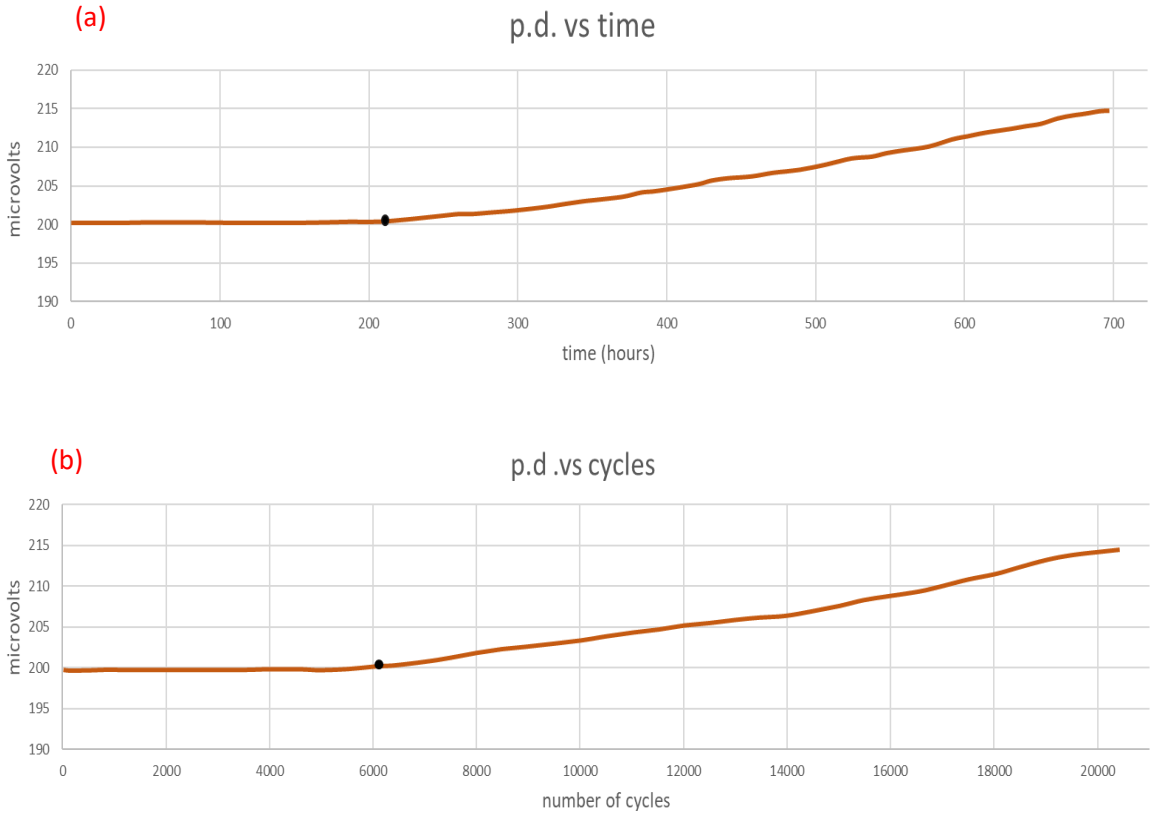

Figure 4-31 The dwell fatigue testing results of the CW sample presented by p.d against (a) time and (b) cycles.

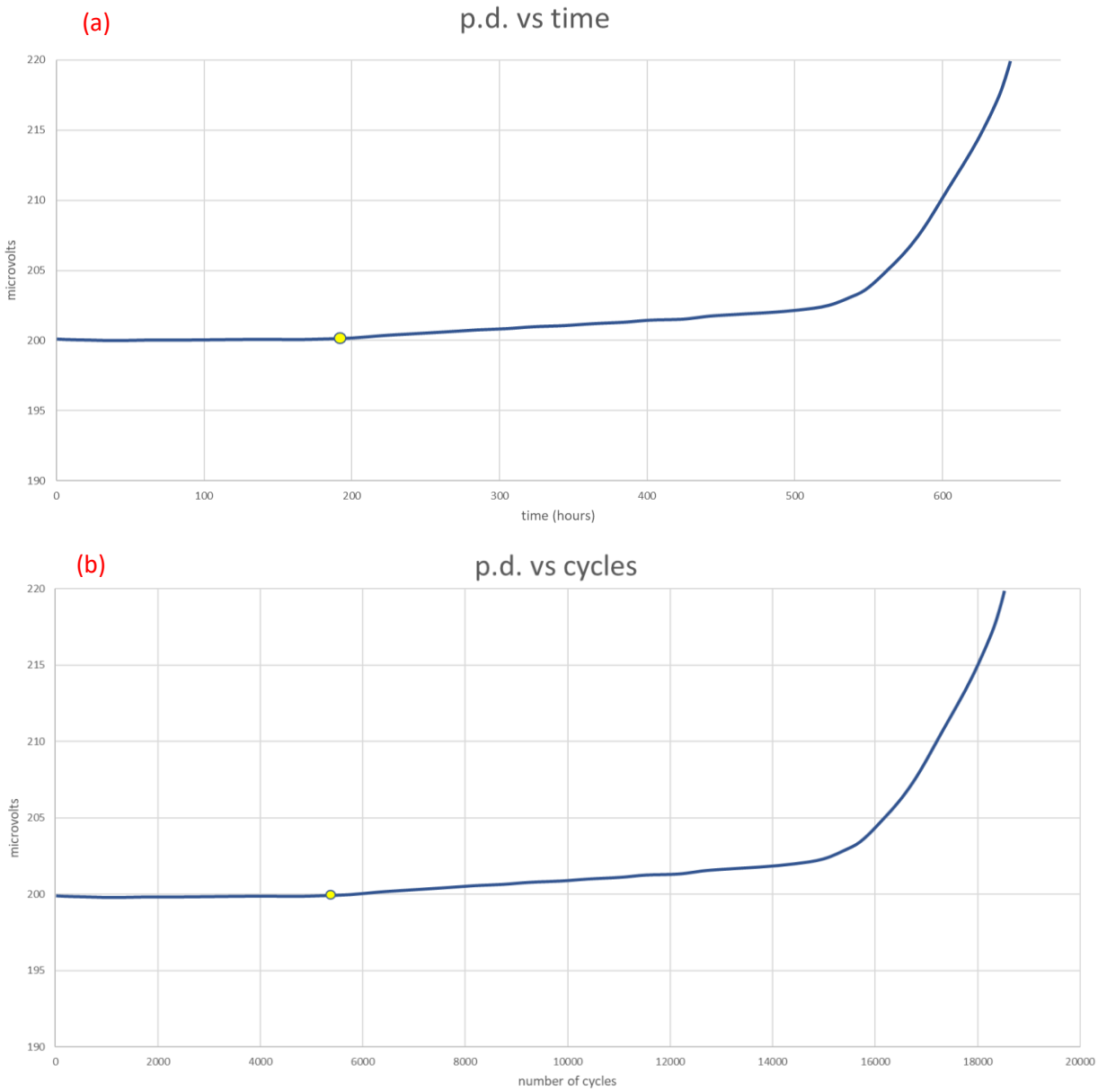

Figure 4-32 The dwell fatigue testing results of the CWF sample presented by p.d against (a) time and (b) cycles.

4.3.4.2 Cross-sectional microstructure

Both tested samples shown in Figure 4-33 were notably bent instead of being fractured, showing the ductile characteristics. The cross-sectional microstructure containing the cracks was investigated, both unseparated samples were cut perpendicular to the threads and the optical images of CW are presented in Figure 4-34. The longest crack in the CW sample is 204μm scope and the cracks were more than 3mm depth in the

CWF sample (Figure 4-35 c). Higher magnification SEM images were taken to study the difference between these two conditions near the cracks at the thread root.

An obvious difference in microstructure at the crack between CW and CWF samples can be seen in Figure 4-35. The crack in the CW sample propagates slowly towards the centre showing no grain structure near the surface, and the crack tip has been blunted by microvoids coalescence in Figure 4-35 (a) and (b), the transformation of new δ precipitates by dissolving γ” precipitates within a depth of 200μm from the thread root surface can be clearly seen and many microvoids appeared around δ phase. Especially within 30μm depth of the surface nearly all δ phase is newly precipitated and γ” phase can be barely detected. At a deeper location towards the centre, around 350μm, the newly precipitated δ phase can no longer be observed, however, the microvoids still exist.

On the other hand, none of these features occurred in the CWF sample in Figure 4-35 (c) and (d). The major crack in the CWF sample penetrated from the thread root to a depth of 1.8mm, shown on the top left in Figure 4-35 (c), then it divided into two directions. The cracks display both intergranular and transgranular behaviour and the secondary cracks separated the grain boundaries in Figure 4-35(c). Whereas the crack tip went through some grains regardless of the weakened grain boundaries shown in Figure 35 (d). What is interesting about the CWF sample is the benefits of δ precipitates at the grain boundaries near the thread root on the bottom left in Figure 4-35(d), holding the loosened grain boundaries. The cross-sectional microstructure show solid evidence that δ phase plays a key role in grain boundary strengthening, and γ” precipitates are distributed evenly within the grains. Moving to the middle section of the samples away from the cracks, a greater amount of γ” phase surrounding the δ

phase covers the whole area. No microvoids and loosened grain boundaries can be observed.

Overall, the results suggest that there is an association between cold work and the mechanical performance.

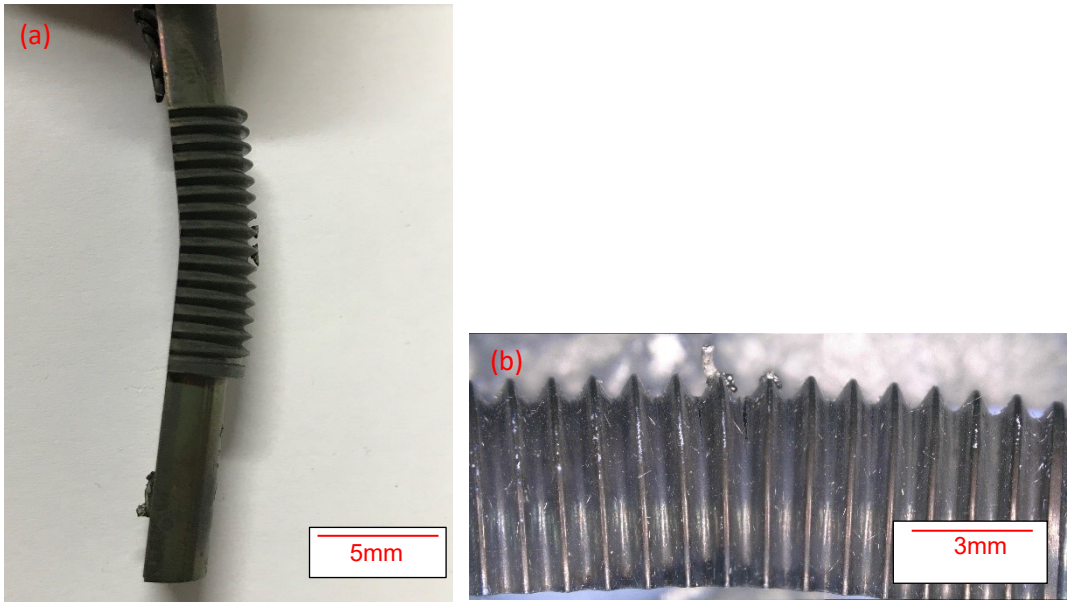

Figure 4-33 The bent CW (a) and CWF (b) samples after dwell testing

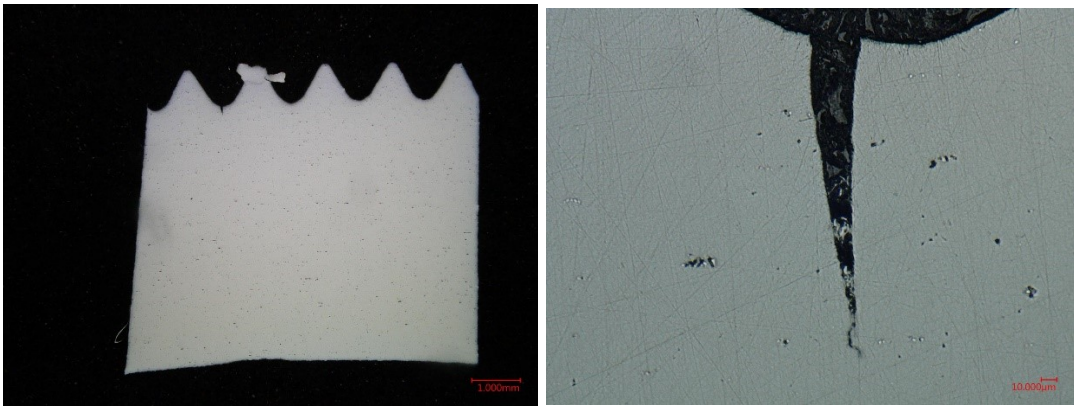

Figure 4-34 Optical images of the CW cross-sectional microstructure for crack observation at 200 and 300 magnifications.

(a)

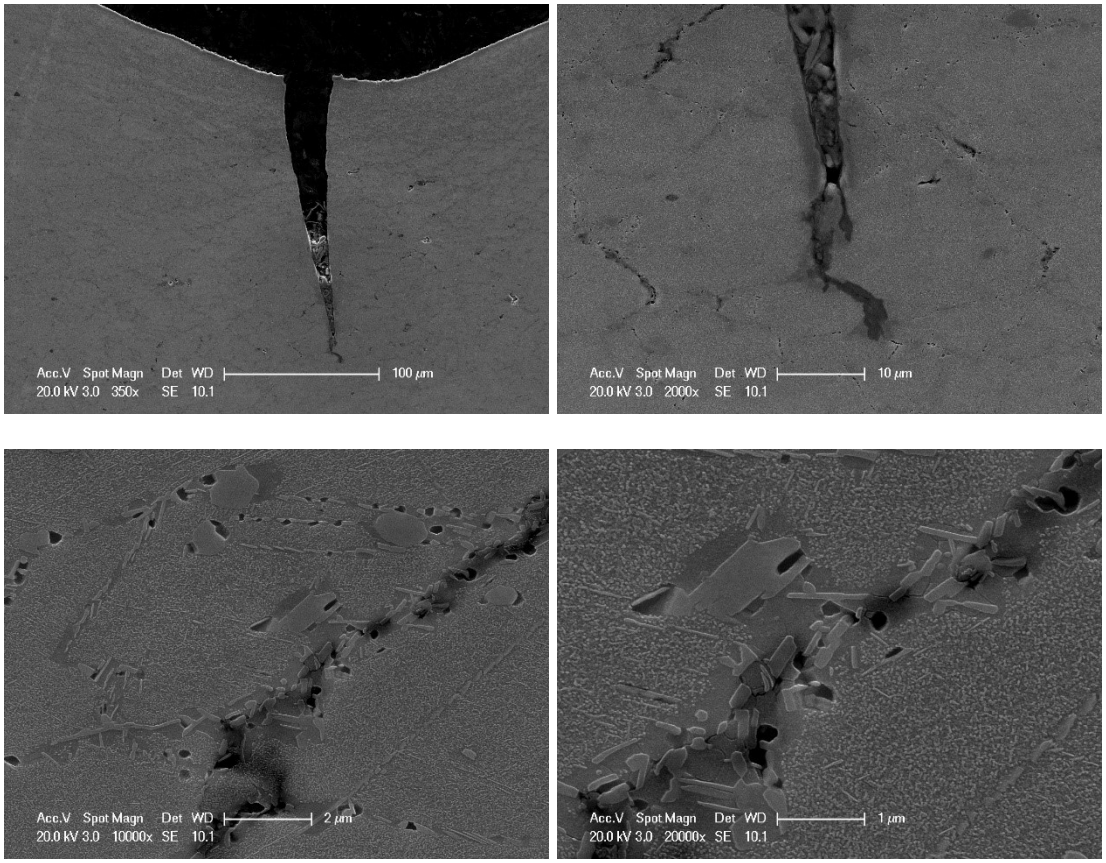

Figure 4-35 (a) SEM images of the crack and crack tip in the CW sample

(b)

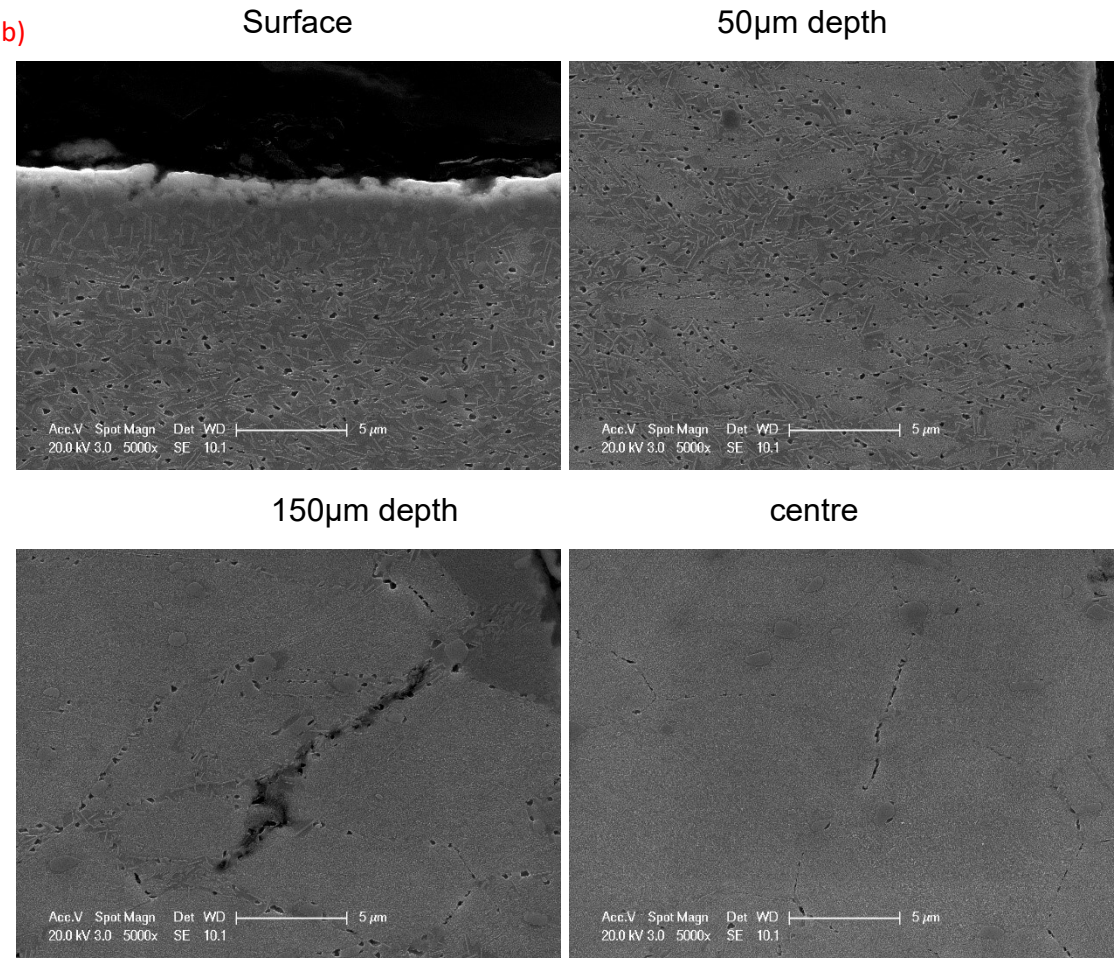

Figure 4-35 (b) Microstructure in the CW sample near the thread root and centre

(c)

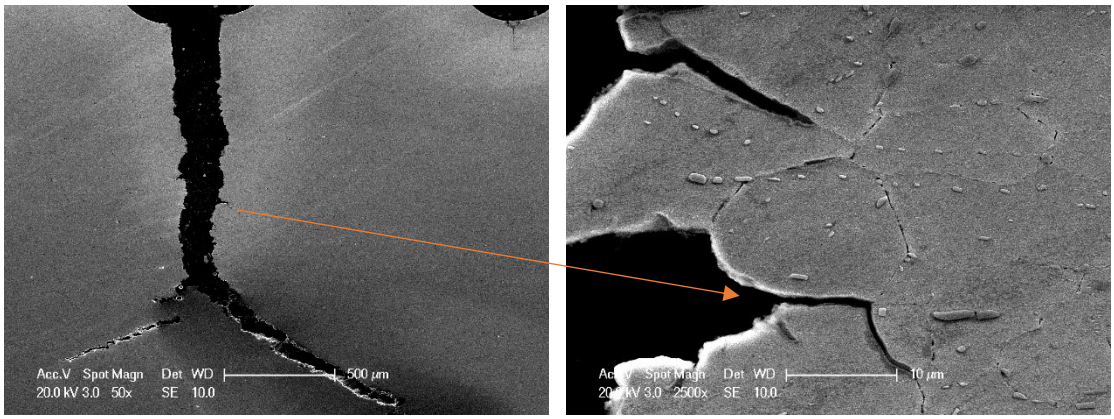

(c)

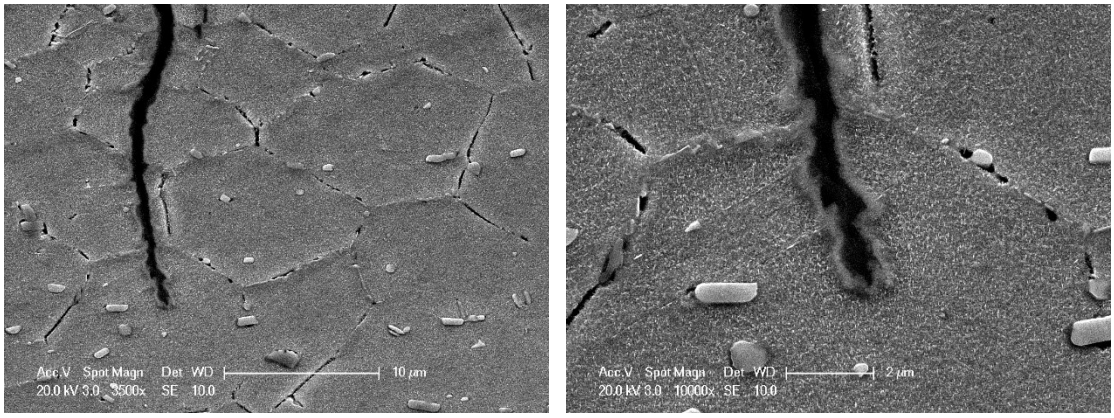

Figure 4-35 (c) SEM images of the crack and crack tip in the CWF sample

(d)

150μm depth Centre

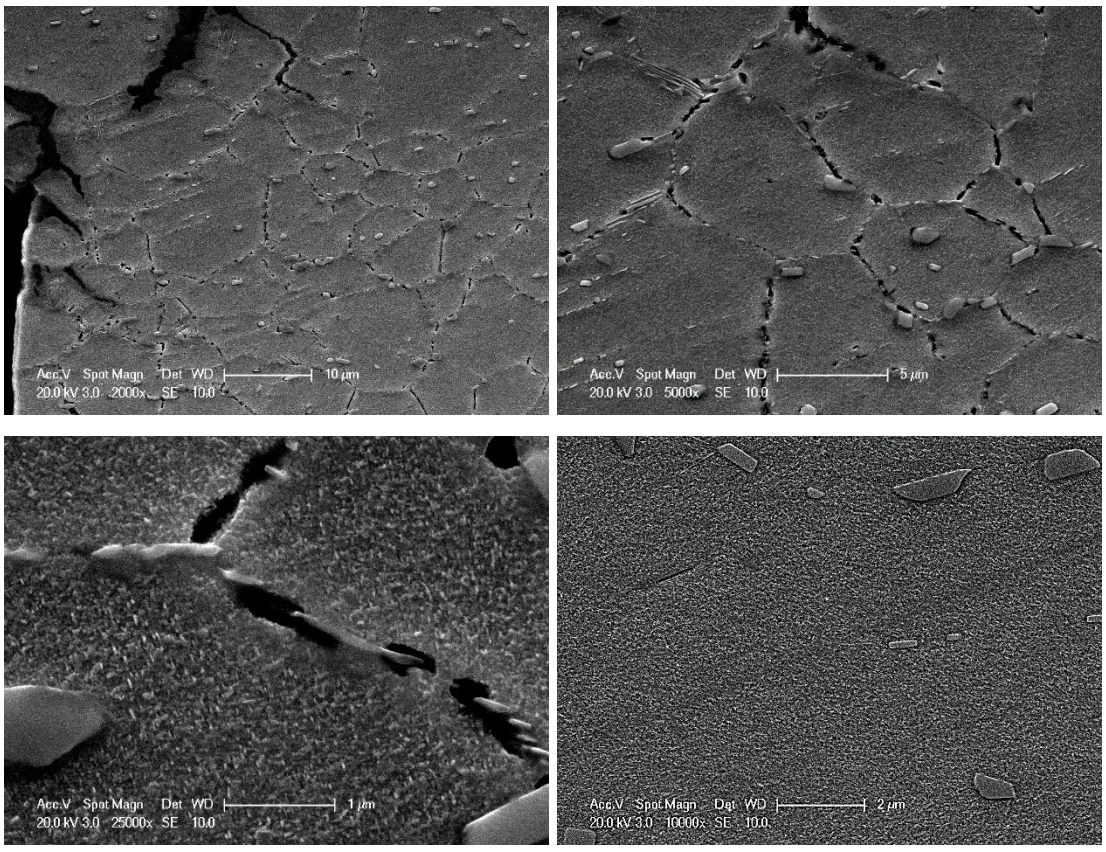

Figure 4-35 (d) Microstructure in the CWF sample near the thread root and centre

4.3.4.3 Crack growth analysis

The crack length against number of cycles and time was determined using the calibration of p.d. vs crack growth of the bending samples (see 4.3.2 above). Three bending tests with valid data were fitted in the calibration and are presented in Figure 4-36. Under the maximum stress 1500MPa, the bending sample in the baseline (1-1-1-1) fatigue frequency needs fewer cycles to develop a crack of equal length compared to the sample in the dwell fatigue mode (1-120-1-1). Moreover, the samples also display a different crack growth situation with cold work. Excluding the initiation life, at the beginning illustrated in Figure 4-36, CW requires nearly twice as many cycles to propagate the crack compared to CWF. It should be noted that the Y axis shows the number of cycles or time for a better demonstration of the trends. As the CW sample stopped the crack propagation, the valid data is limited for acquiring the crack growth rate in this situation.

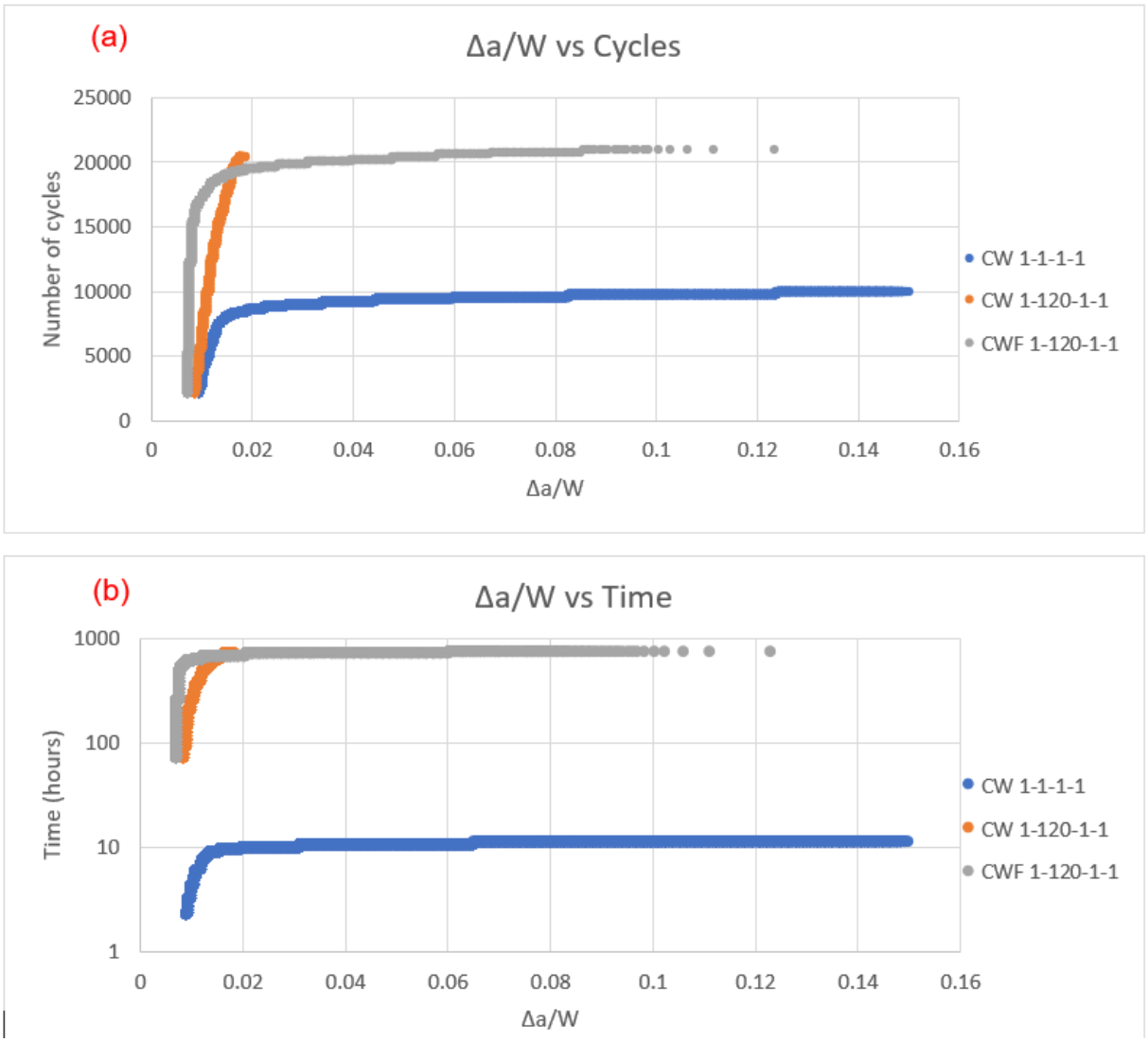

Figure 4-36 The crack growth vs number of (a) cycles and (b) time in different tests

4.4 Axial-tensile fatigue and dwell fatigue testing on large bolts

The as-received ½" large bolts were subjected to axial-tensile fatigue testing and stress-relaxation testing at a high temperature. Some were tested with some threads exposed to the air. This was to investigate the clamping force of IN718 bolts under different conditions. All the tests were carried out on the as-received IN718 large bolts using the designed fixtures to apply the load in the axial direction and replicate real-life

working conditions. The test pieces with 7- 8 threads exposed to the air are referred to here as “partially screwed bolts” (meaning partially engaged bolts), and the ones without threads exposed but the shank are referred to as “fully screwed bolts”. Both partially screwed bolts and fully screwed bolts were tested. All the tests were conducted at an initial load of 75~76KN (the first cycle) under the displacement control at 650˚C, which is the worst and very rare situation that a ½” IN718 bolts could experience under service conditions.

4.4.1 Baseline test

A baseline (1-1-1-1) test, with an R ratio of 0.5 based on the first-cycle displacement (the minimum displacement complies with the displacement at the minimum load in the first cycle), was carried out on a partially screwed bolt to better plan the following dwell fatigue tests and to understand the fatigue resistance of the large bolt at the thread section. After 30 hours (26791 cycles), the sample failed at the first engaged thread. The extensometer was used to monitor the strain more accurately and to verify the displacement control is reliable, it was only used in this test not in the subsequent tests (See Section 3.3.3.1).

4.4.1.1 Results analysis and fractography

The test was conducted under stroke control to closely simulate real in-service conditions. The load changes and the strain at the exposed shank were monitored, and the peak stroke was constant over the whole period of testing. Figure 4-37 shows the peak load and strain. The peak load starts dropping slightly at the beginning from the initial load of 76.4kN to 75kN, then levels off for most of the test time, until after 26 hours (23400 cycles), there is a sharp drop to failure. The peak strain shows a slight increase at the beginning then becomes steady, a noticeable increase in the strain

occurs at the end as the sample goes to failure. The testing results are summarised in Table 4-7.

The sample failed at the first engaged thread and a large crack also appeared at the thread immediately below. The shank length remained the same after the test and the exposed threads showed no significant change in size compared to the engaged threads. The optical fractography in Figure 4-38 exhibits a blue fatigue zone and the brown overload zone. Multiple cracks are circularly distributed at the thread root. Further fracture surface characterisation was carried out by SEM at different locations from the crack origins to the fracture surface centre in Figure 4-39. Within 160μm of the origin, the fracture surface is affected by heavy coldwork and is flat and no grains can be seen. Transgranular fatigue crack growth appears at a depth of 200μm. The mode of crack growth then gradually changes to a mixture of intergranular and transgranular, and intergranular crack growth becomes more distinct close to the ductile zone due to overload in Figure 4-39.

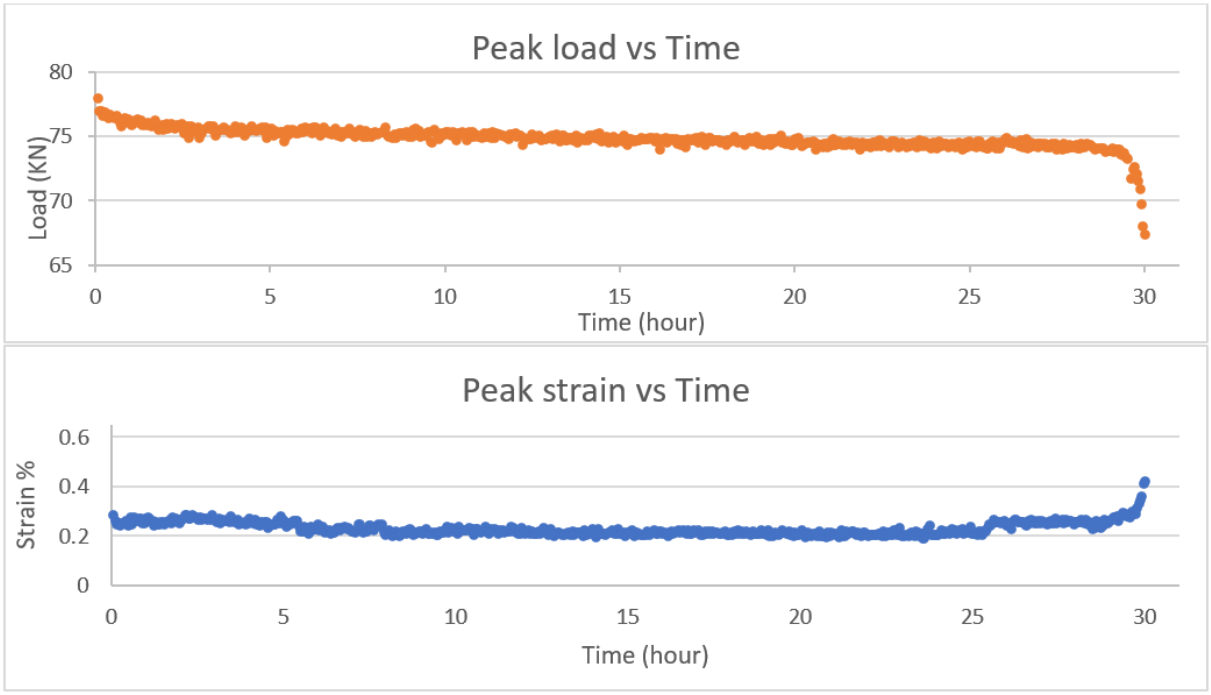

Figure 4-37 The results of baseline trial test on the partially screwed bolt

Table 4-7 Summary of the trial testing results

Size	Initial load	Stress at the shank	Frequency	cycles	time
Partially-screwed ½" bolt	76.4kN	690MPa	1-1-1-1	26791	29.77h

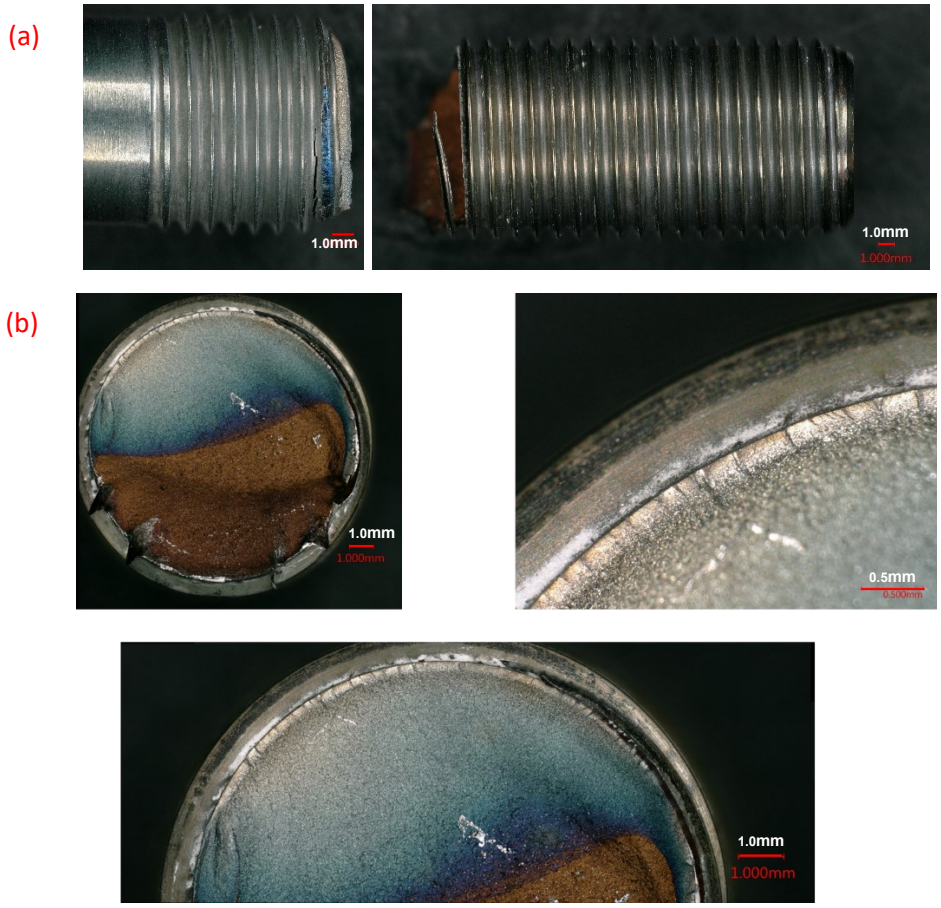

Figure 4-38 (a) Optical micrographs of the partially screwed bolt which failed at the first engaged thread, (b) the fracture surface

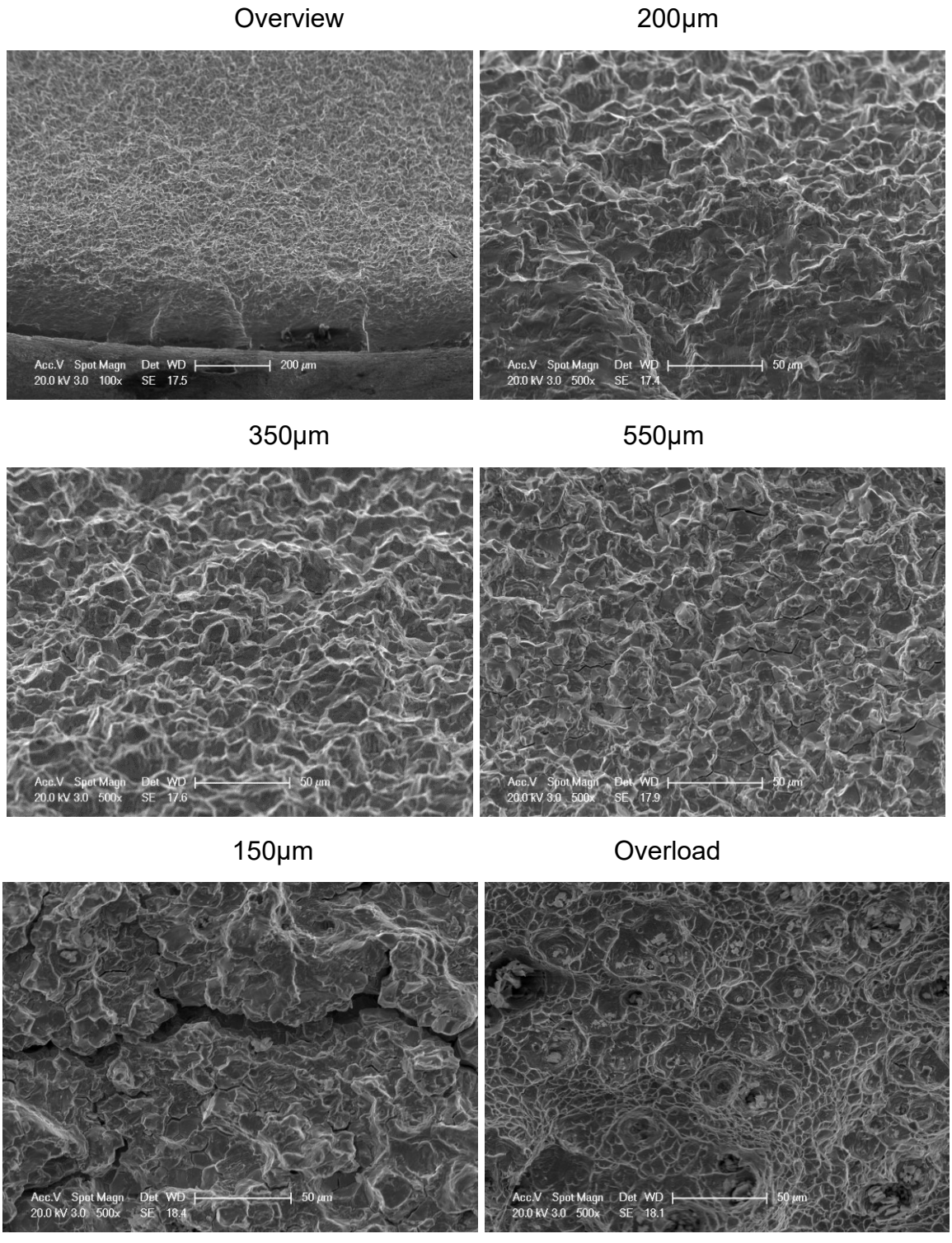

Figure 4-39 SEM fractographies of the fracture surface of trial sample

4.4.2 Partially screwed bolts

The partially screwed bolts were subjected to dwell fatigue testing followed by measuring the thread pitch and analysing the cross-section profiles to observe the fatigue behaviour at the threads. Then a repeating test under the displacement control was conducted afterwards, showing a very similar result which verified the repeatability. The stress relaxation testing under the displacement control was also performed to compare the fatigue and creep behaviour of the partially screwed bolts.

4.4.2.1 Results analysis of dwell fatigue testing

The same conditions as the baseline test were applied to an axial-tensile dwell-fatigue testing, except the frequency which was changed to a 1-120-1-1 waveform. A partially screwed bolt was held at the peak load for 120 seconds, then decreased to the minimum load in one second and held at the load for one second followed by increasing the load back to the peak in another second. The load and stroke were monitored, and the testing results are shown below in Figure 4-40.

The overall peak load constantly descends over the 185 hours and stabilises to the end of testing by stroke control, the test was stopped at 191hours (5590 cycles). The initial load of 75.2kN instantly dropped by 1.5kN at the beginning, then it kept decreasing until the peak load was close to 60kN after 100 hours (2927 cycles). Some small sharp drops followed by rises in the peak load during the test were detected, which showed no influence on the total testing results. The total load dropped by 18.5KN over 180 hours (5268 cycles), stabilising thereafter.

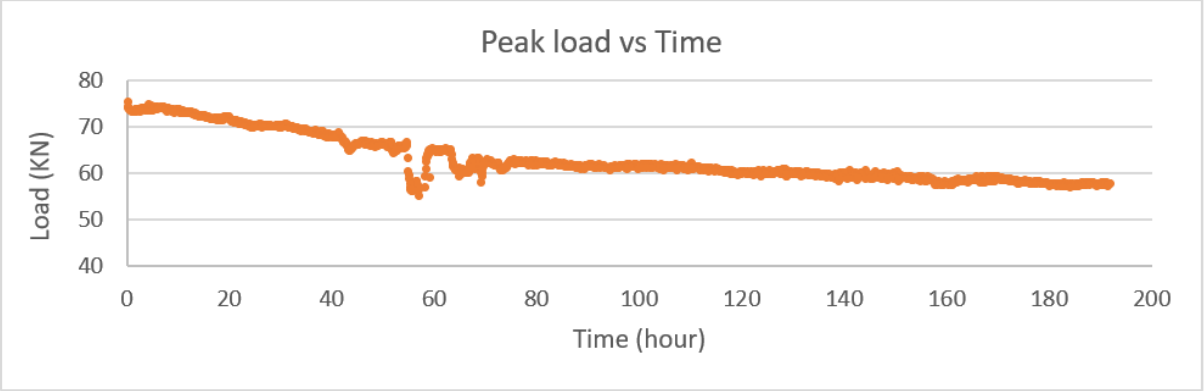

Figure 4-40 The results of a dwell fatigue test on a partially screwed bolt

4.4.2.2 Thread pitch measurements

After testing the large bolt was measured using an optical microscope as shown in Figure 4-41 (a) (b) and a thread gauge was used in Figure 4-41 (c) (d). Each exposed thread, those on the left of the red star appears to be wider compared to the engaged ones on the right. Every five thread-roots were measured in Figure 4-41(b), the front five threads are notably elongated up to 147μm after testing. The thread-gauge measurement further proves shows this, as the standard thread gauge can no longer fit at the exposed threads but only at the lower engaged ones.

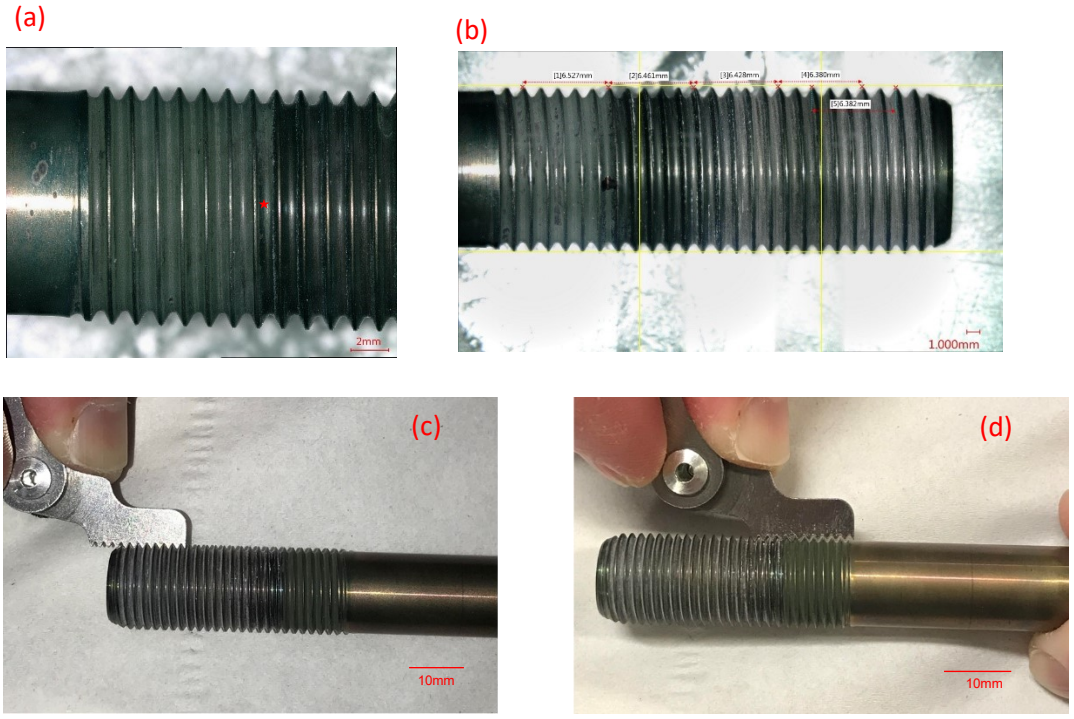

Figure 4-41 (a) and (b) show the optical measurements of a tested bolt, the thread gauge at the engaged threads (c) and the exposed threads (d).

4.4.2.3 Cross-section microstructure

The tested large bolt then was subjected to metallurgical preparation for cross-sectional microstructure. Both the exposed threads and the engaged threads were inspected by SEM in Figure 4-42.

After long-term cyclic loading at a high temperature, the microstructure at the threads (Figure 4-42) is like that of the Group C (thermal exposure with load) treated large bolts in Figure 4-11, although some characteristics are more evident due to the harsher testing conditions. Within 60μm from the thread root surface, both engaged (Figure 4-42b) and exposed threads (Figure 4-42c) contain a large amount of newly precipitated δ phase. There are a greater number of microvoids of a larger size in the exposed section. Moving further towards the centre to a depth of 160μm, the contrast is also obvious with more newly precipitated δ phase and more microvoids in the exposed

section (Figure 4-42b) than the same location at the engaged section (Figure 4-42c). On the other hand, the core section in the centre shows no changes in terms of δ and γ” phase and no microvoids can be detected, and the microstructure at the exposed and engaged centre sections is comparable in Figure 4-42 (b) and (c).

(a)

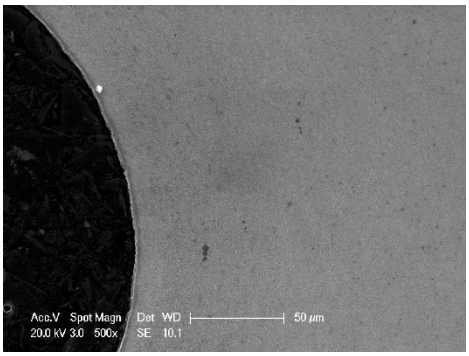

Figure 4-42 (a) Cross-sectional microstructure of o the overview at the threads root

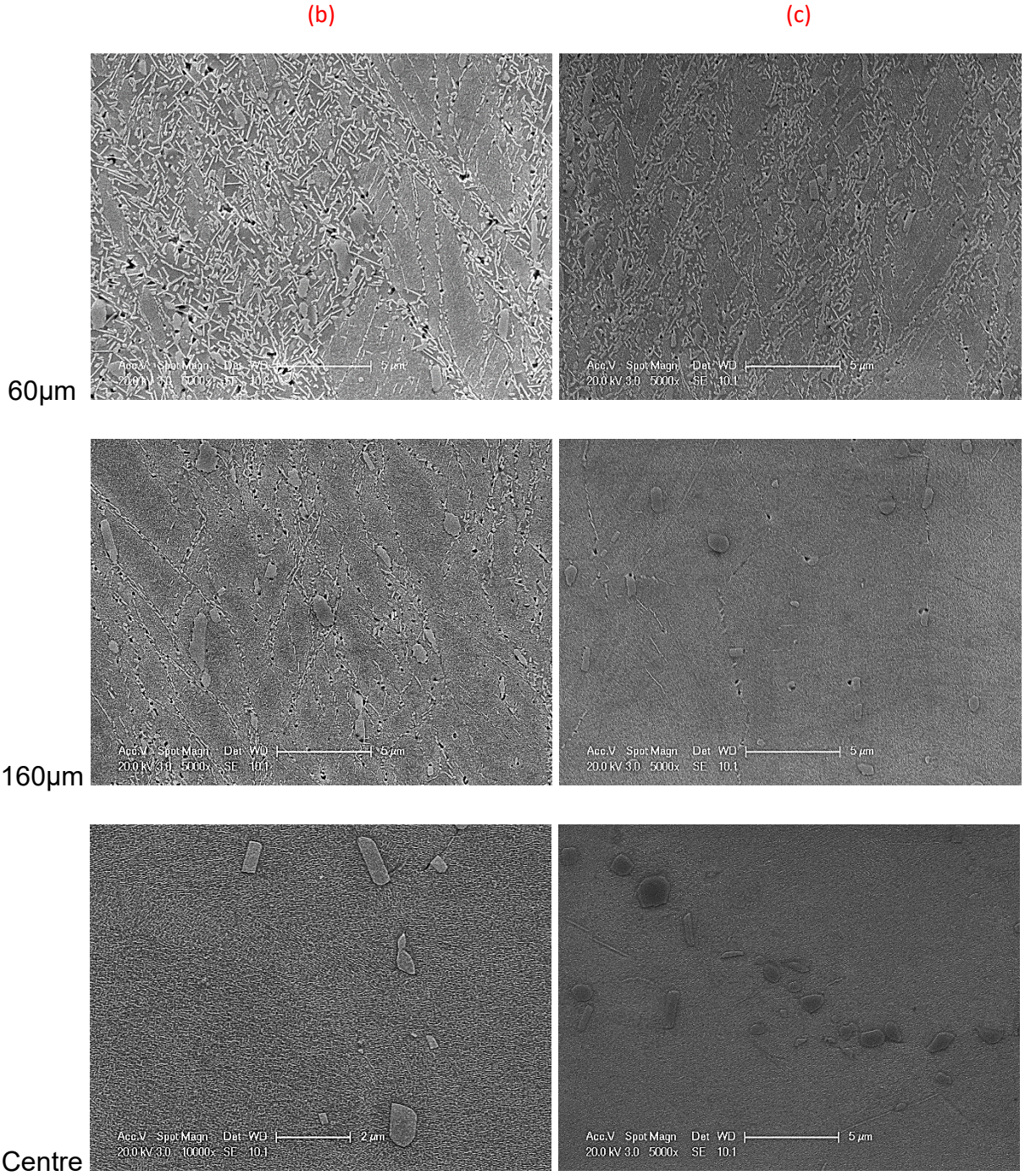

Figure 4-42 (b) and (c) Cross-sectional microstructure of (b) the upper exposed threads root and (c) the lower engaged threads root.

4.4.2.4 Results analysis of stress-relaxation testing

The stress-relaxation test was then conducted on an as-received large bolt under the same conditions by removing the cycling waveform, with an initial load of 76kN. The test was carried out with 7-8 threads exposed and no cracks were observed. However,

the sample was elongated for 300μm compared to the original size, most of the elongation was over the exposed threads. The results are displayed in Figure 4-43. The test was stopped after 185 hours (5414 cycles), as the load levelled off on loading. The peak load immediately dropped to 70kN within the first three hours from the initial load of 76kN. Despite some fluctuations, the load then slowly descended to 63.6kN after 130 hours and then remained the same until a total time of 185 hours was reached. The total load drop was by 12.4kN till the end of the test, which is less than the previous dwell test (18.5kN) in Figure 4-40.

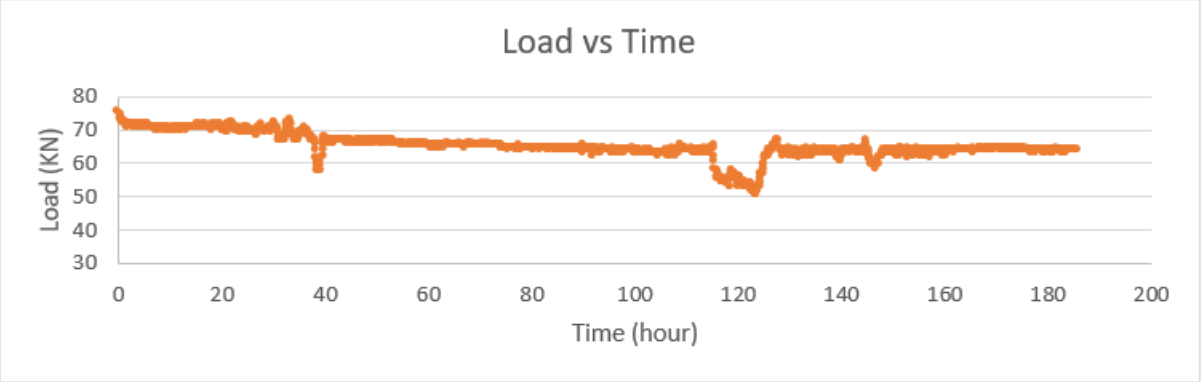

Figure 4-43 The results of stress-relaxation test on a partially screwed bolt

4.4.3 Fully screwed bolts

The large bolts are fully screwed for the dwell and relaxation testing shown in Figure 4-44(a), and the partially screwed large bolt is shown in (b). Apart from this, the testing conditions keep the same as the previous tests.

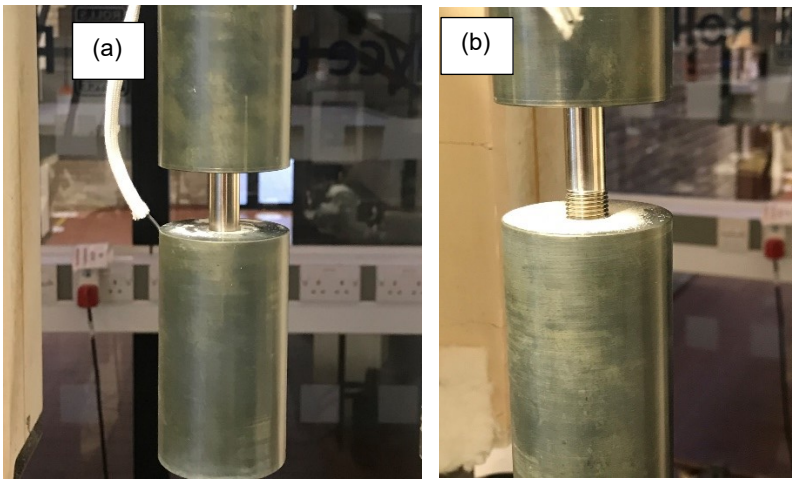

Figure 4-44 (a) Fully screwed bolt and (b) partially screwed bolt on the fixture

4.4.3.1 Results analysis of dwell fatigue testing

After being tested under a 1-120-1-1 waveform for 180hours (5268 cycles) at 650°C, the load dropped from 76kN to 64.6kN shown in in Figure 4-45. A few instabilities occurred during the test due to the local deformation. In contrast to the identical test performed on a partially screwed bolt in Figure 4-40, the fully screwed bolt demonstrated a reduced load drop of roughly 12.5kN and less elongation, measuring approximately 120um after testing.

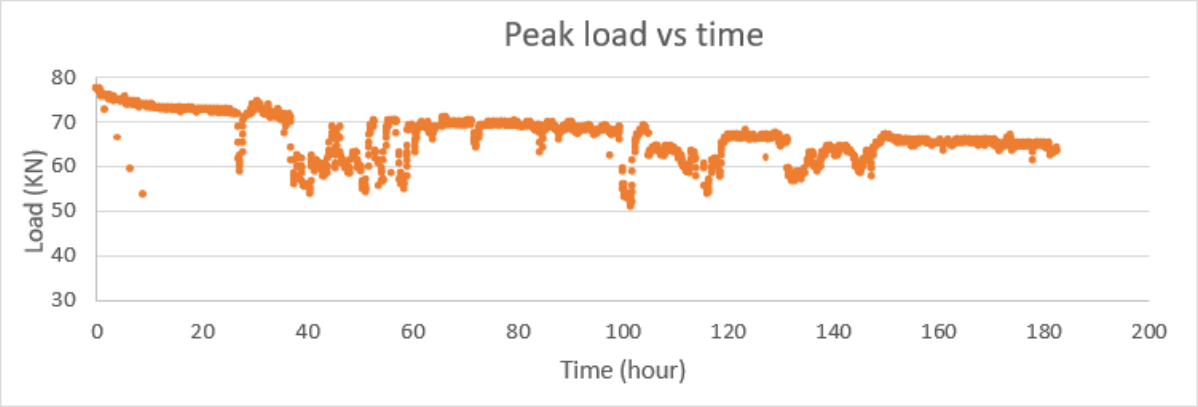

Figure 4-45 The results of dwell fatigue test on the fully screwed bolt

4.4.3.2 Results analysis of stress-relaxation testing

Interestingly, the stress-relaxation test shown in Figure 4-46 had a different outcome. The load dropped more in the fully screwed bolt than the partially screwed bolt, 17.3kN in total. Also, fewer fluctuations were seen in the test. The tested sample was elongated by approximate 130um at the exposed shank area.

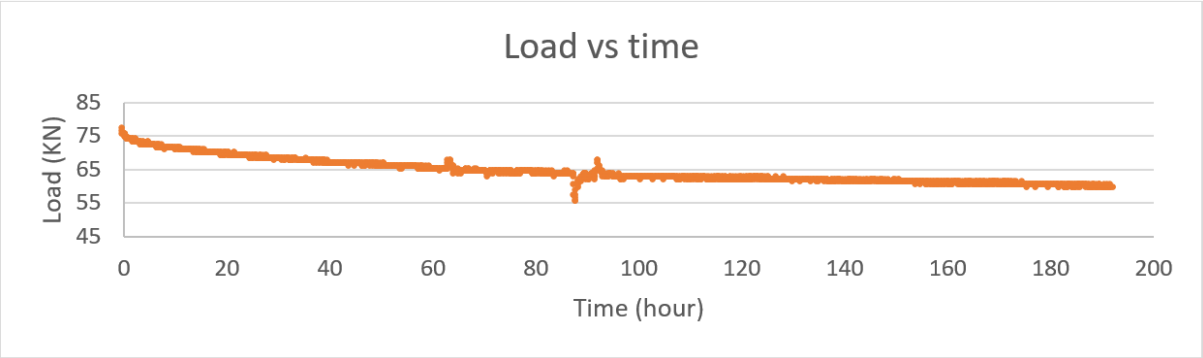

Figure 4-46 The results of stress-relaxation test on a fully screwed bolt

4.4.4 The results in summary

The four testing results are summarised in Figure 4-47, the load change against time (a) and the load drop against the total increase in the sample length (b) was presented by the four conditions. No cracks were detected at the exposed shank or thread roots of all the tested samples. As indicated in Figure 4-47, it is evident that partially screwed bolts, in bolt dwell-fatigue and stress-relaxation tests, exhibit greater deformation compared to fully screwed bolts. This suggests that exposed threads could result in a more rapid loss of clamping force. In addition, the fully screwed bolt on the dwell testing and the partially screwed bolt on the stress-relaxation testing performed well in maintaining the initial load for 180 hours, both situations dropped less than 13kN. Overall, the fully screwed bolt performs the best under the dwell fatigue condition.

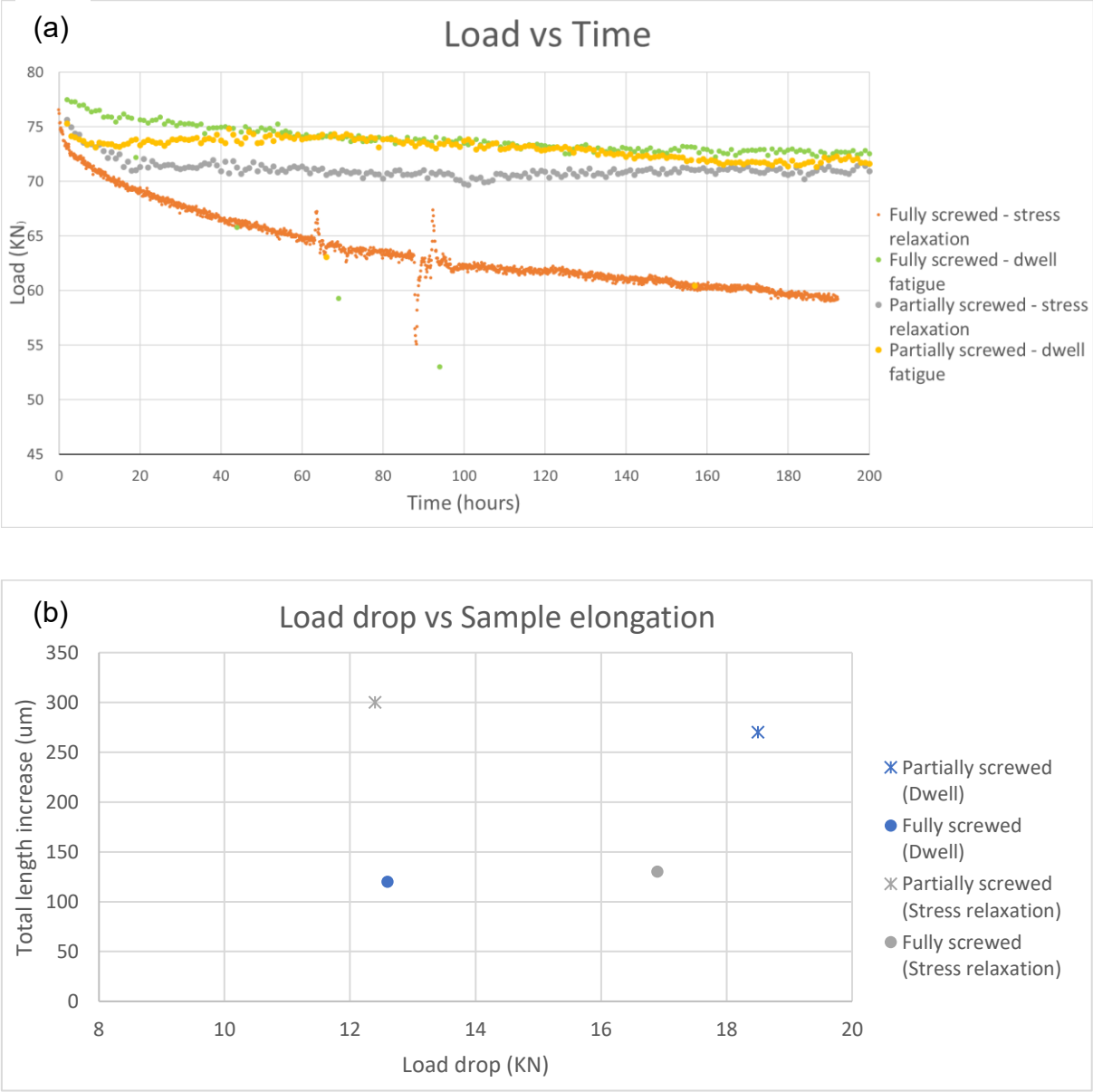

Figure 4-47 Summary of (a) load against time and (b) load drop against sample elongation in different tests

4.5 Axial-tensile fatigue testing on HT samples

4.5.1 Plain samples

Plain samples with a gauge length of 50mm, in the HT1, HT2 and HT3 conditions were subjected to axial-tensile fatigue tests with a 1-120-1-1 waveform to understand the influence of solution treatment temperature on creep and dwell-fatigue performance. The dwell-fatigue testing was conducted under load control at a maximum stress of 750MPa at 650˚C, with an R ratio of 0.5. All the plain samples were tested to failure followed by failure investigation. Load control kept a constant stress applied on the sample during each cycle. Stroke was monitored throughout the tests. The same testing conditions were subjected to HT1 and HT3 samples for repeating the tests.

4.5.1.1 Results analysis

The testing results are summarised in table 4-9 under the same temperature (650˚C) and a maximum stress of 750MPa. Test piece HT1P (plain) prematurely failed after 13 hours (380 cycles) nearly three times shorter than test pieces HT2P and HT3P. The total life of both HT2P and HT3P was over 30 hours, HT3P failed after 1023 cycles for 35 hours performing the best. Figure 4-48 (a) (b) and (c) show the changes in stroke during each test. The failure of test HT3P occurred without noticeable deformation regardless the longest fatigue life, whereas HT1P and HT2P largely deformed prior to failure. Additionally, the area of fracture surfaces was measured, and a distinct difference in area reduction between HT1P, HT2P and HT3P can be seen in table 4-9.

Optical micrographs of the gauge length surface taken of failed HP2P and HT3P samples shown in Figure 4-49 further elaborate this phenomenon. All three conditions show narrow cross section areas close to the fracture surface, which is necking. This

is especially clear in samples HT1P and HT2P, where such tensile deformation is very obvious. The diameter of the shrank cross section against the distance from the fracture surface was measured at 1mm intervals to evaluate the degree of deformation in all tested samples, shown in Figure 4-50. It is notable that sample HT2P was largely deformed consistent with a shorter life and higher ductility whereas sample HT3P has the smallest amount of deformation with a longer life.

Table 4-9 Summary of testing results in the HT plain samples

	Temperature(˚C)	Max Stress (MPa)	Total life (Hours)	Number of cycles	Area reduction %
HT1P	650	750	13.07	385	35.81
HT2P	650	750	30.83	908	38.94
HT3P	650	750	35.13	1023	2.37

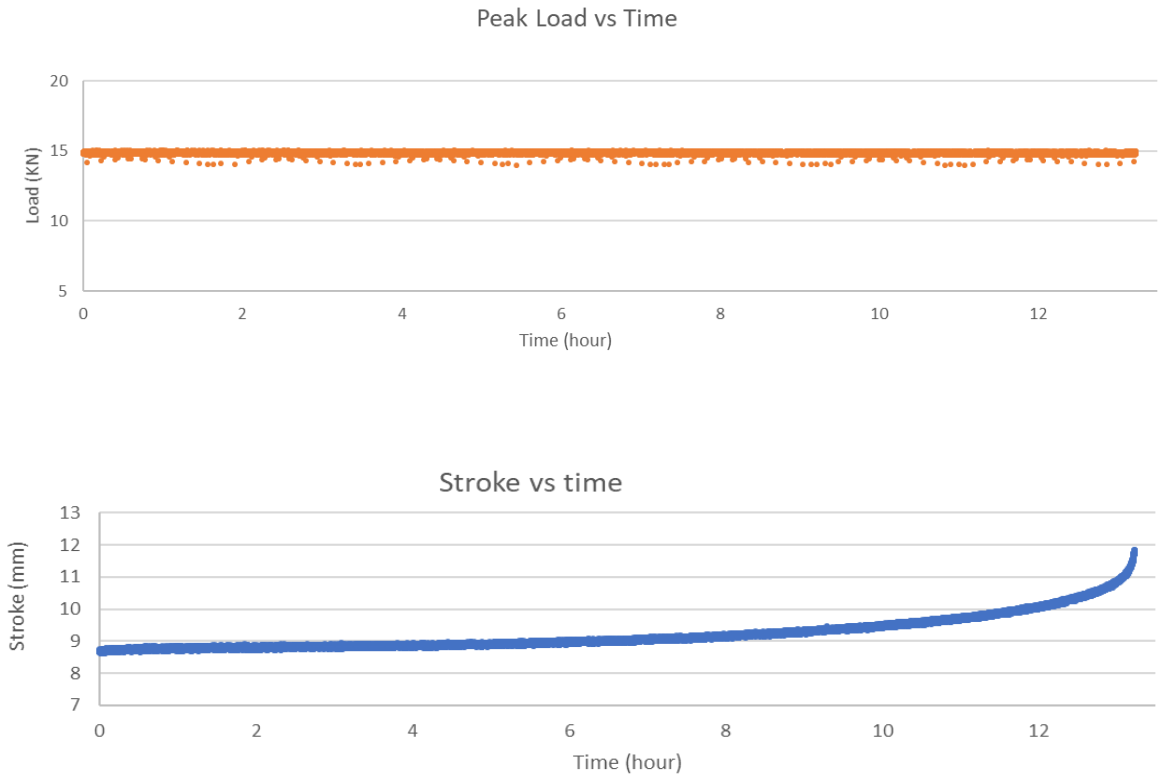

Figure 4-48 (a) The results of HT1 plain sample on dwell fatigue testing

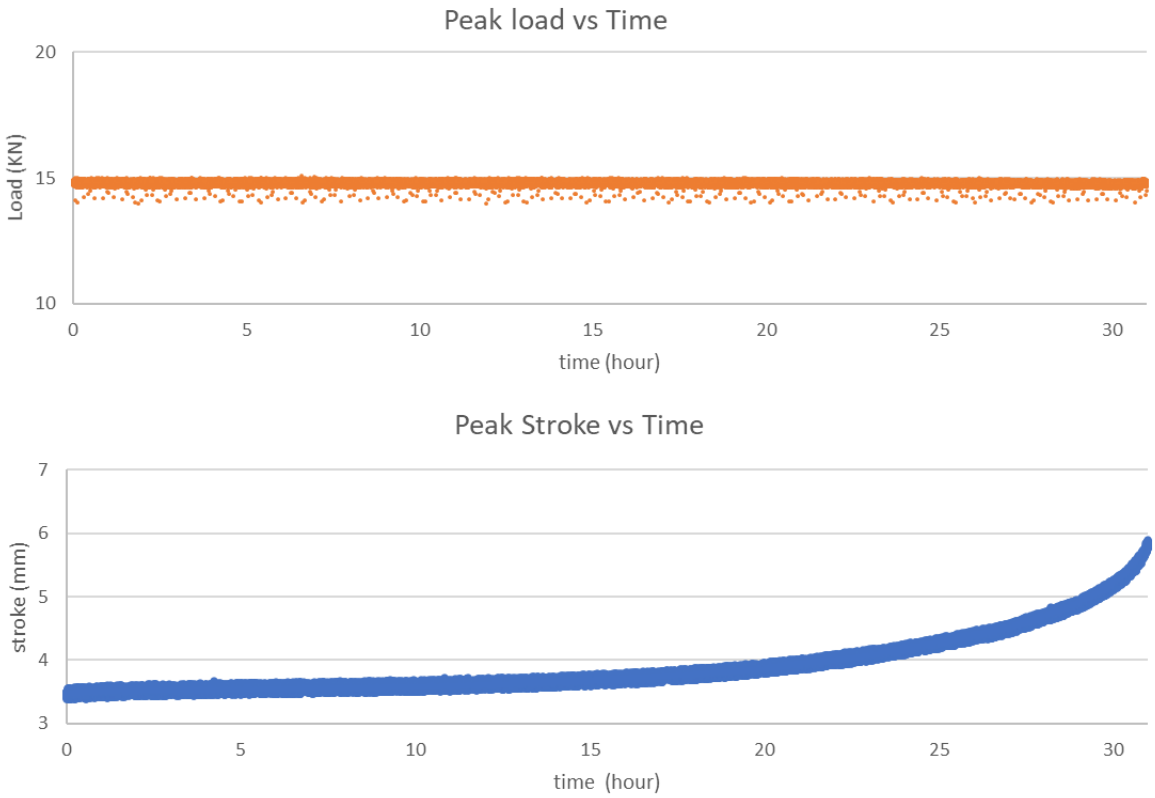

Figure 4-48 (b) The results of HT2 plain sample on dwell fatigue testing

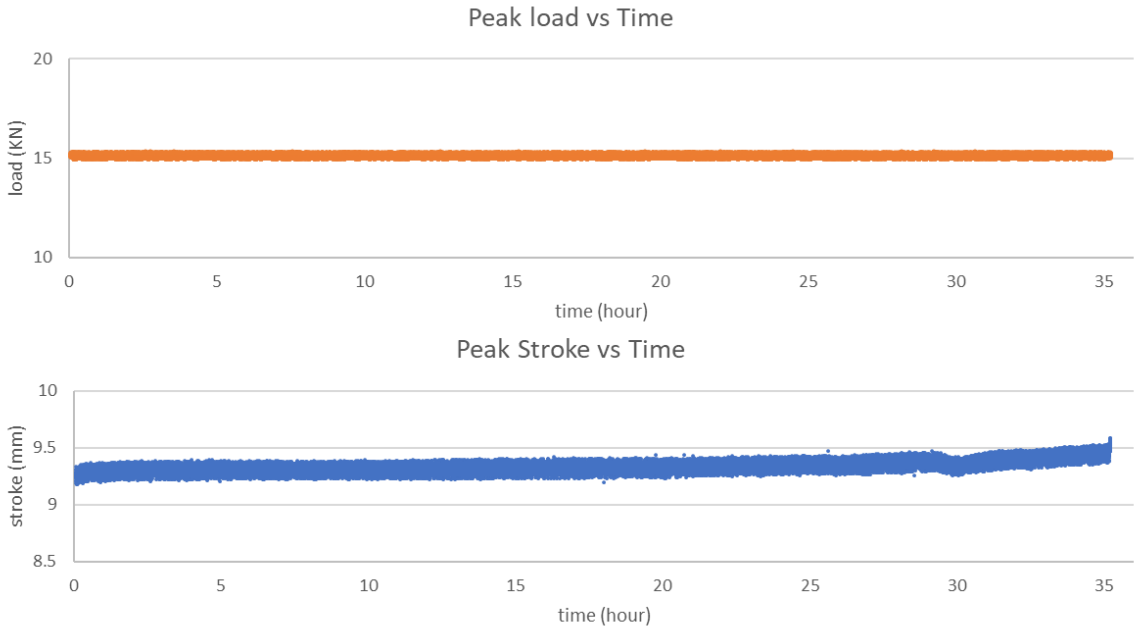

Figure 4-48 (c) The results of HT3 plain sample on dwell fatigue testing

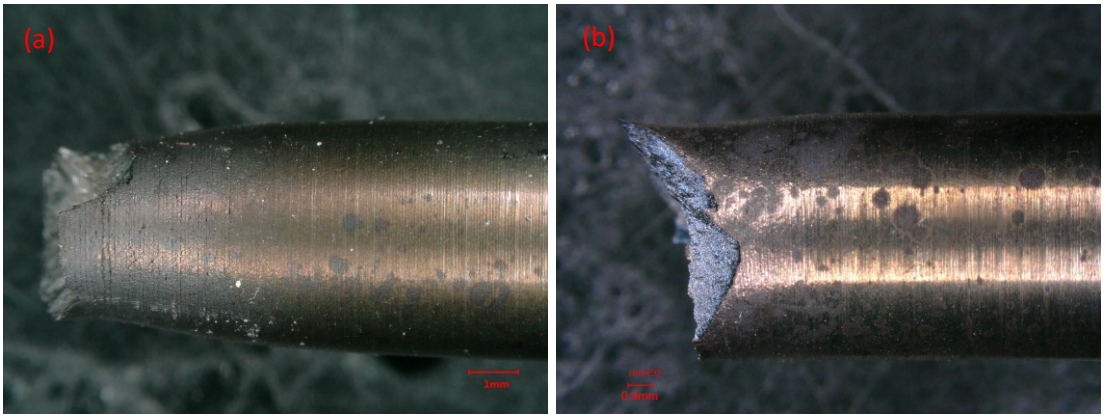

Figure 4-49 The necking sections close to the fracture surface of (a) HT2P and (b) HT3P samples.

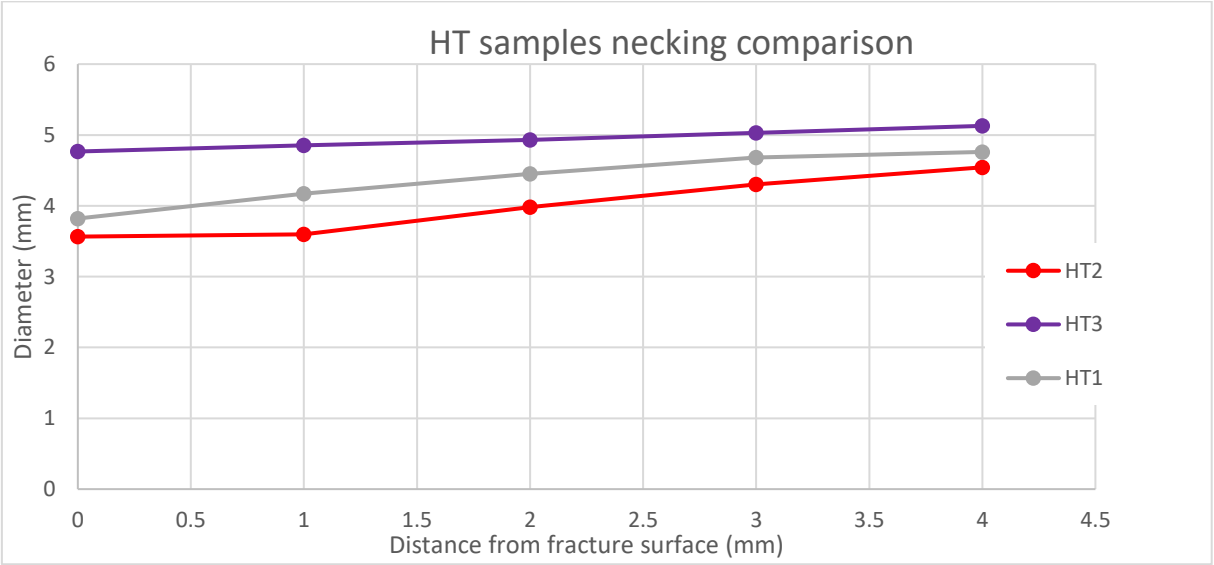

Figure 4-50 Comparison of necking in HTP samples

4.5.1.2 Fractography

The fractography of samples HT1P, HT2P and HT3P was fully investigated after testing and is shown in Figure 4-51 (a) (b) and (c) respectively. The SEM images were taken at the fracture surfaces.

It is interesting that samples HT1P, HT2P display completely different failure mechanisms compared to sample HT3P. The fracture surfaces of HT1P and HT2P are

similar. Both show the tensile shear fracture surfaces. In Figure 4-51(a) HT1P, the shear lip zone and the fibrous zone can be clearly seen. Sample HT2P (b) is like HT1P (a). However, due to severe oxidation, less information can be read from fracture surface of sample HT2P. Instead of ductile fracture, HT3P sample shows intergranular fatigue fracture, yet achieved the best fatigue life among the HT plain test pieces. Intergranular failure covers from the left edge to the centre (~2.5mm) followed by overload fracture on the right edge in Figure 4-51(c).

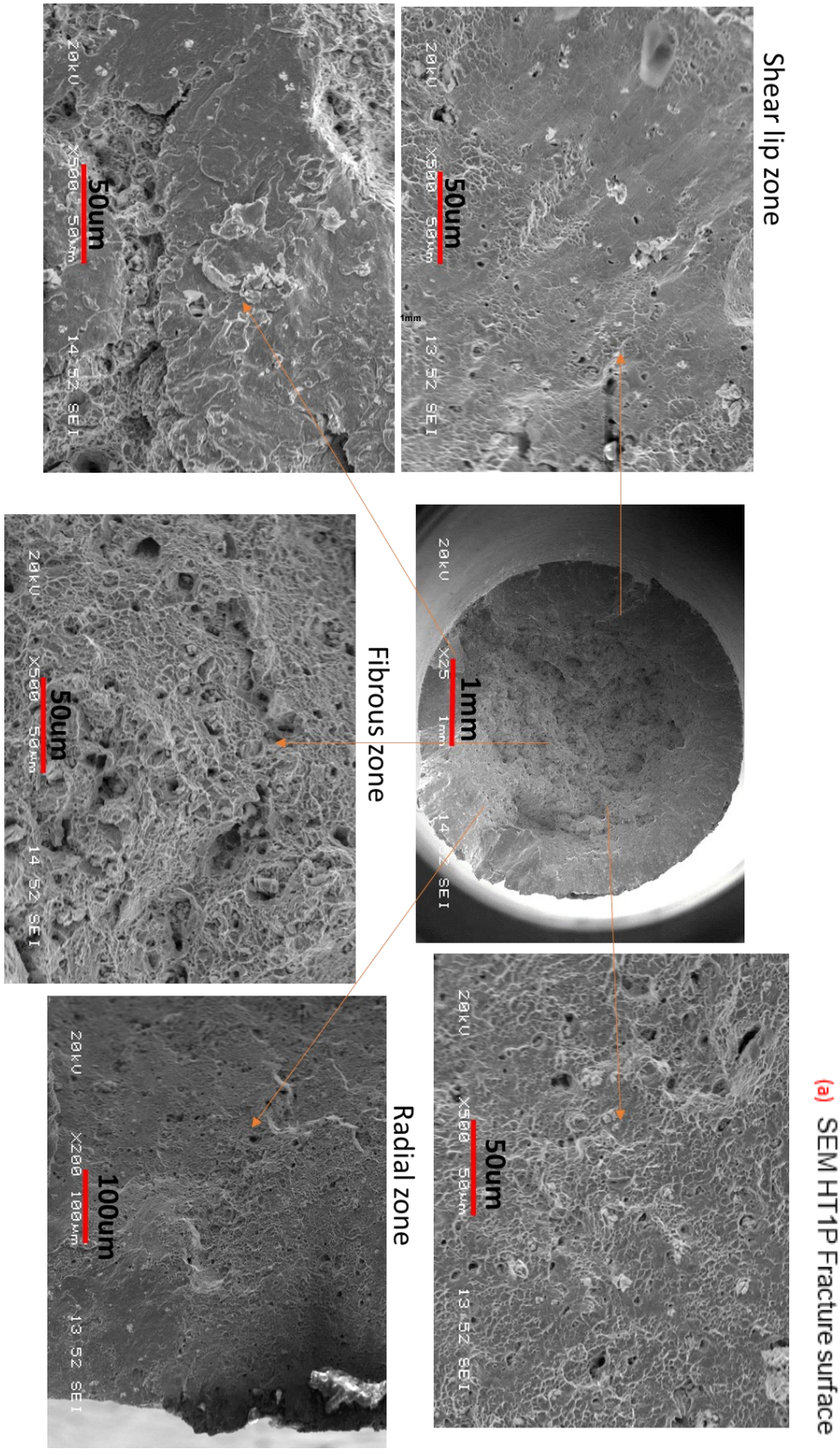

Figure 4-51 (a) Fracture surfaces of HT1P at different locations.

Figure 4-51 (b) Fracture surfaces of HT2P at different locations.

Figure 4-51 (c) Fracture surfaces of HT3P at different locations.

4.5.1.3 Cross-sectional microstructure

The failed test pieces then were metallographically prepared for cross-sectional microstructure, each condition was subjected to a thorough investigation by high-magnification SEM, indicating the locations of the sample in Figure 4-52 (a) (b) and (c). From the overall cross-sectional microstructure, the fracture surfaces of samples HT1P (a) and HT2P (b) are more rugged and uneven compared to that of sample HT3P (c). The high-magnification SEM images in Figure 4-52 present the microvoids surrounding the δ phase at the edge near the fracture surface in samples HT1P and HT2P, and fewer microvoids or δ phase at the centre away from the fracture surface. In sample HT3P, a very small number of δ precipitates exist and no microvoids are observed. It is apparent that the crack penetrates along the grain boundaries, and the secondary cracks open up the adjacent grain boundaries, indicating the intergranular mode.

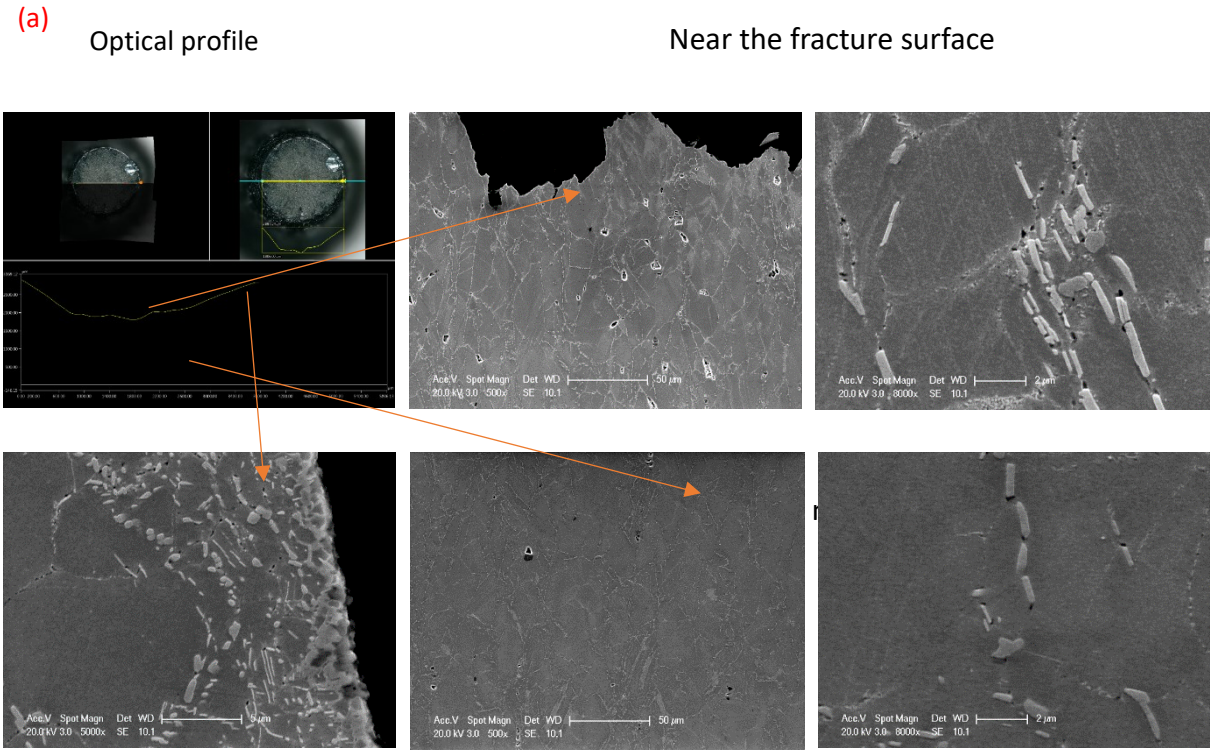

Figure 4-52 (a) Cross-sectional microstructure of the tested HT1P

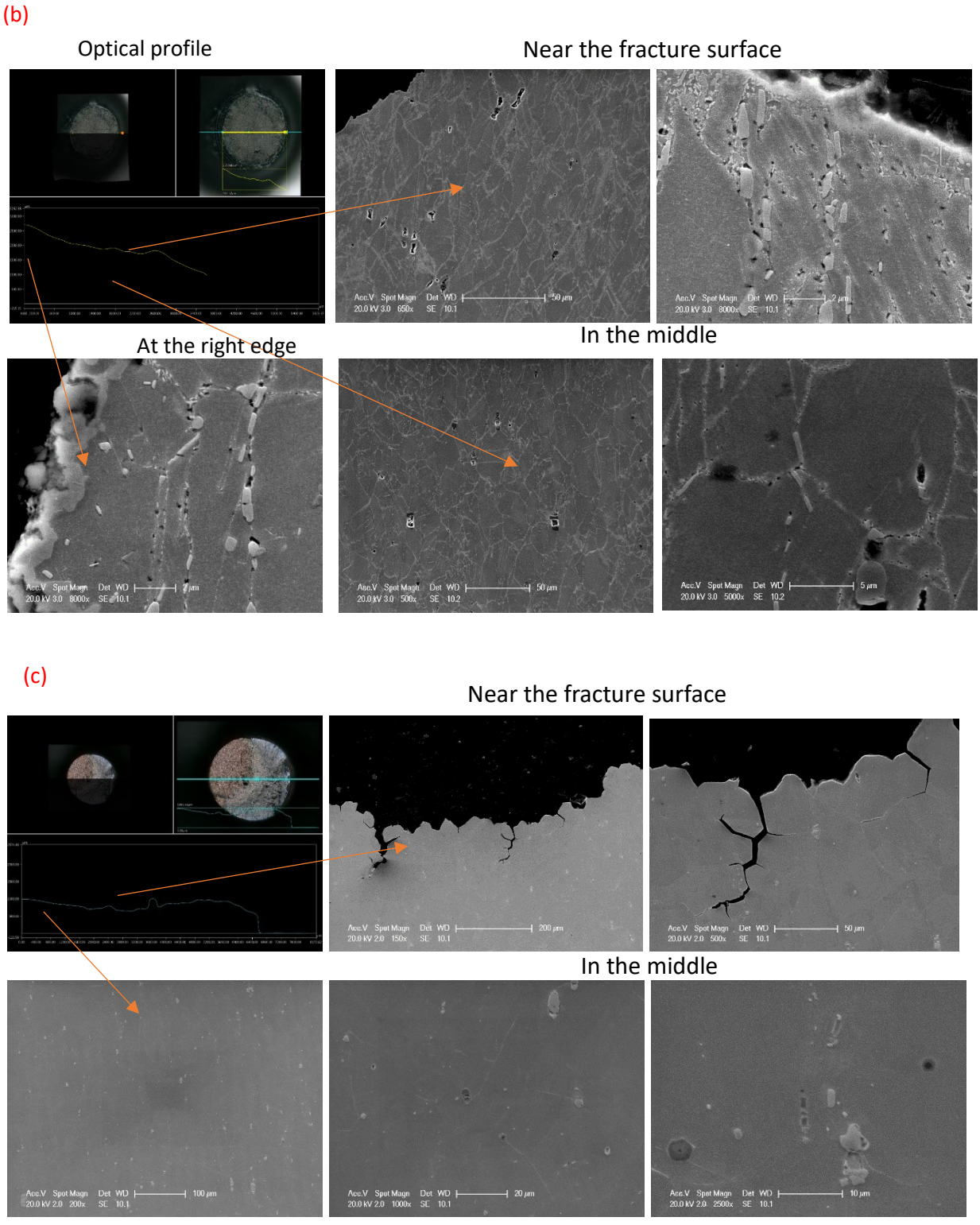

Figure 4-52 (b) and (c) Cross-sectional microstructure of the tested HT2P and HT3P.

4.5.2 Notched samples

In the previous section, it is obvious that HT1P, HT2P and HT3P samples reacted differently to the dwell fatigue testing at high temperature, in terms of fatigue life and deformation of the failed samples. It is worth conducting similar tests but with a stress concentration for simulating the thread feature. The Kt3 HT notched (HTN) samples were tested under the same conditions as the dwell fatigue testing in the HT plain samples. The axial-tensile dwell fatigue (1-120-1-1 waveform) mode with an R ratio of 0.5 at 650°C was applied on samples HT1N, HT2N and HT3N, the load applied was the same as the HT plain test to ensure the same stress of 750MPa at the notch area (the centre diameter of the plain sample is the same as the notch-section diameter, 5mm).

Each sample was tested to failure followed by optical and SEM fractography. The testing was conducted under load control and stroke was recorded. The investigation in microhardness and cross-sectional microstructure were completed on the selected samples, to aid a comprehensive understanding of the changes in microstructure for different heat-treated samples.

In addition, to comprehend the fatigue and creep failure mechanism for HT notched samples under such stress and temperature, the stress rupture testing was performed by removing the cycling waveform for the static load to compare the results.

4.5.2.1 Results analysis of dwell fatigue testing

The dwell fatigue testing results on samples HT1N, HT2N and HT3N are displayed below in Figure 4-53 (a) (b) and (c) respectively. The results contrast with the HT plain samples. Specifically, HT1N demonstrates an extended dwell fatigue life of over 350

hours (10266 cycles), whereas HT3N only reached 84 minutes (41 cycles), as depicted in Table 4-10.

A close look at the stroke chart of HT1N suggests that an obvious elongation at the notch occurs after 27 hours (791 cycles), and it keeps steady for most of the fatigue life for 250 hours. It then starts increasing slowly up to 340 hours followed by a rapid increase to failure. The increase in stroke can also be observed in sample HT2N, although the stroke starts increasing immediately from the beginning until after 97 hours it slows down until approaching the final failure. On the other hand, sample HT3N barely shows any changes in stroke during the short-term cycling life, and the sample failed unexpectedly.

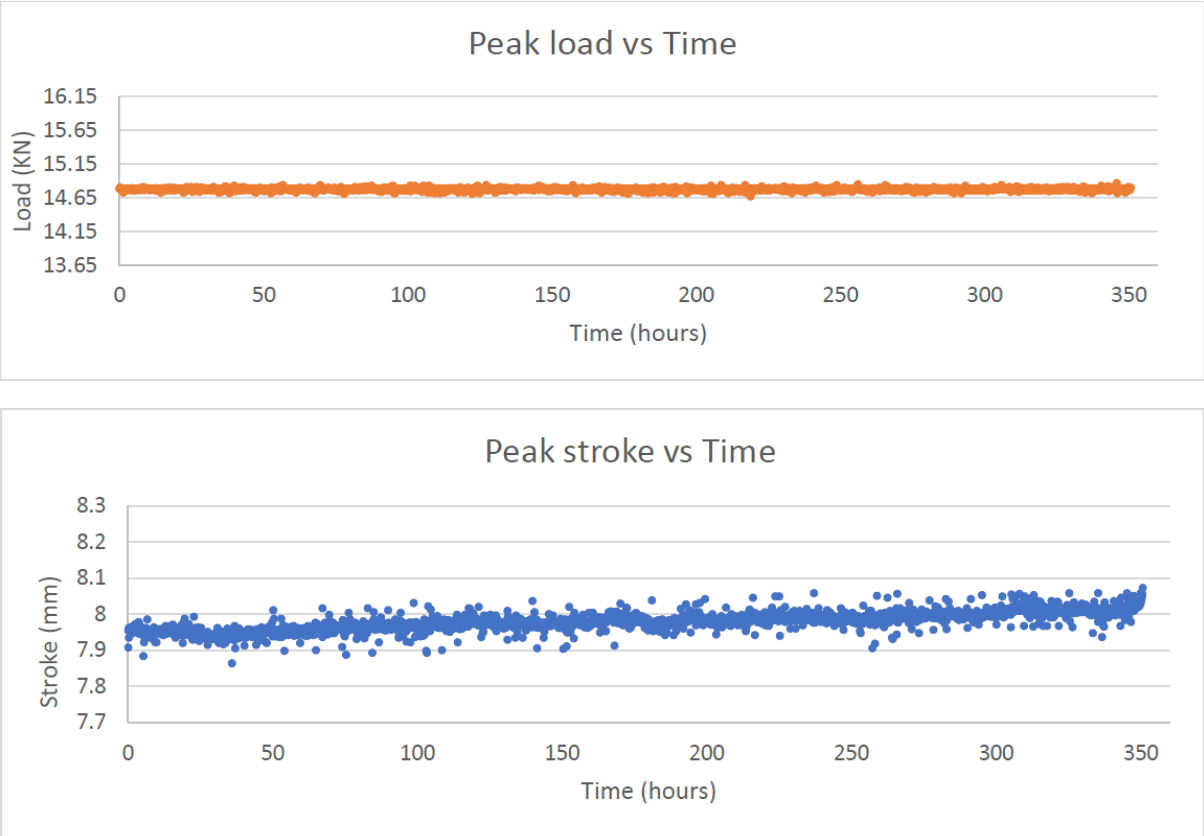

Figure 4-53 (a) The results of HT1 notched sample on dwell fatigue testing

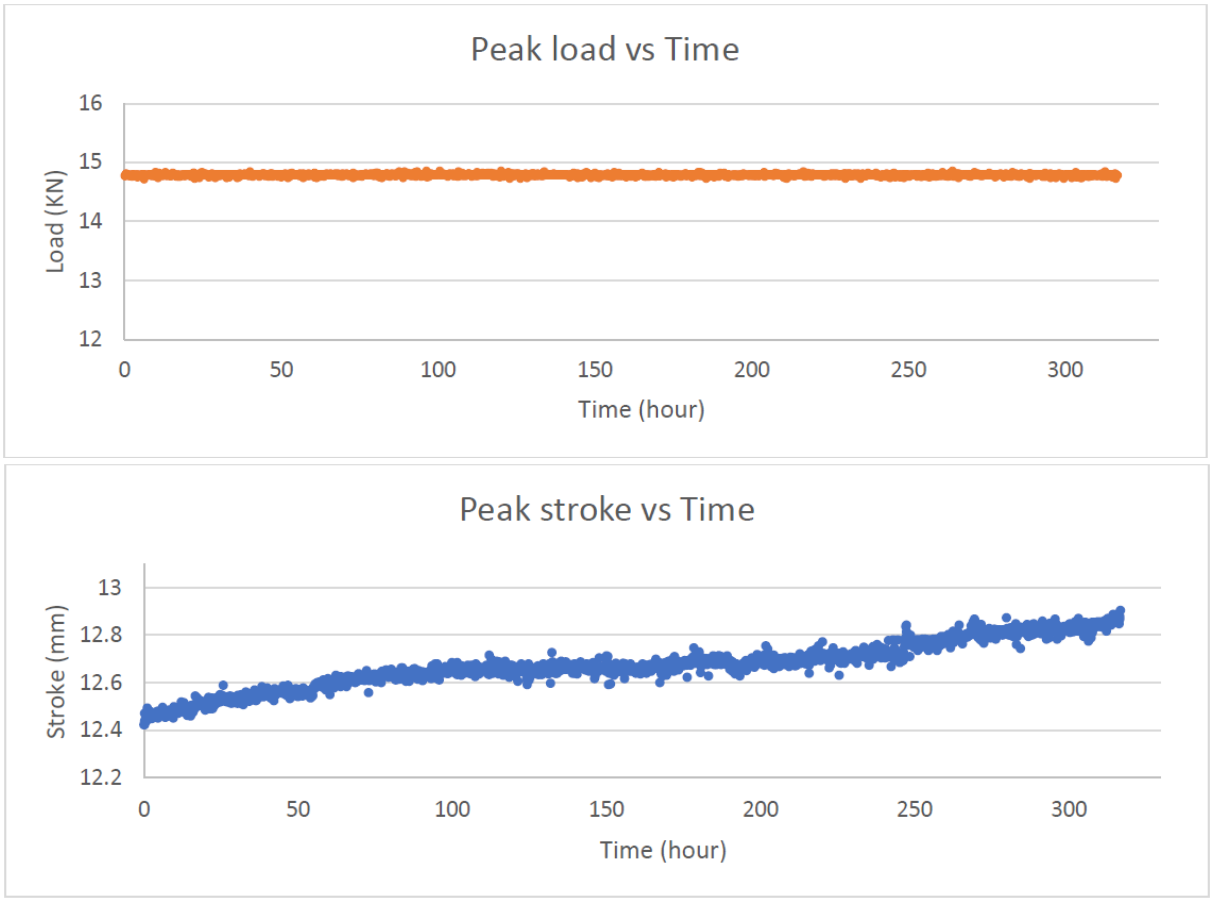

Figure 4-53 (b) The results of HT2 notched sample on dwell fatigue testing

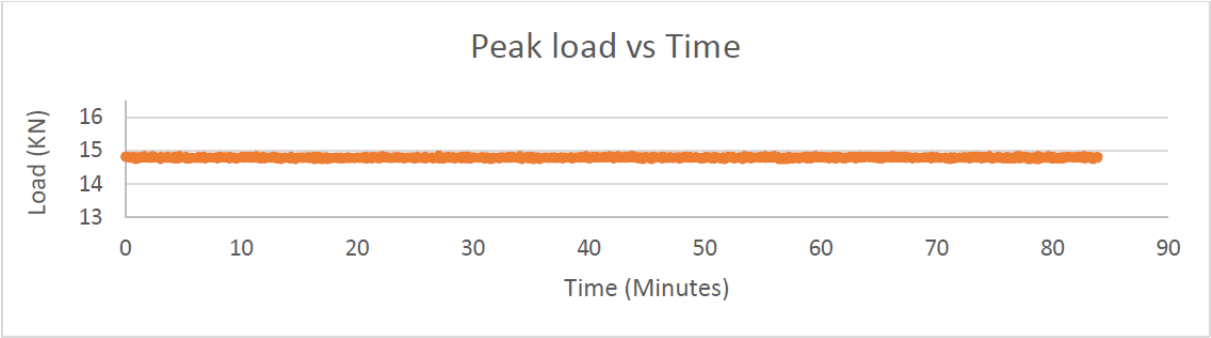

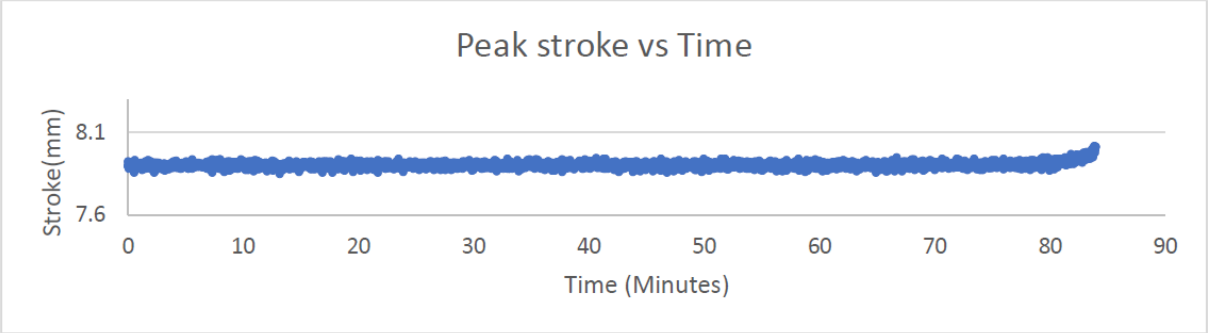

Figure 4-53 (c) The results of HT3 notched sample on dwell fatigue testing

Table 4-10 Summary of testing results in the HT notched and plain samples

	Total life (Hours)	Number of cycles	Temperature(˚C)	Notch section stress (MPa)
HT1N	350.75	10266	650	750
HT2N	316.84	9274	650	750
HT3N	1.35	41	650	750
HT1P	13.07	385	650	N/A
HT2P	30.83	908	650	N/A
HT3P	35.13	1023	650	N/A

4.5.2.2 Fractography

Optical images of the fracture surface of sample HT1N are shown in Figure 4-54 (a). It is clear to see that a shining incomplete ring outlines the light grey and dark brown zones. The SEM images in Figure 4-55 (a) demonstrate that the ring leads to the fatigue fracture in the dark brown zone, which is a mixture of intergranular and transgranular mode from SEM images (circled in red). The overload fracture occurs at the centre and develops the light grey zone at the top. Similar characteristics can be seen in sample HT2N (Figure 4-54 b). A complete ring at the edge is revealed after the test, shown as light grey zone in the optical fractography in Figure 4-54 (b), and the centre is covered in blue and golden oxidise. The following SEM images indicate that the ring zone mainly comprises the fatigue failure and the centre within the ring consists of overload failure in Figure 4-55 (b).

No ring zone can be seen in the optical fractography in sample HT3N in Figure 4-54 (c). The fracture surface shows a light to dark blue gradient from the top to the lower centre area and a dark brown zone in Figure 4-54(c). The SEM images in Figure 4-55 (c) show that the intergranular mode appears from the surface at the notch to the centre of the blue zone, followed by the overload fracture in the brown zone at the lower half.

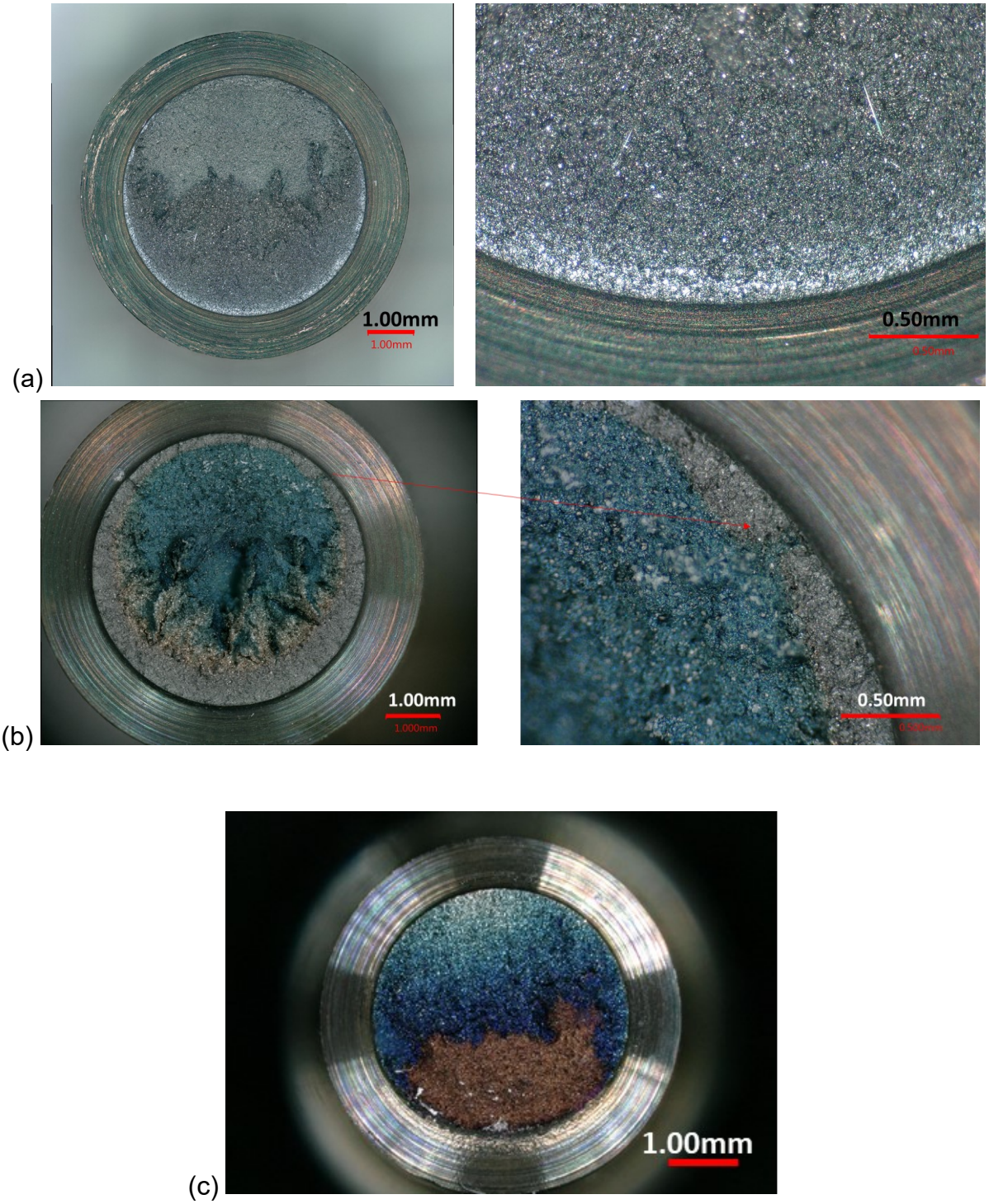

Figure 4-54 Fracture surface of (a) HT1 (b) HT2 and (c) HT3 notched sample under the optical microscope

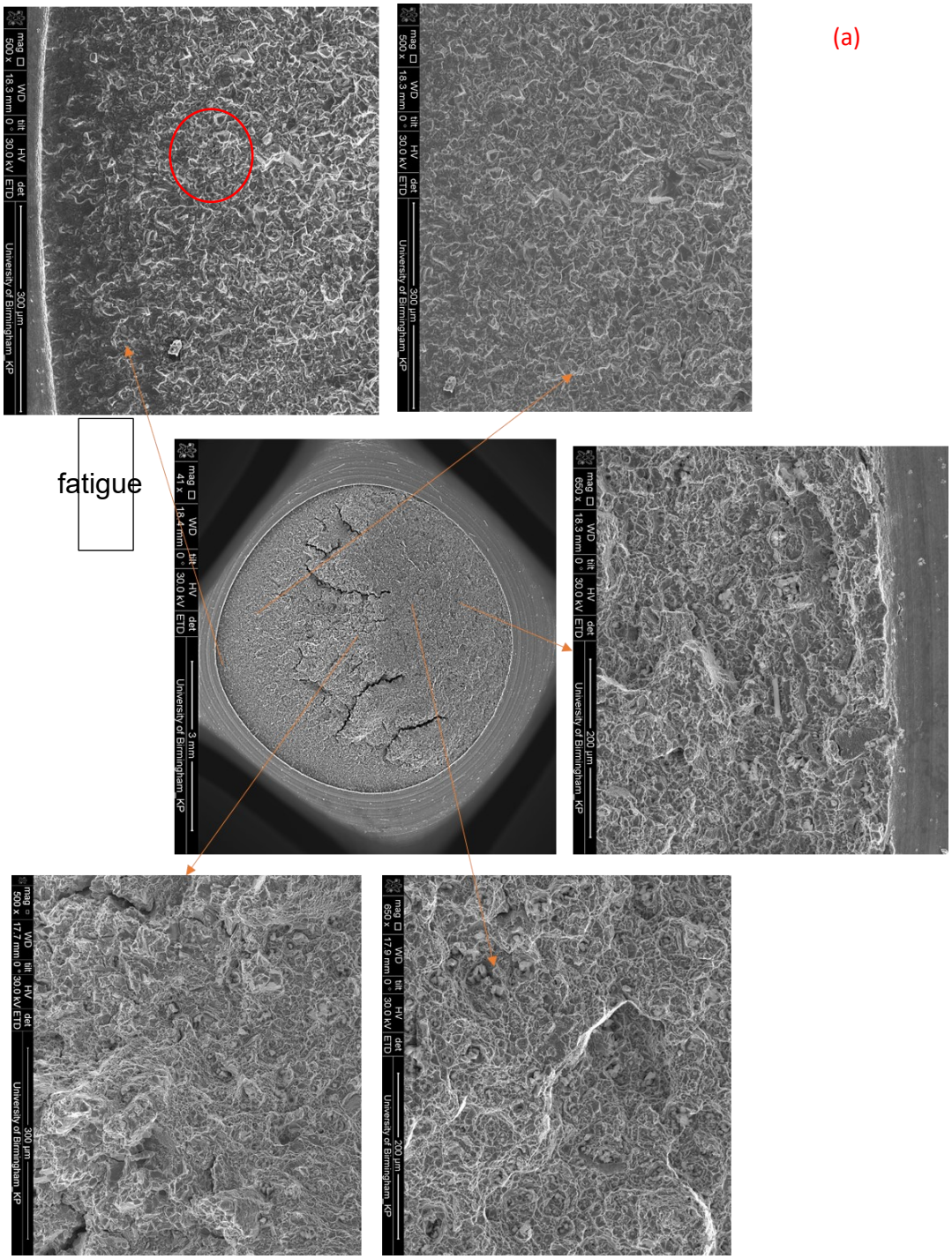

Figure 4-55 (a) HT1 notched sample under SEM

(b)

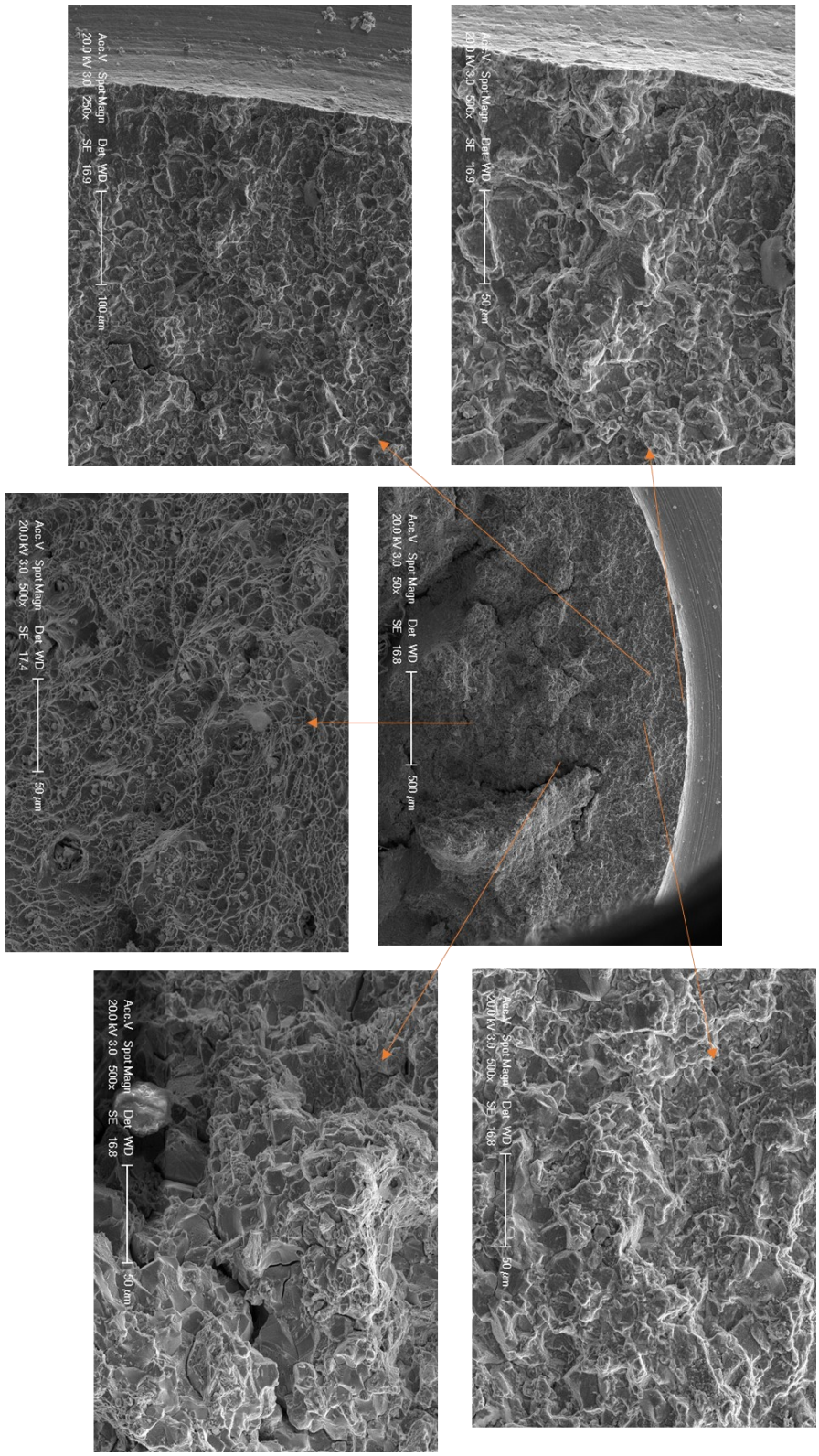

Figure 4-55 (b) HT2 notched sample under SEM

(c)

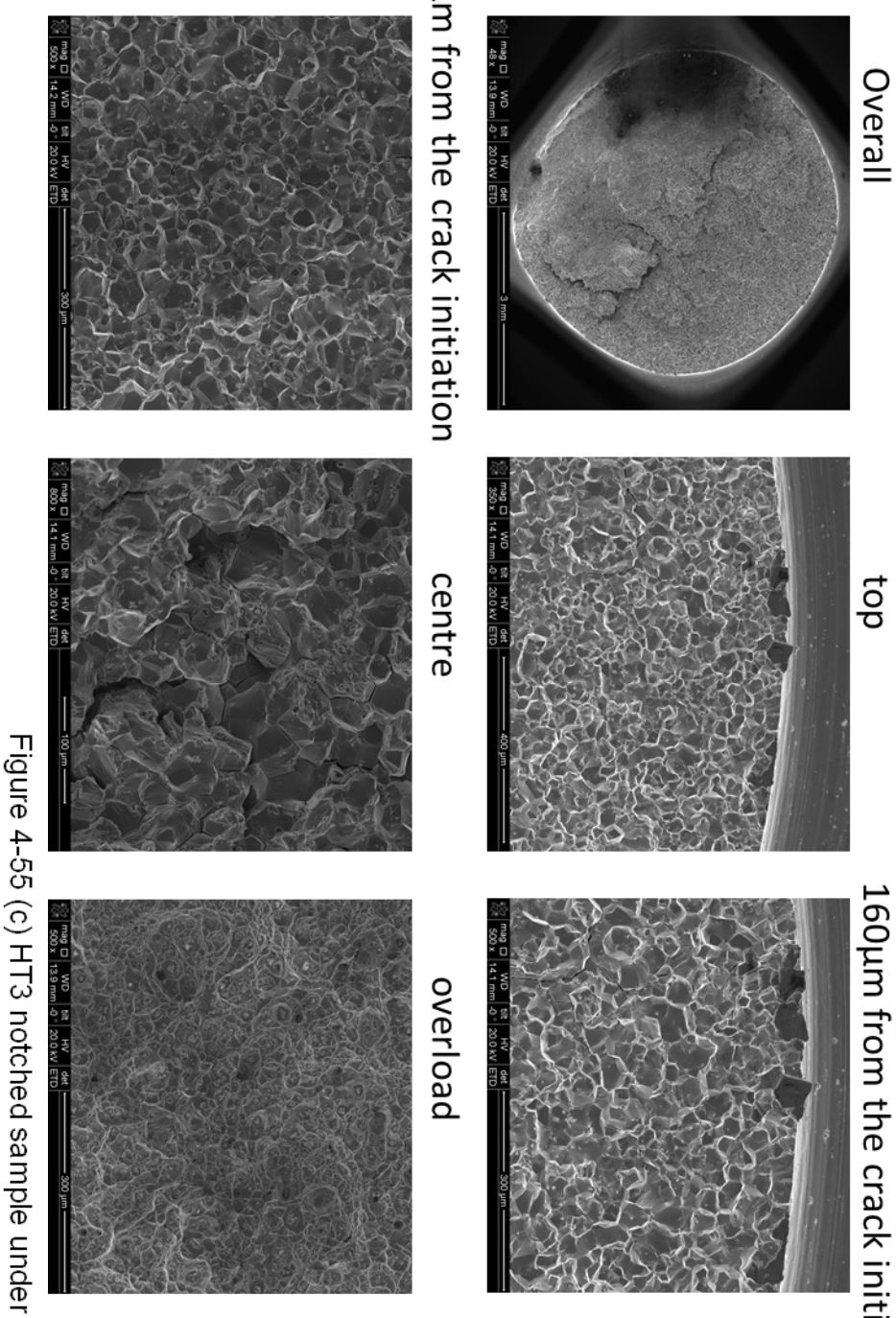

Figure 4-55 (c) HT3 notched sample under SEM

4.5.2.3 Microhardness

Microhardness testing was performed on samples HT2N and HT3N to confirm notch hardening behaviour induced by loading at the notch, yielding the notch. After testing samples HT2N and HT3N were cut in the longitudinal direction and metallographically prepared for microhardness test of the area near the notch (shown in Figure 4-56 the orange zone), as well as in the centre away from the notch (shown in Figure 4-56 the green zone). In sample HTN2 the average microhardness near the notch is 456HV which is nearly 30HV greater than that at the centre (427HV), shown in Table 4-11. In contrast, the microhardness of sample HT3N is even being 448HV at the notch area and 442HV at the centre.

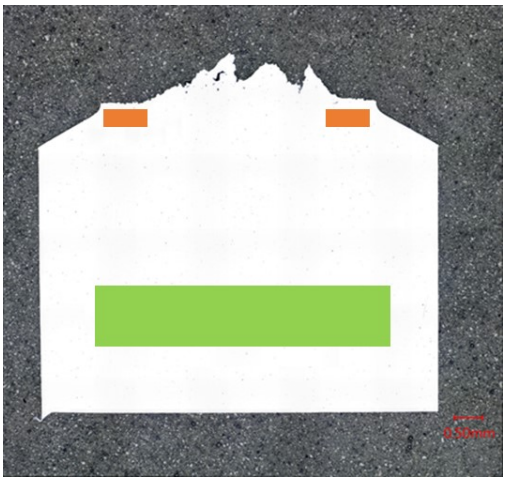

Figure 4-56 Demonstration of the microhardness test applied on cross-sectional microstructure of sample HT2

Table 4-11 Average microhardness of HT2N and HT3N at the notch and centre

	Notch	Centre
HT2N	456HV	427HV
HT3N	448HV	442HV

4.5.2.4 Cross-sectional microstructure

The cross-sectional microstructure of samples HT2N and HT3N then were polished after microhardness testing and etched in Kalling's No.2 reagent and observed using

an optical microscope. The cross-sectional microstructure of samples HT2N (Figure 4-57) and HT3N (Figure 4-58) indicate that the fatigue fracture surface is flatter and even near the notch, whereas the overload surface is bumpy and rough in the middle. Furthermore, more extensive deformation can be seen in sample HT2N (Figure 4-57 a) at the centre compared to sample HT3N in Figure 4-58 (a).

Coarse grains can be seen in sample HT3N (Figure 4-58 b) while a mix of fine and coarse grains are seen in sample HT2N (Figure 4-57b). It is obvious that the grain boundaries are distorted at the notch in sample HT2N elaborating the notch strengthening effect, whereas no such phenomenon appears in sample HT3N. In addition, both conditions show intergranular failure at the fatigue fracture zone and at the secondary cracks.

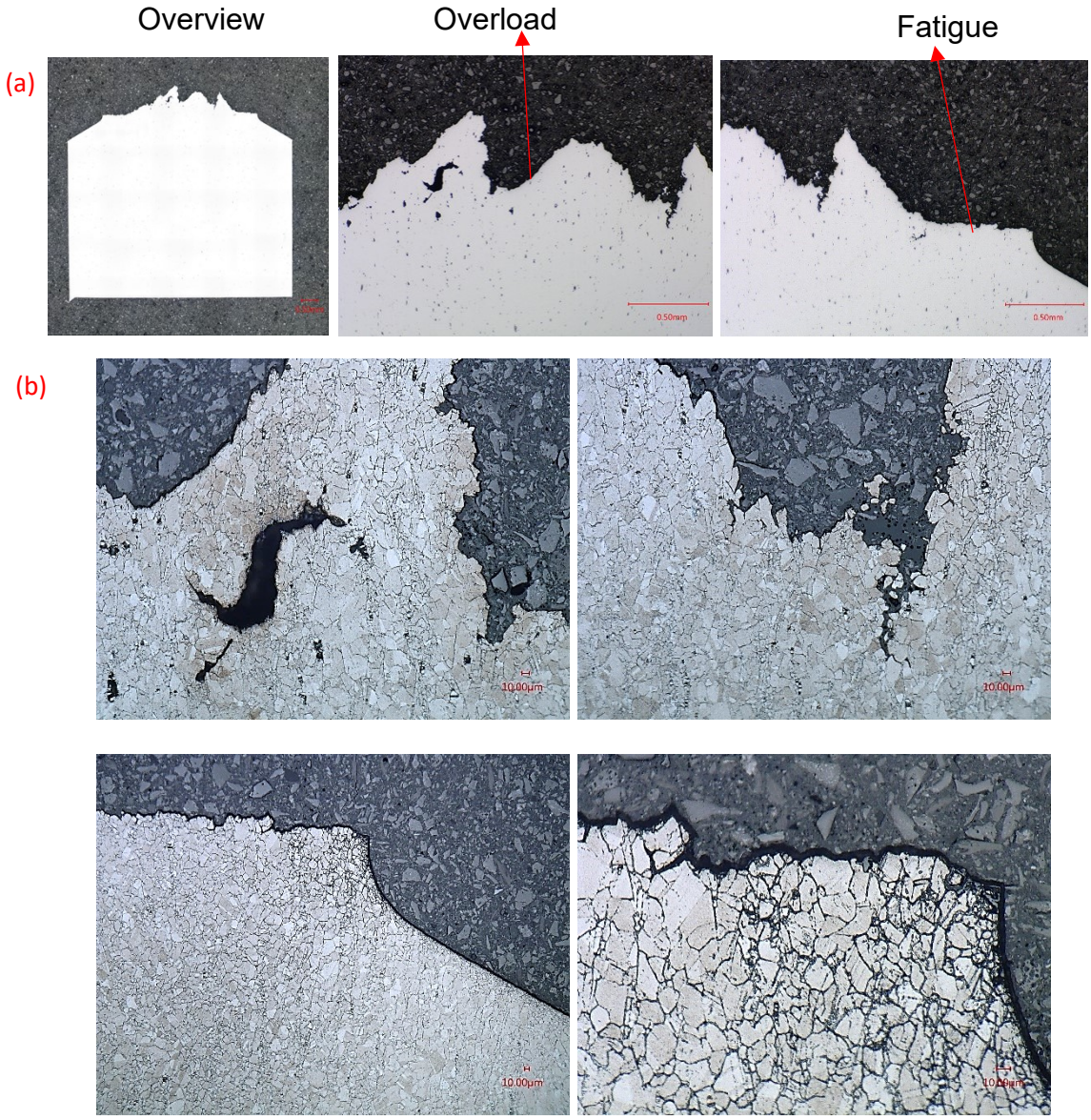

Figure 4-57 Cross-sectional microstructure of sample HT2N (a) as-polish condition and (b) etched condition

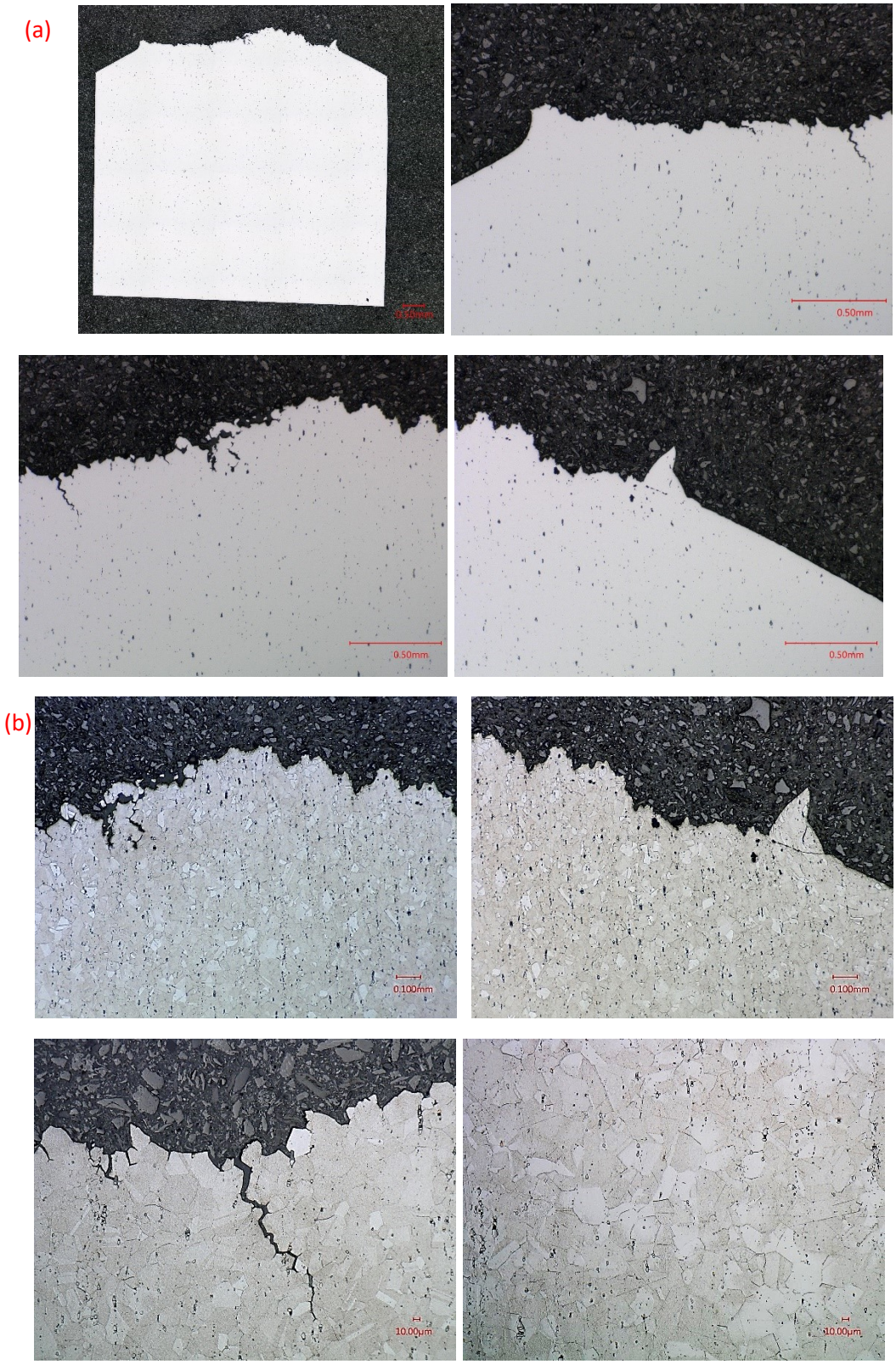

Figure 4-58 Cross-sectional microstructure of sample HT3N (a) as-polish condition and (b) etched condition.

4.5.2.5 Results analysis of stress-rupture testing

Further HT2N (medium grain size) and HT3N (large grain size) samples were subjected to stress-rupture tests under load control at the same load (750MPa at the notch area) at 650˚C. The testing results are displayed below in Figure 4-59. Both samples were tested to failure and the stroke over time was monitored. A rather distinguishing difference in lifetime between HT2N and HT3N can be seen. HT2N with a mix of fine and coarse grain size lasted over 955 hours and the stroke under the static load shows a slowly increasing trend over time from the beginning. The HT3N sample only ran approximately 29 hours followed by sudden failure. The stroke levelled off for most of the sample life and dramatically rose at the very last two hours.

Compared to the dwell-fatigue (1-120-1-1 waveform) testing results, both performances of HT2N and HT3N were improved under the static load, summarised in Table 4-12. The lifetimes increased by approximately three times for HT2N and twenty-three times for HT3N compared to cyclic loading. Due to the long-term exposure in the hot air, the fracture surface of HT2N is mostly covered by oxides. Figure 4-60 (a) shows the cracks propagate transgranularly, mixing with a small amount of intergranular fracture, and the image (b) presents the overload zone of HT2N. The fractography of HT3N is clearer. Cracks develop at the notch and propagate by intergranular fracture (c) until the sample overloads in the centre, followed by a small amount of shear fracture at the edge (d).

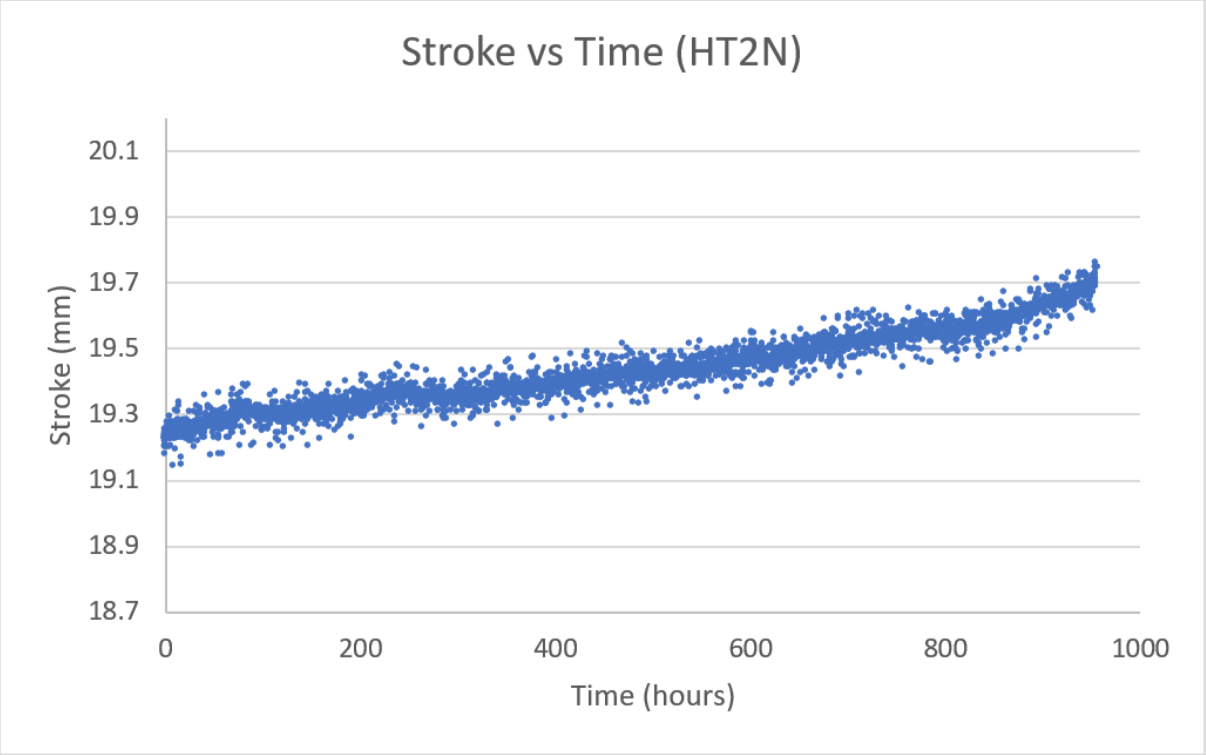

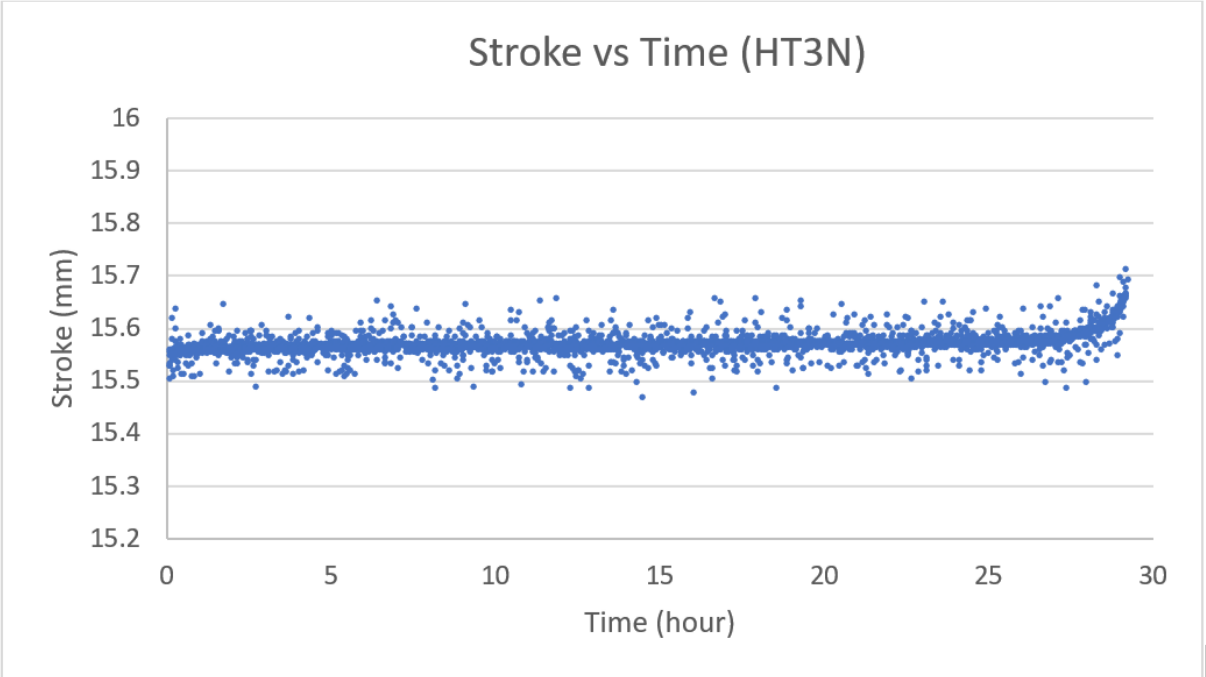

Figure 4-59 The results of HT2 and HT3 notched samples on the stress-rupture testing

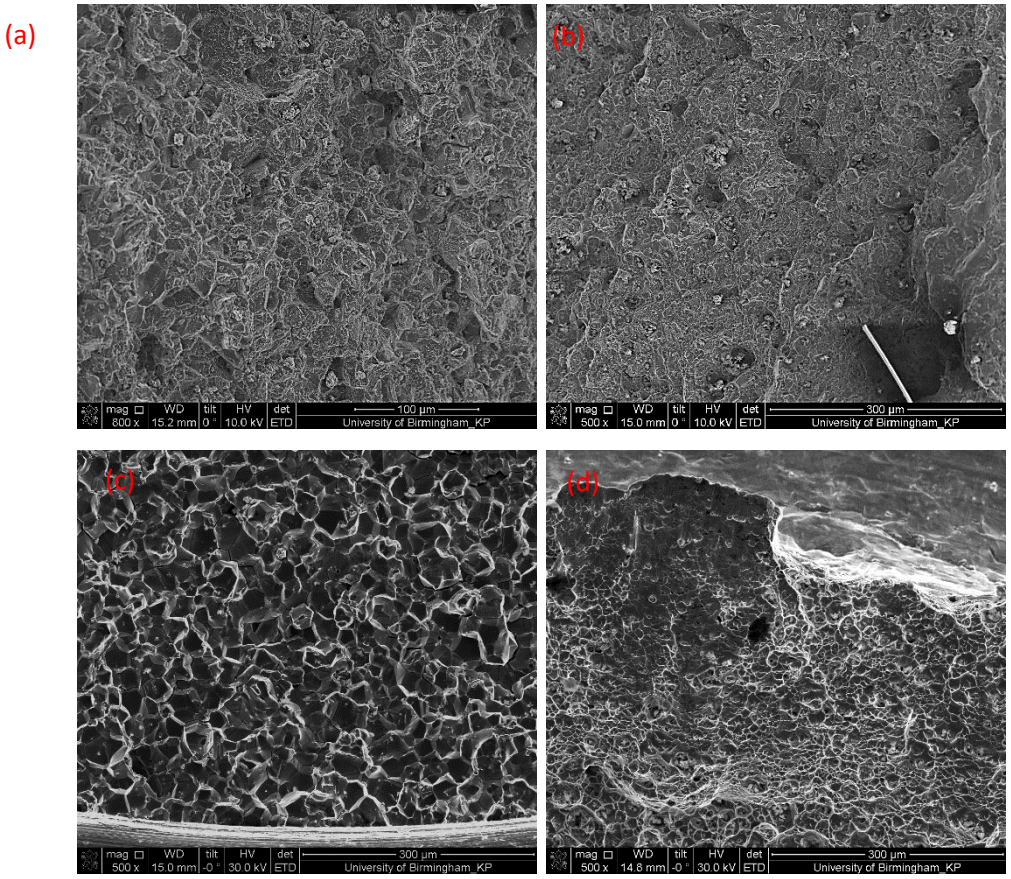

Figure 4-60 Fracture surfaces of (a) (b) HT2 notched sample, and (c) (d)HT3 notched sample

Table 4-12 Summary of testing results in the HT notched under the cyclic and static testing modes

	Total life (Hours)	Number of cycles	Temperature(˚C)	Notch section stress (MPa)
HT2N (cyclic)	316.84	9274	650	750
HT3N (cyclic)	1.35	41	650	750
HT2N (static)	956.24	27988	650	750
HT3N (static)	29.30	858	650	750

Chapter 5

5. Discussion

5.1 IN718 aero-engine bolts

In the modern aeroengines, welding the joints is a developing technique to reduce the weight [117]. However, the traditional method of using fasteners is still a better choice for many critical joints due to the limits of weldability and formability of the materials [118]. To recap the Literature Review, the joints in the aeroengines are required to sustain the high-temperature resistance and maintain the clamping force while suffering the harsh in-service conditions. The mechanical aspects comprising tensile strength, high temperature fatigue performance, creep resistance, corrosion fatigue resistance and cost need to be considered in terms of designing the joints and selecting fastener materials [119].

As previously mentioned, IN718 bolts are used for a large proportion of the overall aeroengine fastening joints [120]. The requirement of increasing turbine entry temperature (TET) in future aeroengines forces the IN718 bolts to face the greatest challenge ever. To meet the requirements and to potentially reduce the material waste by maximising the bolt servicing life, the manufacturing process of IN718 bolts is being discussed and revised in order to optimise the material strength for fastening applications in the aeroengines.

5.1.1 Manufacturing route of IN718 bolts

As introduced previously in Chapter 1, two major variations exist in the manufacturing processes involving metal forming of IN718 bars and the solution temperature of the bolts. A full flowchart of the route is shown in figure 5-1.

Firstly, before delivery to the bolt manufacturer, the bar manufacturer accepts both cold and hot finished IN718 raw materials for further processing according to AMS5662 or AMS5962 to the bar materials[100, 101]. Referring to Figure 5-1, AMS5962 requires a suitable degree of work hardening (cold drawn) after solution heat treatment at 968˚C. This is one of the variations that affects the final products. Apart from the selection of the IN718 bars, the bolt manufacturer forges the bolt head and anneals the products between 925 to 1010˚C. As the δ phase solvus temperature is around 997°C, different microstructures such as δ-rich, δ-lean, or δ-free types and varied grain size could be resulted in the final products. The solution heat treatment is followed by double ageing treatment, then fillet and thread rolling is applied as the final step. In addition, Figure 5-1 shows the bolt microstructure affected by each treatment process during manufacturing the bolts. This project mainly focuses on how the different solution temperatures affect the microstructure and in-service performance of IN718 bolt, and HT samples were designed based on this.

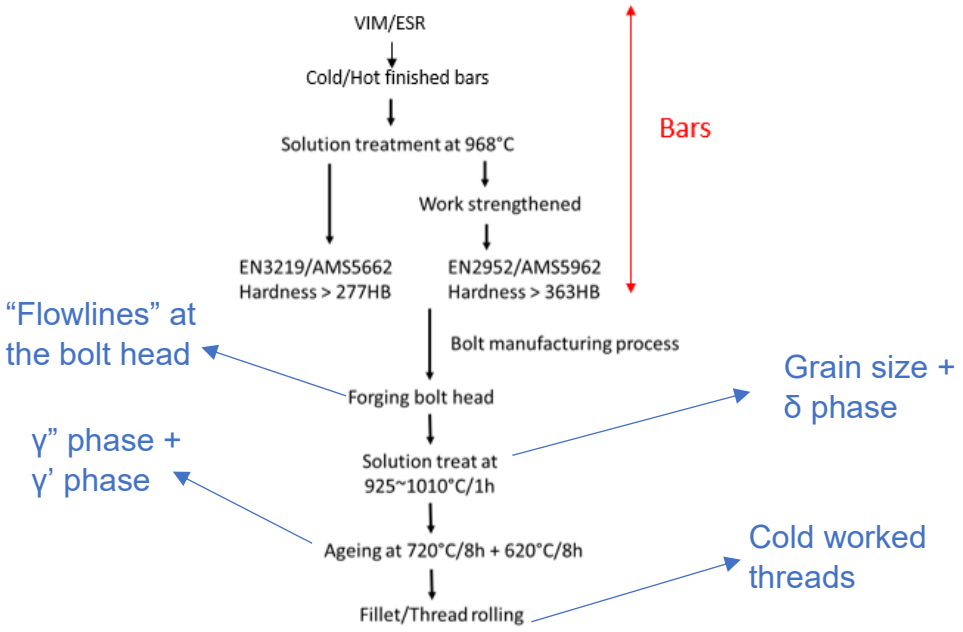

Figure 5-1 the manufacturing process of IN718 aero-engine bolts

5.1.2 Failure mechanisms

The turbine entry temperature (TET) varies during a civil flight cycle. Taking off and climb are the most challenging periods for aeroengine materials including the fastening joints during the intensive engine run [121].The increasing TET over the years results in the higher efficiency of aeroengines [8]. It is critical for aeroengine fasteners to maintain excellent strength under stress at high temperature, securing the aeroengine components. The Figure 5-2 simulates a typical civil flight cycle, during take-off, stress and TET sharply increase to their highest, requiring the engine to work at its hardest. Climbing and reverse thrust will also put a high demand on the engine. Low-cycle fatigue and dwell fatigue are mainly involved in these progresses [122-124]. In the laboratory, the 1-120-1-1 waveform for dwell fatigue testing was designed to simulate the same effect, two minutes at the highest stress and dropping to the minimum holding

load for one second to complete the running cycle. Besides fatigue, it is vital to consider creep as a notable failure mechanism, given that the fasteners endured a substantial and constant load at elevated temperatures. Such dwell fatigue behaviour of aero-engine fasteners accumulates by each fight cycle. Before the aircraft overhaul, the fasteners need to guarantee the safety of sealing the casing and connecting different sections [125].

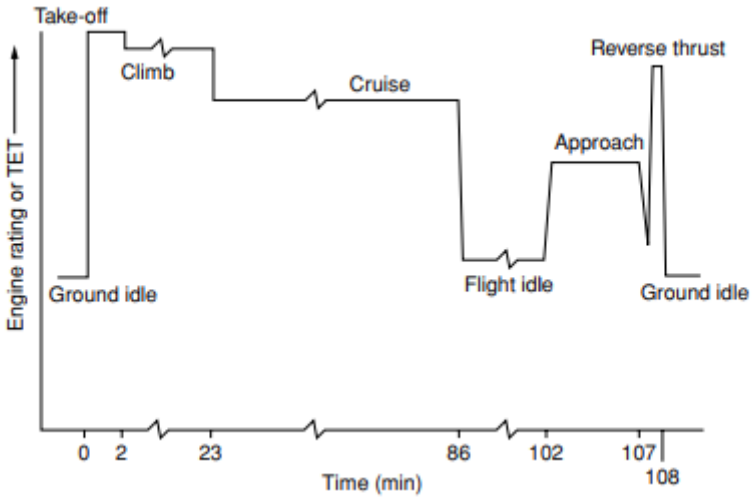

Figure 5-2 Changes in TET during a civil fight cycle [8].

In some extreme situations, if the fasteners loose the clamping force or are damaged during the engine running, high-cycle fatigue may be involved due to the high-frequency vibration at the joints. Hence, the chance of failure of the bolts would be increased. If the in-service fasteners fracture, it is difficult to identify from outside which is the risk to engine safety, as shown in Figure 5-3.

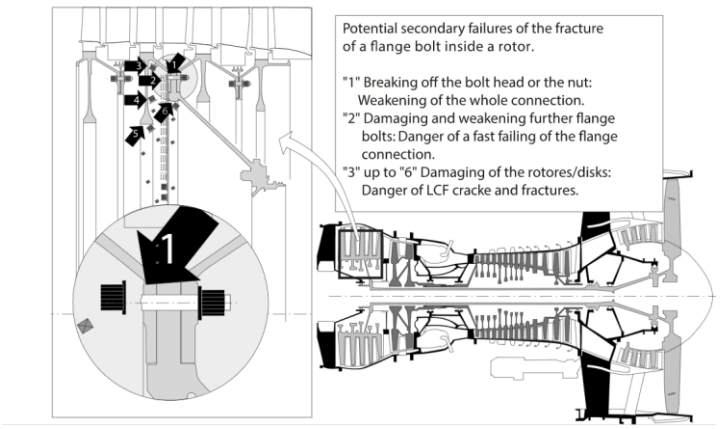

Figure 5-3 The possible outcomes of bolt fracture inside the aeroengine and the subsequent dangers [126].

The potential danger as Figure 5-3 shown could come from the changes in local microstructure and mechanical properties under in-service conditions, or foreign objects impact which is not investigated in this project. As reported in previous studies, the fillet and threads of a bolt are the most vulnerable locations [127-129]. Due to the complex geometry, the stress applied on a bolt is uneven. Compared to the shank, the threads possess a stress concentration of Kt3 and are cold worked by cold rolling, which possibly are the main causes of the failure at the threads. The effects of stress concentration and cold work are discussed in section 5.4 and 5.5 by analysing the testing results.

A series of experiments were designed in the laboratory. Based on the in-service conditions, the stress used in the experiments was designed to be the worst possible in real life. All the tests were conducted at 650°C. This is because the mechanical performance of IN718 is considered to be unstable due to the transformation of γ” to δ precipitates above this temperature. And in reality, IN718 is suggested to operate under 630°C [73, 130]. By analysing the results, this section focuses on discussing the

two key parts, the microstructure evolution of IN718 bolts under in-service conditions and the subsequent mechanical performance. More specifically,

1. Effect of solution heat treatment before manufacturing threads on matrix microstructure.
2. Microstructure evolution of IN718 bolts after thermal exposure.
3. Dwell-fatigue behaviour of solution treated IN718.
4. Fatigue and creep behaviour of cold work IN718.

5.2 Effect of solution heat treatment before manufacturing threads on matrix microstructure

HT samples were machined from IN718 bars and solution treated at 925, 975 and 1010˚C followed by a double ageing process. The selected temperatures cover the full range of the solution heat treatment temperature range likely to receive after forging bolt head, hence could indicate the variation of microstructure seen in actual IN718 bolts. Microstructure characterisation on HT samples was carried out to understand the evolution of the shank section of IN718 bolts by the heat treatments. In accordance with the heat treatment history, the HT samples could represent the shank of the EN3219 small bolts (see Figure 5-1) since no work strengthening was involved during the bar manufacturing process [100].

The results of HT1, HT2 and HT3 (solution heat treated) show the differences in the volume fraction of δ phase, grain size and microhardness. HT1 was solution treated below the δ solvus, leading to a δ-rich microstructure. HT3 displayed a δ-free type, and

HT2 was δ-lean as 975˚C is close to the δ solvus temperature, which partially eliminates δ phase. The δ solvus temperature is affected by the Nb content in IN718 [85]. 997˚C is very close to the real δ solvus in this case based on the material composition. As previously mentioned in the Chapter 1, δ phase pins the grain boundaries and controls the grain size. The average grain size of HT3 (26μm) is noticeably larger than HT1 (12μm) due to lack of δ precipitates at the grain boundaries, see Table 4-2.

Microhardness tests were carried out on HT0 (as-received IN718 bar), HT1, HT2 and HT3 samples, see Table 4-3. The results demonstrate that the microhardness value of HT0 (369.2HV) is much lower than the other conditions because of missing the ageing process. HT3 possesses the highest hardness (449.8HV) among the aged samples. This might be attributed to the higher percentage of γ” phase, resulting in greater strength. The δ and γ” precipitates share the same chemical composition. HT3 with no δ phase contains more γ” precipitates. As introduced in Chapter 1, γ” phase is the main strengthening phase in IN718, Hence HT3 has a higher microhardness value overall. On the other hand, a smaller grain size was observed in the HT1 condition, encompassing a higher density of grain boundaries. As is well known, grain boundaries often offer a grain boundary strengthening effect, which provides the extra hardness in HT1 sample [37]. Therefore, the microhardness results of HT1, HT2, and HT3 samples are similar by balancing the contribution from γ” phase or grain boundaries. The hardness of HT3 is only slightly higher than the other two conditions.

It should be noted that the large bolts used in this project were solution treated at 1000°C prior to the ageing process, whereas the small bolts were solution heat treated at 925°C to 975°C. As a result, the small bolts contain a higher volume fraction of δ

precipitates than the large bolts in the finished products. However, the grain size in both situations is comparable (10μm-18μm) regardless of the differences in δ phase. This might be because the material used for the large bolts (EN2952) was cold worked before manufacturing into the bolts. When the one-hour solution heat treatment at 1000°C was applied, recrystallisation occurred in IN718. This process consumed much of the energy stored by cold work, and the energy was also used to precipitate the δ phase (see chapter 1 Literature Review). Thus, the remaining energy and time for grain growth during the solution heat treatment on the large bolt was limited. In addition, when the temperature elevating to 1000°C, some δ phase would be already precipitated at the grain boundaries since precipitation requires less energy than recrystallisation, leading to the pinning effect at the grain boundaries which effectively controlled the grain size, even though some of the δ phase (needle-like) precipitated at the early stage would be dissolved later during the holding period at 1000°C.

The microhardness results of both large bolts and small bolts have shown that the threads and thread roots are significantly harder than the centre, up to 14%, due to cold work effect by the cold rolling procedure. The results are comparable between these two types of bolts. The etched cross-sectional microstructure of the large bolts reveal piled up grain boundaries at the thread roots. The depth from the thread root surface affected by heavy coldwork is about 200μm, see Figure 4-3.

5.3 Microstructure evolution of IN718 bolts after thermal exposure

5.3.1 Group B and Group C large bolts

To understand the effect of in-service conditions on the microstructure of IN718 bolts, two thermal exposure procedures were conducted on IN718 bolts, designed as Group B and Group C.

Both as-received large bolts and small bolts were treated by Group B conditions (thermal exposure at 650°C for 100 hours). Microvoids appeared in both bolts at the thread root along the stacked grain boundaries that were caused by heavy coldwork in Figure 4-7. Especially in the small bolt, the microvoids were easily seen under low-magnification SEM (Figure 4-12 b and d), whereas no microvoids were observed either at the centre or in the shank in both types of bolts. On the other hand, the HT samples replicating the shank area without cold work were heat treated at 650°C for 100 hours, no significant changes in phases and no microvoids were detected, see Figure 4-18. The results demonstrate that the formation of the microvoids is only related to the cold rolled threads with severe deformation, and thermal exposure changes the microstructure of the heavily coldworked IN718.

A closer look at the distorted grain boundaries of the Group B large bolts revealed another distinctive microstructure change at the thread root in Figure 4-7. A large amount of newly precipitated fine δ phase (~100nm length) was observed at the grain boundaries surrounded by microvoids. It is likely due to the thermal misfit between δ phase and γ matrix. Such new and fine δ phase formed by consuming γ” phase. As

650°C is below the δ precipitation temperature, maximum precipitation rate at 900°C, reported by Azadian, [85]. The δ phase precipitates directly through the γ matrix only when the temperature is over 900°C, and the transformation of δ from γ" phase initiates at grain boundaries where the higher energy locates, as in the cold worked regions [131].

Cold rolling at the thread roots stores enormous energy in the alloy, which largely encourages the transformation of δ phase. According to the IN718 TTT (δ solvus) diagram shown in Figure 5-4, 100 hours thermal exposure at 650°C is neither long enough nor hot enough for precipitation of δ phase, which explains why no newly precipitated δ phase was detected in the treated HT samples or in the shank of the bolts. Thus, the appearance of newly precipitated δ phase at the thread in Group B bolts can be attributed to the extra stored energy which drags the δ solvus curve to the left and down in the TTT diagram (as indicated by the red arrow in Figure 5-4). In addition, 650°C is highlighted in a purple dash line in Figure 5-4 and the yellow dot indicates the Group B treatment (100h thermal exposure), which is lower than the δ precipitating or γ" dissolving temperature or time. As previously mentioned, cold work largely encourages this process to prematurely occur.

The results of the small bolts show that the existing δ precipitates were surrounded by microvoids. This might be due to the different thermal coefficients of the δ phase and the γ matrix, promoting the formation of microvoids. When the thread area is thermally exposed for a long time, the changes in volume of δ precipitates and matrix are incoherent, which causes and enlarges the microvoids.

Further investigation including the effect of stress on the microstructure at a high temperature was addressed by Group C large bolts (static axial tensile loading at 650°C for 100 hours). More microvoids and newly precipitated δ phase were present at the threads root, and the disappearance of γ” phase around the newly precipitated δ phase was present as small flat areas circled in red in Figure 4-11 (d). Such a phenomenon shows the transformation of γ” to δ phase under the cold work condition, and external stress exaggerated the results with a notable increase in the number of microvoids and a larger size of the newly precipitated δ phase. This implies that the precipitation of δ phase occurred even earlier and the δ solvus curve was dragged even further to the left and down by applying a static stress of 600MPa (net stress) to the large bolts, as the external stress brought extra energy. The transformation of γ” to δ phase can also be found in the axial-dwell-fatigue tested large bolts. The newly precipitated δ phase replaced almost the entire γ” phase within 30μm of the threads root surface, and microvoids were found in Figure 4-42 (b).

5.3.2 Bending test pieces

The three-point bending test results have also demonstrated a clear phases evolution at the thread roots. With a higher stress and longer testing period, the transformation of the newly precipitated δ phase in the bending tested sample was obvious, especially near the fracture area in Figure 4-35 (a). For instance, compared to the Group C bolts, the cross-sectional microstructure of the coldwork bending sample (1-120-1-1) tested for nearly 700 hours under 1500MPa evidently showed a larger size of the new δ phase with a needle-like morphology, and the newly formed δ phase covered the whole area at the 30μm depth from the thread root surface in Figure 4-35 (b). This indicates that more γ” phase has transferred to δ phase, and the longer thermal exposure also

allowed the newly formed δ phase to grow. However, the cold work free sample retained the original γ” phase at the thread root without phase transformation during testing in Figure 4-35 (d).

Both the CW (coldwork) and CWF (coldwork free) samples experienced the same dwell test conditions, and both lasted over 700 hours. A rather distinct difference in microstructure at the cracks between CW and CWF was observed in Figure 4-35 (a) and (c). The crack in CW sample went straight to 200μm depth until the grains were less distorted, then it started to propagate along the grain boundaries and develop the microvoids coalescence at the tip as retardation. Referring to section 1 Literature Review, this led to bluntness at the crack tip due to a small degree of creep and deformation under the two-minute dwell test. This partially released some of the stress concentration in the adjacent matrix to slow down or stop the crack propagation [51].

Unlike the CW sample, the CWF sample showed none of these features. The main crack was sharp and straight in Figure 4-35 (c) and the secondary cracks opened up the grain boundaries, transgranular behaviour was mainly involved. The overall grain shape was equiaxial throughout the sample as a result of the thorough recrystallisation. Within 200μm below the thread root surface, a lot of porosity appeared grain boundaries, and the δ precipitates happened to pin the grain boundaries in Figure 4-35 (d). This is because the CWF sample had none of the cold work strengthening and presented the fine to medium sized grains. More grain boundaries were damaged when the two-minute dwell fatigue was applied then the static tests. It was much easier for diffusional creep to occur, leading eventually to grain boundary separation [132]. The δ phase played an important role in pinning or stabilising the grain boundaries and avoiding intergranular fracture. However, even without losing the strength from γ”

phase, the main cracks still propagated transgranularly to failure regardless of the benefits of δ phase.

5.3.3 Correlation to IN718 TTT Diagram

Thus, cold work at the thread roots significantly improves the dwell fatigue life of IN718 fasteners, even though it also brings several concerns in terms of microstructure. Cold rolling on the thread rood stores a great deal of energy in IN718 which means a shorter time or lower temperature is required to precipitate or dissolve a phase. As a result, both the δ phase and γ” solvus curves are dragged to the left and down in the standard IN718 TTT diagram under in-service conditions, resulting in the premature dissolution of the main strengthening γ” phase and precipitation of a large amount of δ phase surrounded by microvoids. However, the acceleration of the phase transformation does not appear to have deteriorate effect. Considering the great strengthening effect by cold work, cold rolled threads are still necessary.

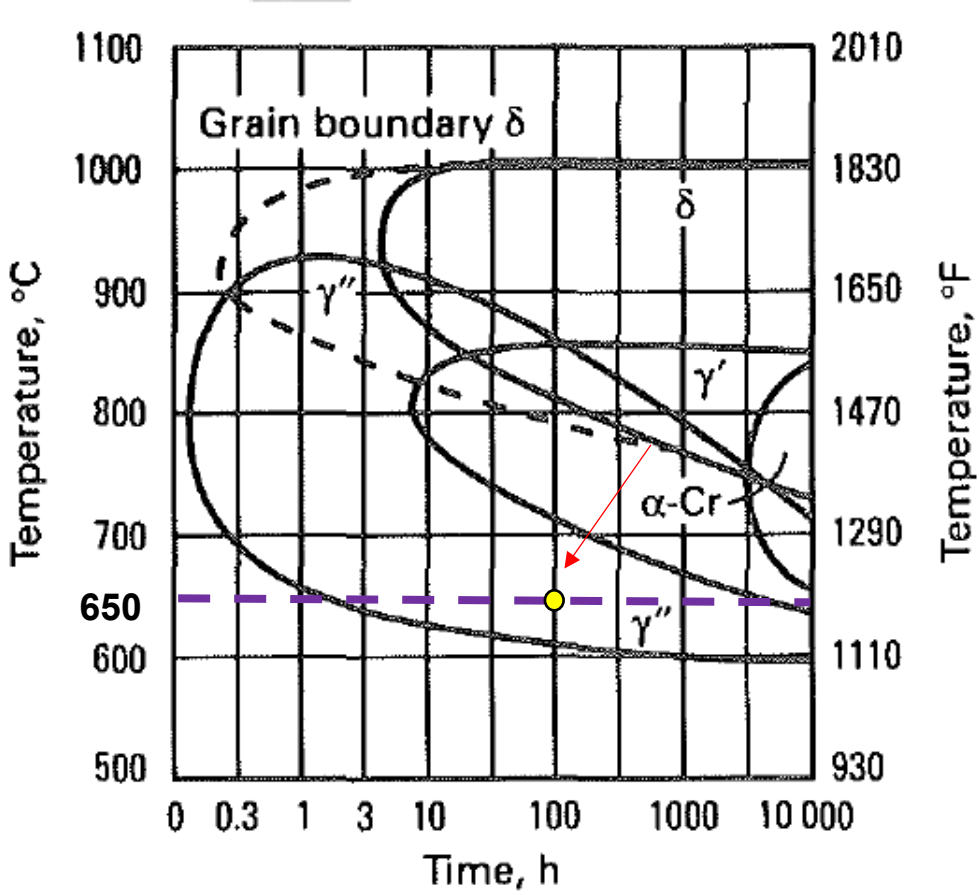

Figure 5-4 original TTT diagram [133]. In this work, the yellow dot indicates the appearance of δ phase under such conditions at the heavy cold-work zone.

Apart from phases analysis, microhardness comparison was also carried out on the thermal-exposure-treated HT and bolts samples. The average microhardness results of Group B HT1 and HT3 were slightly increased compared to the original HT1 and HT3 samples in Table 4-4. This might be because such a prolonged ageing process encouraged more γ" precipitates to form from γ matrix without external load and cold work effect, which contributes more strength and an increased hardness. Similarly, the centre area of the Group B large bolts is harder than the as-receive large bolts in Figure 4-9, whereas the thread area slightly decreased in hardness after being treated. The possible reason can be attributed to the new formation of δ phase and the appearance

of microvoids which potentially lower the strength. The results of small bolts show the same trend, the as-receive small bolts is harder than Group B small bolts overall in Figure 4-13, and the difference between the microhardness is smaller towards the centre. This shows the strength of the Group B small bolts decreases more than the Group B larger bolts compared to the as-received condition at the thread area. The small bolts are the δ-rich type, resulting in more microvoids after thermal exposure, especially at the thread area.

In summary, the microhardness at the centre or shank area of the IN718 bolts without cold work is less affected by thermal exposure. However, the threads section tends to soften after the thermal-exposure treatment, especially for the δ-rich bolts. A possible cause of this is the consumption of γ” phase and the formation of microvoids.

5.4 Dwell-fatigue behaviour of solution treated IN718

The technical specifications for IN718 aero-engine bolts allow the solution-treatment temperature to vary from 925 to 1010˚C. As one of the most important parts of the manufacturing process, the solution heat treatment before ageing process effectively homogenises the material, leading to a uniform microstructure in the alloy. The temperature range of the solution heat treatment covers the δ phase solvus temperature, resulting in δ-free, δ-lean and δ rich types of microstructures, as well as the variation in grain size. Therefore, it is important to understand how the mechanical performance of IN718 alloys is affected by different solution temperatures for aero-engine applications.

As previously discussed, a two-minute dwell fatigue waveform (1-120-1-1) represents the stress-thermal condition when time-dependent damage mechanism is activated. Both fatigue and creep processes could be involved in such dwell fatigue loading. The axial dwell fatigue testing was conducted on HT plain samples (HTP) and HT notched samples (HTN). Each group contained samples solution heat treated at 925˚C (HT1) 975˚C (HT2) and 1010˚C (HT3). These were subjected to the same maximum net stress (750MPa) and temperature (650˚C). Such conditions were designed to replicate the worst-case scenario for IN718 bolts in aeroengines. The test results were unexpected as shown in Table 4-10. The HT1 condition performed the worst in the plain sample and the best in the notched sample, whereas for the HT3 condition the notched sample failed earliest in and the plain sample had the longest fatigue life.

The total life of the HT3P sample (1023 cycles) is nearly three times longer than that of the HT1P sample (385 cycles), and life of the HT2P sample is in the middle (908 cycles). The fracture surfaces of HT1P and HT2P appear similar (Figure 4-51 (a) and (b)), both show the characteristics of shear fracture and necking with an obvious increase in strain, Figure 4-49 (a) and (b). The fracture surfaces of HT1P and HT2P are bumpy and uneven from the cross-sectional microstructure. Both were relatively prone to creep deformation and microvoids coalescences occurred at the centre. While HT3P displays the typical fatigue failure mode with a flatter fracture surface in Figure 4-51(c), the crack propagates intergranularly from the surface defects (such as heavy machining marks, surface drag) to the centre, followed by overload. HT3P took the longest time to initiate the cracks without creep, proving that the coarse grain structure with abundant γ” phase behaves the best against creep. Different from H3P, the δ-rich HT1P with fine-grain structure failed first due to the creep behaviour and the deficiency

of γ” phase, presenting a lower tensile strength and lower creep resistance. HT2P was mixed with fine and coarse grains with balanced δ and γ” phases, and the reduced amount of grain boundaries improved the creep resistance comparing to HT1P.

The Kt3 notched samples demonstrate a reversal of these results. Sample HT1N last over 350 hours whereas HT3N failed in just over 80 minutes, shown in Figure 4-53 (a). Sample HT2N also has a longer life over 300 hours in Figure 4-53 (b). All fracture surfaces show the fatigue failure and overload regions. The main reason for the surprising performance of HT1N and HT2N can be attributed to the notch strengthening. Since the net stress is 750MPa at the notch section, the linear elastic stress at the notch tip is up to three times as much, at 2250MPa. Samples HT1N and HT2N are more ductile and relatively low in strength so under such a large stress the materials at the notch immediately yields at 650°C, creating a plastic deformed zone which can be observed in the etched cross-sectional microstructure in Figure 4-57 [134, 135].

The minor deformation causes a distortion in the grains hardening the material at the notch root. This affects the notched samples in the same way as work hardening. Thus, the strength at the notch root of samples HT1N and HT2N is significantly improved, leading to a prolonged fatigue life. Additionally, the applied stress focused more on the strengthened groove notch and the inner section was less affected. This also means that the inner section is “strain controlled”, since the hardened groove notch restrains the displacement of the inner section. Thus, even the stress applied was very high at 750MPa, the inner section was still less affected. Therefore, it was even harder to fail for HT1N and HT2N. The notch strengthening effect can be also seen in the fracture surfaces. Whereas the yield strength and creep resistance of HT3N is the highest, the

local plastic zone at the HT3N notch is minimum, and stress redistribution is the lowest. Moreover, the creep relaxation is also the minimum at the HT3N notch area, thus, the elastic stress is the highest for HT3N.

Both samples HT1N and HT2N display a shining ring zone observed as the transgranular-fracture-dominated failure at the outer edge, and ductile failure at the centre in Figure 4-54 and 4-55 (a) and (b). It was difficult to initiate the cracks at the strengthened notch at the beginning, whereas the inner section without strengthening effect was much easier to creep as it suffered from high stress at 650°C. Subsequently, the creep deformation initiated at the inner section. The etched cross-sectional microstructure of HT2N in Figure 4-57 (b) also proved the microvoids-coalescence (MVCs) phenomenon at the centre. With the accumulation of MVCs, the stress concentration became higher from inner section. Eventually, the cracks at the notch are allowed to initiate from both inner and outer sections, leading its failure.

On the other hand, the same test on sample HT3N further proves that the notch sensitivity is very high in coarse grain and δ-free IN718. The fracture surface presented a clear intergranular failure at the notch until it was overloaded in Figure 4-55 (c). As HT3 samples contain a greater volume fraction of γ” phase, the creep resistance and hardness are the highest (after balancing the grain-boundary strengthening and γ” phase). Barely any deformation can be observed at the notch area of the failed HT3N sample in Figure 4-58, such brittle fracture meant that HT3N crack initiation life made up most of its fatigue life.

In conclusion, the dwell fatigue performance of IN718 is largely dependent on the solution temperature within 925 to 1010°C. At a lower solution temperature, below the

δ solvus temperature (HT1), a large amount of δ phase was present at the grain boundaries effectively controlling the grain size. The fine grain size means the creep resistance is lower, yet the low-cycle fatigue life is higher. As δ phase and γ” share the same chemical compositions, HT1 and HT2 samples containing a lower density of γ” phase but higher δ are less sensitive to notches. For the notched samples, both HT1N and HT2N yield instantly under the high stress concentration and develop a notch strengthening effect which considerably improves the strength close to the surface and the dwell fatigue life. However, without work hardening, especially HT1P sample, the fine grain size is associated with lower creep resistance. Thus, the premature dwell fatigue failure of HT1P and HT2P is dominated by creep fracture. The grain size of δ-free HT3P samples is larger, resulting in a stronger resistance to creep. Additionally, the strength is also contributed by the high content of γ” phase. However, such rich density of γ” may cause brittleness in the alloy, having a negative impact on the notch sensitivity.

The combination of relatively small grain size and a certain amount of δ phase with adequate γ” phase is ideal for the shank area. The mixing fine and coarse grain structure is to lower the notch sensitivity and offer the strength. It can be accomplished by precipitating a certain amount of δ phase, rather than enhancing strength, it benefits the notch sensitivity and brings the brittleness down.

The needle-like δ phase has previously proved to be harmful for strength, see section 1 Literature Review, while the blocky δ phase benefits IN718 by effectively controlling the grain size. It has been found that 1000°C is an appropriate temperature to only precipitate the latter in the large bolt. Solution heat treatment at 1000°C for the large bolt, or around the δ phase solvus (997°C), but lower than 1010°C to prevent the δ-

free environment, shall be a suitable solution-treatment temperature of IN718 aero-engine bolts. For example, the CWF (cold-work-free) bending sample solution heated at 1000°C followed by a double ageing process demonstrates a high strength combining with low notch sensitivity, running over 700 hours under the two minutes dwell testing.

The shank of the aero-engine bolt is required to maintain excellent creep resistance under the in-service conditions, to prevent loss of the clamping force between the flange and the thread section. Under normal circumstances, aero-engine fasteners are installed with fully engaged threads. The fully engaged large bolts and the partially engaged bolts were tested in the lab under cyclic loading (1-120-1-1) and static load to understand the fatigue and stress relaxation behaviour at the shank and at the threads. The test was set up with the highest stress that the IN718 large bolts possibly experience in rare cases. The fully engaged bolts presented a notably smaller elongation than the partially engaged bolts under both cyclic and static loading in Figure 4-47, which indicates the possibility of losing clamping force at the severe cold work section while being thermally exposed. The static loading mode was purely to test the creep behaviour, whereas the cyclic loading mode involved both fatigue and creep. The results of the fully engaged samples reveal the difference in load drop between these two modes (see Figure 4-47). The statically loaded large bolt lost nearly 30% load more than the cyclic one for the same period of time. This suggests that the shank area of the large bolt is prone to creep deterioration rather than fatigue damage, which can be attributed to a higher density of grain boundaries in the large bolt. However, this effectively lowers the notch sensitivity and enhances the tensile strength.

On the other hand, the partially engaged bolts performed better with a smaller drop in the stress relaxation testing. Such a phenomenon was also observed in the HT notched samples considering the notch strengthening. The stress rupture tests on both HT2N (medium grain size) and HT3N (large grain size) showed a significant improvement in terms of lifespan of the samples compared to the dwell fatigue tests in Table 4-12. Both samples benefit from the static load by removing the cyclic waveform, the lifespan of HT2N was over 900 hours and that of HT3N effectively increased by twenty-three times, which shows why IN718 with a stress concentration shows a worse response to fatigue than creep. Additionally, generic data shows that the stress rupture life of solution heat treated and double aged IN718 test pieces (plain samples) is only up to 40 hours under 750MPa at 650°C, this proves the notch strengthening effect of the HT1N/HT2N samples in this project, further verifying the improvements in IN718 stress rupture life by work hardening.

IN718 fasteners are loaded under the dwell fatigue mode at a high temperature in aeroengines, it is critical to enhance the fatigue resistance of IN718 at the thread section which possess the same stress concentration factor (Kt3) as the notched HT samples. Especially for coarse grain size IN718, HT3N performed relatively poorly in the dwell fatigue testing. Cold work has been proved to be one of the most effective ways to improve the fatigue performance and lower the notch sensitivity. The testing involving the fatigue and creep behaviour on the large bolt threads is discussed in the next section.

5.5 Fatigue and creep behaviour of cold worked IN718

The fatigue and creep behaviour of heavily coldworked IN718 is significantly different from the solution treated and directly aged IN718, which suggests that the shank area and the thread area of aero-engine IN718 bolts would react differently under in-service conditions. The bending and axial tensile fatigue tests carried out at the thread section can represent the fatigue and creep performance of the severe cold work IN718 with a stress concentration.

Both the as-received threads (CW samples) and the treated threads (CWF samples) were subjected to bending fatigue tests. The “baseline” fatigue tests (1-1-1-1 waveform) showed that the fatigue life of the CW sample was twice that of the CWF sample (see Table 4-5). This can be seen as evidence that cold work benefits the fatigue performance. The fracture surface of the CW sample displays typical fatigue failure in Figure 4-26 (a) and 4-27 (a). The crack initiates at the heavy coldwork zone near the thread root surface and develops intergranular behaviour mixing with a small amount of transgranular fracture. Since no creep was involved in the baseline fatigue testing, brittle fracture was observed in both samples. The CW sample failed at the stress concentration point in the middle of the test piece, whereas cracks initiated unexpectedly in the CWF sample might due to the sharp edge between the threads and the beam. Since no cracks were found at the threads in the failed CWF sample, it could be concluded that the fatigue life of the CW and CWF samples were equivalent at the threads where the stress is concentrated.

The results of dwell fatigue testing (1-120-1-1 waveform) were comparable for CW and CWF samples, both lasted over 700 hours and show the tip-retardation behaviour.

However, the test on the CW sample was manually interrupted since the p.d. levelled off and the crack was no longer growing due to the bluntness at the crack tip in Figure 4-35, whereas the CWF sample ran to failure. Referring the section 5.3 of analysing the microstructure in bending samples, even though the heavily coldworked condition might bring some concerns such as microvoids and excessive δ phase, however, the strengthening effect of cold work benefits more for IN718 aero-engine bolts in the bending fatigue testing.

To recap: the axial fatigue and creep behaviour of cold worked IN718 was also investigated. The IN718 aero-engine bolts were installed on the customised fixtures with 7-8 threads exposed in the air and subjected to both cyclic and static loading at 650˚C in stroke control. The changes in microstructure at the exposed threads, the load drop and the sample elongations elaborate the behaviour of heavily coldworked IN718. This was also to verify the fully engaged installation of bolts from losing the clamping force and further to understand the mechanism of high temperature dwell fatigue for heavily coldworked IN718. Referring the load vs elongation results in Table 4-47, the samples with the threads exposed in the air elongated approximately twice than the fully engaged samples, and the elongation was mainly contributed by the threads section instead of the shank, showing that the thread section is prone to plastic deformation and stress relaxation under static or dwell cyclic loading at high temperature. However, brittle fracture occurred without deformation when the thread-exposed sample was subjected to baseline fatigue testing (1-1-1-1 waveform), showing no sign of creep behaviour in Figure 4-38 and 4-39. Like the bending test, the 1-1-1-1 waveform testing condition led to failure from the cold worked thread roots. Compared to the fracture in the baseline fatigue testing, the behaviour was affected by

both dwell fatigue (1-120-1-1 waveform) and stress relaxation (static load) at the thread section including load drops, sample elongation and microvoid formation, which explains why the creep relaxation behaviour dominates in dwell fatigue tests for cold worked IN718.

To conclude, cold rolling notably benefits the fatigue performance at the thread section and considerably enhances the tensile properties. The heavy coldwork introduces a great number of dislocations and the plastic deformation of the crystal structure entangled in the alloy, leading to great difficulty in further dislocation movements, thus, the strength is significantly improved [136]. In addition, since the grains are heavily deformed and no complete grain boundaries can be found near the cold worked zone, the grain boundaries is also optimised to resist the slip bands, resulting in a lower sensitivity to crack initiation at the thread root [137]. However, the heavy coldwork also brings disadvantages when the section is exposed in the air under in-service conditions, such as the formation of microvoids, prematurely dissolving γ” phase and excessive δ phase. As a result, the exposed cold-rolled thread section tends to be elongated and softened while dropping the load. In real life, such a situation causes a loss of clamping force and needs to be avoided by fully screwing in the threads. Overall, cold work benefits more in terms of the mechanical performance of IN718 bolts, regardless the less welcoming changes in microstructure.

Chapter 6

6. Conclusions, industrial implications and future work

6.1 Conclusions

The raw materials for manufacturing the IN718 aero-engine bolts and the final products were studied in this project. A comprehensive understanding was achieved by carrying out the microstructure and mechanical characterisations on the IN718 bars and the real IN718 aero-engine bolts. The purpose of the experiments is to identify the optimum solution temperature within specifications and metal forming procedures of the IN718 aero-engine bolts, at the same time, learning the changing behaviours at the local areas of the IN718 bolts during in-service conditions. The final conclusions can be drawn:

1. Both large bolts and small bolts were characterised at the local areas, such as threads and threads root under the optical microscope. The etched samples displaying slip trends demonstrated the severe plastic deformations at these location by cold rolling of shaping a bolt. The microhardness results strongly proved the high degree of cold work brought by cold rolling process at the threads and thread root, demonstrating the uneven microstructure in an IN718 aero-engine bolt.
2. Delta phase precipitation HT vs bolts (quantity and morphology)

The solution-treatment temperature of manufacturing the IN718 aero-engine fasteners can be selected within 925°C-1010°C. Such wide temperature range covers the delta phase solvus temperature (997°C), resulting in the delta-rich, delta-lean, and delta-free types in the final products. To study the mechanical properties of these three types of IN718, phase analysis and grain size analysis were carried out on the HT samples. HT1 solution-treated at the lowest temperature within the range (925°C) temperature contained the highest content of delta phase, subsequently the lowest in γ" phase since delta phase and γ" share the same chemical composition Ni_3Nb. The pinning effect of delta phase resulted in the fine grain size in HT1. On the contrary, HT3 was solution-treated at the highest temperature (1010°C) presented a delta-phase free microstructure with the largest grain size. HT2 is intermediate of HT1 and HT3.

3. The microhardness results were interesting that HT1, HT2 and HT3 presented the similar hardness, even though the phases in each situation were largely different. HT1 with the lowest γ" phase was strengthened by a high density of grain boundaries, whereas the coarse grain HT3 was mainly strengthened by a great amount of γ" phase. Thus, the microhardness results reflected the balanced strengths in IN718 from phase fraction and grain size.
4. The raw IN718 bars were machined into the plain and notched test pieces, and applied the heat treatment as HT1, HT2 and HT3 for mechanical testing, which is considered to replicate the shank area of the IN718 bolts. HT1P (Plain) performed the worst in the axial-tensile dwell fatigue testing, presenting the tensile-dominated fracture surface, it prematurely failed possibly due to lack of the main strengthening phase, γ" precipitates. HT2P improved the dwell fatigue

life by reducing the delta phase content and offering adequate γ” phase to maintain the strength, a mixing structure of fine and coarse grain size effectively lowers the notch sensitivity. HT3P had a slightly longer fatigue life than HT2P, showing a typical brittle intergranular fracture surface. Large grain size in HT3 effectively improved the creep resistance.

Thus, it is better to avoid HT3 condition when choosing the shank heat treatments, since an impeccably smooth surface finish is highly impossible to achieve, additionally, the wear on surface during operation could be also disastrous for HT3 condition. The HT2 condition with mixed fine and coarse grain microstructure offers a low notch sensitivity, grain boundary strengthening and adequate γ” phase, which could be a good option for the shank section of IN718 bolts.

5. The notched HT samples further proved the notch sensitivity related to the solution temperatures. The HT3N sample failed the earliest by initiating cracks from the notch and showed an intergranular fatigue fracture surface. Whereas HT1N and HT2N with a higher ductility and a smaller grain size benefited from the notch strengthening with a larger deformation zone at the notch, which was equivalent to work hardening.

   Applying the static load on the notched sample showed the same trend, however, the life of all the samples considerably increased comparing to the dwell fatigue testing. This was also proved in the axial-tensile fatigue testing, the partially screwed bolt was damaged more under the cyclic load with a great load relaxation, implying that the fatigue mixing with creep mode worsen the work hardened IN718.

6. The as-receive large bolts were treated under the Group B and Group C conditions. A rather distinct microstructure change at the thread root was observed in both treatments. Several newly precipitated delta phase appeared by consuming the adjacent γ” phase with several microvoids surrounding close to the thread root surface. With static loading (Group C), the phenomenon was even clearer. Such change in microstructure can be concerning to the property and it is also found in small bolts after being treated. Similarly, the cross-sectional microstructure of the long-term tested large bolts at 650°C showed the maximum new delta phase and all γ” phase was dissolved within 30μm depth from the surface of the thread root.

   No newly formed delta phase or microvoids was detected in HT samples after the Group B treatment, this strongly proved that such microstructure change was related to the heavy coldwork at the threads area. Cold work stores considerable energy in IN718, which encourages the precipitation of delta phase and dissolution of γ” phase even though the temperature is lower than the IN718 TTT diagram requires.

7. A small amount of blocky δ precipitates were observed in the shank with a relatively fine grain size (Ø15μm-20μm, comparable to HT2 condition) in the as-receive large bolts, such few δ precipitates might not be able to well control the grain size. This is possibly due to the cold drawn process before delivering the bars to the bolt manufacturer, effectively restricting the grain size in the final products by encouraging the recrystallisation during the following solution treatment at 1000°C. The solution treatment temperature is close to the δ phase

solvus temperature which avoids the excessive needle-like δ precipitates and precipitates the blocky δ phase for the grain-boundary strengthening.

8. The bending fatigue properties on the real IN718 bolt were investigated in this study. Both CW and CWF samples ran more cycles in the dwell testing than the baseline testing, the dwell testing on the CW samples was discontinued, showing a blunt crack tip. The cross-section profiles near the crack showed the same phenomenon that the new δ phase consumed the original γ” phase with many microvoids at the thread root, however, the performance of CW sample was still better than the CWF sample. The CWF sample failed unexpectedly on the edge instead of the thread root with only half fatigue life of the CW sample under the baseline test. The dwell test opened the bigger cracks in the CWF sample compared to the CW sample at the same testing period. Thus, the cold rolling process at the thread root in IN718 bolts is necessary for aero-engine applications, even though it might raise a concern in terms of microstructure changing during in-service, the benefits are still over the concerns. Additionally, δ phase strongly stabilised the grain boundaries against creep, the super-solvus solution treatment on IN718 that eliminates δ phase is not ideal.
9. The axial-tensile fatigue testing and the stress-relaxation testing demonstrated that the partially screwed bolts elongated approximately twice than the fully screwed bolts after being tested, and a major load relaxation was found under the dwell fatigue test on the partially screwed bolts. This reveals that partially screwed bolts are highly risky when servicing in aeroengine, it is necessary to fully engage the threads to maintain the clapping force.

10. Based on the microstructure and mechanical characterisation carried out in this project, the optimal manufacture process of IN718 fasteners for aero-engine applications is proposed as follow:

    Alloy VIM/ESR – IN718 bars – Solution treatment at 968°C – Cold drown process (EN2952/AMS5962) – Forging bolt head – Solution treatment at 1000°C (around the delta phase solvus temperature ±3°C) – Ageing at 720°C/8h + 620°C/8h – Fillet/Threads rolling.

6.2 Industrial implications

This study has identified several microstructure changes of the existing IN718 fasteners during servicing in aeroengines. Significant microstructural instability was found at the thread root after the long-term thermal exposure under the high stress. The results from this project elaborated that the cold rolling process stores considerable energy and leads to the IN718 TTT diagram shifting down. A proposal in narrowing the manufacturing specifications was raised to closely control the microstructure and prevent the premature failure of IN718 bolts for aero-engine applications. Several refined requirements of examining the products can be added in the technical specification of IN718 aero-engine bolts, as follow:

1. Relatively fine grain size (Ø15~20μm) at the shank.

   This is to offer a medium to high bulk strength, a lower notch sensitivity, the improved tensile strength and LCF life.
2. A small amount of blocky δ phase.

This is to control the grain size and increase the creep resistance and ensure enough γ” in the matrix. No needle-like δ precipitates shall exist since they could deteriorate the strength.

3. Microvoids check at the thread root during the engine overhaul.

   Forming microvoids at the thread root can be an early sign of losing the clapping force. The excessive microvoids accompanied by the newly precipitated δ phase with missing γ” indicates the microstructural instability, the local deformation might have occurred in this case and the failure could happen soon.

6.3 Future work

The correlation between the manufacturing process of the IN718 bolts and the subsequent microstructure in the final products have been thoroughly discussed. An ideal microstructural model of IN718 aero-engine bolts was selected by carrying out a series of mechanical testing with the replicated real working conditions. The study also analysed how temperature, stress and heavy coldwork affected the microstructure changes and performance of IN718 by isolating these key factors on the testing.

It is also important to understand the limitation of this project and put forward to the ideas of future investigation based on the current results, involving in a few considerations:

- Predicting the bending fatigue life of the real IN718 large bolts by delivering more tests under the different conditions using the p.d. calibration created in this study.

- Optimising the cold rolling process at the threads and fillet to prevent the microstructural instability.
- More microstructure characterisation to investigate if cold work also encourages the other phases to precipitate or dissolve during the in-service condition, such as γ'.
- Looking for a solution to minimise the microvoids at the severely deformed regions over the long-term thermal exposure, considering the different coefficients of thermal expansion between δ phase and γ matrix.
- Answering the question of how it would be affected on the aero-engine bolts performance after the appearance of the microvoids at the thread root.
- Conducting more tests focusing on the tensile behaviour, creep behaviour and notch sensitivity at the shank using a lower stress to replicate the in-service condition.
- Looking for a substitute material instead of IN718.

  For instance, Alvac 718Plus is a promising candidate, more research focusing on the industrial implications of aero-engine fasteners shall be considered.

Chapter 7

7. References

1. Dietrich Eckardt, P.R. *Advanced Gas Turbine Technology: ABB/BBC Historical Firsts*. in *Proceedings of the ASME Turbo Expo 2001: Power for Land, Sea, and Air. Volµme 3: Heat Transfer; Electric Power; Industrial and Cogeneration.* 2001. New Orleans, Louisiana, USA.
2. Walsh, P.P. and P. Fletcher, *Gas turbine performance*. 2004: John Wiley & Sons.
3. Guide, A., *Aircraft Gas Turbine Engines Types and Construction*.
4. Aainsqatsi, K., *Schematic diagram illustrating the operation of a 2-spool, low-bypass turbofan engine, with LP spool in green and HP spool in purple.* 2018, Vector version of Turbofan operation (lbp).png by Emoscopes.
5. Sourmail, T., *The Gas Yurbine*. 2009.
6. Rolls-Royce plc., Section 3 Deliver, *The Jet Engine* (5th Ed.) 2015.
7. Czachor, R.P., *Unique challenges for bolted joint design in high-bypass turbofan engines.* J. Eng. Gas Turbines Power, 2005. **127**(2): p. 240-248.
8. Reed, R.C., *The Superalloys: Fundamentals and Applications*. 2008: Cambridge University Press.
9. Cervenka, M., *The Rolls-Royce Trent Engine*. 2000.
10. Miller, S., *Advanced materials mean advanced engines.* Interdisciplinary Science Reviews, 1996. **21**(2): p. 117-129.
11. Naeem, M., R. Singh, and D. Probert, *Implications of engine deterioration for a high-pressure turbine-blade's low-cycle fatigue (LCF) life-consumption.* International journal of fatigue, 1999. **21**(8): p. 831-847.
12. Zhenzhong, C., et al., *Failure mechanisms of bolted flanges in aero-engine casings subjected to impact loading.* Chinese Journal of Aeronautics, 2021. **34**(12): p. 125-144.
13. Melhem, G.N., *Aerospace fasteners: use in structural applications.* Encyclopedia of aluminum and Its Alloys, 2018.
14. Bing, Z., Z. Shouyang, and W. Hui. *Stability analysis of nut coefficient of aero-engine rotor connection bolt*. in *2020 6th International Conference on Mechanical Engineering and Automation Science (ICMEAS)*. 2020. IEEE.
15. Li, W., et al. *Development of ati 718Plus® for high temperature high strength fastener applications*. in *8th International Symposium on Superalloy 718 and Derivatives*. 2014. Wiley Online Library.
16. Roach, T.A., *Alloy 718 Fasteners Versatility and Reliability for Aerospace Design.* Superalloy, 1989. **718**: p. 381-389.
17. Tohit, K., et al. *Identifying Inconel 718 Fasteners Failure Using Structured Problem Solving Method*. in *IOP Conference Series: Materials Science and Engineering*. 2018. IOP Publishing.
18. Fazel, B., *Nonlinear Analysis and Structural Optimization of Aero-engine Casings Bolted Flange Connections*. 2016, University of Toronto (Canada).

19. Civil Aviation Authority (CAA), *Safety Regulation Group, CAP 718*, in *First Edition 24*. 2002, *Human Factors in Aircraft Maintenance and Inspection*.
20. A.Romeyn, N.T.S.B.A., *Technical Analysis Report 17/03, „Bolt Fracture High Pressure Turbine Disk Assembly*. 2003. p. 1-21.
21. Felinks, N., et al., *Enhanced Surface Quality of Internal Machined Contours.* Procedia CIRP, 2021. **96**: p. 313-318.
22. Merrison A, *The effect of cold work on the properties of high temperature fastener materials*, thesis, 2021.
23. Morad, A. and Y. Shash. *Nickel base superalloys used for aero engine turbine blades*. in *The International Conference on Applied Mechanics and Mechanical Engineering*. 2014. Military Technical College.
24. Muktinutalapati, N.R., *Materials for gas turbines–an overview.* Advances in gas turbine technology, 2011. **23**.
25. Hertzberg, J. and G. Was, *Isolation of carbon and grain boundary carbide effects on the creep and intergranular stress corrosion cracking behavior of Ni-16Cr-9Fe-xC alloys in 360 C primary water.* Metallurgical and Materials Transactions A, 1998. **29**(3): p. 1035-1046.
26. Soares, C., *Gas Turbines Chapter 12 - Maintenance, Repair, and Overhaul*, in *Gas turbines: a handbook of air, land and sea applications*. 2011, Elsevier.
27. Yong, C.K., et al., *A critical review of the material characteristics of additive manufactured IN718 for high-temperature application.* Metals, 2020. **10**(12): p. 1576.
28. Wilson, A., *Formation and effect of topologically close-packed phases in nickel-base superalloys.* Materials Science and Technology, 2017. **33**(9): p. 1108-1118.
29. Akca, E. and A. Gürsel, *A review on superalloys and IN718 nickel-based INCONEL superalloy.* Periodicals of Engineering and Natural Sciences (PEN), 2015. **3**(1).
30. Kang, B.-I., et al., *Effects of boron and zirconium on grain boundary morphology and creep resistance in Nickel-based superalloy.* Journal of Materials Engineering and Performance, 2019. **28**(11): p. 7025-7035.
31. Srivastava, R.R., et al., *Resource recycling of superalloys and hydrometallurgical challenges.* Journal of Materials Science, 2014. **49**(14): p. 4671-4686.
32. Durand-Charre, M., *The microstructure of superalloys*. 2017: Routledge.
33. Shao, J., et al., *Grain size evolution under different cooling rate in laser additive manufacturing of superalloy.* Optics & Laser Technology, 2019. **119**: p. 105662.
34. Torster, F., et al., *Influence of grain size and heat treatment on the microstructure and mechanical properties of the nickel-base superalloy U 720 LI.* Materials Science and Engineering: A, 1997. **234**: p. 189-192.
35. Du, B., et al., *Effects of grain size on the high-cycle fatigue behavior of IN792 superalloy.* Materials & Design (1980-2015), 2015. **65**: p. 57-64.
36. Williams, J.C. and E.A. Starke Jr, *Progress in structural materials for aerospace systems.* Acta materialia, 2003. **51**(19): p. 5775-5799.
37. Shi, D., et al., *Investigation on the grain boundary strengthening effect of a nickel-based superalloy.* Fatigue & Fracture of Engineering Materials & Structures, 2021. **44**(3): p. 822-831.

38. Hansen, N., *Hall–Petch relation and boundary strengthening.* Scripta materialia, 2004. **51**(8): p. 801-806.
39. Alabort, E., et al., *Grain boundary properties of a nickel-based superalloy: characterisation and modelling.* Acta Materialia, 2018. **151**: p. 377-394.
40. Products, B.W.A., in *Publication Grain Size and Material Strength*, U.f.O.S. Publication, Editor. 2010.
41. Du, B., et al., *Effects of Grain Refinement on the Low-Cycle Fatigue Behavior of IN792 Superalloys.* Crystals, 2021. **11**(8): p. 892.
42. Lukáš, P. and L. Kunz, *Role of persistent slip bands in fatigue.* Philosophical magazine, 2004. **84**(3-5): p. 317-330.
43. Michael D. Sangid etc., *The role of grain boundaries on fatigue crack initiation – An energy approach,* International Journal of Plasticity, 2010.
44. Kumar, S.S., et al., *Strain rate dependent microstructural evolution during hot deformation of a hot isostatically processed nickel base superalloy.* Journal of Alloys and Compounds, 2016. **681**: p. 28-42.
45. Turan, D., D. Hunt, and D. Knowles, *Dwell time effect on fatigue crack growth of RR1000 superalloy.* Materials science and technology, 2007. **23**(2): p. 183-188.
46. Saarimäki, J., *Cracks in superalloys*. Vol. 1897. 2018: Linköping University Electronic Press.
47. Gustafsson, D. and E. Lundström, *High temperature fatigue crack growth behaviour of Inconel 718 under hold time and overload conditions.* International Journal of Fatigue, 2013. **48**: p. 178-186.
48. Saarimäki, J., *Effect of Dwell-times on Crack Propagation in Superalloys*. Vol. 1739. 2015: Linköping University Electronic Press.
49. Gustafsson, D., E. Lundström, and K. Simonsson, *Modelling of high temperature fatigue crack growth in Inconel 718 under hold time conditions.* International journal of fatigue, 2013. **52**: p. 124-130.
50. Moverare, J.J. and D. Gustafsson, *Hold-time effect on the thermo-mechanical fatigue crack growth behaviour of Inconel 718.* Materials Science and Engineering: A, 2011. **528**(29-30): p. 8660-8670.
51. Saarimäki, J., M. Lundberg, and J.J. Moverare, *Grain Size Depending Dwell-Fatigue Crack Growth in Inconel 718.* Advanced Engineering Materials, 2018. **20**(6): p. 1700930.
52. Hertzberg, R.W., R.P. Vinci, and J.L. Hertzberg, *Deformation and fracture mechanics of engineering materials*. 2020: John Wiley & Sons.
53. Suzuki, A., H. Inui, and T.M. Pollock, *L12-strengthened cobalt-base superalloys.* Annual Review of Materials Research, 2015. **45**: p. 345-368.
54. Strondl, A., et al., *Investigations of MX and γ'/γ "precipitates in the nickel-based superalloy 718 produced by electron beam melting.* Materials Science and Engineering: A, 2008. **480**(1-2): p. 138-147.
55. Harte, A., et al., *The effect of solid solution and gamma prime on the deformation modes in Ni-based superalloys.* Acta Materialia, 2020. **194**: p. 257-275.
56. Choi, B.G., et al. *Eta phase formation during thermal exposure and its effect on mechanical properties in Ni-base superalloy GTD 111*. in *Superalloys 2004 (Tenth International Symposium)*. 2004.

57. Collier, J., A. Selius, and J. Tien, *On developing a microstructurally and thermally stable iron-nickel base superalloy.* J. P. Collier, A. O. Selius, J. K. Tien, Superalloys 1988, 1988: p. 43-52.
58. Collier, J.P., et al., *The effect of varying Al, Ti, and Nb content on the phase stability of INCONEL 718.* Metallurgical Transactions A, 1988. **19**(7): p. 1657-1666.
59. Bhadeshia, H.K.D.H., *Crystal structure of γ and γ'. Nickel Based Superalloys*.
60. Wei Li, *Machining-induced Residual Stress on a High Strength Nickel-Base Powder Superalloy*, thesis, 2008.
61. Rahimi, S., M. King, and C. Dumont, *Stress relaxation behaviour in IN718 nickel based superalloy during ageing heat treatments.* Materials Science and Engineering: A, 2017. **708**: p. 563-573.
62. Qin, H., et al., *Influence of stress on γ "precipitation behavior in Inconel 718 during aging.* Journal of Alloys and Compounds, 2018. **740**: p. 997-1006.
63. Dodaran, M., et al., *Effect of alloying elements on the γ'antiphase boundary energy in Ni-base superalloys.* Intermetallics, 2020. **117**: p. 106670.
64. Sundararaman, M., P. Mukhopadhyay, and S. Banerjee, *Some aspects of the precipitation of metastable intermetallic phases in INCONEL 718.* Metallurgical Transactions A, 1992. **23**(7): p. 2015-2028.
65. He, J., et al., *Interfaces in a modified Inconel 718 with compact precipitates.* Acta materialia, 1998. **46**(1): p. 215-223.
66. Dong Jianxin, X.X., Zhang Shouhua, *Coarsening behavior of γ" precipitates in modified inconel 718 superalloy.* Scripta Metallurgica et Materialia,, 1995. **33**(12): p. 1933-1940.
67. Sundararaman, M., P. Mukhopadhyay, and S. Banerjee, *Carbide precipitation in nickel base superalloys 718 and 625 and their effect on mechanical properties.* Superalloys, 1997. **718**(625): p. 367-378.
68. Reed, R.C., *The physical metallurgy of nickel and its alloys.* Superalloys-Fundamentals and Applications, 2006: p. 33-120.
69. Soni, P., *Mechanical alloying: fundamentals and applications*. 2000: Cambridge Int Science Publishing.
70. Garosshen, T., T. Tillman, and G. McCarthy, *Effects of B, C, and Zr on the structure and properties of a P/M nickel base superalloy.* Metallurgical Transactions A, 1987. **18**(1): p. 69-77.
71. Szczotok, A. and K. Rodak. *Microstructural studies of carbides in MAR-M247 nickel-based superalloy*. in *IOP Conference Series: Materials Science and Engineering*. 2012. IOP Publishing.
72. Hosseini, E. and V. Popovich, *A review of mechanical properties of additively manufactured Inconel 718.* Additive Manufacturing, 2019. **30**: p. 100877.
73. Deng, D., *Additively Manufactured Inconel 718: Microstructures and Mechanical Properties*. Vol. 1798. 2018: Linköping University Electronic Press.
74. Deng, D., *On the microstructures and anisotropic mechanical behaviours of additively manufactured IN718*. 2019, Linköping University Electronic Press.
75. Moiz, M., *The influence of grain size on mechanical properties of Inconel 718*. 2013.
76. Mitchell, A., et al., *Primary carbide and nitride precipitation in superalloys containing niobium.* High Temperature Materials and Processes, 1996. **15**(1-2): p. 27-40.

77. Liu, W., M. Yao, and Z. Chen, *Effect of cold rolling on the precipitation behavior of δ phase in Inconel 718.* Metallurgical and Materials Transactions A, 1999. **30**(1): p. 31-40.
78. Kañetas, P.J.P., et al., *Influence of the Delta Phase in the Microstructure of the Inconel 718 subjected to "Delta-processing" Heat Treatment and Hot Deformed☆.* Procedia Materials Science, 2015. **8**: p. 1160-1165.
79. Zhang, S., et al., *Precipitation behavior of δ phase and its effect on stress rupture properties of selective laser-melted Inconel 718 superalloy.* Composites Part B: Engineering, 2021. **224**: p. 109202.
80. Cheng, H., et al., *Influences of stress-aging on the precipitation behavior of δ phase (Ni3Nb) in a nickel-based superalloy.* Materials & Design, 2021. **197**: p. 109256.
81. Zhang, H., et al., *Microstructure evolution of IN718 alloy during the delta process.* Procedia engineering, 2017. **207**: p. 1099-1104.
82. Mei, Y., et al., *Effects of cold rolling on the precipitation and the morphology of δ-phase in Inconel 718 alloy.* Journal of Materials Research, 2016. **31**(4): p. 443-454.
83. Desvallées, Y., et al., *Delta phase in Inconel 718: mechanical properties and forging process requirements.* Superalloys, 1994. **718**(625): p. 281-291.
84. Manriquez, J.A., et al., *The high temperature stability of IN718 derivative alloys*. 1992, TMS Warrendale, PA, USA. p. 507-516.
85. Azadian, S., L.-Y. Wei, and R. Warren, *Delta phase precipitation in Inconel 718.* Materials characterization, 2004. **53**(1): p. 7-16.
86. Hassan, B. and J. Corney, *Grain boundary precipitation in Inconel 718 and ATI 718Plus.* Materials Science and Technology, 2017. **33**(16): p. 1879-1889.
87. Mahadevan, S., et al. *Evolution of δ phase microstructure in alloy 718*. in *Proceedings of the 7th International Symposium on Superalloy*. 2010.
88. FZE, B.B.C., *Delta Phase in Super-alloy Inconel 718: Its Characterization, Precipitation and Dissolution Kinetics.* 2018.
89. Shailesh Patel, J.d., Stephen Coryell, *Superalloy 718: Evolution of the Alloy from High to Low Temperature Application*, in *The Minerals, Metals & Materials Series. Springer, Cham*. 2018. p. 23-49.
90. Slama, C. and M. Abdellaoui, *Structural characterization of the aged Inconel 718.* Journal of alloys and compounds, 2000. **306**(1-2): p. 277-284.
91. Sabol, G. and R. Stickler, *Microstructure of nickel-based superalloys.* physica status solidi (b), 1969. **35**(1): p. 11-52.
92. Petkov, V.I., *Alloy 718 manufactured by AM selective laser melting: evaluation of microstructure and weldability.* 2018.
93. Koul, A., et al., *Development of a damage tolerant microstructure for Inconel 718 turbine disc material.* Superalloys, 1988. **1988**: p. 3-12.
94. Akca, E. and E. Trgo, *Metallographic procedures and analysis–a review.* Periodicals of Engineering and Natural Sciences (PEN), 2015. **3**(2).
95. W.J.Jensen, K.v., *Metals Handbook Ninth Edition, Volume 11 "Failure Analysis and Prevention", Failures of Mechanical Fasteners*.
96. Yunhao K, etc., *Phase Transformations During Continuous Cooling in Inconel 718 Alloys Manufactured by Laser Powder Bed Fusion and Suction Casting*. Materials Characterization, 185, 111764, 2022.

97. Nechache, A. and A.-H. Bouzid, *Creep analysis of bolted flange joints.* International Journal of Pressure Vessels and Piping, 2007. **84**(3): p. 185-194.
98. Akkurt, A., et al., *Comparison of hole surface finishing processes with roller burnishing method applied in copper materials.* Gazi University Journal of Science, 2014. **27**(1): p. 721-734.
99. Denkena, B., et al. *Development of combined manufacturing technologies for high-strength structural components*. Advanced Materials Research. 2010. Trans Tech Publ.
100. 5962, A.M.S., *Nickel Alloy, Corrosion and Heat-Resistant, Round Bars and Wire, 52.5Ni - 19Cr - 3.0Mo - 5.1Cb - 0.90Ti - 0.50Al - 18Fe, Consumable Electrode or Vacuum Induction Melted, 1775 °F (968 °C) Solution Treated and Work Strengthened, Precipitation Hardenable* 2012, SAE International Group.
101. 5662M, A.M.S., *Nickel Alloy, Corrosion and Heat-Resistant, Bars, Forgings, and Rings 52.5Ni - 19Cr - 3.0Mo - 5.1Cb (Nb) - 0.90Ti - 0.50Al - 18Fe Consumable Electrode or Vacuum Induction Melted, 1775 °F (968 °C) Solution Heat Treated, Precipitation-Hardenable*. 2009, SAE International Group.
102. Standards, S.A.I., *Technical Specification No.24, Manufacturing Specification For bolts* 2007, The Society of British Aerospace Companies Limited.
103. Theska, F., et al., *On the early stages of precipitation during direct ageing of Alloy 718.* Acta Materialia, 2020. **188**: p. 492-503.
104. Morris, J., *Dislocation-controlled plasticity of crystalline materials: Overview.* Encyclopedia of Materials: Science and Technology, 2011: p. 2245-2255.
105. Hayes, R., et al., *Effect of heat treatment on the combination stress-rupture properties of allvac 718plus™.* Materials Science and Engineering: A, 2009. **510**: p. 256-261.
106. D.o.I.f.t.P.o.M., *Introduction to Deformation Processes,* University of Cambridge, 2005.
107. Eigenmann, B., V. Schulze, and O. Volringer, *Surface residual stress relaxation in steels by thermal or mechanical treatment.* Society for Experimental Mechanics, Inc.(USA), 1994: p. 598-607.
108. Prevéy, P.S., *The effect of cold work on the thermal stability of residual compression in surface enhanced IN718*. 2000, LAMBDA RESEARCH CINCINNATI OH.
109. Rongbin, L., et al., *Effects of cold rolling on precipitates in inconel 718 alloy.* Journal of materials engineering and performance, 2002. **11**(5): p. 504-508.
110. Rafiei, M., H. Mirzadeh, and M. Malekan, *Micro-mechanisms and precipitation kinetics of delta (δ) phase in Inconel 718 superalloy during aging.* Journal of Alloys and Compounds, 2019. **795**: p. 207-212.
111. Páramo-Kañetas, P.J., et al., *Analysis of strain-induced precipitates by delta-processing in Inconel 718 superalloy.* Materials Characterization, 2021. **173**: p. 110926.
112. Jambor, M., et al., *Phase transformations in nickel base superalloy inconel 718 during cyclic loading at high temperature.* Production engineering archives, 2017. **15**.
113. Asthana, R., A. Kumar, and N.B. Dahotre, *Materials processing and manufacturing science*. 2006: Elsevier.
114. Humphreys, F.J. and M. Hatherly, *Recrystallization and related annealing phenomena*. 2012: Elsevier.

115. Sellars, C., *Recrystallization of metals during hot deformation.* Philosophical Transactions of the Royal Society of London. Series A, Mathematical and Physical Sciences, 1978. **288**(1350): p. 147-158.
116. S. Masters , *External Thread Dimensions for Unified UNF Screw Threads*,. 2016, SM Fastener Manufacturers and Distributors
117. Rolls-Royce plc., *Section 1 Design, The jet engine (5th edition)*. 2015.
118. Manikandan, S., D. Sivakumar, and M. Kamaraj, *Welding the Inconel 718 superalloy: Reduction of micro-segregation and laves phases*. 2019: Elsevier.
119. Totten, G.E., L. Xie, and K. Funatani, *Handbook of mechanical alloy design*. Vol. 164. 2003: CRC press.
120. Elefterie, C., et al. *Aeronautical requirements for Inconel 718 alloy*. in *IOP conference series: materials science and engineering*. 2017. IOP Publishing.
121. Soares, C., *Gas turbines: a handbook of air, land and sea applications*. 2011: Elsevier.
122. Jordon, J.B., et al., *Fatigue in Friction Stir Welding*. 2019: Butterworth-Heinemann.
123. Wu, Z., et al., *Recent developments in cold dwell fatigue of titanium alloys for aero-engine applications: A review.* Journal of Materials Research and Technology, 2022.
124. Evans, W., *Time dependent effects in fatigue of titanium and nickel alloys.* Fatigue & Fracture of Engineering Materials & Structures, 2004. **27**(7): p. 543-557.
125. Panigrahi, S.K. and N. Sarangi, *Aero Engine Combustor Casing: Experimental Design and Fatigue Studies*. 2017: CRC Press.
126. Hall, J., *Safety Recommendation*. 2000, NATIONAL TRANSPORTATION SAFETY BOARD WASHINGTON DC.
127. Shipley, R.J., B.A. Miller, and R.J. Parrington, *Introduction to Failure Analysis and Prevention.* Journal of Failure Analysis and Prevention, 2022. **22**(1): p. 9-41.
128. Becker, W.T., et al., *ASM handbook.* Failure analysis and prevention, 2002. **11**: p. 107.
129. Jensen, W.J., *Failures of mechanical fasteners.* ASM International, ASM Handbook., 1986. **11**: p. 529-549.
130. Koul, K. and P. Immarigeon, *Effect of microstructure on fatigue crack growth rate of alloy 718 at 650 C.* Superalloys 718 Metallurgy and Applications (1989), 1989: p. 697-712.
131. FZE, B.B.C., *Delta Phase in Super-alloy Inconel 718: Its Characterization, Precipitation and Dissolution Kinetics*. 2022.
132. University of Cambridge, *12.7: Designing for Creep Resistance - Nickel Based Superalloys*. 2020.
133. Chandler, H., *Heat treater's guide: practices and procedures for nonferrous alloys*. 1996: ASM international.
134. Lei, X., et al., *Notch strengthening or weakening governed by transition of shear failure to normal mode fracture.* Scientific reports, 2015. **5**(1): p. 1-10.
135. Nixon, W.A. and E.M. Schulson, *A notch-strengthening effect in fresh-water ice.* Journal of Glaciology, 1990. **36**(122): p. 107-111.

136. Beere, W., *Stresses and deformation at grain boundaries.* Philosophical Transactions of the Royal Society of London. Series A, Mathematical and Physical Sciences, 1978. **288**(1350): p. 177-196.
137. Cui, C., et al., *Notch sensitivity of heavily cold-rolled Ni3Al foils.* Scripta materialia, 2005. **53**(12): p. 1339-1343.

Appendix

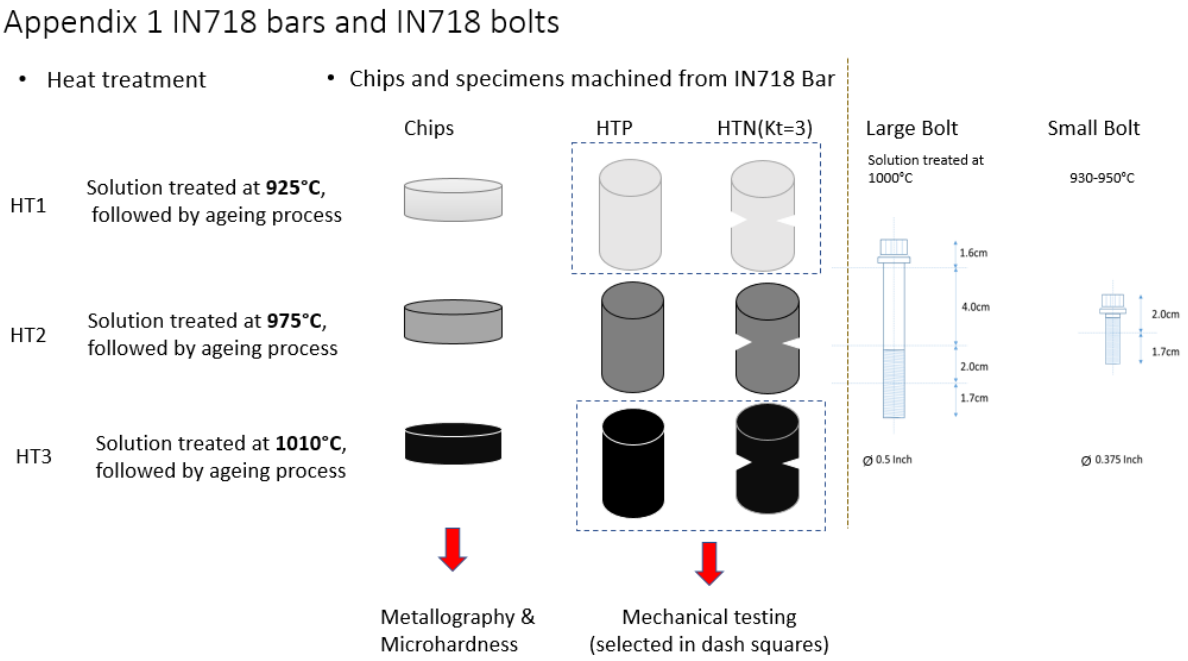
Appendix 1 IN718 bars and IN718 bolts
• Heat treatment
• Chips and specimens machined from IN718 Bar
Chips
HTP
HTN(Kt=3)
Large Bolt
Solution treated at 1000°C
Small Bolt
930-950°C
HT1
Solution treated at 925°C, followed by ageing process
HT2
Solution treated at 975°C, followed by ageing process
HT3
Solution treated at 1010°C, followed by ageing process
1.6cm
4.0cm
2.0cm
1.7cm
Ø 0.5 Inch
2.0cm
1.7cm
Ø 0.375 Inch
Metallography & Microhardness
Mechanical testing (selected in dash squares)

Appendix 2 Microstructure Characterisation

Samples	Tasks	Comments
HT1, HT2 and HT3	Grain size & phases characterisation, microhardness	Microstructure comparison under the different solution temperatures.
Group B HT1, HT2 and HT3	Group B treated HT samples followed by grain size & phases characterisation.	Effect of thermal exposure on the microstructure of HT samples.
Large Bolt	Grain size & phases characterisation, microhardness	Microstructure of the as-received Large Bolt.
Group B Large Bolt	Phases characterisation, microhardness	Effect of thermal exposure on the microstructure of Large Bolt.
Group C Large Bolt	Phases characterisation, microhardness	Effect of static loading at 650°C on the microstructure of Large bolt.
Small Bolt	Grain size & phases characterisation, microhardness	Microstructure of the as-received Small Bolt.
Group B Small Bolt	Phases characterisation, microhardness	Effect of thermal exposure on the microstructure of Small Bolt.
Bending sample (CW)	EBSD, hardness	Local observation at threads
Bending sample (CWF)	EBSD, hardness	Microstructure of cold-work free condition; comparison of as CW samples.

Appendix 3 Mechanical Testing

Samples	Testing	Comments
Bending samples (CW)	Three-point baseline bending fatigue (1-1-1-1)* Three-point dwell bending fatigue (1-120-1-1)*	Bending fatigue behaviour at cold worked threads
Bending samples (CWF)	Three-point baseline bending fatigue (1-1-1-1)* Three-point dwell bending fatigue (1-120-1-1)*	Bending fatigue behaviour at cold-work free threads
Large bolts (Partially screwed)	Axial-tensile fatigue (1-1-1-1) # Axial-tensile dwell fatigue (1-120-1-1) # Stress-relaxation #	Large bolt axial-tensile fatigue behaviour with stress concentrating at the threads
Large bolts (Fully screwed)	Axial-tensile dwell fatigue (1-120-1-1) # Stress relaxation #	Large bolt axial-tensile fatigue behaviour with stress concentrating at the shank/1st engaged thread.
HTP	Axial-tensile dwell fatigue (1-120-1-1)*	IN718 axial-tensile fatigue behaviour
HTN	Axial-tensile dwell fatigue (1-120-1-1)* Stress relaxation*	IN718 with stress concentration axial-tensile fatigue behaviour

* Load control
# Displacement control